Experimental Investigations of Long-Distance Cryogenic Helium Pulsating Heat Pipes and The Development of a Novel Orientation Independent Hybrid Conventional-Pulsating Heat Pipe

by

Logan M. Kossel

A dissertation submitted in partial fulfillment of

the requirements for the degree of

Doctor of Philosophy

(Mechanical Engineering)

at the

UNIVERSITY OF WISCONSIN – MADISON

2024

Date of final oral examination: 8/15/2024

The dissertation is approved by the following members of the final oral committee:
    John M. Pfotenhauer, Professor Emeritus, Mechanical Engineering
    Franklin K. Miller, Associate Professor, Mechanical Engineering
    Gregory F. Nellis, Professor, Mechanical Engineering
    Mark H. Anderson, Associate Professor, Mechanical Engineering
    Jennifer A. Franck, Assistant Professor, Engineering Physics

Approved

_____

John Pfotenhauer

Professor Emeritus

Department of Mechanical Engineering

_____

Franklin Miller

Associate Professor

Department of Mechanical Engineering

Abstract

A large-scale experimental study of extended-length helium pulsating heat pipes in the vertical orientation was performed in which the adiabatic length, applied heat load, and fill ratio were varied. From time-averaged data, trends in thermal performance are identified with respect to these parameters, as well as thermodynamic phases utilizing redundant temperature and pressure measurements on adjacent tubes in the adiabatic section. While the PHPs tested showed excellent performance when the operating fluid is two-phase, fully or partial single-phase operating states were stable and common, with excellent performance observed when half the tubes contained subcooled liquid for some fill ratios. Identifying thermodynamic phases at different locations of the PHP also allowed for the identification of uni-directional flow modes. Furthermore, a persistent imbalance in the mass contained in adjacent tubes was observed for nearly every combination of parameters, suggesting that gravity is the primary driving force for helium PHPs in the vertical orientation and that their behavior is not unlike that of a two-phase thermosiphon, explaining the observed length independence. From time-series data, the unique adiabatic section measurement configuration allows for fluid velocity estimations when single-phase. Phase and flow observations were utilized to explain thermal performance trends, including failure modes. Additional experiments of long-distance helium pulsating heat pipes in the horizontal orientation confirmed their gravity-dependence, as the PHPs were nonfunctional.

Due to the observed gravity dependence of long-distance helium pulsating heat pipes (PHPs), alternative remote cooling options in the saturated helium temperature range are required for applications where gravity is nonexistent or the orientation is not gravitationally favorable. A novel orientation-independent helium heat pipe design, named the Hybrid-Conventional Pulsating Heat Pipe (HCPHP), which operates similarly to a conventional heat pipe yet retains the advantageous geometry of a pulsating heat pipe, is presented and experimentally verified. The

HCPHP is capable of transferring significantly more heat with greater thermal conductance over longer distances than the current state-of-the-art helium heat pipes. Indeed, the HCPHP demonstrated up to 195 mW of heat transfer with thermal conductances up to 324 mW/K with a 250 mm heat transfer distance. Experimental investigations of the HCPHP consisted of parametric studies concerning the condenser temperature, fluid fill ratio, and applied heat load. The thermal performance of the HCPHP is characterized and analyzed in terms of these varied operational parameters. Additionally, a framework for understanding the equations of motion for the fluid in a PHP is established from a simple one-dimensional momentum balance, demonstrating PHPs' positive correlation between their adiabatic length and gravitational dependence. Finally, features of the HCPHP's unique thermohydraulic behavior are analyzed in detail to describe several interesting experimental observations in terms of the capillary driving forces and the viscous resistive forces.

<u>Acknowledgements</u>

First and foremost, I would like to express my deepest gratitude to my advisors, Professors John Pfotenhauer and Franklin Miller. I never would have thought that the 2018 China study abroad program would have led to one of the most impactful experiences of my life: being your student. John – Beyond the academic realm, I am grateful for our friendship that has developed over the course of my PhD. Your mentorship has not only shaped my research but has also enriched my life in many ways. Franklin – I think I could spend an eternity talking with you and picking your brain on topics within and far beyond cryogenics. Your excitement for science is admirable, and you have never failed to get me excited about learning a new topic.

It is difficult to articulate how honored I am to have had the opportunity to learn from you both. I appreciate your patience and the countless hours you've invested in helping me navigate the complexities of our work. I will sorely miss our weekly meetings together.

Also, a HUGE thank you to Wes Johnson from NASA Glenn Research Center for essentially being my third advisor. Your invaluable guidance and perspective have shaped this project and ensured its success. I remember someone at Glenn said that you "have forgotten more than most people know," and I certainly found that to be true, as any problem I presented to you was swiftly answered. Thank you for playing such an active role in advising me on my project. You've helped me a lot, and I really appreciate it.

Thank you to Professor Greg Nellis, who taught numerous classes of mine beginning in my first year of college in 2016. Throughout my time at SEL, you have always been a reliable source of information and support, and your books will always have a place on my shelf. Moreover, thank you to Professors Jennifer Franck and Mark Anderson for also serving on my dissertation committee.

However, this adventure began long before I started graduate school. Most of all, I would like to thank my family and friends for supporting me every step of the way from the very beginning. To my mom, Jane, and my sisters, Olivia and Natalie: The list of things I could thank you for would be longer than this thesis. I am so grateful for your never-ending support and encouragement in following my dreams. Sam Potter, Dean Zillner, Chris Lindblom, Zandar Bursac, Brandon Munoz, David Marrone, and Mike Mavroulis: You are the best friends a guy could ask for. Love ya buds.

To those listed here: you have forged the path for me; all I had to do was take it.

Funding

Table of Contents

List of Figures

List of Tables

1. Background and Literature Review

1.1. Introduction

Pulsating Heat Pipes (PHPs) [1], also known as Oscillating Heat Pipes (OHPs), are a unique variant of heat pipe that have gained considerable research interest in recent years [2, 3] due to their ability to transfer heat with significantly higher effectiveness compared to traditional thermal conductors. Like other heat pipes, PHPs take advantage of phase change processes as the driving forces for fluid movement, making them entirely passive and thermally driven with no external flow devices required. Despite their invention being over thirty years ago by Akachi [1] and the abundance of contemporary research, many aspects of the pulsating heat pipe's operation as still unknown owing to the large number of potential design parameters, nonintuitive experimental results, and modelling difficulty [4 - 7]. As a next-generation heat pipe technology, pulsating heat pipes have numerous advantages over the current state-of-the-art, Loop Heat Pipes (LHPs) [8], such as their simple and cost-effective construction, physical and operational flexibility, as well as their reduced mass.

A PHP is primarily composed of a small-diameter capillary tube that traverses a given distance multiple times, turning each time, and connecting at the ends to form a closed loop. Several key aspects of a PHP's design are described by the schematic in Figure 1.1, such as the serpentine shape of the capillary tube, the plug-slug flow regime, and the distinct sections defined by the heat flow direction. The inner-diameter of the capillary tubes is sized such that the surface tension forces acting on the working fluid dominate over the gravitational forces, which gives rise to the plug-slug flow regime, where alternating and distinct sections of saturated vapor and liquid exist along the length of the tube. This distribution of liquid and vapor is essential to a PHP's function, since otherwise the liquid would pool at the lowest point and the vapor at the highest.

Furthermore, PHPs are typically comprised of three sections: (1) The evaporator, where a heat load is absorbed by the fluid, (2) the condenser, where the previously absorbed heat is rejected to a cooling source, and (3) the adiabatic section, where no external heat transfer occurs, and the fluid travels between the other two sections. Phase change occurs in the aptly named condenser and evaporator sections that drives the fluid through the adiabatic section, with condensation reducing the fluid's specific volume (contraction) in the condenser, and boiling increasing the fluid's specific volume (expansion) in the evaporator. The expansion and contraction of the fluid in these sections occurs continuously and simultaneously, resulting in flow between them through the adiabatic section.
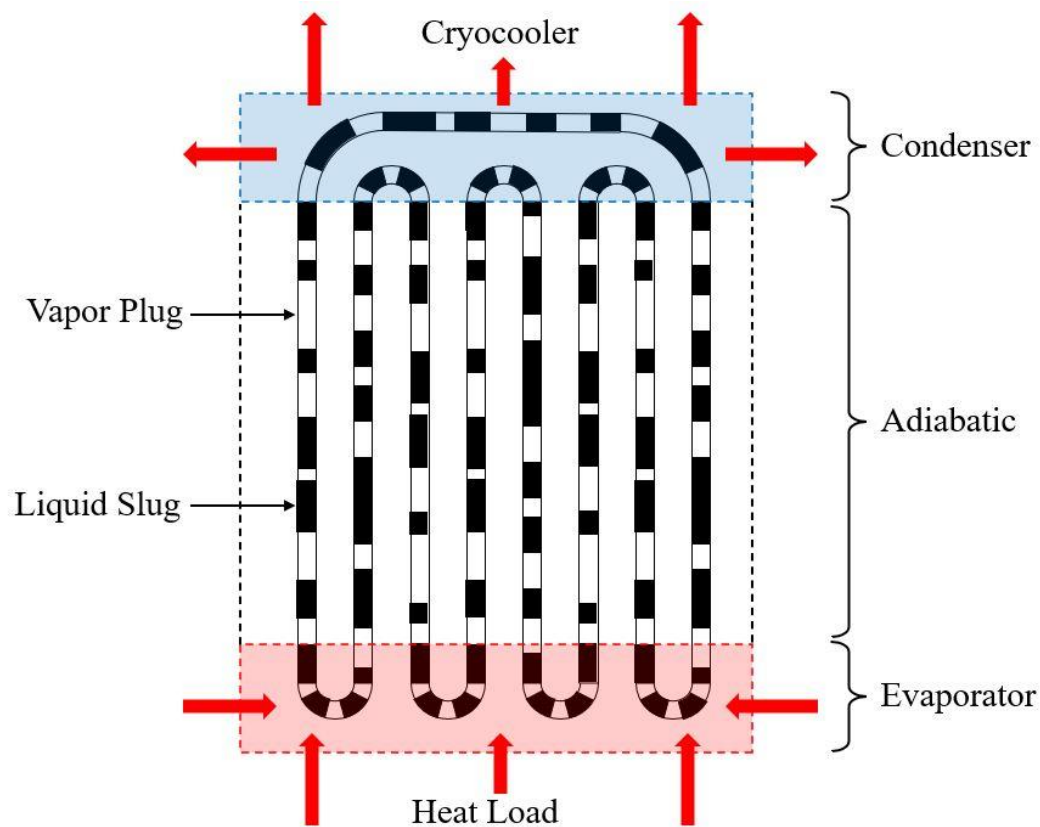
Figure 1.1. PHP schematic showing the serpentine shape of the capillary tubes, the three distinct sections defined by heat flow direction, and the plug-slug mass distribution.

While the above description gives a high-level explanation of a PHP's function, it is not enough to accurately describe, let alone model, the complex motion of the fluid. In fact, the behavior of the plugs and slugs is inherently chaotic due to the two-phase flow instabilities originating in the evaporator and condenser sections. The pulsating (or oscillating) motion of the fluid is the namesake for these devices. Indeed, while the motion of individual plugs and slugs essentially random, pulsating heat pipes reach a pseudo steady-state at a constant heat load with a small number of thermal oscillation modes, implying that the random motions sum to result in a net uni-directional mass transfer.

Characterizing the fluid and thermal behavior of pulsating heat pipes is a deceptively complicated problem. While the pseudo steady-state thermal behavior suggests that the traditional quasi-equilibrium thermodynamic modelling approach is warranted, there is not enough known information to invoke such a simple analysis. The oscillatory and random behavior of the fluid may suggest that a thermoacoustic or statistical analysis is more appropriate. Ultimately, there is a large number of interrelated variables that affect the behavior of pulsating heat pipes, which make the problem somewhat intractable. Future adoption of pulsating heat pipes may very well rely on empirical correlations stemming from experiments.

As previously mentioned, the magnitudes of the surface tension and gravitational forces relative to one another are a defining aspect of pulsating heat pipes. The ratio of these two forces defines the dimensionless Eotvos number, expressed in Equation 1.1. Taking the square root of the Eotvos number results in the Bond number, which is also commonly used to compare the surface tension and gravitational forces and is expressed in Equation 1.2.

$$Eo = \frac{F_g}{F_s} = \frac{(\rho_l - \rho_v)gD^2}{\sigma} \qquad (1.1)$$

$$Bo = \sqrt{Eo} = \sqrt{\frac{(\rho_l - \rho_v)gD^2}{\sigma}} \tag{1.2}$$

Where Eo is the Eotvos number, Bo is the Bond number, F_g is the gravitational force, F_s is the surface tension force, ρ_l is the saturated liquid density, ρ_v is the saturated vapor density, σ is the two-phase surface tension, g is the gravitational acceleration, and D is the diameter of the capillary tube. Experimental studies from White and Beardmore [9] compare the Froude number, the ratio of the inertial and gravitational forces, with the Eotvos number for numerous two-phase fluids. The key result is that for all fluids, the Eotvos number converges to 4 when the Froude number is zero. What this means is that for a two-phase fluid, a vapor bubble will be confined by surface tension to the walls, restricting its movement upwards when the surface tension forces are greater than one-fourth of the gravitational forces. The Froude number as a function of Eotvos number derived from this study is shown in Figure 1.2. Similarly, for a given fluid, the Froude number reaches a constant value with increasing Eotvos number, meaning that the when the surface tension forces become negligible, a vapor bubble will rise through the liquid at terminal velocity.

This result can be applied to the capillary tubes of a pulsating heat pipe to define the critical diameter at which the required plug-slug regime can exist. The critical diameter can be calculated by setting the expression for Eotvos number in Equation 1.1 equal to 4, and rearranging for the hydraulic diameter, which has been done in Equation 1.3. The critical diameter is the upper limit for the plug-slug mass distribution to exist, and decreasing the tube diameter from the critical value will further reduce the effects of gravity. An interesting implication of Equation 1.3 is that other than gravity, the critical diameter only depends on two-phase fluid properties, and therefore the saturation temperature (or pressure). The Bond number requirement is more lenient when

considering the existence of a thin liquid film coating the microchannel walls. Therefore, the coefficient of 2 in Equation 1.3 has been adjusted in some PHP studies [5, 10, 11] to account for the thin film, up to values of 2.74.
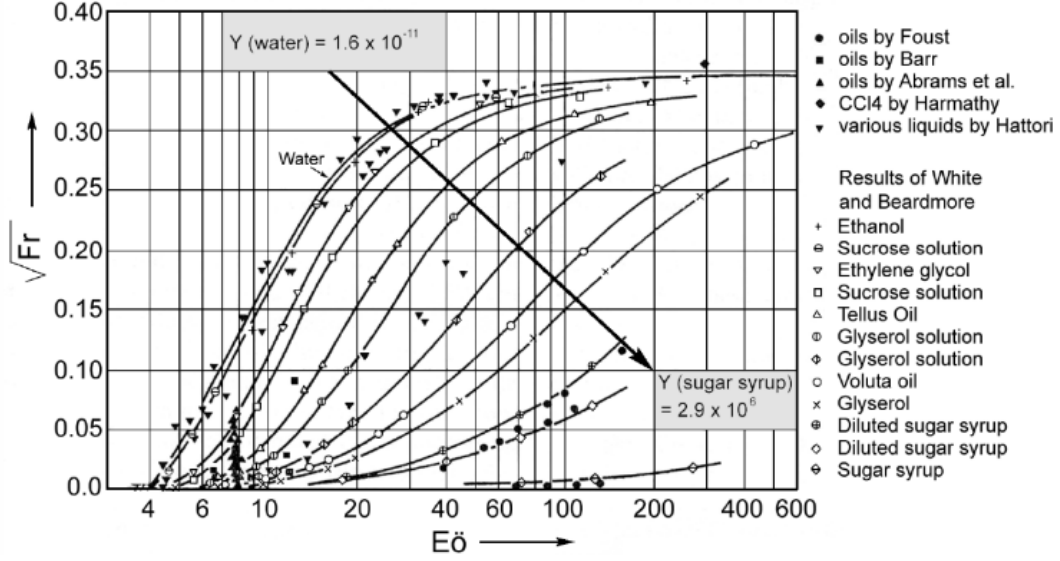
Figure 1.2. Froude number as a function of Eotvos number for several fluids with varying two-phase surface tension [9].

$$D_{crit} = 2\sqrt{\frac{\sigma}{(\rho_l - \rho_v)g}} \tag{1.3}$$

Where D_{crit} is the critical diameter. Another essential operating parameter of pulsating heat pipes is the liquid fill ratio, which is defined as the liquid volume fraction of the two-phase working fluid, and is expressed in Equation 1.4. The fill ratio is typically expressed as a percentage, hence the factor of 100 in Equation 1.4. In analyses of other types of heat pipes, the fill ratio of a PHP would be analogous to the liquid inventory, however, PHPs are unique in that the liquid inventory is stored in the primary fluid flow loop rather than in an external reservoir.

$$FR = 100\frac{V_l}{V_{tot}} \tag{1.4}$$

Where FR is the fill ratio, V_l is the saturated liquid volume, and V_{tot} is the total PHP volume. In the extreme cases of 0% and 100% fill ratios, a PHP will be filled entirely with saturated vapor and liquid, respectively. In both cases, PHPs will behave similarly to single-phase thermosiphons, albeit ineffective ones due to the nature of the PHP geometry. This suggests that an optimal value of the fill ratio exists in between. Logically, excess vapor would result in evaporator dry-out at low heat loads, while excess liquid would require a higher driving force due to higher inertia and viscous damping. Indeed, several experimental studies have identified an optimal fill ratio, which can depend on adiabatic length, working fluid, number of turns, and potentially many other parameters. For example, a helium PHP experiment conducted by Fonseca, Pfotenhauer, and Miller [12, 13] showed that for a 21-turn PHP, the optimal fill ratio was 70% for an adiabatic length of 0.3 m, and 58% for an adiabatic length of 1 m. Moreover, experiments of helium PHPs by Li, Li, and Xu [14] showed that the optimal fill ratio can also be a function of the applied heat load. For a 24-turn helium PHP with a 0.1 m adiabatic length in the vertical orientation, it was found that a fill ratio of 48.8% was optimal for heat loads up to 0.8 W, while beyond 0.8 W, a fill ratio of 66.1% was optimal.

Furthermore, analyses by Sun, et. al. [15] demonstrate that the fill ratio changes with the fluid's saturation temperature, which supports the idea that fill ratio could depend on applied heat load. Thus, most studies define the fill ratio at which tests are conducted with the initial fill ratio, FR_0, when no heat load is applied. Depending on whether the initial fill ratio for a given experiment results in the PHP's fluid having a specific volume less than or greater than the critical specific volume, the temperature-dependent fill ratio will either increase or decrease, respectively, as shown for Nitrogen in Figure 1.3. Near the critical point, the temperature dependance of the fill ratio becomes stronger.
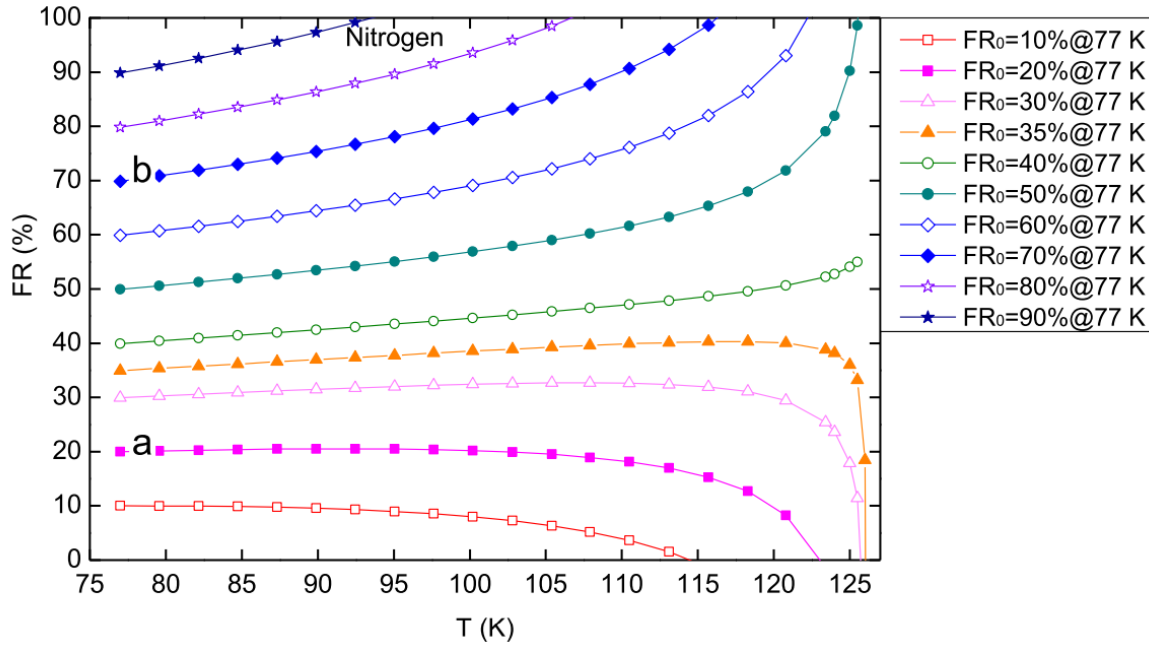
Figure 1.3. Fill ratio as a function of saturation temperature for nitrogen at several initial fill ratios, showing that the temperature-dependent fill ratio will either increase or decrease depending on the initial specific volume [15].

1.2. Heat Pipe Background

A heat pipe is an advanced heat transfer technology that utilizes passive fluid flow to transfer heat over a specified distance with very low thermal resistance. Heat pipes have been the subject of decades of experimental and theoretical research due to their significant thermal advantage over solid conductors, which are commonly utilized for a wide range of applications in many industries. For example, computer chips' ever-increasing performance and heat output have warranted greater cooling capabilities. Due to their excellent thermal performance, heat pipes and vapor chambers have become a vital component of the thermal architecture of many computers, especially compact systems such as laptops and tablets. Additionally, heat pipes are a critical element of many spacecraft thermal control systems since they can transfer orders of magnitude more heat per mass than solid conductors. Indeed, various unique heat pipe technologies have been developed to suit specialized applications in many industries.

1.2.1. Conventional Heat Pipes

The most common type of heat pipe is the conventional heat pipe, sometimes referred to simply as a "heat pipe" due to its ubiquity. Conventional heat pipe flows are driven by the pumping pressure generated by high-curvature vapor-liquid interfaces, also known as the capillary or surface tension force. A wick structure, which transfers saturated liquid in one direction, provides many parallel flow paths while also providing a porous surface for many high-curvature interfaces to form. The saturated vapor flows antiparallel to the saturated liquid from the evaporator to the condenser in a space free of structure. With no heat applied, the curvature of the two-phase interfaces in the evaporator and condenser sections is equal, resulting in no net pumping force. However, with a heat load applied, the evaporator interface recedes into the wick, increasing its curvature. Meanwhile, the condenser section floods with liquid, decreasing the interface curvature. Thus, the capillary pumping forces at each end are unbalanced, resulting in uni-directional circulation of the fluid. Figure 1.4 shows a general schematic of a conventional heat pipe.
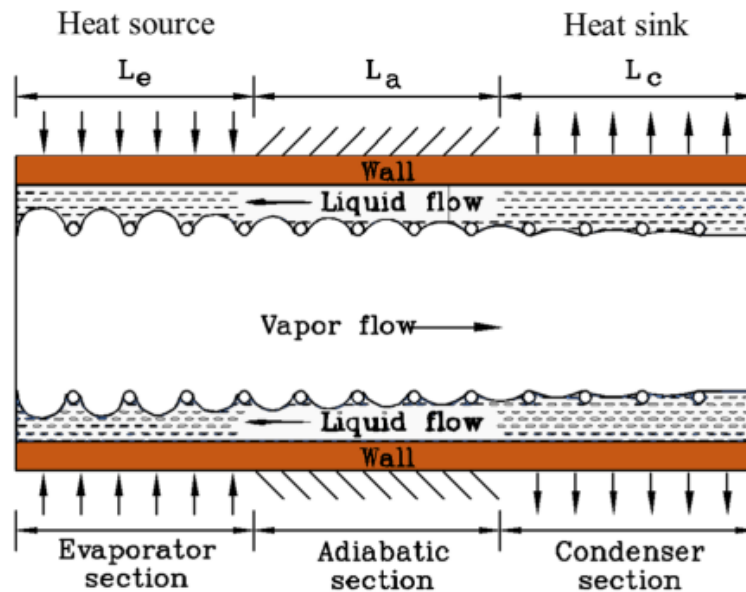
Figure 1.4. A schematic of the axial cross section of generalized conventional heat pipe, showing the liquid and vapor flow paths, various heat pipe sections, and the liquid-vapor interface shapes [16].

The design of conventional heat pipes is centered around its wicking structure. The wick is responsible for transporting the saturated liquid from the condenser to the evaporator while simultaneously providing a porous surface to generate high-curvature two-phase interfaces. The primary challenge of wick design is the opposing geometric requirements of the capillary driving force and the viscous resistive force. The capillary driving force requires small flow passages to maximize the interface curvature and, therefore, the overall pumping effect. However, the viscous force requires large flow passages to minimize the flow energy lost via viscous dissipation.

Moreover, viscous effects are exacerbated in the wick due to the higher viscosity of saturated liquid relative to saturated vapor. Hence, many wick designs provide numerous parallel liquid flow paths that reduce the flow's mean velocity while maintaining adequate mass flow. Sintered metals, wrapped screens, and axial grooves are examples of common structures, schematics of which are shown in Figure 1.5. Alternatively, liquid arteries may be incorporated into wick structures, which provide a large axial path for liquid to flow while forcing the radial phase change to occur across a fine porous structure.

| (a) | (b) | (c) |
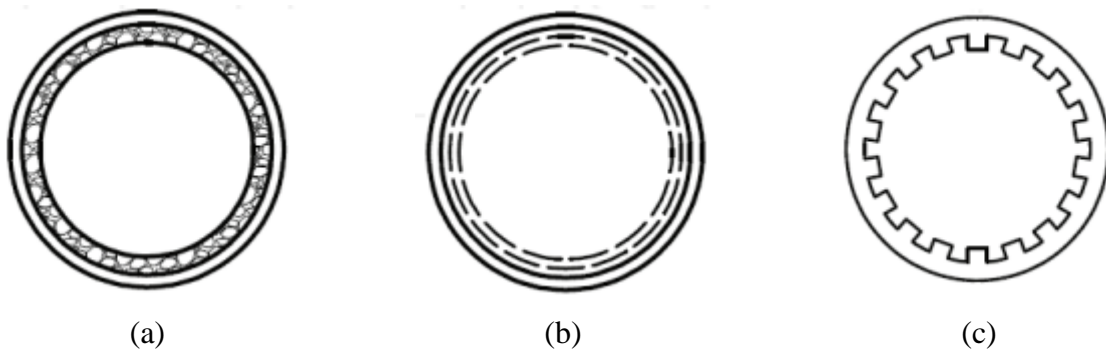
Figure 1.5. Radial cross-section schematics of a conventional heat pipe with a (a) sintered metal wick, (b) wrapped screen wick, and (c) axial groove wick [17].

Several operational limits constrain the heat transfer abilities of conventional heat pipes. First, the capillary limit dictates heat pipe failure from the capillary pump's inability to overcome adverse forces, such as viscosity. This limit is the foremost to consider when analyzing a heat pipe

design, and it mainly concerns the structure of the wick. Additionally, the boiling limit is reached when nucleate boiling occurs in the wicked part of the evaporator section, which reduces the effectiveness of the wick in creating stable two-phase interfaces. With an excessive applied heat flux, relatively large vapor bubbles can become trapped in the wick, blocking liquid and rendering a significant fraction of the wick useless due to the lack of two-phase interfaces. The sonic limit, which is not necessarily a failure mode, occurs when the vapor flow becomes choked. Indeed, the mass injection and removal experienced by the vapor flow causes the vapor passage to act as a converging-diverging nozzle, causing a lack of pressure communication between the evaporator and condenser under sonic flow conditions.

1.2.2. Thermosiphons

Another common heat pipe variant is the thermosiphon, which relies on gravity. The gravitationally driven nature of thermosiphons stems from phase change and the saturated density difference between the liquid and vapor. Thus, thermosiphons require the condenser section to be located above the evaporator section so that condensed liquid is pulled down towards the evaporator, and returning vapor rises towards the condenser, resulting in fluid circulation. Moreover, wicks are not required for thermosiphons to operate; however, some designs have incorporated wicks to improve their thermal performance. Figure 1.6 shows a general schematic of a thermosiphon. Additionally, the liquid inventory of the working fluid is an important design parameter for thermosiphons, where an optimal fill between fully saturated vapor and fully saturated liquid exists that provides the best heat transfer ability.

Since thermosiphons are typically wick-less, the capillary limit is irrelevant. Generally, the boiling and entrainment limits constrain thermosiphons' heat transfer abilities. For thermosiphons, the boiling limit does not occur due to nucleate boiling as with conventional heat pipes; instead, it

occurs due to film boiling. Indeed, the generation of vapor bubbles via nucleate boiling is a primary

mode of operation for thermosiphons. However, the development of a continuous vapor film at the

heat transfer surface in the evaporator will result in poor thermal communication between the wall

and the fluid. Moreover, due to the free interface between the vapor and liquid, the antiparallel

flow of the high-velocity vapor can entrain some liquid and carry it back to the condenser before

it reaches the evaporator, hydrodynamically shorting the device and reducing the overall mass flow

rate of the circulating flow.
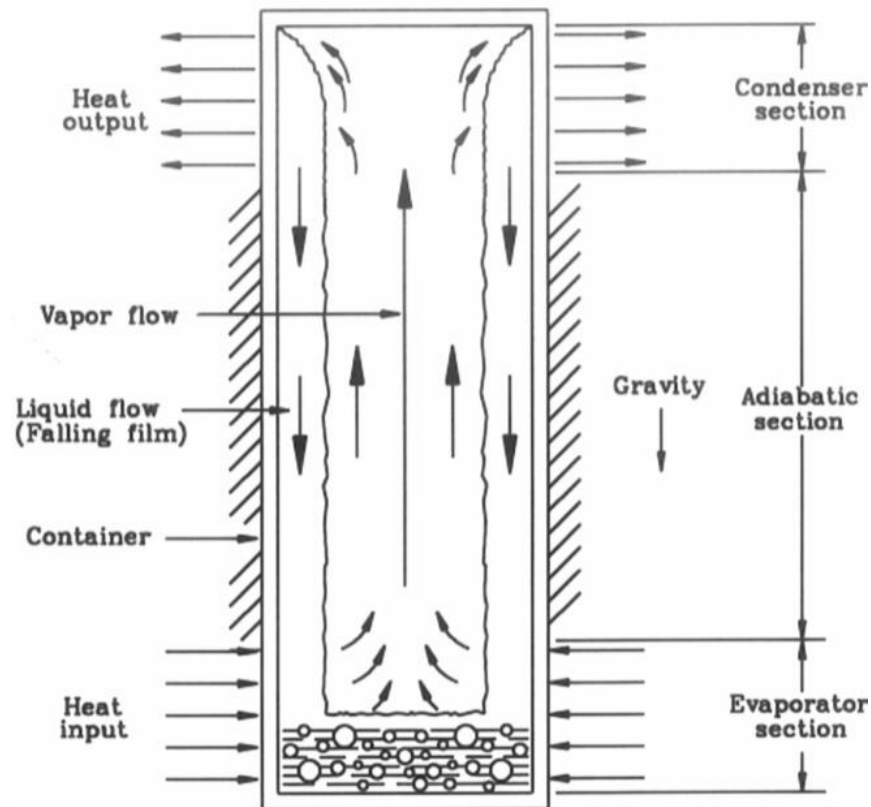
Figure 1.6. A schematic of a thermosiphon depicting the gravity-driven vapor and liquid flows [18].

1.2.3. Other Heat Pipes

While gravity and surface tension are intuitive choices for heat pipe driving forces, any arbitrary force steadily acting on the fluid can drive circulatory flow within a heat pipe. For example, rotating heat pipes take advantage of the centrifugal force of a steadily rotating chamber. In essence, the design of a rotating heat pipe is identical to that of a thermosiphon as the liquid will be pulled toward the outside of the chamber and the vapor towards the inside due to their density difference. Additional heat pipe designs include loop heat pipes (LHPs), capillary pumped loops (CPLs), annular heat pipes, vapor chambers, and gas-loaded heat pipes, all of which provide specialized features such as improved microgravity performance, variable conductance, or high heat flux capabilities, yet still rely on surface tension as the flow impetus.

1.3. Pulsating Heat Pipes

Heat pipes typically have a steady driving force (unchanging with time) that promotes the uni-directional fluid flow circulation. Thermosiphons are driven by gravity, conventional heat pipes are driven by surface tension, and rotating heat pipes are driven by the centrifugal force, but what drives a pulsating heat pipe? Indeed, the pulsating heat pipe distinguishes itself from other heat pipes by its persistent oscillatory driving forces and flows instead of steady and uni-directional ones. The opposing and simultaneous phase changes in the evaporator and condenser sections generate persistent and stochastic non-equilibrium conditions that drive fluid segments back and forth through the adiabatic section between the two ends. For a PHP operating without the assistance of a steady body force (such as gravity), no steady fluid streaming should occur, and the fluid movement should be purely oscillatory.

The exact nature of the PHP's stochastic driving force and the resulting heat transfer mechanisms have evaded understanding by researchers for decades. However, Yoon and Kim [7,

19, 20] currently give the clearest description of PHPs' thermohydraulic behavior. The oscillatory component of the PHP flow can be isolated and analyzed by neglecting gravity and viscosity in a one-dimensional momentum balance of a liquid slug surrounded by two vapor plugs. The resulting dynamic equations for multiple liquid slugs connected via vapor plug springs in series can be solved semi-analytically and numerically. The results of these analyses, which agree with experiments, suggest that each adiabatic section tube of the PHP contains a single liquid slug that oscillates in place, with one side of the slug reaching the evaporator section during the oscillation peak and the other side of the slug reaching the condenser during the oscillation trough. Moreover, the dynamics of the quasi-linear multiple mass-spring system cause the liquid slugs in adjacent adiabatic tubes to oscillate out of phase by $2\pi/N_t$, where N_t is the number of turns, and it is precisely the out-of-phase oscillations of adjacent slugs that result in uni-directional heat and mass transfer.

The mechanisms by which heat is transferred and the oscillating forces are generated depend significantly on several operational parameters such as the working fluid, number of turns, orientation, tube size, section lengths, and more. Thus, numerous experimental and theoretical studies have been dedicated to probing PHPs' dependencies on such parameters.

1.3.1. Effect of Fluid Properties

The choice of working fluid will coincide with the required temperature range of a given application, for which the fluid must be two-phase and have a reasonable saturation pressure. Therefore, the working fluid is likely to be a constraint rather than a parameter, but regardless, the properties of the working fluid can significantly affect the performance of a pulsating heat pipe. For example, the fluid's viscosity, primarily in the liquid phase, is important to consider as viscous dissipation is one of the two flow restriction mechanisms. The importance of liquid viscosity is

most apparent in studies of long-distance pulsating heat pipes where the fluid must travel long distances to transfer heat between the evaporator and condenser. Testing of a 1-meter-long helium PHP was performed by Fonseca, Pfotenhauer, and Miller [12, 13] showed that the low viscosity of helium in the saturated liquid phase makes it an excellent fluid choice for long-distance PHPs. However, studies of long-distance nitrogen PHPs by Barba, et. al. [21] suggest that nitrogen, with a saturated liquid viscosity comparable to most room-temperature fluids, is an inferior fluid choice for long-distance PHPs, since an unstable performance and thermal runaway were observed with their 3-meter-long PHP. Indeed, at atmospheric pressure, the saturated liquid viscosity of nitrogen is more than fifty times that of helium. The other flow restriction is the shear stress created by the dynamic surface tension forces, although the two-phase surface tension is more likely to be constrained by the Bond number requirement rather than a flow impedance limit of the PHP.
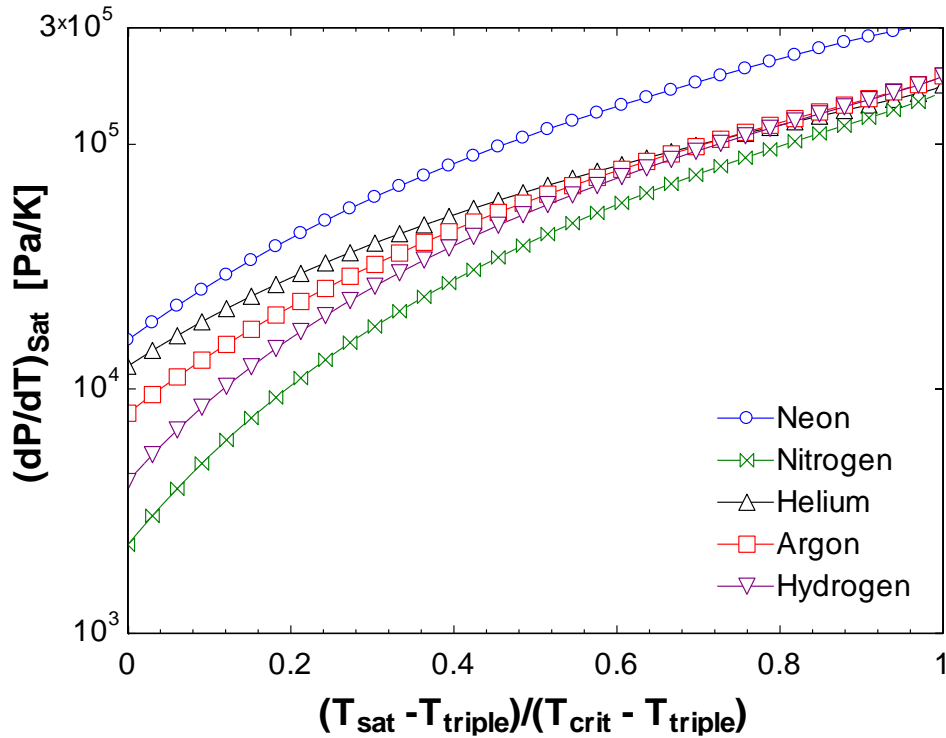
Figure 1.7. Saturated pressure differential $\left(\frac{dP}{dT}\right)_{sat}$, as a function of non-dimensional temperature for several cryogenic fluids.

From the perspective of a net uni-directional mass transfer, the saturation pressure difference between the evaporator and condenser constitutes another potential driving force. Thus, the slope of the liquid-vapor saturation line defined by Clapeyron equation is another relevant fluid property. A high value of $\left(\frac{dP}{dT}\right)_{sat}$ will result in a greater pressure differential between the evaporator and condenser with increasing saturation temperature differential, which is desired in PHPs since mass transfer is constrained by the bulk flow in this direction. Figure 1.7 shows $\left(\frac{dP}{dT}\right)_{sat}$ as a function of temperature normalized by the critical and triple point (lambda point for helium) temperatures for several cryogenic working fluids. For all fluids, as the saturation temperature increases from the triple to critical point, $\left(\frac{dP}{dT}\right)_{sat}$ also increases, indicating that the driving force originating from saturation pressure differential becomes stronger near the top of the vapor dome. Figure 1.7 also suggests that neon and helium provide the greatest saturation pressure differential, making them good working fluids for PHPs.

Intuitively, the saturated density ratio of the saturated liquid and vapor phases will also affect a PHP's performance. For example, at atmospheric pressure, the saturated density ratio of helium is 7.4, and is 174.8 for nitrogen. Indeed, nitrogen expands significantly more when boiling than helium, which suggests that the driving forces induced by phase change are stronger for nitrogen than helium. Another layer of complexity is added since the ratios of saturated properties are dependent on the saturation temperature or pressure, so for many studies of a single working fluid, the fluid properties change with the applied heat load since the saturation temperature is also changing. Therefore, operational properties (heat load and performance) of pulsating heat pipes are interrelated with fluid properties, making the effect of any given fluid property somewhat ambiguous. It is uncommon for experimental studies to consider multiple working fluids, and so

the effects of most fluid properties have yet to be directly explored. While some properties are obvious (viscosity, surface tension, density ratio, etc.) and have been discussed theoretically [10, 22], others may be more subtle, such as the thermal diffusivities of the saturated phases.

1.3.2. Effect of Gravity and Bond Number

It is important to note that the Bond number criterion for the critical diameter, expressed in Equation 1.3, only defines the requirement for the plug-slug mass distribution to exist. This criterion does not, however, imply that the effect of gravity is negated entirely. Indeed, gravity is typically a relevant body force, particularly for the liquid slugs due to their higher density. Therefore, a vertically oriented PHP with the evaporator beneath the condenser is the most favorable orientation in a gravitational field, and deviations from this position are less favorable. For this reason, PHP experiments are typically performed with a vertical orientation.

For a fixed orientation, the working fluid's Bond number can be adjusted through variations of either the fluid's saturation temperature, or the PHP's tube diameter. While most experimental studies inadvertently and inevitably vary the Bond number via the applied heat load, no studies have been performed that intentionally adjust the Bond number by means of varying the tube diameter. However, less cumbersome methods of studying the effect of Bond number would be to vary the evaporator or condenser temperature while maintaining a constant applied heat load, or to vary the orientation angle.

Additionally, the relevance of the Bond number defined in Equation 1.2 comes into question as the orientation angle of a PHP changes with respect to the direction of the gravitational field (or, 'becomes more horizontal'). The Bond number defined in Equation 1.2 can be modified to account for a varying orientation angle by defining an effective diameter, shown in Equation

1.4, that satisfies the assumption that the surface tension force acts parallel to the gravitational field direction, or normal to the vapor-liquid interface.

$$D_{eff} = \frac{D}{\cos(\theta)} \tag{1.4}$$

Where D_{eff} is the effective diameter, D is the tube diameter, and θ is the orientation angle. Using the definition of the effective diameter (Equation 1.3), the modified Bond number as a function of orientation angle is expressed in Equation 1.5.

$$Bo(\theta) = \sqrt{\frac{(\rho_l - \rho_v)gD^2}{\sigma \cos^2(\theta)}} = \frac{Bo(\theta = 0)}{\cos(\theta)} \tag{1.5}$$

Simply put, the standard (vertical) Bond number is multiplied by a factor of $1/\cos(\theta)$ to account for the orientation angle. The function $\frac{1}{\cos(\theta)}$, and therefore $Bo(\theta)$, monotonically increases from 1 to infinity for $0 < \theta < \pi/2$, which indicates that the Bond number always increases with increasing orientation angle, and asymptotes to infinity for the horizontal orientation. Furthermore, an adjusted expression for critical diameter resulting from Equation 1.5 is shown in Equation 1.6.

$$D_{crit}(\theta) = 2\sqrt{\frac{\sigma \cos(\theta)}{(\rho_l - \rho_v)g}} = D_{crit}(\theta = 0)\sqrt{\cos(\theta)} \tag{1.6}$$

The modified critical diameter expression is equal to the critical diameter for the vertical case multiplied by a factor of $\sqrt{\cos(\theta)}$, which is a monotonically decreasing function for $0 < \theta < \pi/2$, which indicates that as the orientation angle increases, the diameter required to recover vertical Bond number decreases.

For a horizontally oriented PHP, the fluid flow direction and gravitational field direction are perpendicular. In this scenario, the plug-slug mass distribution should not exist statically, as the Bond number approaches infinity. However, dynamic surface tension forces exist parallel the flow direction when the fluid is moving. Therefore, the Weber number, defined as the ratio between the inertial and surface tension forces, becomes the relevant dimensionless number to establish distinct plugs and slugs. Here, the plug-slug mass distribution would instead be disrupted by excess vapor inertia where vapor plugs pierce through adjacent liquid slugs (resulting in annular flow), rather than gravity-induced phase separation. For angles between horizontal and vertical, both the Weber and Bond numbers are relevant when considering the existence of distinct plugs and slugs.

Many studies have investigated the effect of orientation angle, and therefore gravity, on the performance of PHPs. For example, helium PHP experiments by Li, Li, and Xu [14] investigated the fill ratio and orientation angle simultaneously. As expected, the effective conductivity and maximum allowable heat load were negatively impacted by an increase in the orientation angle towards horizontal, for all fill ratios. However, the vertical and 30-degree cases performed similarly for all but one fill ratio tested. This likely occurred because the effective diameter at the 30-degree orientation angle still satisfied the Bond number requirement, where larger orientations did not.

Pulsating heat pipes are candidates for numerous aerospace applications, and so there is research interest in their performance under microgravity conditions. Thus, experimental studies have been performed with PHPs on parabolic flight campaigns [23 - 25], yielding short periods of microgravity. Using FC-72 as a working fluid, Mameli, et. al. [23] found that the magnitude of the gravitational force did not significantly impact the PHPs performance when in the horizontal

orientation, however, the effect of gravity was substantial for the vertical orientation. Conversely, a study by Gu, Kawaji, and Futamata [24] showed not only that all orientations were affected by microgravity, but also that the thermal performance of the PHP was enhanced by microgravity. This discrepancy could be a result of the choice of working fluid, indicating that further research is necessary. A flow visualization study was conducted by Slobodeniuk, et. al. [25] that showed flow disturbances and re-activation during microgravity, as well as evidence of transitions to annular from plug-slug flow. There has yet to be an experimental study published that investigates the effect of microgravity on cryogenic PHPs.

1.3.3. Effect of Number of Turns

While it is true that increasing the number of turns allows for more energy to be transferred by a PHP, it has been found experimentally that the thermal conductance of a PHP does not scale linearly with increasing number of turns. As with the fill ratio, there seems to also be an optimal value for a PHP's number of turns. A study by Li, Li, and Xu [26] investigated the thermal performances of an 8-turn and a 48-turn helium pulsating heat pipe, finding that while the 48-turn PHP could accommodate a higher applied heat load, the 8-turn PHP showed a lower thermal resistance at low heat loads. This implies that an array of six 8-turn PHPs operating in parallel is a more efficient configuration than a single 48-turn PHP. Figure 1.8 shows the effective thermal conductivities as a function of heat load for each case.

In a parametric study by Charoensawan, et. al. [5], the number of turns was among the variables investigated experimentally. An interesting relationship between the number of turns and the orientation was found in this study: There exists a critical number of turns beyond which the effects of orientation angle become insignificant, implying that the more turns a PHP has, the less important gravity is. This result was confirmed for PHPs with several different working fluids at

room temperatures. The authors credit this phenomenon to more aggressive internal perturbations occurring with a larger number of turns.
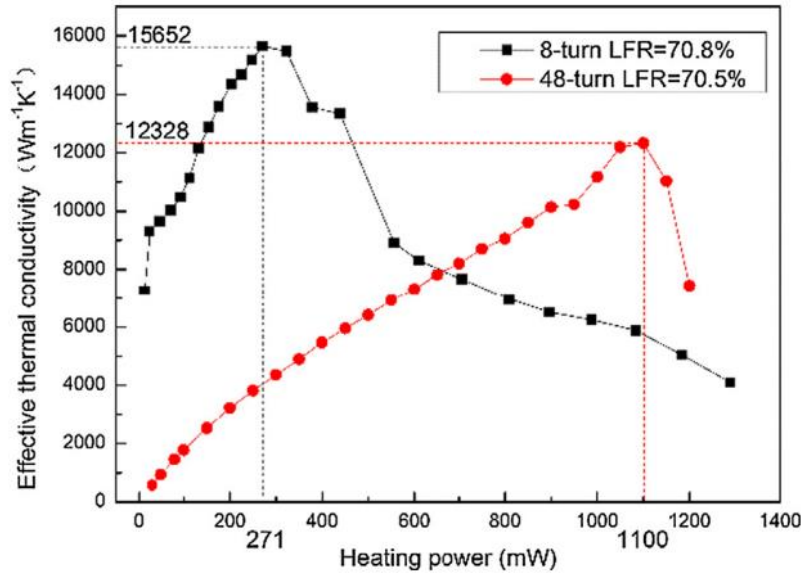
Figure 1.8. Performance as a function of applied heat load for an 8-turn and 48-turn helium PHP, showing a better maximum effective conductivity for the 8-turn case [26].

1.3.4. Visualization Studies

PHP experiments are limited in the kind of measurements that can be made, as most studies report only temperature measurements. While temperature measurements can characterize PHPs' thermal performance, the amount of information about the flow behavior that can be deduced from them is limited. Therefore, some researchers have turned to capturing the fluid movement inside transparent PHPs with high-speed cameras. PHP visualization studies have provided valuable qualitative information about the mass distribution and phase-change phenomena of room-temperature pulsating heat pipes, as well as flow velocity predictions [6, 27 - 29].

One such study by Xue and Qu [29] investigates an ammonia PHP with 6 turns made from 2 mm ID quartz glass tubes, with a fill ratio of 70%. The motion of the fluid at various applied heat loads was captured using a high-speed camera, revealing a primarily uni-directional flow regime with superimposed oscillations. With increasing heat load the velocity of the fluid

increased, which was on the order of 0.5 m/s. Additionally, noticeable changes in the shape of the liquid-vapor interfaces occurred when the heat load was increased. The leading contact angle became sharper, and the receding contact angle blunter, as the slug velocity, and therefore applied heat load, increased. Furthermore, as the applied heat load was increased, a discrepancy in the liquid-vapor distribution arose. Tubes containing fluid moving from the evaporator to the condenser was primarily vapor, while the adjacent tubes with fluid moving in the opposite direction contained primarily liquid. Another visualization experiment by Khandekar, et. al. [6] also observed the liquid-vapor mass imbalance of adjacent adiabatic tubes, shown in Figure 1.9.
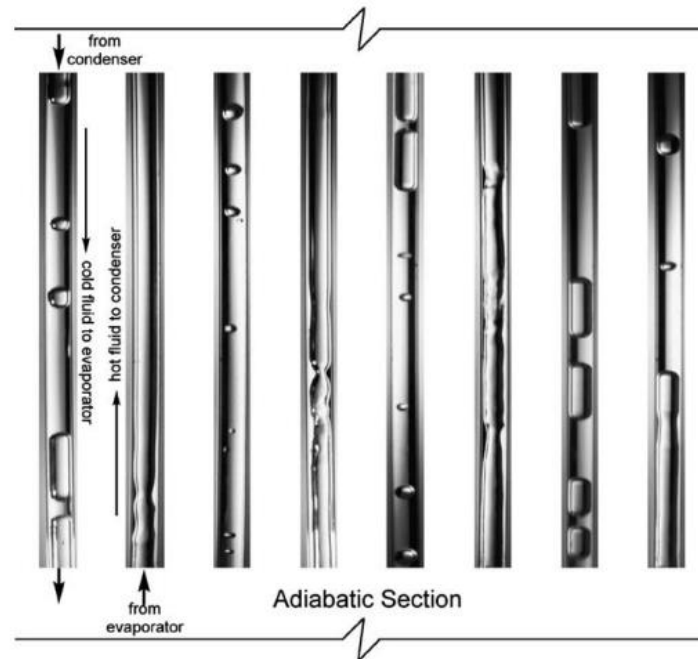
Figure 1.9. Flow visualization results showing a mass imbalance between adjacent tubes during uni-directional flow [18].

1.3.5. Cryogenic Pulsating Heat Pipe Applications

PHP research utilizing cryogenic working fluids, such as Nitrogen, Argon, Neon, Hydrogen, and Helium, has become more prevalent in recent years, with notable efforts from the Technical Institute of Physics and Chemistry at the Chinese Academy of Sciences [14, 26, 30],

CEA Paris-Saclay [21, 31], and the University of Wisconsin – Madison [12, 13, 22, 32 - 44]. Many cryogenic systems incorporate conductive links where low thermal resistance is desired where PHPs could provide an improvement. Helium PHPs, in particular, have been proposed as efficient and low-mass thermal links for superconducting magnets and space applications.

NASA has identified cryogenic heat pipes as a critical technology for future missions [45]. For example, cryogenic pulsating heat pipes could be used to help thermalize large liquid fuel storage containers for space missions [46, 47]. Boil-off of liquid fuel (oxygen, hydrogen, and methane) resulting from parasitic heat leaks is important to manage, since boiled liquid fuel is typically wasted. Cryogenic pulsating heat pipes could be incorporated into zero boil-off (ZBO) systems to improve their efficiency and reduce their mass.
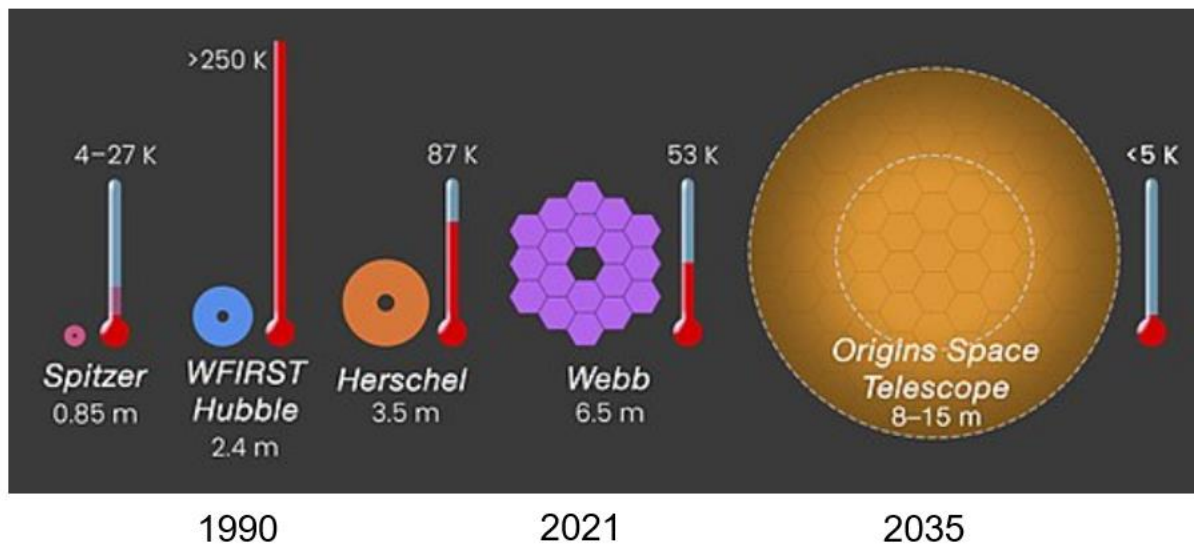
Figure 1.10. History of NASA space telescopes, including the planned OST, showing their sizes and operating temperatures [48].

Furthermore, cryogenic pulsating heat pipes are a potential candidate for cooling large space telescopes. The optical arrays of next-generation space telescopes, such as the James Webb interpret infra-red light from cosmic sources millions of light years away. As such, these detectors and their electronics must be kept at cryogenic temperatures to minimize thermal noise in their

measurements. Figure 1.10 shows the sizes and optical temperatures of several space telescopes, including the proposed Origins Space Telescope (OST) [48 - 53]. PRIMA [54] is another proposed space telescope that will require active cooling. Compared to the recently launched James Webb telescope, the OST is expected to be larger in diameter and to operate around liquid helium temperatures. Thus, helium pulsating heat pipes would be great candidates for spreading the cooling power from a centralized source, like a cryocooler, to several locations around the optical array [39, 48 - 55].

Additionally, helium PHPs are great candidates for future dry MRI systems. Many current MRIs are wet systems in which a superconducting magnet is submerged in a large bath of liquid helium, resulting in a significant share of the world's annual helium market being dedicated to MRIs due to their ubiquity in healthcare [56]. Closed-loop cryocoolers would be a great candidate to replace the helium bath and significantly reduce the amount of helium lost via liquid boil-off; however, the crucial magnetic materials contained in commercial cryocoolers' regenerators prevent them from operating correctly in a strong magnetic field. Long-distance helium PHPs could prove to be essential thermal links between the cryocooler and the superconducting magnet of an MRI [36, 37, 57]. They would place the cryocooler at an acceptable distance from the magnet while maintaining a minimal temperature difference between the two components.

While pulsating heat pipes have been a subject of experimental research for a few decades, helium PHPs have not been thoroughly investigated despite their numerous potential applications. Table 1.1 lists most of the helium PHP experiments and their results available in the literature.

Table 1.1. List of helium pulsating heat pipe experiments with their parameters and results.

Orientation (w.r.t. vertical)	# of Turns	Fill Ratio [%]	Adiabatic Length [m]	Max k_{eff} [kW/m-K]	Ref.
0	21	70	0.3	50	[7, 8]
0	21	58	1	140	
0	4	70.8	0.1	16	[25]
15	4	70.8	0.1	15.6	
30	4	70.8	0.1	13	
60	4	70.8	0.1	11.5	
90	32	25.35	0.09	2.46	[32]
0	24	31.8	0.1	4.5	[9]
30	24	31.8	0.1	5	
60	24	31.8	0.1	4	
0	24	48.8	0.1	10	
30	24	48.8	0.1	6	
60	24	48.8	0.1	5	
0	24	66.1	0.1	12	
30	24	66.1	0.1	12	
60	24	66.1	0.1	10.5	
0	24	94.2	0.1	8	
30	24	94.2	0.1	8.2	
60	24	94.2	0.1	7	
80	5	N/A	0.092	35	[58]
0	21	30	0.3	31	[10]
0	21	43	0.3	36	
0	21	50	0.3	38	
0	21	90	0.3	20	

1.4. Project Motivation

Of the numerous PHP design parameters to investigate, the length of the adiabatic section is of interest in this work since it defines the heat transfer distance, and as such, dictates the range of potential applications. For helium pulsating heat pipes in particular, the effect of adiabatic length

has not been thoroughly researched. The only published study that considers the adiabatic length a variable is from Fonseca, Pfotenhauer, and Miller [12, 13], where 21-turn helium PHPs with adiabatic lengths 0.3 meters and 1 meter were tested for several fill ratios and applied heat loads. The key result from this experiment is both exciting and unintuitive: When operating at the optimal fill ratio, the 0.3-meter and 1-meter helium PHPs performed with the same thermal resistance over a range of applied heat loads. Figure 1.11 shows both the resulting conductance (inverse of thermal resistance) and temperature difference from these tests, as functions of applied heat load.

Typically, it is expected that thermal resistance should increase with an extended heat transfer distance, however this is not the case with helium PHPs which exhibit length-independent thermal performance. The research outlined and proposed in this report serves as an extension of the experiments by Fonseca, Pfotenhauer, and Miller [12, 13, 35]. Here, the effect of adiabatic length on the performance of helium pulsating heat pipes will be studied by testing helium PHPs with various adiabatic lengths beyond 1 meter.

(a)   (b)
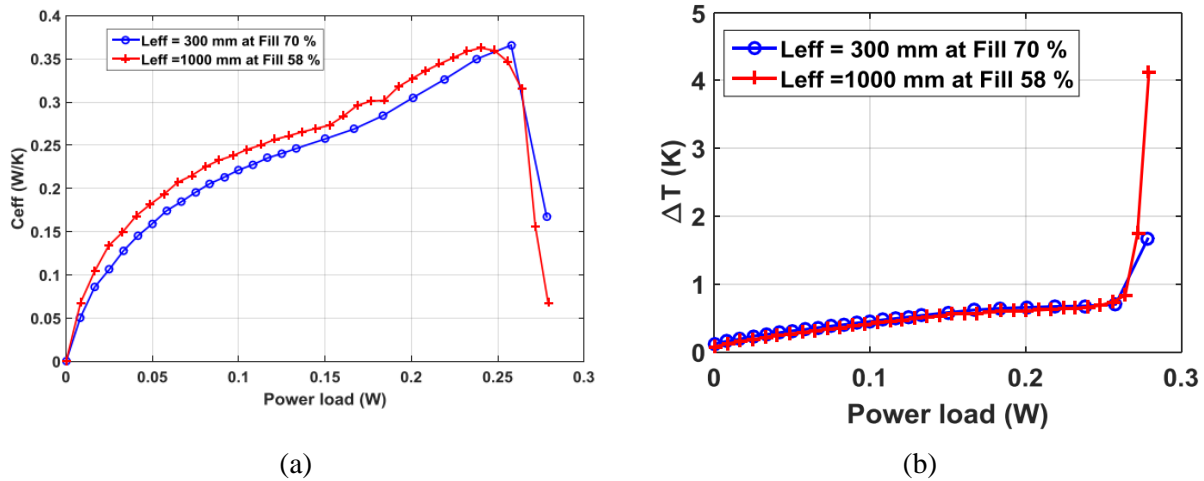
Figure 1.11. The (a) performance as a function of applied heat load for both the 0.3 m and 1 m PHP at their respective optimal fill ratios, and (b) temperature difference between the evaporator and condenser for the two PHPs as a function of applied heat load. [12].

1.4.1. Objectives

The outcomes that this research attempts to realize are summarized with the following objectives. Success in the first objective would result in a better understanding of the phenomenon that occurs when a PHP's adiabatic length is varied, which would facilitate the design of long-distance PHPs. Furthermore, the purpose of the second objective is to determine the extent to which this phenomenon occurs.

1. Characterize the thermal performance of cryogenic pulsating heat pipes as a function of their adiabatic length and orientation.

2. Determine the limits of length independence for the conductance of cryogenic pulsating heat pipes as a function of fluid properties for Helium.

Additionally, it is expected that general insights on the operational characteristics, design, and construction of helium PHPs will be gained as well.

2. Vertical PHP Experimental Configuration

2.1. Vertical Helium PHP Testing Facility

An experimental test facility was constructed to house vertical helium pulsating heat pipes experiments with extended adiabatic lengths up to 1.75 m. This facility consists of a large in-ground vacuum chamber with approximate dimensions of 2 m (diameter) by 3 m (depth) and a test rig built around a Sumitomo SHI RDK-415D2 two-stage cryocooler. The test rig, a CAD model of which is shown in Figure 2.1, consists of a cold valve, heat exchanger, and a long cylindrical radiation shield thermally anchored to the cryocooler's 1st stage, and the condenser section of the PHP mounted to the 2nd stage. With the aid of thermal modeling with EES and ANSYS, the heat exchanger and radiation shield were designed to ensure that room temperature helium is entirely thermalized to the 1st stage temperature while filling, and that the radiation shield is as isothermal as possible to minimize radiative heat leak to the 2nd stage. The radiation shield is covered by a 20-layer MLI blanket, which keeps the shield's temperature below 40 K. The purpose of the cold valve is to isolate the PHP fluid from the fluid contained in the plumbing upstream. Moreover, parasitic heat leaks from plumbing, wiring, support structures, and radiation were identified and minimized to achieve adequately low temperatures. Figure 2.2 shows a CAD model of the entire experimental test facility with the test rig sealed to the vacuum chamber. Additionally, pictures and descriptions of the experimental test facility are given in Figures 2.3 – 2.9. Data from previous helium PHP studies using this experimental setup have been published in [39 - 44].
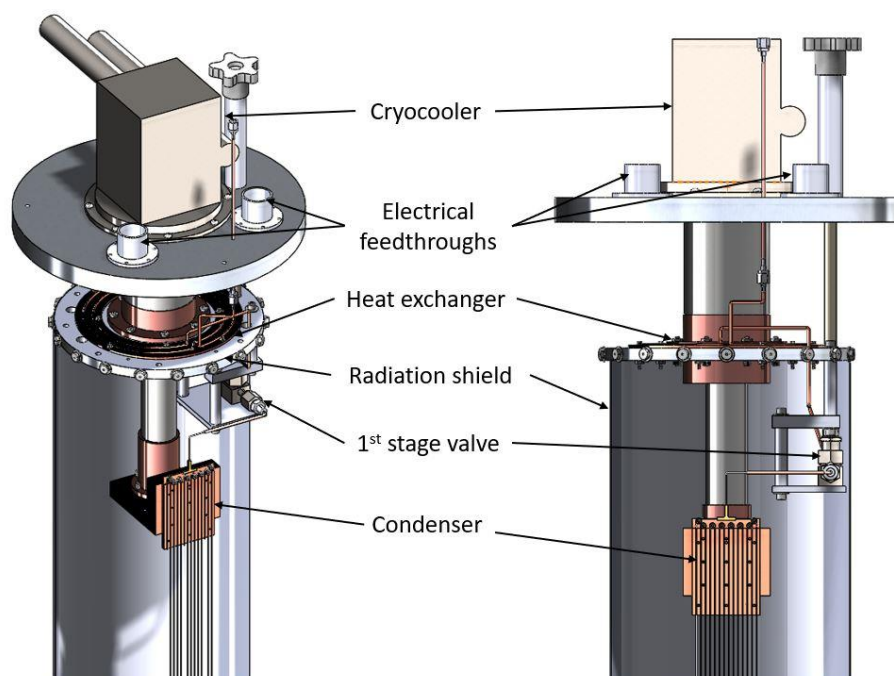
Figure 2.1. CAD model of the experimental test rig, outlining the components connected to the two stages of the 4 K GM cryocooler.
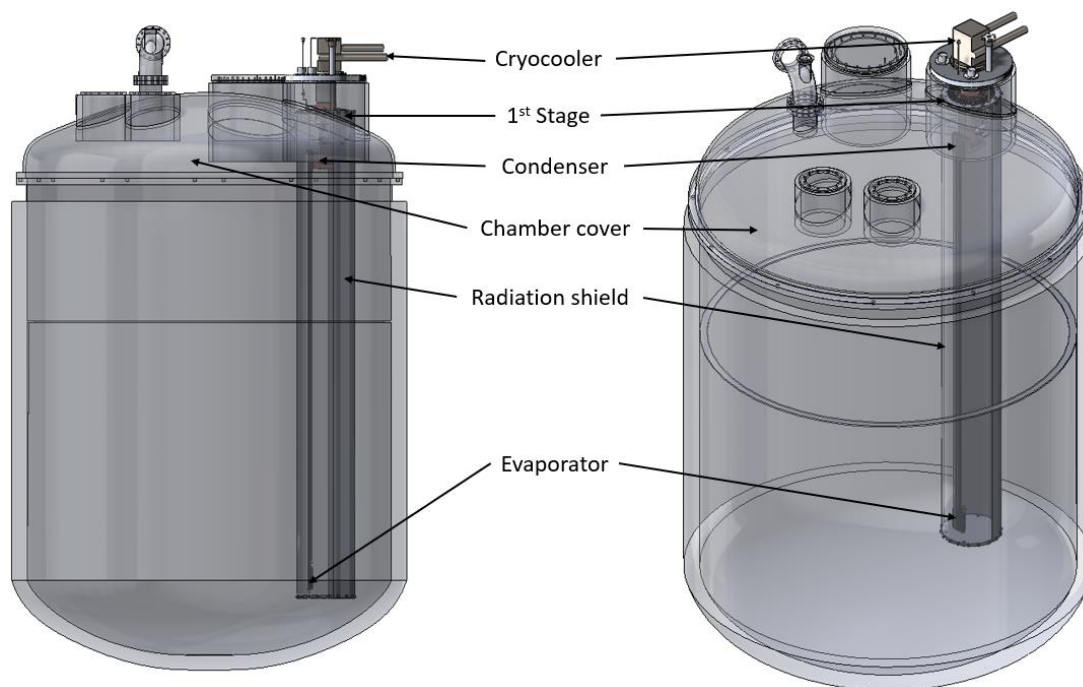
Figure 2.2. CAD model of the experimental test facility, showing the test rig in context with the large vacuum chamber.
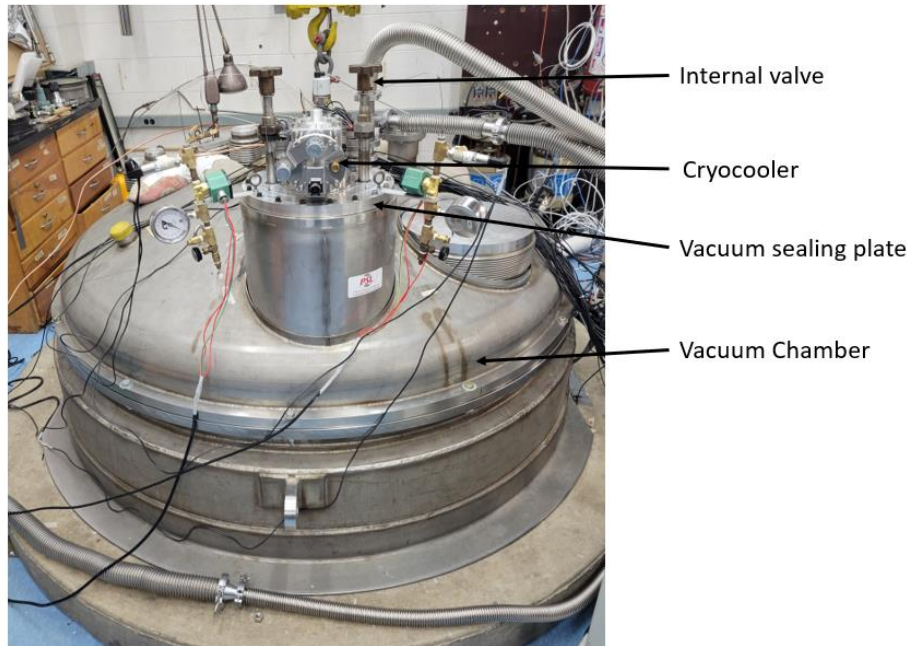
Figure 2.3. The experimental test facility in operation with the test rig mounted and sealed to the vacuum chamber.
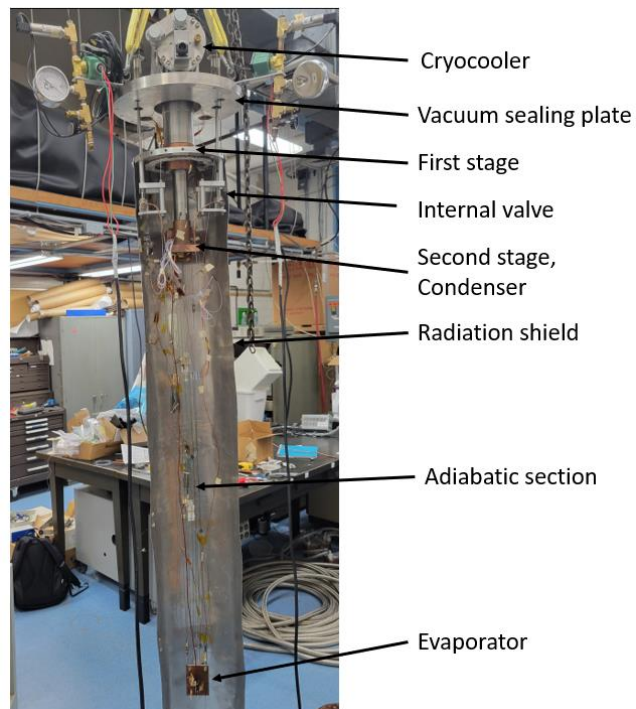
Figure 2.4. The test rig outside of the vacuum chamber with the radiation shield open, showing its internal components.
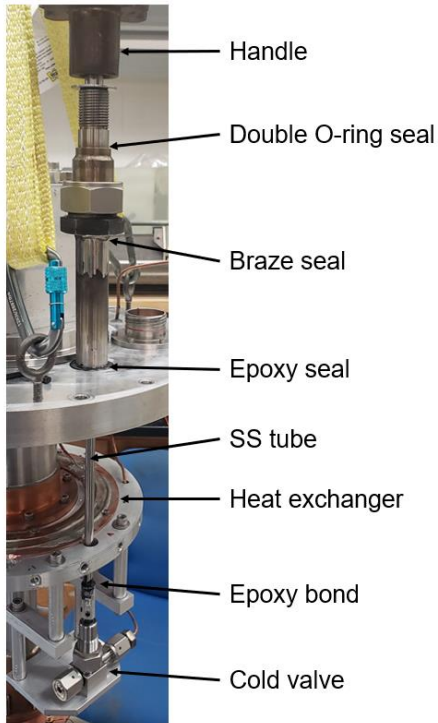
Figure 2.5. The internal valve configuration.
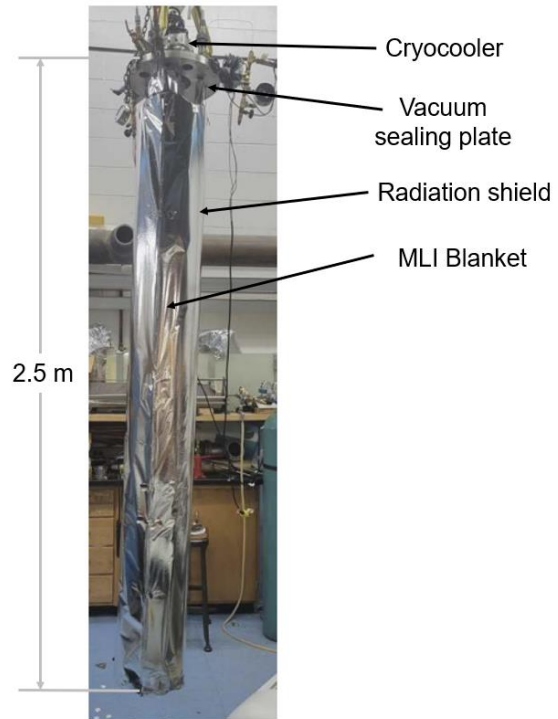
Figure 2.6. The test rig outside of the vacuum chamber with the radiation shield closed and covered with an MLI blanket.
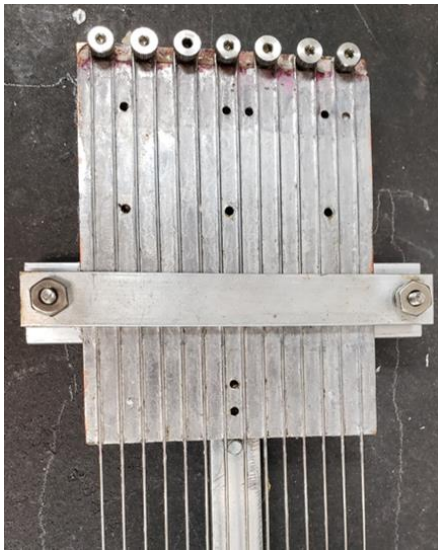
Figure 2.7. The evaporator section, which consists of a copper plate to which the PHP tubes are soldered.

Figure 2.8. The condenser section, fabricated like the evaporator section, including a fill line.

Figure 2.9. A picture of the 1.75 m PHP, demonstrating its very large length/width ratio.

2.2. External Plumbing and Fill Ratio Calculation

One of pulsating heat pipes' most critical operating parameters is the fill ratio, defined as the liquid volume fraction of the two-phase working fluid, expressed in Equation 2.1. The fill ratio is typically expressed as a percentage, hence the factor of 100 in Equation 2.1. In analyses of other types of heat pipes, the fill ratio of a PHP would be analogous to the liquid inventory; however, PHPs are unique in that the liquid inventory is stored in the primary fluid flow loop rather than in an external reservoir. In the extreme cases of 0% or 100% fill ratios, a PHP will be filled entirely with saturated vapor or liquid, respectively. In both cases, PHPs will behave similarly to single-phase thermosiphons, albeit ineffective ones, due to the nature of the PHP geometry. Therefore, an optimal fill ratio value exists between 0% and 100%. Logically, excess vapor would result in evaporator dry-out at low heat loads, while excess liquid would require a higher driving force due to higher inertia and viscous damping. Indeed, several experimental studies have identified an optimal fill ratio, which can depend on adiabatic length, working fluid, number of turns, and many other parameters [12, 14, 35].

$$FR = 100 \frac{V_l}{V_{tot}} \tag{2.1}$$

Thus, effectively measuring and controlling the fill ratio is necessary to examine its effect on PHP performance and behavior. Indeed, the fill ratio is one of the primary parameters of this study, along with adiabatic length and applied heat load. External to the vacuum chamber, a buffer cylinder is installed between the high-pressure helium supply and the experimental plumbing, which is sized such that a measurable pressure difference results from transferring the mass required to fill the PHP with liquid helium while maintaining reasonable system pressures (under 3 atmospheres). The fill ratio is ultimately determined by the pressure drop resulting from mass transfer to the PHP:

$$\Delta P = P_{charge} - P_f \tag{2.2}$$

Where ΔP is the measured pressure difference, P_{charge} is the initial buffer volume charge pressure, and P_f is the final buffer pressure after filling. The amount of fluid mass transferred to the PHP and preceding plumbing from the buffer cylinder can be determined by converting the measured pressure difference to a density difference via an equation of state [59]:

$$m_{sys} = V_b \Delta \rho = V_b \left[\rho \big(He, T = 295 \, [K], P = P_{charge} \big) - \rho \big(He, T = 295 \, [K], P = P_f \big) \right] \tag{2.3}$$

Where m_{sys} is the mass transferred from the buffer to the system, V_b is the buffer volume, $\Delta \rho$ is the difference in the buffer gas density after filling, ρ is density, T is temperature, and P is pressure. The buffer cylinder is external to the vacuum chamber, so a temperature of 295 K is assumed. The mass removed from the cylinder can also be expressed as the sum of mass contained in the upstream plumbing components at their respective temperatures. The component temperatures are 295 K for ambient plumbing, 30 K for first-stage components, 3 K for second-

stage components, and for volumes spanning these temperature regions, the average value is taken. The mass contained for each temperature region can be expressed as the product of volume and density:

$$m_{sys} = V_{295\,K}\rho_{295\,K} + V_{295\,K,30\,K}\rho_{295\,K,30\,K} + V_{30\,K}\rho_{30\,K} + V_{30\,K,3\,K}\rho_{30\,K,3\,K}$$
$$+ V_{295\,K,3\,K}\rho_{295\,K,3\,K} + V_{PHP}[FR\rho_l + (1-FR)\rho_v] \tag{2.4}$$

Where V_T and ρ_T are the measured volumes and gas densities of the experimental components at temperature T, $V_{T1,T2}$ and $\rho_{T1,T2}$ are the measured volumes and gas densities of experimental components spanning temperatures T_1 and T_2, V_{PHP} is the PHP volume, and ρ_l and ρ_v are the saturated liquid and vapor helium densities, defined as:

$$\rho_{l,v} = \rho(He; T = 3\ [K]; x = 0,1) \tag{2.5}$$

Where x is the vapor mass quality. The only second-stage component is the PHP, which contains two-phase helium. Therefore, the masses of saturated liquid and saturated vapor in the PHP can be distinguished using the fill ratio and helium saturation densities. Because the PHP fluid is saturated, the remaining plumbing components equilibrate at the saturation pressure of helium at 3 K. Thus, the densities of the helium contained in each temperature region are:

$$\rho_T = \rho(He; T = T; P = P_{sat}(He; T = 3\ [K])) \tag{2.6}$$

Where P_{sat} is the saturation pressure. Simultaneously solving Equations 2.3 and 2.4, along with the appropriate fluid density calculations via an equation of state, gives a relationship between the buffer cylinder pressure drop and the fill ratio of the PHP. These calculations were performed using Engineering Equation Solver (EES) [50]. Moreover, as described in section 2.6, the volumes of all plumbing components were either known from manufacturer specifications or carefully measured by hand to ensure adequate certainty of the fill ratio calculation.

Figure 2.10 shows a picture of the external buffer volume and its associated plumbing. The buffer volume consists of a 3.57-liter accumulator cylinder fitted with a pressure transducer and serves as the intersection between the PHP, the vacuum pump, and the helium cylinder. The buffer volume is connected to the experiment plumbing through two solenoid valves. Due to the flow directionality of the solenoid valves, two in series are necessary to prevent internal leaks when the low side pressure exceeds the high side pressure. The solenoid valves are controlled using solid-state relays that are triggered with DAQ voltage outputs and, as such, are controllable with a Boolean switch in LabVIEW. This valve configuration allows for the experiment to be operated remotely. Moreover, the solenoid valves are normally open for safety during a power outage or excessive experimental temperatures or pressures.
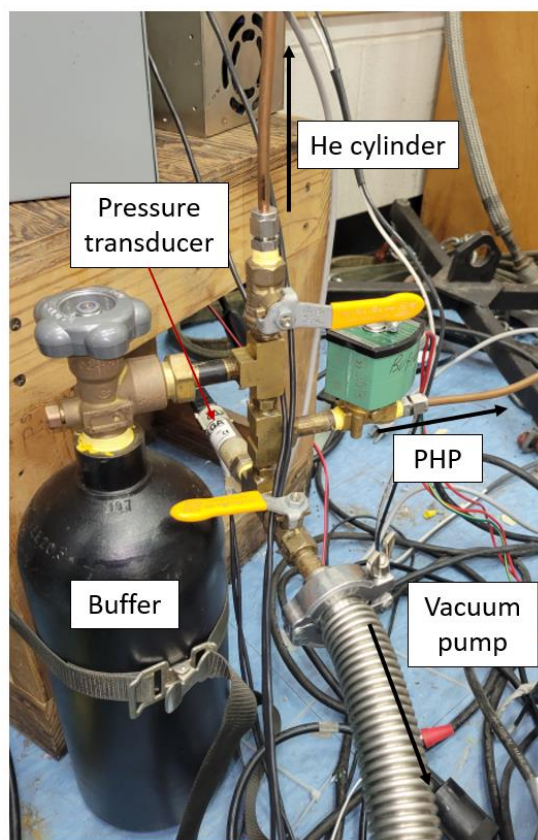
Figure 2.10. The buffer volume and its various plumbing connections.

The plumbing system external to the vacuum chamber was designed to control and measure the PHP's fill ratio, pump and flush the PHP with helium, and pump on the vacuum chamber. Figure 2.11 shows the plumbing diagram for this system. During operation, the fill ratio is adjustable by moving helium back and forth from the buffer tank to the PHP or vice-versa. This is accomplished by adjusting the temperature of the condenser with a resistive heater, where excess condenser heating pushes helium to the buffer tank, and a lack of heating pulls helium into the PHP.
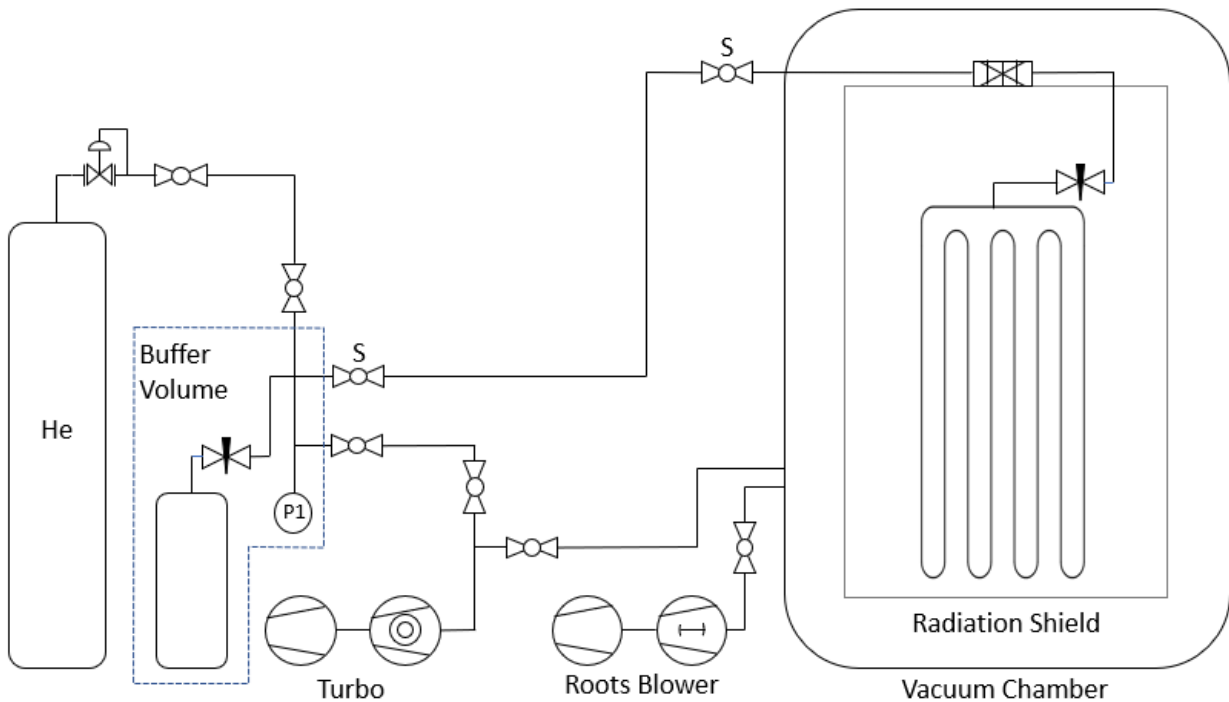
Figure 2.11. Plumbing diagram of the vertical helium PHP testing facility.

Helium gas purity is essential and challenging for pulsating heat pipes. Since the inner diameter of the tubes is very small, even a small amount of impurities (water or air) will clog the tubes at low temperatures and prevent the PHP from operating. Thus, gas purity was ensured by an extensive pumping and flushing process. This process is lengthy due to the extremely low vacuum pumping conductance of the PHP tubing, again due to the small inner diameter, but also

due to the extended adiabatic lengths of interest in this study. Furthermore, air could be introduced into the plumbing circuit during the pumping portion of the pumping/flushing cycle if leaks were present in the external plumbing components. Therefore, all components in the PHP's plumbing circuit were leak tested to a leak rate sensitivity of around 5e-10 Torr-liter/s using an Adixen ASM 142 helium leak detector.

Achieving an appropriate vacuum chamber pressure first requires pumping with a RUVAC WSU-501 roots blower, throttled to 20 mTorr at the pump inlet. When the vacuum pressure, measured by a Granville-Phillips 275 Convectron gauge, reaches 100 mTorr, a Pfeiffer HiCube 80 Pro turbomolecular pumping station begins pumping on the chamber, and the roots blower is shut down. After two days of pumping, the chamber reaches a vacuum pressure of 1 mTorr. Moreover, while the experiment was running, the cold surface of the radiation shield cryo-pumps the chamber, further reducing the vacuum pressure to around 1e-6 Torr. Residual gas conduction to both cryocooler stages is negligible at these pressures. At chamber pressures lower than 1 mTorr, a Granville-Phillips 354002-YK-T hot cathode ion gauge is used for vacuum measurement.

2.3. Thermal Modeling

Thermal modeling was extensively utilized in designing the vertical helium PHP test facility. Models implemented using EES and ANSYS aided in balancing the thermal, geometric, manufacturing, and structural constraints of the experiment's design.

2.3.1. Second Stage Interface

Due to the relatively low cooling capacity of the cryocooler's second stage (1.5 W @ 4 K), minimizing the thermal resistance between the cold head and the PHP's condenser section is imperative. Doing so expands the range of allowable heat applied to the evaporator, especially when the condenser temperature is controlled. Thus, the second stage interface was simulated in

ANSYS to determine its thermal resistance as a function of material and thickness. Notably, a balance between thermal resistance, cost, and manufacturability must be met.

The second stage interface is an L-shaped block that connects to the cryocooler's second-stage cold head, to which the PHP's condenser section is mounted. Figures 2.12 and 2.13 show the potential geometries of the interface. Figure 2.12 also shows the steady-state thermal simulation setup, with heat flow entering the interface at the condenser mounting face and with the cryocooler mounting face constant at 4 K. One of the parameters in this study is the thickness of the block, which varies from 10 mm – 20 mm. The geometries of the interface for the two thickness values are shown in Figure 2.13, which also shows the resulting temperature profiles. Moreover, the materials considered in this study are three different purity coppers (RRR = 50, 100, and 150), and Aluminum 6061, for comparison. The heat load applied to the condenser face of the interface is 0.5 W, which is a moderately high heat load for the 7-turn helium PHPs tested in this work.

The cooling capacity at the cryocooler's lowest temperatures changes with temperature at an approximate rate of 0.927 W/K, according to the published capacity curve [61]. Thus, a 25 mK temperature gradient across the interface results in approximately 23 mW of lost cooling capacity. While this seems small, this heat load is greater than one increment of the progressively increasing heat load tests. Therefore, the desired temperature gradient of the interface is less than 25 mK. The results of the parametric study are displayed in Table 2.1, which lists the maximum temperature difference and thermal resistance for each combination of parameters. With a 10 mm thickness, the interface material purity must be greater than RRR150 to meet the temperature gradient requirement, which is costly. However, with the thickness increased to 20 mm, the desired temperature gradient can be achieved with a copper purity of RRR100, which is more readily available.
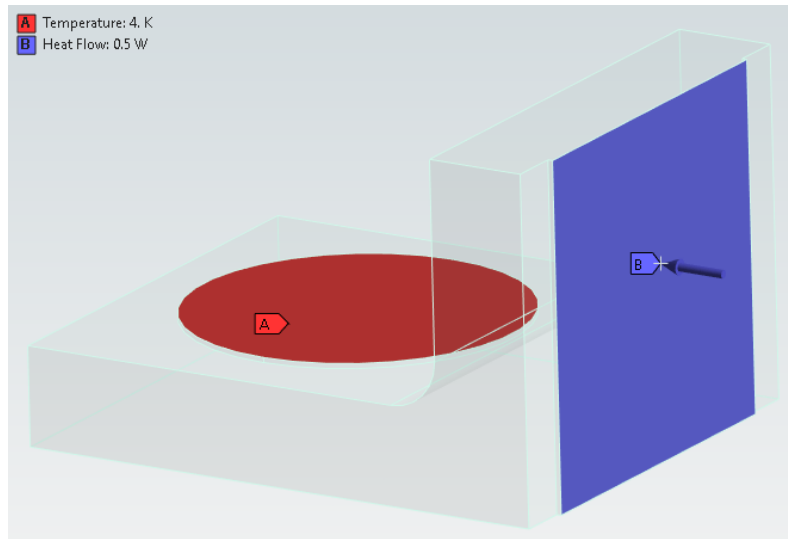
Figure 2.12. Steady-state thermal simulation setup in ANSYS Workbench.

(a)	(b)
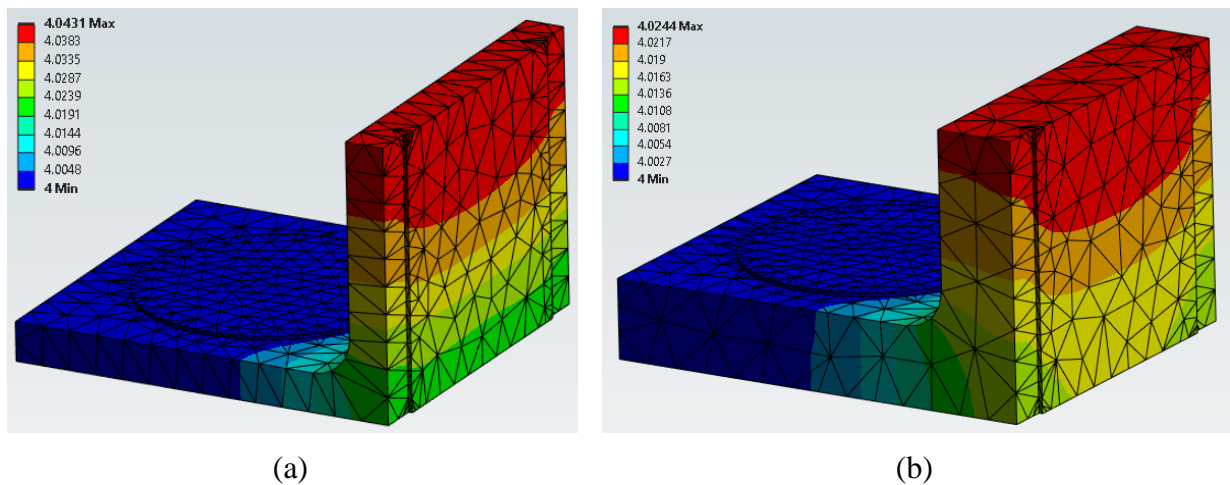
Figure 2.13. Geometries and temperature profiles for (a) 10 mm thickness and (b) 20 mm thickness, using Copper RRR100 as the material.

In retrospect, the thickness of the interface could have been larger, which would have further improved the temperature gradient and made manufacturing easier. However, this would have warranted additional analyses of the clamping bolts' shear stress and clamping force due to a larger required bolt length.

Table 2.1. ANSYS Parametric study results.

	dT [K]	R [K/W]
10 mm		
Copper (RRR = 50)	0.0859	0.1718
Copper (RRR = 100)	0.0431	0.0862
Copper (RRR = 150)	0.0288	0.0576
Aluminum 6061	2.4008	4.8016
20 mm		
Copper (RRR = 50)	0.0488	0.0976
Copper (RRR = 100)	0.0244	0.0488
Copper (RRR = 150)	0.0163	0.0326
Aluminum 6061	1.4091	2.8182

2.3.2. Thermal Radiation Shield

One of the most important components of the vertical helium PHP testing facility is the long, cylindrical radiation shield attached to the first stage of the cryocooler. This shield intercepts radiation heat load from the vacuum chamber walls at ambient temperature and shuttles it to the cryocooler's first stage, with cooling capacities of around 10 - 30 W at temperatures between 30 K and 40 K. The cooling capacity of the cryocooler's first stage is much greater than the second stage, which is why the shield is necessary. Moreover, the radiation heat load from the shield (at the first stage temperature) to the second stage is insignificant relative to the typical heat loads applied to the evaporator section during operation.

A well-designed radiation shield minimizes the temperature gradients within the shield, so a thermally conductive high-purity 1100-series Aluminum alloy is used for the shield walls. However, due to the very long length of the helium PHPs being tested, the radiation shield encapsulating the PHPs must be over 2 m long, making it challenging to keep thermal gradients

small. Thus, the shield walls' thickness must be optimized to minimize the shield's thermal gradients while maintaining malleability and a reasonable number of MLI layers.

A one-dimensional, steady-state numerical thermal model was created in EES to meet the following prescribed requirements for the experimental facility's radiation shield: (1) Maximum temperature gradient less than 10 K, (2) number of MLI layers less than 20, and (3) shield wall thickness less than 2 mm. Due to the simple geometry of the shield, the model does not require FEA software such as ANSYS and can be written from scratch. A schematic of the problem is shown in Figure 2.14.
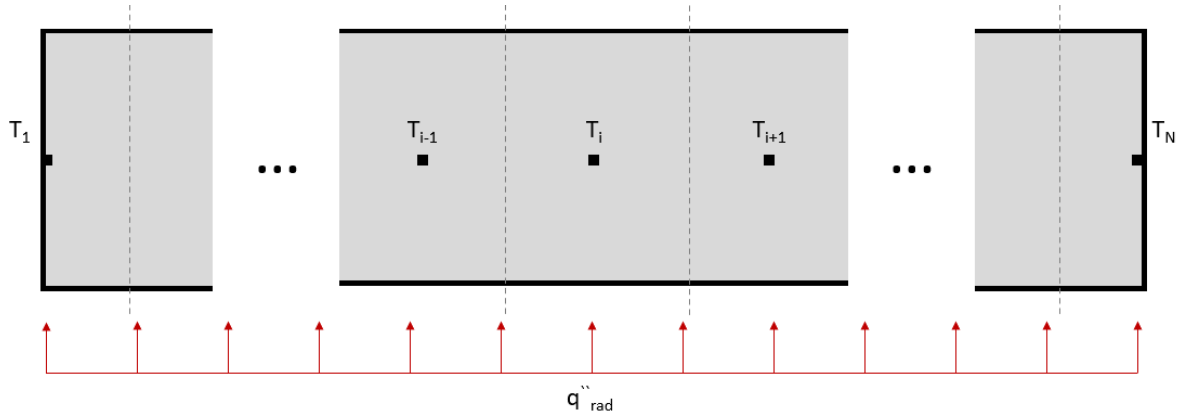
Figure 2.14. Schematic of the radiation shield thermal model's discretization.

Energy balances for each node must be solved simultaneously for nodal temperatures, T_i. The first node is prescribed at an estimated cryocooler first-stage temperature of 30 K:

$$T_1 = 30 \; K \tag{2.7}$$

The energy balances for internal nodes T_2 through T_{N-1} are:

$$\frac{kA_C(T_{i-1} - T_i)}{dx} + \frac{kA_C(T_{i+1} - T_i)}{dx} + A_S q_{rad}^{``} = 0 \tag{2.8}$$

Where k is the average thermal conductivity, A_C is the cross-sectional area for conduction, dx is the width of a node, A_S is the surface area of each node exposed to radiation, and $\ddot{q}_{rad}$ is the thermal radiation heat flux. Equation 2.8 can be expanded as:

$$\frac{\pi(2r_s th + th^2)(k_{i-1} + k_i)(N-1)}{2L}(T_{i-1} - T_i)$$

$$+ \frac{\pi(2r_s th + th^2)(k_i + k_{i+1})(N-1)}{2L}(T_{i+1} - T_i) + \frac{2\pi(r_s + th)}{N-1}\ddot{q}_{rad} \quad (2.9)$$

$$= 0$$

Where r_s is the radius of the shield, th is the shield thickness, N is the number of numerical nodes, and k_i is the thermal conductivity of the ith node. Similarly, the end node energy balance is:

$$\frac{\pi(2r_s th + th^2)(k_{N-1} + k_N)(N-1)}{2L}(T_{N-1} - T_N)$$

$$+ \left(\frac{2\pi(r_s + th)}{N-1} + \pi(r_s + th)^2\right)\ddot{q}_{rad} = 0 \quad (2.10)$$

Because the shield is covered with a MLI blanket, the typical Stefan-Boltzmann law for the radiation heat flux is insufficient. Indeed, the thermal behavior of MLI can be complicated since residual gas heat transfer and conduction between adjacent layers are important. Thus, the following empirical equation is used to determine the radiation heat flux [62]:

$$\ddot{q}_{rad} = \frac{\left(C_1\left(C_2 + C_3(C_4 - T_{avg}) + C_5\ln(T_{avg})\right)\right)\bar{N}_l^{C_6}(T_{amb} - T_S)}{N_l + 1} + \frac{C_7\varepsilon\left(T_{amb}^{C_8} - T_S^{C_8}\right)}{N_l}$$

$$+ \frac{C_9 P\left(T_{amb}^{C_{10}} - T_S^{C_{10}}\right)}{N_l} \quad (2.11)$$

Where N_l is the number of MLI layers, $\bar{N}_l$ is the layer density, T_{amb} is the ambient temperature, T_S is the shield temperature, T_{avg} is the average of T_{amb} and T_S,

ε is the emissivity of a single reflective layer, P is the vacuum chamber pressure, and C_1 through C_{10} are empirically derived constants listed in Table 2.2. Furthermore, Table 2.3 lists the other known parameters used in the simulation.

Table 2.2. Radiative heat flux empirical model coefficients [62].

C_1	2.4e-4	C_6	2.63
C_2	0.017	C_7	5.39e-10
C_3	7e-6	C_8	4.67
C_4	800	C_9	1.46e4
C_5	2.28e-2	C_{10}	0.52

Table 2.3. Radiation shield thermal model parameters.

ε	0.05	L	2.25 m
$\overline{N}_l$	1.3 1/mm	N	30
P	5e-5 Torr	r_S	0.127 m
T_{amb}	295 K		
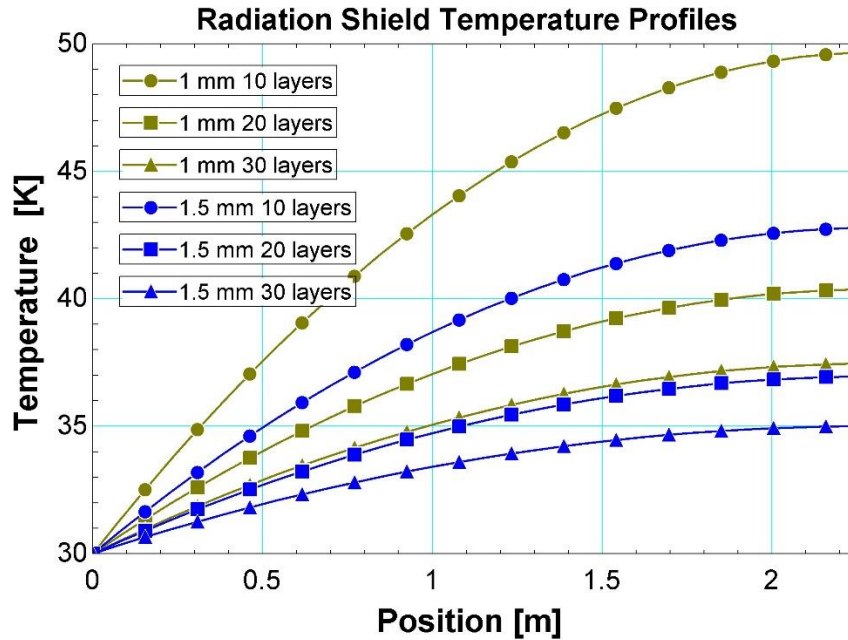
Figure 2.15. Temperature profiles resulting from the radiation shield numerical model, with th and N_l as parameters.

The N energy balances were solved simultaneously in EES, producing the temperature profiles shown in Figure 2.15. The wall thickness, th, and number of MLI layers, N_l, were varied from 1 mm – 1.5 mm and 10 layers – 30 layers, respectively. The results of this thermal modeling

effort informed the final shield design, which featured 1.5 mm thick walls and 20 MLI layers, which fit the requirements mentioned above.

2.3.3. Heat Leak Management

As previously mentioned, minimizing the parasitic heat leak from ambient temperatures to the cryocooler is imperative, especially to its second stage. Therefore, all sources of heat leak are evaluated and accounted for, including thermal radiation, conduction and Joule heating of thermometer and heater wires, conduction of PHP fill line and pressure taps, and residual gas conduction. This heat leak accounting aims to aid the experimental design to minimize heat leak to both cryocooler stages such that the no-load temperature of the second stage is less than 3 K.

The results of the thermal radiation shield model described in section 2.3.2 also give an estimate of the radiative heat load from the vacuum chamber's inner walls, at room temperature, to the cryocooler's first stage. With a 1.5 mm wall thickness and 20 MLI layers, the model predicts a radiative heat load of 2.34 W to the cryocooler's first stage. MLI is ineffective at temperatures below 10 K since the typical wavelength of radiation at such temperatures is around 0.5 mm, greater than the thickness of a single MLI layer, so there is no radiation protection covering the second-stage components. Using the standard Stefan-Boltzmann law and the known surface area of the second-stage components, an estimated radiative heat load of 10.1 mW is incident on the cryocooler's second stage. This approximation conservatively assumes a uniform shield temperature of 40 K and that the second-stage components behave as a blackbody. Moreover, this analysis demonstrates the importance of the radiation shield in intercepting large radiative heat loads from ambient temperatures.

Next, heat leaks through the instrumentation wires are thermally modeled to determine their associated parasitic heat leaks. Since some wires carry current, there is energy generation via

Joule heating that is simultaneous with conduction. A steady-state energy balance on an infinitesimal cross-section of a current-carrying wire results in the following ODE:

$$\frac{d}{dx}\left[k(T)\frac{dT}{dx}\right] = \dot{g}''' = \frac{I^2\rho_e(T)}{A_c^2} \tag{2.12}$$

Where k is the thermal conductivity, T is the local temperature, I is the current, ρ_e is the electrical resistivity, A_c is the wire cross-sectional area, and $\dot{g}'''$ is the uniform volumetric energy generation from Joule heating. Although the generation ODE is simple enough to be solved analytically, it is simulated numerically for ease in dealing with the temperature-dependent thermal conductivity and electrical resistivity, which is necessary since the wires span a large temperature range in this situation. The expanded discrete energy balances for the internal nodes of the numerical simulation are:

$$\frac{\pi D^2(k_{i-1}+k_i)(N-1)}{8L}(T_{i-1}-T_i) + \frac{\pi D^2(k_{i+1}+k_i)(N-1)}{8L}(T_{i+1}-T_i)$$
$$+ \frac{4LI^2\rho_{e,i}}{(N-1)\pi D^2} = 0 \tag{2.13}$$

Where D is the wire diameter, L is the wire length, and N is the number of simulated nodes. The end nodes are set to the known temperatures of the two cryocooler stages or ambient. The characteristics of the heater and thermometer wires are listed in Table 2.4. Since the wire lengths of each heater and thermometer are unique, the values were carefully measured by hand for use in the simulation and are not listed. However, the average wire distance between the ambient temperature and the first stage is around 0.3 m, and the average wire distance between the first and second stages is 1.5 m. To minimize heat leak to the second stage, all wires are thermally sunk to the first stage with varnish, so no wires conduct heat from ambient temperature directly to the second stage.

Table 2.4. Characteristics of the heater and thermometer wires.

	Heater Wires	Thermometer Wires
Diameter	0.558 mm	0.127 mm
Material	Copper	Stainless Steel
Number to 1st stage	8 total, 4 carrying current	30, 10 carrying current
Number to 2nd stage	8 total, 4 carrying current	16, 8 carrying current
Current	Up to 0.134 A	$1\ \mu A - 1$ mA

Due to the relatively high currents required by the resistive heaters, their wires are made from low-resistance copper to minimize Joule heating. The thermometers, however, use copper-nickel clad stainless steel wires that are robust under multiple thermal cycles to liquid helium temperatures. Since the thermometer wire currents are small, conduction dominates the parasitic heat leak calculation, and therefore, the significantly greater electrical resistance of the thermometer wires is not an issue. Moreover, it is important to note that since the heater wires carry significantly more current than the thermometer wires, care must be taken to eliminate unwanted induced currents in the thermometer wires that could cause measurement errors. The methods used to eliminate induced currents include using shielded wires outside the vacuum chamber, twisted wire pairs inside the vacuum chamber, separating the heater and thermometer wires with different electrical feedthroughs, and thermally sinking them to the first stage at different locations.

There are voltage tap wires for the thermometers and heaters alike to measure the resistance and power, respectively. These voltage tap wires do not carry current, so only the conduction terms in Equation 2.13 are considered in the simulation. Additionally, an ambient temperature of 295 K, a first-stage temperature of 35 K, and a second-stage temperature of 3 K are assumed in the simulation. Solving the N equations represented by Equation 2.13 in EES, the resulting total heat leak to the first stage from instrumentation wiring is approximately 800 mW, and the total heat

leak to the second stage from instrumentation wiring is approximately 70.47 mW. These heat leak values are well within the acceptable range for the desired baseline cryocooler performance.

Additional conduction heat leak occurs through the fill line, pressure taps, and valve stems. Since there is no thermal generation in the plumbing components, their heat leaks can be determined using integrated thermal conductivities instead of a numerical simulation. For plane wall conduction over a large temperature range with which the thermal conductivity of the material may significantly vary, the heat flow can be defined as:

$$q = \frac{A_c}{L}[K(T_1) - K(T_2)] \tag{2.14}$$

Where q is the conduction heat flow, L is the length, A_c is the cross-sectional area, and $K(T_1)$ and $K(T_2)$ are the integrated conductivities evaluated at temperatures T_1 and T_2, respectively. The integrated conductivity as a function of temperature is tabulated in EES for the materials of interest, which captures the temperature dependency of the thermal conductivity over an extensive temperature range. Table 2.5 tabulates the resulting parasitic heat leaks from the miscellaneous conduction.

Table 2.5. Characteristics of the miscellaneous conduction heat leaks.

	Temperature span	Length	Material	Total heat leak
Evaporator pressure taps	295 K – 3 K	2.5 m	304 Stainless	2.29 mW
Condenser pressure taps	295 K – 3 K	0.5 m	304 Stainless	11.44 mW
Fill line to 1st stage	295 K – 35 K	0.2 m	Copper	3.88 W
Fill line to 2nd stage	35 K – 3 K	0.1 m	304 Stainless	1.33 mW
Valve stems	295K – 35 K	0.25 m	Various	461.30 mW

An additional source of heat leak is residual gas heat transfer through the kinetic motion of the gas molecules remaining in the vacuum. Equation 2.15 characterizes the residual gas heat flux between two concentric cylindrical surfaces with different temperatures:

$$q''_{RG} = \left[\frac{1}{\alpha_1} + \frac{A_1}{A_2}\left(\frac{1}{\alpha_2} - 1\right)\right]^{-1} \frac{\gamma + 1}{\gamma - 1} \sqrt{\frac{R}{8\pi M T_{avg}}} P(T_2 - T_1) \tag{2.15}$$

Where q''_{RG} is the residual gas heat flux, α_1 and α_2 are the accommodation coefficients of the surfaces, A_1 and A_2 are the surface's areas, γ is the specific heat ratio of the residual gas, M is the molar mass of the residual gas, and T_1 and T_2 are the temperature of the two surfaces exchanging energy, with T_{avg} as the average temperature between the two. The accommodation coefficient characterizes the extent to which a molecule thermally equilibrates with a surface before it is reemitted into the vacuum space and is dependent on the temperature, type of gas, and surface conditions. Thus, it is typically difficult to determine experimentally, and therefore, a conservative value of 0.7 is assigned for α_1 and α_2 in this rough calculation. Additionally, the residual gas is assumed to be nitrogen, and the vacuum pressure is conservatively assumed to be 1e-5 Torr. Using Equation 2.5., the estimated residual gas heat transfer to the first stage from the vacuum chamber is 37.35 mW, and assuming the surface areas of the second stage components are approximately cylindrical, the estimated residual gas heat transfer to the second stage from the first stage is 8 mW.

Table 2.6 summarizes the parasitic heat leaks evaluated in this section to both stages of the cryocooler. A total of 7.51 W is estimated for the first stage, while 103.56 mW is estimated for the second stage. Using the cooling capacity map for the cryocooler provided by the manufacturer, these parasitic heat leaks correspond to baseline first and second-stage temperatures of 30 K and 3 K, respectively, which matches nearly perfectly with the temperatures measured when in operation. Two design flaws could be improved for future experimental configurations, although they are not detrimental to reaching the desired temperatures for this experiment. First, the copper heater wires are likely oversized and could be reduced to minimize their conduction heat leak to

the second stage. Additionally, the fill line to the first stage from ambient is too short and could be made from stainless instead of copper to minimize the conduction heat leak to the first stage.

Table 2.6. Summary of heat leaks.

	First stage	Second stage
Radiation	2.34 W	10.1 mW
Instrumentation wiring	800 mW	70.47 mW
Miscellaneous conduction	4.34 W	15.06 mW
Residual gas conduction	34.35 mW	8 mW
Total	**7.51 W**	**103.56 mW**

Due to the very low off-state conductance of the PHP, the evaporator section constitutes an isolated thermal mass in which the thermal resistance from the evaporator to the cryocooler's second stage is large when the PHP is not operating. Although this is a subtle aspect of the experimental configuration, it results in unreasonably long cool-down times and significantly reduces the allowable parasitic heat leak to the evaporator section. Therefore, a thermal strap connects the cryocooler's second stage to the evaporator section. An energy balance on the PHP's evaporator yields the following expression for the evaporator temperature:

$$T_e = T_c + q_{p,e}\frac{k(T_{avg})N\pi D^2}{4L} \tag{2.16}$$

Where T_e is the evaporator temperature, T_c is the condenser temperature, $q_{p,e}$ is the parasitic heat leak to the evaporator, $k(T_{avg})$ is the thermal conductivity of the strap taken at its average temperature, N is the number of wires in the strap, D is the diameter of the strap wire, and L is the length of the strap. Furthermore, the temperatures of the evaporator and condenser are close enough that an average of their temperatures is appropriate for a single conductivity value instead of using integrated thermal conductivities.

The thermal strap must be designed to remove sufficient parasitic heat incident on the evaporator section without significantly affecting the PHP's performance. However, this requirement is not difficult to achieve since these conductances are in parallel, and the PHP on-state conductance is orders of magnitude larger than the strap conductance. Thus, the thermal strap is made from 36 AWG 19 copper wires. Using this strap geometry in conjunction with Equation 2.16, the evaporator temperature as a function of parasitic heat leak can be determined, which is plotted in Figure 2.16. Figure 2.16 demonstrates the significantly reduced allowable parasitic heat leak to the evaporator section. In order for the PHP to start up, liquefaction must occur in the evaporator section, so the ultimate temperature of the evaporator must be less than helium's critical temperature, 5.19 K. With the aforementioned strap geometry, this requirement corresponds to a maximum allowable heat leak of only 10 mW.
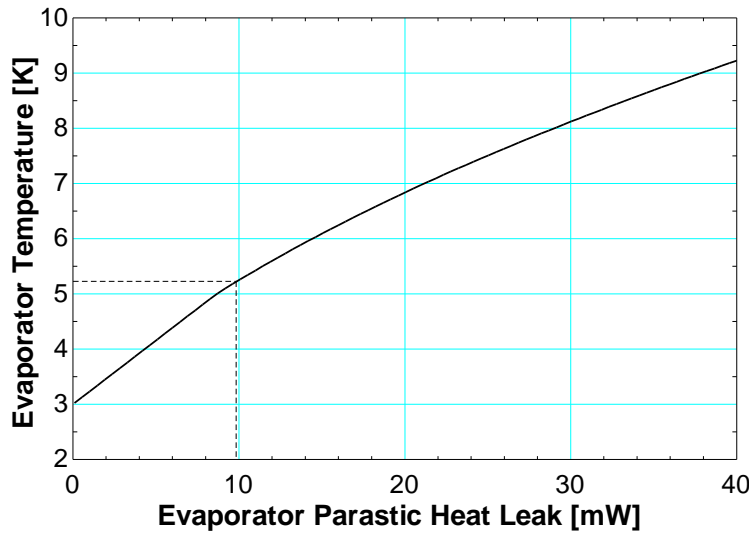
Figure 2.16. Evaporator temperature as a function of parasitic heat leak with the 36-wire AWG 19 thermal strap, displaying the minimum heat leak requirement for helium liquefaction.

Furthermore, from the previous heat leak analyses, the estimated parasitic heat leaks to the evaporator section are listed in Table 2.7 and sum to nearly 39 mW. Indeed, the conduction through the large copper heater wires is the primary contributor and would prevent the evaporator from

reaching helium liquefaction temperatures. However, to prevent this issue, the evaporator heater wires are thermally sunk to the cryocooler's second stage using varnish, eliminating this heat leak. Thus, the total remaining heat leaks sum to only 5.36 mW, satisfying the evaporator liquefaction requirement.

Table 2.7. Summary of parasitic heat leaks incident on the evaporator section.

Source	Heat leak
Radiation	1.27 mW
Pressure tap conduction	2.29 mW
Residual gas conduction	1.72 mW
Thermometer wire conduction	0.08 mW
Heater wire conduction	33.56 mW

2.4. Sensor Configuration, PHP Specifications, and Test Procedure

Primarily, the helium PHPs in this study were tested with a progressively increasing heat load, where starting from 0 mW, the heat load applied to the evaporator is increased by 20 mW increments via a resistive heater. After a transient response period (typically around 30 seconds), data for each heat load is recorded for 10 minutes while the PHP operates at a steady state. The heat load continues to be incremented until the temperature or pressure stop criteria (10 K and 310 kPa) are met for safety and to protect the pressure sensors. This process was repeated for fill ratios between 25% and 85%. Additionally, randomized heat load tests were conducted, where the evaporator heat load takes on any value between zero and slightly less than the maximum heat load determined by the progressive heat load test. Ten randomly generated heat load values are applied to the evaporator heater, each persisting for 10 minutes. Unlike the progressively increasing heat load test, this method allows for large differences in consecutive heat loads. Here, the temperature limits were relaxed to allow for extreme transient responses. Finally, progressively

increasing condenser temperature tests were conducted in which, at a constant applied heat load and beginning at 3 K, the condenser temperature is incremented by 0.1 K until the condenser temperature reaches 5.2 K or the pressure stop criterion is met.

Moreover, the geometric and operating specifications of the helium PHPs tested are listed in Table 2.8. Unless otherwise stated, the condenser temperature is fixed at 4 K and is maintained using a digital PI controller with the condenser temperature measurement as the input and power to a resistive heater thermally anchored to the condenser section as the output.

Table 2.8. PHP specifications.

Adiabatic Lengths	1.25, 1.5 m, and 1.75 m
Evaporator/Condenser Length	90 mm
Tube ID/OD	0.5/0.8 mm
Number of Turns	7
Orientation	Vertical
Condenser Temperature	4 K

Temperatures and pressures were measured at several locations in the adiabatic section, as seen in the schematic in Figure 2.17. First, temperatures are measured on the evaporator and condenser sections, which, in combination with the known heat applied by a resistive heater and the PHP geometry, determine the effective thermal conductivity, defined in Equation 2.17. This performance metric for PHPs is an analogy to heat conduction and is commonly used despite the complexity of PHPs' fluid behavior. Regardless, the effective conductivity is a valuable comparison tool for PHPs versus solid conductors and other heat pipe variants, and for the helium PHPs tested in this study, effective conductivities up to 500 kW/m-K are achievable.

$$k_{eff} = \frac{\dot{Q} L_{ad}}{N A_c (T_e - T_c)} \qquad (2.17)$$

Where k_{eff} is the effective conductivity, $\dot{Q}$ is the applied heat load, N is the number of PHP turns, A_c is the cross-sectional area of fluid flow, and T_e and T_c are the measured evaporator and condenser temperatures, respectively. Comparing the performance of pulsating heat pipes with varying adiabatic lengths requires a different performance metric since the effective thermal conductivity considers the geometry of the PHP and is thus artificially inflated by increasing the adiabatic length. Instead, the effective conductance, defined in Equation 2.18, is preferred since the formula is independent of geometry, and thus, only the overall thermal resistance is considered.

$$C_{eff} = \frac{\dot{Q}}{T_e - T_c} = \frac{\dot{Q}}{\Delta T} \tag{2.18}$$

Where C_{eff} is the effective conductance and ΔT is the temperature difference between the evaporator and condenser. Additionally, temperatures and pressures are measured at several strategic locations on the adiabatic section to extract flow and phase information during operation. On two adiabatic tubes adjacent to one another, three temperature sensors are thermally anchored to each tube, and are equally spaced along the adiabatic length, as shown in Figure 2.17. Furthermore, pressures are measured near the condenser and evaporator sections for each adiabatic tube. The combination of temperature and pressure measurements allows for the phase of the fluid contained in each tube to be determined. The key idea is that the adiabatic section measurements are taken on tubes adjacent to one another since the thermohydraulic behavior of the fluid contained in adjacent tubes can vary significantly. Thus, this measurement configuration enables novel insights into the operational characteristics of helium PHPs. Absolute pressures were measured in the adiabatic section near the evaporator, and for each tube, differential pressures were measured across the entire adiabatic section, from the evaporator to the condenser. Temperatures were measured using Lakeshore CX-1050-CU-HT thermometers, absolute pressures were

measured using Omega PX419-050A5V transducers, and differential pressures were measured using Omega PX2300-1BDI differential transducers. Finally, heat is applied to the evaporator section using a Keithley 2200-20-5 programmable power supply and a 150-ohm resistive heater (TE Connectivity HSA50150RJ). A picture of one of the pressure measurement configurations is shown in Figure 2.18.
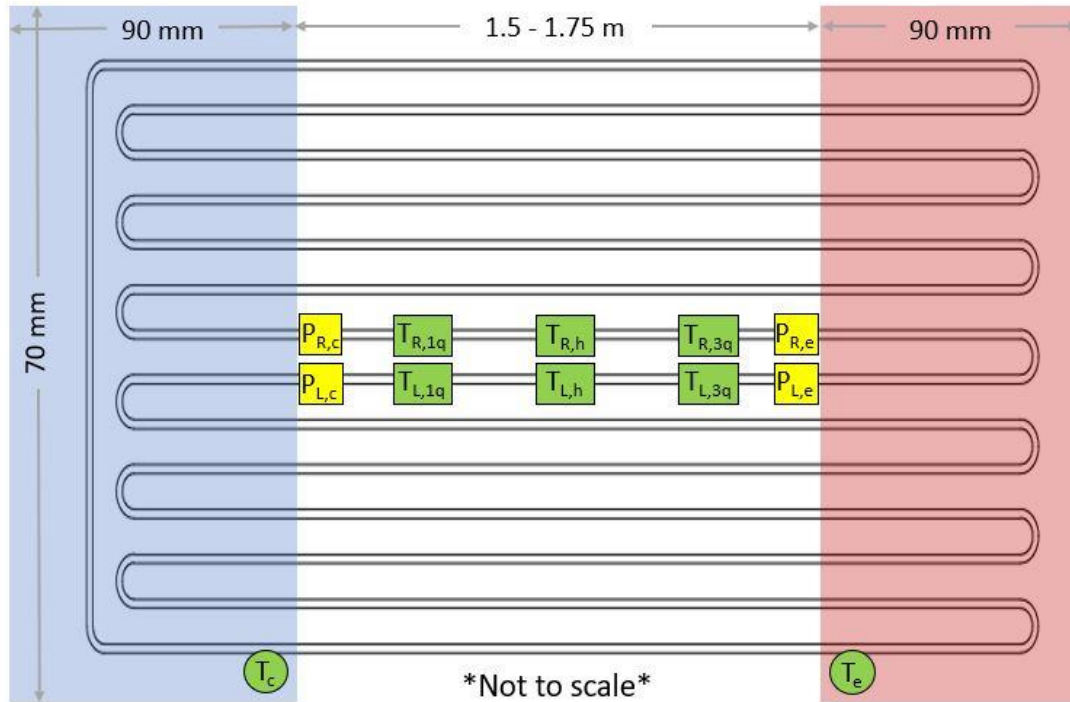
Figure 2.17. A schematic outlining the size of the PHPs tested and the locations of temperature and pressure sensors on the PHPs.

2.5. Adiabatic Section Temperature Measurement Description

Temperatures measured in the adiabatic section are essential for analyzing the fluid behavior of helium pulsating heat pipes. Figure 2.19 shows a schematic of this study's adiabatic tube temperature measurement configuration. For each temperature sensor, a copper fixture, with approximate dimensions 2 cm by 2 cm, is soft soldered to the stainless-steel capillary tube. Each sensor is then fixed to the copper with Indium foil and spring washers to reduce the contact resistance.
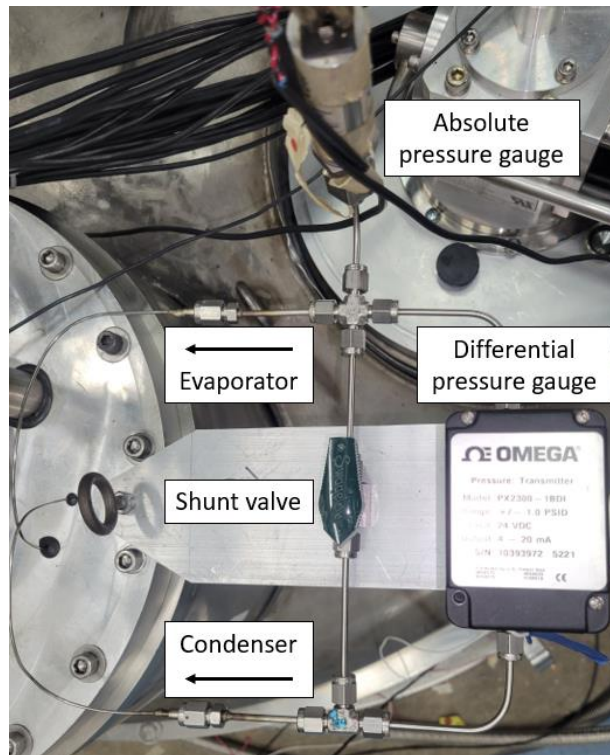
Figure 2.18. The pressure measurement configuration for one of the two adjacent adiabatic tubes.

Temperature measurements in the adiabatic section differ from the condenser and evaporator measurements since heat flows to and from the evaporator and condenser sections. Therefore, the thermal resistances between the thermometers and the fluid in these sections, in combination with the prescribed heat flow, generate a temperature difference between the fluid and the thermometer locations. In other words, the temperatures measured on the evaporator and condenser sections that determine the PHP's performance do not directly measure the temperature of the fluid contained in these sections. This fact also implies that the performance is a strong function of the thermal resistance between the evaporator/condenser sensors and the fluid, especially when the fluid is two-phase at all locations within the PHP. In the adiabatic section, however, the heat flow between the fluid and the sensors is relatively small and is only present when the sensors are equilibrating with the fluid since there is no externally applied heating or

cooling. Thus, after the PHP has reached a steady state, the adiabatic temperature measurements measure the exact temperature of the fluid when averaged in time, allowing for in-depth analyses of the fluid flow and phase behavior in addition to the thermal performance evaluation.
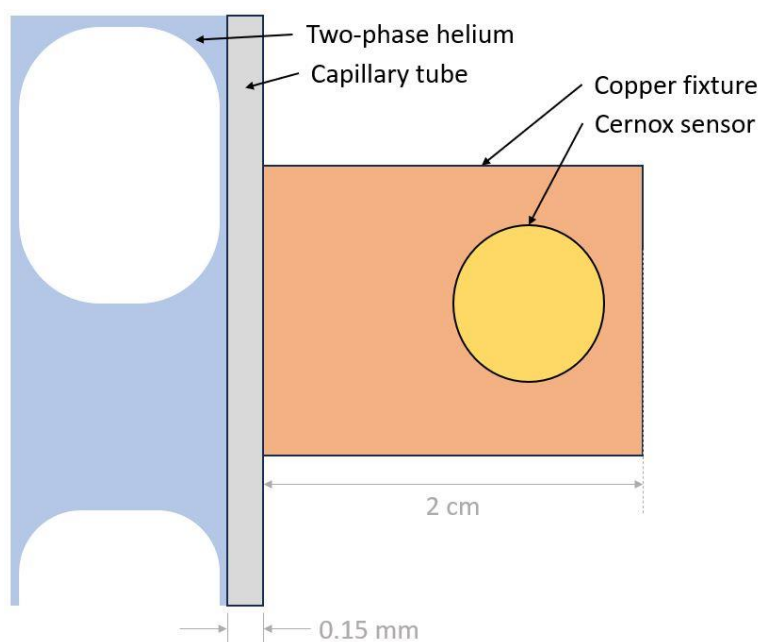
Figure 2.19. Diagram of the adiabatic tube temperature sensor configuration mounted to the capillary adiabatic tube.

Furthermore, the adiabatic temperature measurements also closely track the dynamics of the fluid temperature due to the very low heat capacity of metals below 10 K. The thermal equilibration time constant, defined in Equation 2.19, dictates the temporal resolution of the measured temperature signal. Since the thermal capacitance of the system is small, a given temperature signal will be only slightly damped and phase-lagged as it travels from the fluid to the sensor, resulting in temporal resolutions adequate for observing fluid flow phenomena. This is a novel measurement technique for PHPs and is only possible for helium (and perhaps neon) as a working fluid since the heat capacity of the thermometers and their fixtures are sufficiently low. For other cryogenic and room-temperature working fluids, many of the dynamic characteristics of the fluid temperature measurements are not resolvable.

$$\tau_{ad} = R_{ad}C_{ad} = \frac{[\rho_{cu}V_{cu}c_{cu} + \rho_{ss}V_{ss}c_{ss}]}{\bar{h}_{ad}A_{s,ad}} \qquad (2.19)$$

Where τ_{ad} is the thermal time constant for the adiabatic section temperature measurements, R_{ad} and C_{ad} are the relevant thermal resistance and capacitance, ρ_{cu}, V_{cu}, and c_{cu} are the density, volume, and specific heat capacity of copper, ρ_{ss}, V_{ss}, and c_{ss} are the density, volume, and specific heat capacity of stainless steel, $\bar{h}_{ad}$ is the heat transfer coefficient, and $A_{s,ad}$ is the surface area of convective heat transfer. Evaluating the sensors' thermal time constant requires an estimation of the heat transfer coefficient in the adiabatic tubes, $\bar{h}_{ad}$, which can vary greatly depending on the fluid phase and velocity at the sensor location. Conservative estimates place this time constant around 0.4 s, but by using the fluid velocity and phase data reported in later sections, the time constant would be closer to 0.05 s. In either case, it will be shown in a later section that the PHP's thermal behavior is dominated by frequencies at or below the cryocooler frequency of 1.2 Hz, corresponding to time scales longer than both time constant estimations. Thus, the temporal resolution of the adiabatic temperature sensor configuration is fine enough to capture the fluid's dynamic thermal behavior in the PHP's adiabatic section.

2.6. Uncertainty Analysis

Table 2.9 outlines the uncertainties of the measurements necessary to compute the PHP performance metrics. The range for the capillary inner tube diameter, D, is provided by the manufacturer, while the adiabatic length, L_{ad}, was measured by hand and assigned a conservative uncertainty value. The Cernox temperature sensors were calibrated to a factory-calibrated sensor, using linear interpolation with 120 and 80 data points below and above 10 K, respectively, resulting in essentially the same measurement uncertainty as the factory-calibrated sensor for the temperature range of interest. The power supply used to apply heat to the evaporator section reports

relative uncertainties in the voltage, V, and current, I, readings, resulting in absolute uncertainties dependent on the respective magnitudes of the readings.

Table 2.9. Measurement uncertainties.

Measurement/Parameter	Absolute Uncertainty
D	± 0.019 mm
L_{ad}	± 2 cm
$\bar{T}_{evap}, \bar{T}_{cond}$	± 5 mK
V	$V * 0.03\%$
I	$I * 0.05\%$
P	± 275.8 Pa
dP	± 34.47 Pa

The uncertainties for the performance metrics of interest are evaluated using the method described by Moffat [63], shown in Equation 2.20, where Y is the computed variable of interest, x_i are the measured variables on which Y is dependent, σ_Y is the total computed uncertainty, and σ_{x_i} are the prescribed measurement uncertainties.

$$\sigma_Y = \sqrt{\sum_i \left(\sigma_{x_i} \frac{\partial Y}{\partial x_i} \right)^2} \tag{2.20}$$

Furthermore, the formulae for the uncertainties of the effective conductivity, C_{eff}, and effective conductance, K_{eff}, are expressed in Equations 2.21 and 2.22.

$$\sigma_{C_{eff}} = \left[\sigma_{T_c}^2 \left(\frac{VI}{(T_e - T_c)^2} \right)^2 + \sigma_{T_e}^2 \left(-\frac{VI}{(T_e - T_c)^2} \right)^2 + \sigma_V^2 \left(\frac{I}{T_e - T_c} \right)^2 \right.$$
$$\left. + \sigma_I^2 \left(\frac{V}{T_e - T_c} \right)^2 \right]^{1/2} \tag{2.21}$$

$$\sigma_{k_{eff}} = \left[\sigma_{T_c}^2 \left(\frac{4VIL_{ad}}{N\pi D^2 (T_e - T_c)^2} \right)^2 + \sigma_{T_e}^2 \left(-\frac{4VIL_{ad}}{N\pi D^2 (T_e - T_c)^2} \right)^2 \right.$$

$$+ \sigma_{L_{ad}}^2 \left(\frac{4VI}{N\pi D^2 (T_e - T_c)} \right)^2 + \sigma_D^2 \left(\frac{-8VIL_{ad}}{N\pi D^3 (T_e - T_c)} \right)^2 \qquad (2.22)$$

$$\left. + \sigma_V^2 \left(\frac{4IL_{ad}}{N\pi D^2 (T_e - T_c)} \right)^2 + \sigma_I^2 \left(\frac{4VL_{ad}}{N\pi D^2 (T_e - T_c)} \right)^2 \right]^{1/2}$$

The capillary tube inner diameter uncertainty dominates the relative uncertainty of the effective conductivity and is typically around 7.5% for all combinations of fill ratio, applied heat load, and adiabatic length. However, the relative uncertainty of the effective conductance is dominated by the temperature sensor uncertainties and, therefore, depends on the many operational parameters that affect the magnitude of these temperatures, such as fill ratio, applied heat load, and adiabatic length. Depending on these parameters' values, the effective conductance's relative uncertainty can range from 0.5% to 10%, with the uncertainty inversely related to the temperature difference. However, with optimal values of fill ratio and applied heat load, the uncertainty of the effective conductance is typically around 1%.

In addition to measurement uncertainties, there is additional uncertainty to consider when time-averaging the performance metrics and temperature measurements since they oscillate around a mean value in time. Thus, the standard deviations of the temporal oscillations are included as additional squared terms under the radicals in Equations 2.21 and 2.22. The error bars for subsequent plots of time-averaged values represent the combined measurement and oscillation uncertainties.

Calculating the uncertainty of the fill ratio is more arduous due to the large number of plumbing components and the complex relationship between the fill ratio and fluid properties. Indeed, the number of terms under the radical in Equation 2.20 would exceed 40, and the fluid

property dependence is difficult to express analytically due to the complexity of the preferred equation of state for helium [59]. Thus, the calculation uses EES' uncertainty propagation feature and fluid property database [60]. For tube diameters, specified manufacturer uncertainties are used, while for tube lengths, measurements are made carefully by hand with a conservative relative uncertainty of 5% applied. Similarly, manufacturer specifications are used to determine the volumes and uncertainties for all pre-manufactured components in the fluid circuit, such as the buffer cylinder, pressure transducers, valves, and fittings. Finally, for calculated fluid properties, the sensor uncertainties of the thermometers and pressure transducers are used as the inputs for EES' fluid property functions. Furthermore, the calculated uncertainties for the fill ratios tested in this study are listed in Table 2.10. The differences in the fill ratio uncertainties between the 1.5 m PHP and 1.75 m PHP are insignificant since these uncertainties are dominated by the capillary tube inner diameter, which is unchanging throughout this study.

Table 2.10. Fill ratio uncertainties for 1.5 m PHP, which are comparable for the 1.75 m PHP.

Fill Ratio	Uncertainty	Fill Ratio	Uncertainty	Fill Ratio	Uncertainty
27.71%	±2.33%	46.83%	±3.77%	61.18%	±4.85%
32.47%	±2.69%	51.66%	±4.13%	66.01%	±5.21%
37.30%	±3.05%	54.11%	±4.32%	70.78%	±5.57%
42.06%	±3.41%	56.42%	±4.49%	75.54%	±5.93%
				80.37%	±6.29%

Like the effective conductivity, the uncertainty of the fill ratio is dominated by the manufacturer-specified tolerances of the capillary tubes' inner diameter. Since the value of D is much smaller than all other variables in SI units, the term under the radical in Equation 2.20 that contains the partial derivative with respect to D will be significantly larger than all other terms since both the fill ratio and conductivity are inversely proportional to D, resulting in a higher power of D in the denominator for that term. Indeed, for both the fill ratio and the effective conductivity,

the uncertainty in *D* is responsible for over 95% of the total uncertainty and is the reason for the somewhat high uncertainties reported for the effective conductivity and fill ratio.

2.7. Helium PHP Design and Fabrication

The techniques with which helium PHPs are fabricated can significantly impact their thermal performance and maximum allowable heat load. Following best practices for heat pipe fabrication similar to those outlined by Faghri [18] is crucial. The fabrication methods described in this section are not as extensive as those from Faghri [18], but address the unique issues encountered with helium heat pipes well enough to create excellently performing prototypes.

As mentioned previously, there is little margin for error for the gas purity of helium PHPs. Since the capillary tubes are very small, it does not take much for them to clog at the PHP's operating temperatures. The most common impurities are water, oils, metal particulate, and air. While air impurities can be eliminated with leak-tight internal and external plumbing, all other impurities are introduced during the manufacturing process. Thus, reducing the likelihood of contamination of the capillary tubes during fabrication is crucial. First, cleaning should only be done with isopropanol or a similar alcohol (methanol, for example). Most importantly, water should not be used during any part of the fabrication process as it is very challenging to completely remove since it strongly adsorbs to the metal surface and can chemically diffuse into the bulk material. Additionally, acetone is a poor solvent choice as it often leaves residues inherited from its container, although a secondary rinse with an alcohol could remove the unwanted residue.

Since the capillary tubes are manufactured in lengths much shorter than the overall PHP length, as opposed to a continuous spool, cutting and brazing are necessary for construction. First, the capillary tubes are cut using a rotary Dremel with a cutoff wheel, which does not deform the shape of the tube's cross-section. The Dremel is also used to grind the end of the tube normal to its

length, and an appropriately-sized needle is used to deburr the inside of the tube. However, unwanted stainless steel particulate is generated while cutting and deburring, which inevitably gets stuck inside the tube. To ensure the tubes are clean from particulate, they should be flushed with alcohol after cutting, followed by around 30 seconds of flow with compressed air. Additional potential contaminants in the system include metals from over-tightened fittings, back-diffusion of vacuum pump oil from poorly-designed vacuum plumbing, and solid particulate or oils from dirty metal gaskets, all of which are easily avoidable.

Furthermore, brazing is essential in fabricating the long-distance cryogenic PHPs described in this work. Depending on the PHP size, between 28 and 56 braze joints were required. It should be noted that other PHPs, such as those made from glass tubes or manufactured with MEMS technology, do not require brazing. However, nearly all cryogenic PHPs are constructed with metal capillary tubes. The PHPs built for this work were brazed using an oxy-acetylene microtorch with a tip size of 0.28 mm, typical for jewelry. The braze alloy used was BAg-5 alloy with a 1/16" diameter, an appropriate size for helium PHP capillary tubes. Finally, the flux used was Harris Stay-Silv FB3-A.

Successfully brazing together capillary tubes can be challenging due to leaks, clogs, and rapid oxidation of the stainless steel surface. First, the joint area should be completely covered to avoid leaks; however, excess braze material on the joint or excessive heating time can cause the braze alloy to wick into the capillary tube and partially or fully clog it. Thus, the overlap between the larger "sleeve" (which joins the two PHP tubes) and the PHP tube should be somewhat large. The PHPs in this study employ overlaps of around 25 mm; however, the minimum overlap to eliminate all braze clogs was found to be about 15 mm. The sleeves should be cut and cleaned similarly to the PHP tubes, and the inner diameter of the sleeves should be no more than 0.05 mm

greater than the outer diameter of the PHP tubes. Notably, if a braze joint leaks, the remedy is to apply some flux to the joint, reheat the joint until the existing braze alloy flows, and finally melt additional alloy to the joint. Figures 2.20 and 2.21 show a schematic and a picture of PHP braze joints, respectively. Additionally, the surfaces of the stainless steel tubes are easily oxidized when exposed to the torch for prolonged periods. When overheated, the tubes will glow red, and upon cooling, the braze alloy will no longer adhere to the surface since it has oxidized. Thus, it is necessary to prevent overheating of the tubes when brazing.
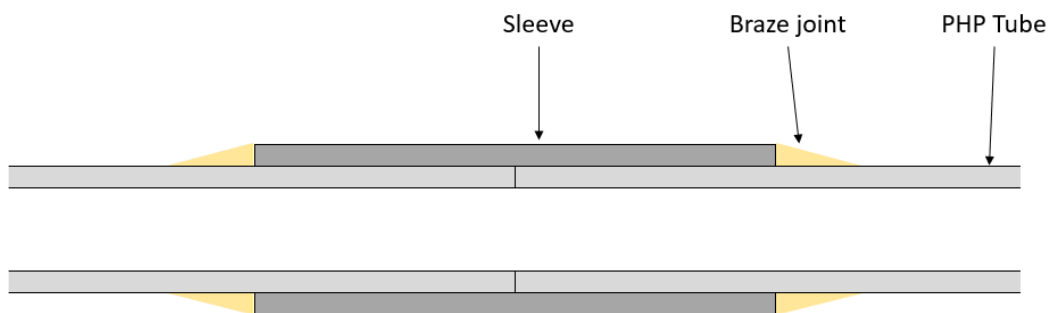
Figure 2.20 A schematic of the radial cross-section of a typical PHP braze joint.
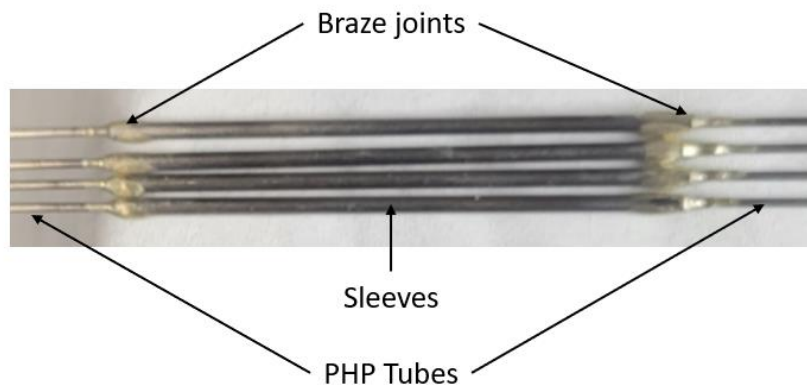
Figure 2.21. A picture of multiple PHP braze joints.

Cleanliness during the brazing process is also important to reduce the likelihood of leaks and contamination. The following steps should be followed to ensure a high-quality braze joint:

1. Wipe capillary tube and alloy rod surfaces with a Scotch-Brite scuff pad to remove surface oxidations or other unwanted particulate.

2. Clean the areas with isopropyl alcohol using Kim-Wipes.

3. Avoid touching the surfaces after cleaning with alcohol.

4. Apply a moderate amount of flux to the joint: Too much will fall off when heated, and too little will not adequately cover the joint area.

5. Apply a small amount of flux to the tip of the braze alloy rod.

6. Set the microtorch to the smallest flame possible. The oxygen-to-acetylene flow ratio should be such that the flame is entirely blue with a small blue cone.

7. Heat the stainless surfaces semi-uniformly, with more time spent heating the larger sleeve than the PHP tube. Be sure to avoid overheating the tubes, which may require intermittent heating.

8. Once the flux is transparent, running freely, and fully covering the joint area, touch the alloy rod between the sleeve and the PHP tube and continue heating.

9. As the braze melts, intermittently heat the joint to avoid overheating and move the alloy rod around in the melt pool.

10. Continue until there is adequate coverage of the braze joint area.

Once cooled, the remaining flux will solidify into a transparent glass around the braze joint. Since the flux is acidic, uncleaned residual flux remaining on the joint after brazing will eventually corrode the stainless steel tube, causing leaks. To avoid corrosion, the following steps should be taken for each braze joint:

1. Remove the bulk of the residual flux by scraping the joint and surrounding areas with a razor blade or a similar tool.

2. Rub the joint and surrounding areas with a Scotch-Brite scuff pad until the joint is completely clean.

3. Wipe the area with alcohol and Kim-Wipes.

4. Coat the area with a basic solution such as baking soda and water or dish soap and water. Dish soap is preferred since it is easier to apply.

5. Leave the basic solution on the joint for at least 30 minutes.

6. Rub the joint and surrounding areas with a Scotch-Brite scuff pad and rinse with alcohol.

The following are some additional tips for brazing:

1. Apply flux partway through the overlap area but not near the tip.

2. The flux should be partially liquid. Expired or dried-out flux will not sufficiently penetrate the gap between the sleeve and the PHP tube, resulting in a high probability of leaks.

3. The fill line and pressure taps tees should be made from a brazeable and easily machined material, such as brass.

4. Ensure that there is no gap between the two PHP tubes being brazed and that the tube does not move during brazing.

After brazing every two joint pairs, the path formed by the chain of brazed tubes is tested for clogs by flowing dry nitrogen through it and measuring the volumetric flow rate with a rotameter. The measured flow rate is compared with an analytical calculation of the predicted flow rate for the relevant flow path. It is up to the manufacturer's discretion how often the flow rate is tested; however, it is recommended that it is done at least once when all brazes are finished.

Leak testing the many PHP braze joints is tedious yet crucial. Due to the long PHP capillary tubes' very low vacuum pumping conductance, the time between spraying helium on a joint and the resulting response from a mass-spectrometer leak detector can be very long. A rough estimate

for helium to travel from the furthest braze joint to the pumping inlet is around 2 minutes. Therefore, each joint or joint-pair of one sleeve should be sprayed with helium individually, with the rest of the joints covered with polyethylene (Saran) wrap, which does not allow helium permeation. The leak rate displayed on the leak detector should be monitored for at least 2 minutes between testing each joint or joint-pair, which should not significantly change aside from typical background fluctuations. The leak rate should be in the 1e-9 torr-l/s range, preferably in the 1e-10 torr-l/s range. Furthermore, it can take up to 30 minutes for the leak detector to fully pump the air, water, and helium from the PHP before testing.

The following chapter shows that the quality of the PHP's construction can be one of the most important factors determining its thermal performance. Imperfections such as partial braze clogs, non-uniform flow paths at the sleeve junctions and pressure taps, and low-quality tube bends will likely cause additional viscous or fluid expansion losses that reduce the PHP's ability to transfer heat. However, it is hypothesized that poor bends with small kinks are the primary sources of additional flow losses. A design flaw of the PHPs tested in this study is the small bend radius of the tubes at the condenser and evaporator sections. Indeed, the bend radius is 1.5 mm, while the tube OD is around 0.8 mm, which does not meet the general guideline that the bend radius of a pipe should be twice its OD. Although the viscous losses due to the bends are not significant compared to the viscous losses through the long, straight adiabatic section tubes, the small bend radius increases the likelihood of small kinks or other aberrations to the flow cross-section that constrict the flow and act as orifices. Therefore, PHPs should be designed such that creating the bends is easy and does not change the shape of the tube's cross-section.

3. Vertical PHP Experimental Results and Analysis

3.1. Time-Averaged Performance and Temperature Trends

Figure 3.1 displays the time-averaged performances (right axes) and temperature measurements (left axes) as functions of applied evaporator heat load for the low fill ratio range (27.71% - 42.06%) of the 1.5 m PHP. For all fill ratios within this range and at low heat loads, the measured adiabatic tube temperatures are essentially the same, while at higher heat loads, the temperatures of the two adjacent tubes diverge. Interestingly, each adiabatic tube was isothermal along its length for all combinations of heat loads and fill ratios tested. It will be shown later that although the time-averaged values of the temperature measurements along the length of a given tube match, the oscillation patterns of these temperatures will vary depending on the fill ratio and applied heat load.

Moreover, the fluid phase of each tube can be determined by comparing the average tube temperature with the saturation temperature calculated from the pressure measurements. If the measured temperature matches the saturation temperature, the fluid in the tube is two-phase. If, instead, the tube temperature is either higher or lower than the saturation temperature, the fluid is superheated or subcooled, respectively. By using this method to analyze the phases of adjacent tubes, it can be determined that in the low heat load regions where the measured tube temperatures match, the fluid contained in both tubes is two-phase. For each fill ratio within this range, the plots in Figure 3.1 have a dark blue background for the heat loads that satisfy the condition that both tubes contain two-phase fluid. Since the PHP geometry is symmetric, it can be argued that, on average, the phases and temperatures determined for the two measured tubes extend to the rest of the tubes, suggesting that at low heat loads when the adjacent tube temperature match, the PHP is filled entirely with two-phase fluid. Therefore, at low heat loads, the time average data displayed

in Figure 3.1 suggest that the heat is almost entirely transferred as latent heat since no fluid temperature measurements deviate from the pressure-derived saturation temperature.
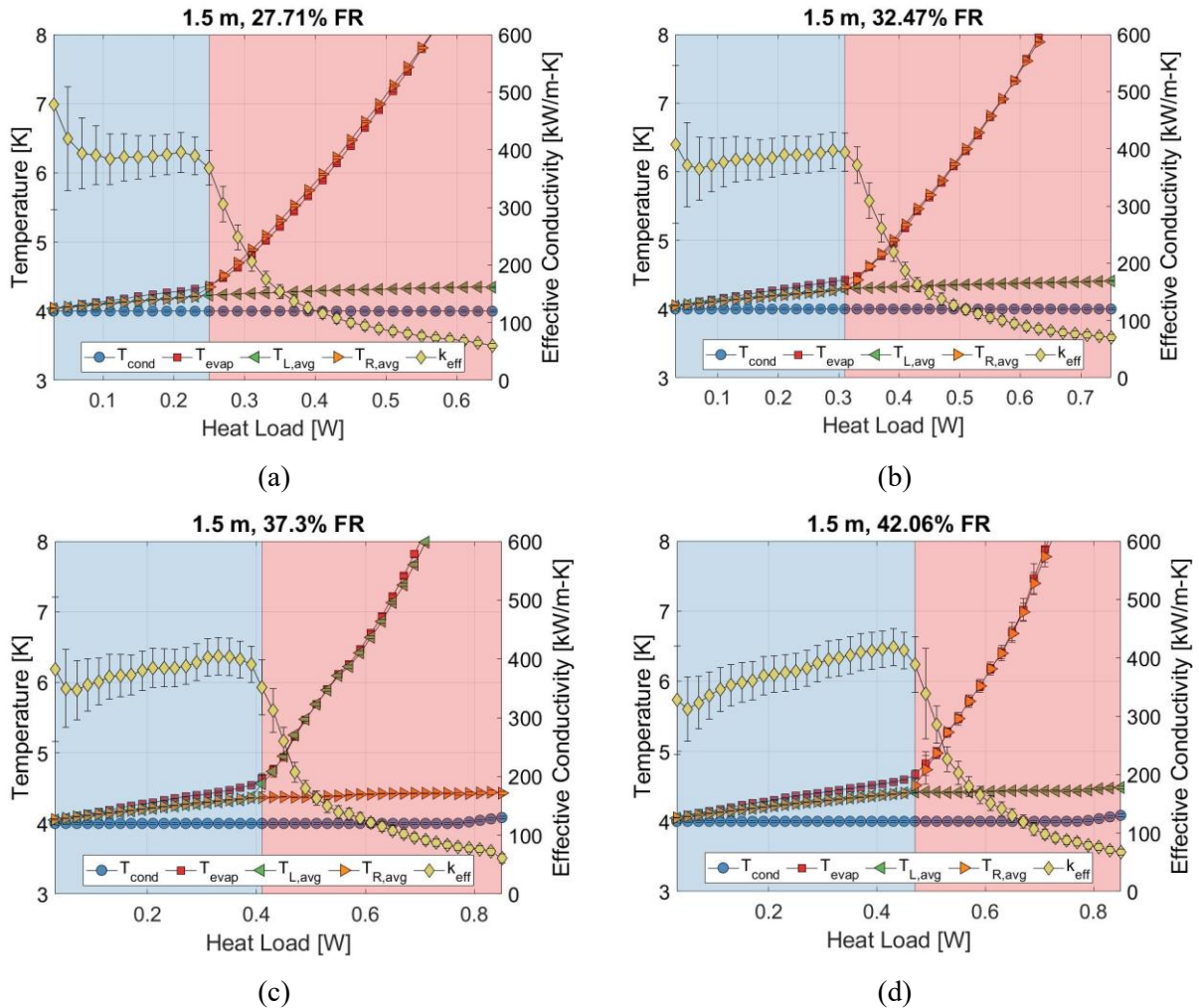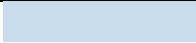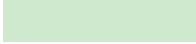
Figure 3.1. Time-averaged effective conductivity and condenser, evaporator, and spatially-averaged adiabatic temperatures as functions of applied heat load for the low fill ratio range (27.71% - 42.06%) of the 1.5 m PHP.

At a high enough applied heat load, the adjacent tube temperatures begin to diverge, and their temperature difference continues to increase by further increasing the applied heat load. By using the previously defined phase analysis, it can be determined that this divergence occurs when the fluid in the hot tube transitions from two-phase fluid to superheated vapor. For all fill ratios shown in Figure 3.1, this transition coincides with a significant spike in the evaporator temperature,

which, in turn, results in a degradation of the effective thermal conductivity. The fluid of the adjacent tubes remains two-phase despite this phase change in neighboring tubes. This heat load region is shown with red backgrounds in Figure 3.1 and also marks the onset of significant sensible heat transfer. Table 3.1 outlines the color codes used in Figures 3.1, 3.3, and 3.5 to define the many different phase-defined heat load regions.

Table 3.1. Phase color codes.

Hot tube phase	Cold tube phase	Color code	Performance
Two-phase	Two-phase		Good
Superheated	Two-phase		Poor
Superheated	Subcooled		Poor
Two-phase	Subcooled		Good
Supercritical	Subcooled		Poor
Subcooled	Subcooled		Poor

Furthermore, first law intuition suggests that the fluid flow must be primarily uni-directional, albeit with superimposed oscillations upon temperature divergence. After the temperature divergence, the adjacent tubes may be labeled either the "hot" or "cold" tube, where the cold tube must contain fluid moving from the condenser section to the evaporator, and the hot tube must contain fluid moving in the opposite direction. It should be noted that the observed flow direction could change from test to test and was seemingly random, but the flow direction never changed in the middle of a given test once the initial heat load was applied. Prior to the temperature divergence of the adjacent tubes, the directionality of the flow cannot be determined since the absence of sensible heating prevents the previous thermodynamic argument.

Because the PHP's volume and the helium mass contained in the PHP are constant for a given fill ratio, the phase change to superheated vapor in half of the PHP's tubes indicates that there exists a mass imbalance between alternating tubes, in which every other tube will either

contain primarily vapor or liquid. Furthermore, it can be concluded that in the high heat load (red background) regions for the fill ratios shown in Figure 3.1, increasing the applied heat load also increases the observed mass imbalance since the hot tube fluid temperature, and therefore, the specific volume, increases with the applied heat load. Potentially, this trend could be extrapolated backward to the low heat load two-phase regions (dark blue background); however, the temperature and pressure measurements are redundant in this region since the fluid is two-phase, and not enough information is known to determine the difference in vapor quality between adjacent tubes. In a later section, time-series data are analyzed to show that the mass imbalance does indeed extend into the low heat load two-phase regions.

One notable discrepancy between these data and the fundamental theory of pulsating heat pipes is the existence of single-phase fluid in at least half of the PHP's volume at high heat loads. Since plugs and slugs cannot exist in the hot tubes (which contain single-phase superheated vapor at high heat loads) and because the flow direction of the low-density superheated vapor in the hot tubes is upwards from the evaporator to the condenser, it is likely that the fluid circulation is primarily gravity driven. In other words, the strong mass imbalance in combination with the lack of opposing surface tension forces in at least half the tubes likely causes gravity to become the dominating force. Thus, the PHP behaves more like a thermosiphon, which is undesirable since horizontal or microgravity operation at high heat loads would not be possible. A subsequent section argues that vertically oriented pulsating heat pipes operate nearly exactly like gravity-driven thermosiphons, even when fully two-phase. Furthermore, upon sensible heating of the hot tube fluid, the cold tube fluid increases temperature more gradually than the hot tube fluid, indicating that the mass imbalance grows with increasing applied heat. Although single-phase fluid only

exists at low-performing heat loads for the low fill ratio range, the performance is still excellent

compared to solid conductors, and no thermal runaway or instabilities were observed.
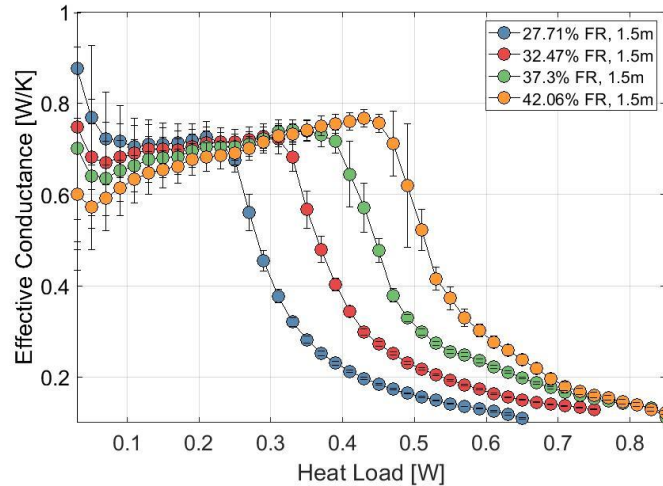
Figure 3.2. Time-averaged effective conductivity as a function of applied heat load for the low fill ratio range (27.71% - 42.06%) of the 1.5 m PHP.

Moreover, even though all fill ratios within the low range (27.71% - 42.06%) display

similar phase behavior, the heat load at which phase change occurs in the hot tube increases with

increasing fill ratio. A higher fill ratio means that the total mass, and therefore, liquid inventory,

inside the PHP is increased. Additionally, sensible heating of the fluid in the evaporator (better

known as "dry-out") occurs when the mass flow rate of the saturated liquid entering the evaporator

section multiplied by the enthalpy of vaporization is less than the applied heat load. Thus, a higher

fill ratio will stave off dry-out via increased liquid replenishment to the evaporator since the heat

that the incoming liquid could absorb before completely vaporizing is greater.

The 1.5 m PHP's effective thermal conductivities as functions of heat load for the low fill

ratio tests are displayed simultaneously in Figure 3.2. Before dry-out, the performance is nearly

independent of the applied heat load, apart from the lowest heat loads where some deviation is

observed. In the very-low heat load range, the performance is inversely proportional to the fill

ratio, which could be due to differences in the two-phase flow regimes that are only prevalent at very-low heat loads; however, the source of the performance deviation is unknown. It is important to note the high standard deviation of the performance oscillations (stemming from the evaporator temperature measurements) at very-low heat loads.

Moreover, the performance for each fill ratio within this range follows the same trend where conductivity increases with increasing heat load. Since the fluid is two-phase and heat is entirely transferred via latent heat (prior to dry-out), increasing the heat load while maintaining the same fluid temperature difference between the condenser and evaporator sections results in a positive correlation between performance and heat load, as observed in Figure 3.2. Additionally, a drastic performance drop resulting from sensible heating of the fluid in the evaporator section is observed in Figure 3.2, where the extension of the allowable heat load range due to the increased liquid inventory of higher fill ratios is also observed. Effective conductivity values between 300 – 400 kW/m-K are typical in this low fill ratio range, dependent on the applied heat load. Interestingly, low fill ratios at low applied heat loads outperform fill ratios in the middle and high fill ratio ranges, consistent with previous experimental studies [12, 14]. Additionally, the maximum heat load allowed (prior to dry-out) ranges from 0.25 W to 0.45 W and strongly depends on the fill ratio.

The low fill ratio range is defined by the phase behavior of the adjacent tubes, where the cold tube remains two-phase for all heat loads, and the hot tube transitions to superheated vapor at some heat load. However, increasing the fill ratio beyond 42.06% affects the cold tube's phase behavior, where fluid sub-cooling becomes possible. The temperature and performance of the 1.5 m PHP as functions of applied heat load for the middle fill ratio range (46.83% - 56.42%) are displayed in Figure 3.3. For the 46.83% fill ratio, sub-cooling of the cold tube fluid occurs at 0.63

W while superheating of the hot tube fluid occurs at 0.57 W, meaning that at heat loads higher than 0.63 W, all the fluid in the PHP is single-phase with alternating tubes containing either superheated vapor or subcooled liquid. This condition is shown with a green background in Figure 3.3. Moreover, while the observed fully single-phase operating states are not the best performing, they are interesting nonetheless since they deviate significantly from the expected two-phase PHP flow regime.

(a)

(b)

(c)

(d)
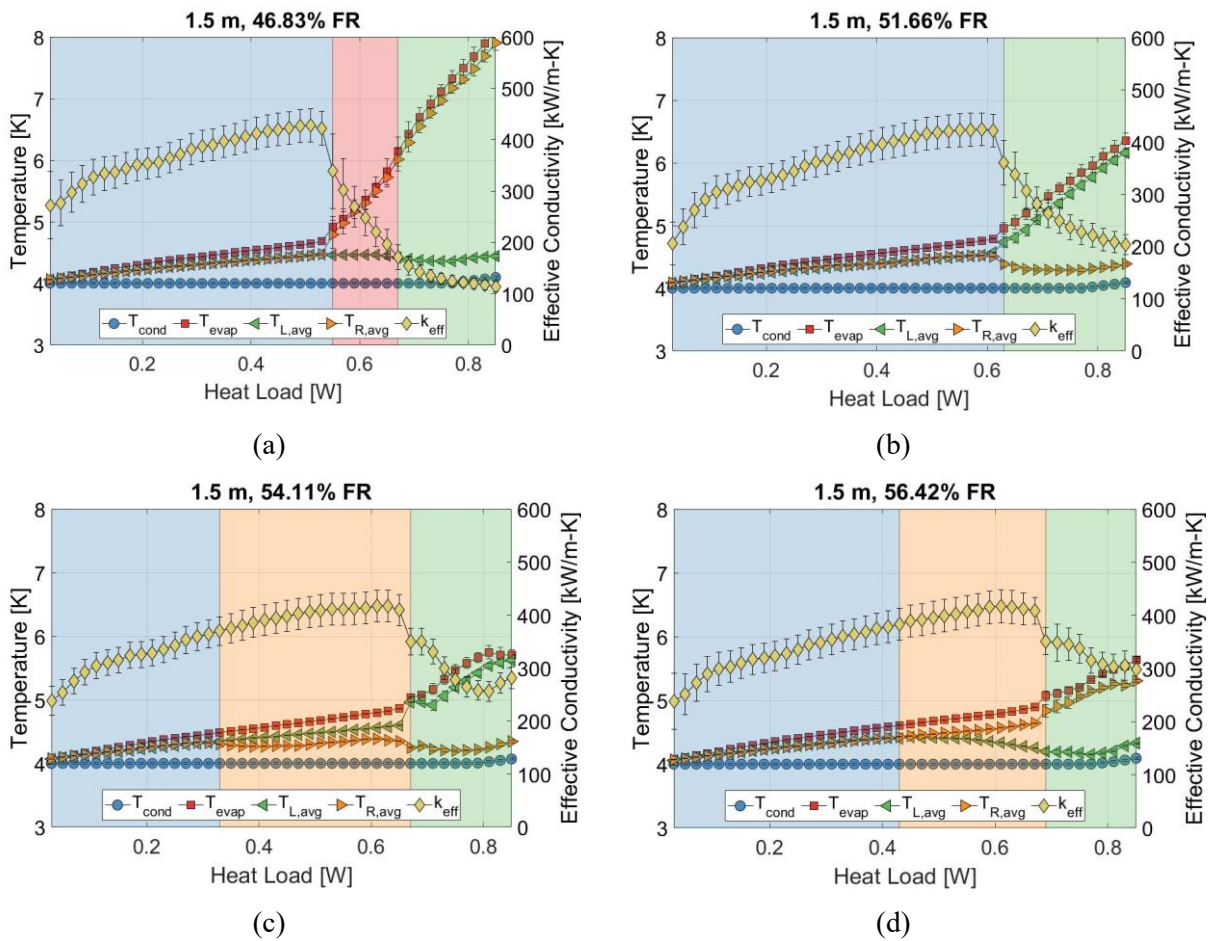
Figure 3.3. Time-averaged effective conductivity and condenser, evaporator, and spatially-averaged adiabatic temperatures as functions of applied heat load for the middle fill ratio range (46.83% - 56.42%) of the 1.5 m PHP.

When the fill ratio is increased within the middle range, the heat load at which superheating of the hot tube fluid first occurs increases, while the heat load at which subcooling of the cold tube

fluid first occurs tends to decrease, apart from the 56.42% fill ratio. This observation is consistent with an increased liquid inventory since there is less vapor to condense (which promotes subcooling in the condenser section) and more liquid to evaporate (which prevents dry-out in the evaporator section). The best performing fill ratios for the 1.5 m PHP were 54.11% and 56.42%, both of which have a high-performing hea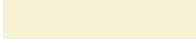t load region where the cold tube fluid was sub-cooled liquid and the adjacent hot tube fluid was two-phase, shown with an orange background in Figure 3.3.

Therefore, sub-cooling of the cold tube fluid does not negatively affect the PHP's performance despite the absence of plug-slug flow. Similar to dry-out at low fill ratios, subcooling of the cold tube fluid results in a temperature divergence of the adjacent tubes, stemming from sensible cooling of the fluid in the condenser. Since the total heat capacity of the liquid helium in the condenser volume is considerably higher than that of helium vapor in the evaporator volume, the temperature divergence resulting from sub-cooling is not as drastic as when the hot tube fluid transitions to superheated vapor.
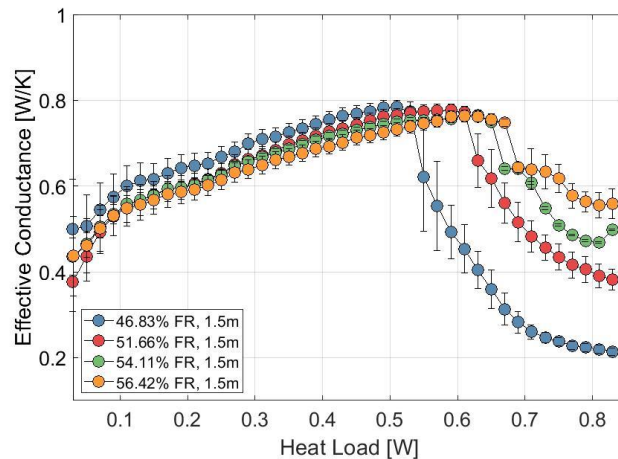
Figure 3.4. Time-averaged effective conductivity as a function of applied heat load for the middle fill ratio range (46.83% - 56.42%) of the 1.5 m PHP.

Figure 3.4 shows the effective conductivities of the 1.5 m PHP for the middle fill ratio tests as functions of applied heat load. Like the low fill ratio tests, the PHP's performance is not significantly affected by the fill ratio. The fill ratio seemingly only affects the heat load at which dry-out, and therefore, the performance degradation, occurs. However, the low heat load behavior is consistent for the middle fill ratio range, while a deviation was observed for the low fill ratio tests. Additionally, for the 46.83% fill ratio, the PHP's performance curve is slightly higher than the other fill ratio tests in the middle range. The performance trend with increasing heat load is characterized by an initial steep increase in performance with increasing heat load, which subsequently becomes less steep but still increasing, at a heat load of around 0.1 W for all fill ratios in this range.

Moreover, the heat load at which the performance drop occurs positively correlates with the fill ratio, as expected. The best performance for the 1.5 m PHP was 427.8 kW/m-K, which occurred at a heat load of 0.51 W and a fill ratio of 46.83%. However, higher fill ratios provided comparable conductivity values at significantly higher applied heat loads. For example, with a 56.42% fill ratio, the 1.5 m PHP performed with a conductivity of 408.5 kW/m-K at an applied heat load of 0.67 W. Notably, the heat load that the 1.5 m PHP (with 7 turns) is capable of transporting with excellent performance is a significant fraction of the cooling capacity of a typical commercial 4 K cryocooler.

It is well known that continuing to increase a PHP's fill ratio does not further improve performance [12, 14]. While the low liquid inventory of low fill ratios prevents PHPs from performing well at high heat loads due to a lack of liquid mass flow rate to the evaporator, high fill ratios suffer from excessive liquid inventory, which results in increased energy dissipation through viscous losses and low intermediate energy storage potential in the vapor plugs, which

should act as gas springs that propel the liquid slugs. Indeed, it is typical that an optimal value exists, which has been identified as either 46.83% or 56.42% for the 1.5 m helium PHP, depending on which criterion is used: Maximum effective conductivity or maximum allowable heat load.

(a)

(b)

(c)

(d)

(e)
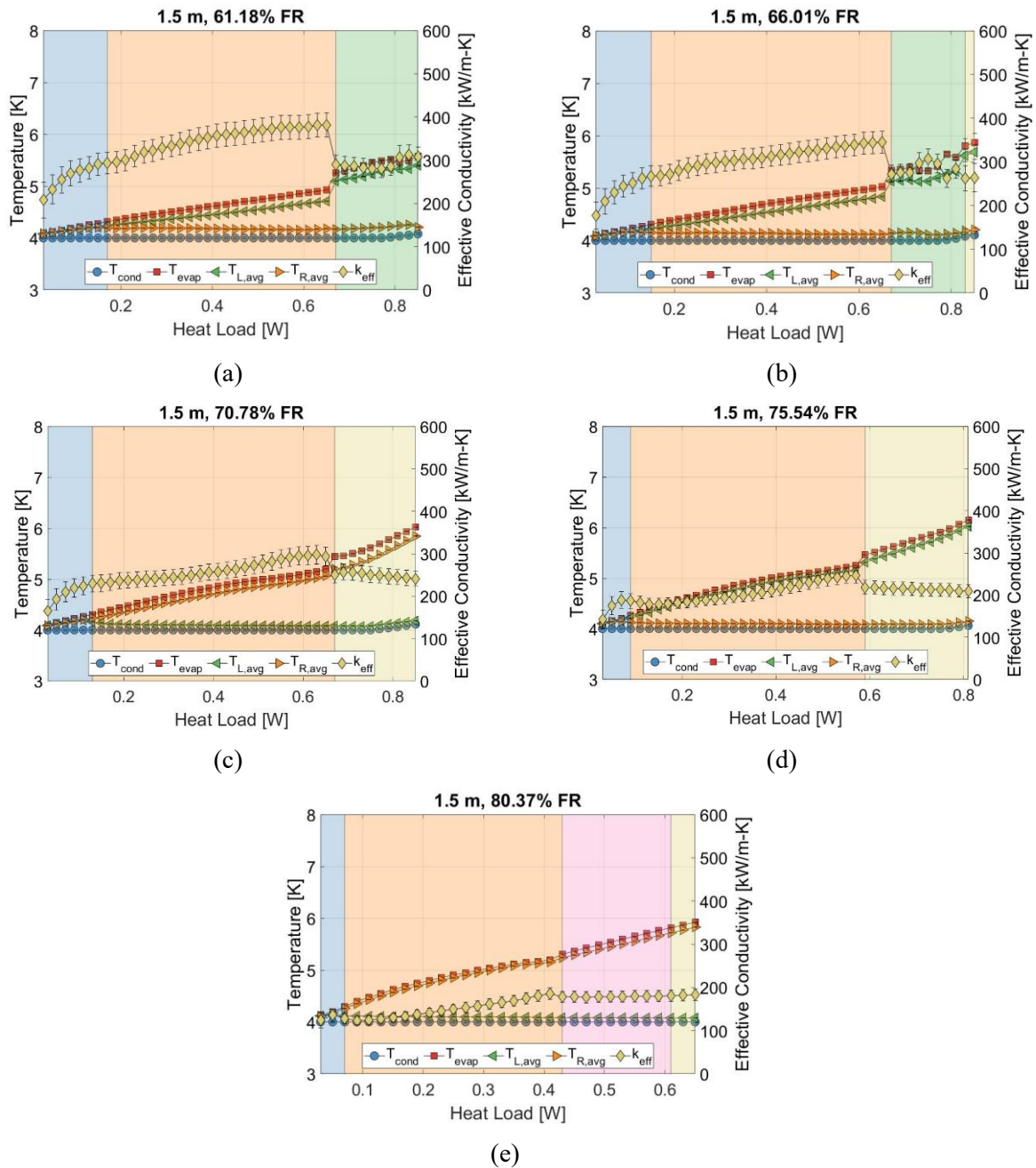
Figure 3.5. Time-averaged effective conductivity and condenser, evaporator, and spatially-averaged adiabatic temperatures as functions of applied heat load for the high fill ratio range (61.18% - 80.37%) of the 1.5 m PHP.

As seen in Figure 3.5, high fill ratios are confirmed to perform poorly for long-distance helium PHPs. The high fill ratio range (61.18% - 80.37%) for the 1.5 m PHP is defined as the fill ratios that perform significantly worse than the optimal fill ratio. For the 61.18% fill ratio test in Figure 3.5 (a), dry-out occurs at a high heat load of 0.63 W, similar to the optimal 54.11% and 56.42% cases. However, the performance has decreased by more than 10% for the 61.18% fill ratio test. This result is due to the higher liquid inventory promoting additional sensible cooling of the fluid in the condenser section and, as described in a later section, excess liquid storage in the hot tubes, which reduces the gravitational driving force and increases viscous flow resistance. Indeed, the heat load at which the sub-cooling of the cold tube fluid begins is much lower (0.19 W). The degrading performance trend continues as the fill ratio increases beyond 70%. Eventually, the PHP's performance decreases to 150 – 300 kW/m-K, which is around half of the optimal performance and significantly lower than the high-performing heat load ranges of the low fill ratio tests.

Furthermore, the phase change behavior of the adjacent adiabatic tubes continues to change with increasing fill ratio. First, the heat load at which sub-cooling begins continues the previous trend from the middle fill ratio range, decreasing with increasing heat load. This observation suggests that uni-directional flow, confirmed through the existence of a temperature divergence of the adjacent adiabatic tubes, is either more prevalent for high fill ratios, or first becomes evident at lower applied heat loads when the fill ratio is high. Regardless, the existence of single-phase liquid in the cold tubes becomes ubiquitous at high fill ratios, implying a breakdown of plug-slug flow in at least half of the PHP's tubes. Because the PHP's volume is fixed, increasing the mass of fluid inside also increases the global pressure, allowing for supercritical operating states at high enough fill ratios.

Supercritical states are not observed for fluids other than helium due to their extremely high critical pressures. However, helium's relatively low critical pressure of 227 kPa can easily be reached during regular operation, albeit only with high initial fill ratios. Supercritical fluid was first observed in the hot tube for the 66.01% fill ratio test at an applied heat load of 0.81 W. It is important to note that, like dried-out operating states, supercritical operating states do not thermally run away and will reach a stable pseudo-steady-state. Moreover, the phase regime in which the cold tubes contain sub-cooled liquid and the hot tubes contain supercritical flow is shown with a yellow background in Figure 3.5. Because the flow is uni-directional, only the hot adiabatic tubes returning fluid from the evaporator to the condenser can contain supercritical fluid due to the fluid sensibly heating above helium's critical temperature (5.19 K) as it flows through the evaporator. Conversely, the fluid in the adjacent cold adiabatic tubes, which contain fluid moving from the condenser to the evaporator, cannot be supercritical because flowing through the condenser section (controlled at 4 K) cools the fluid below the critical temperature. Furthermore, the heat load at which the hot tube fluid transitions to supercritical tends to decrease as the fill ratio increases.

Apart from the 61.18% fill ratio case, where the hot fluid transitions from superheated vapor to supercritical fluid, the performance drop associated with the supercritical transition from two-phase fluid is small compared to the dry-out transitions prevalent in the low and middle fill ratio ranges. Additionally, upon the supercritical transition of the hot tube fluid, the entirety of the PHP is devoid of two-phase fluid, which represents another operating condition that deviates significantly from the plug-slug flow regime upon which substantial theory and modeling efforts are based on. Furthermore, for the highest fill ratio test, a unique phenomenon occurs where the hot tube phase transitions from two-phase fluid to subcooled liquid before transitioning to

supercritical fluid at a later heat load. This observation is an artifact of the PHP being a constant specific volume system in conjunction with the initial thermodynamic states of the PHP being close to the saturated liquid line for high fill ratio cases.
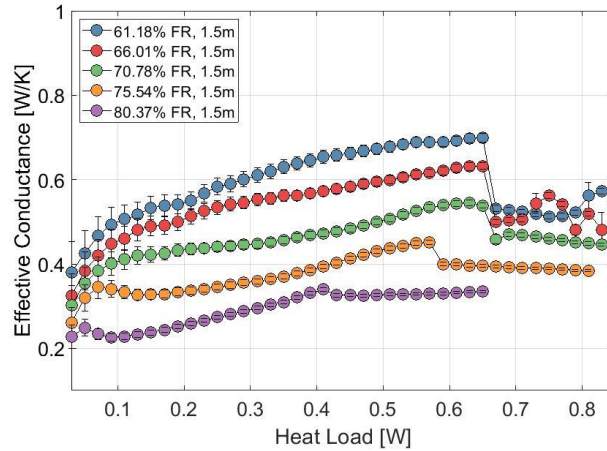
Figure 3.6. Time-averaged effective conductivity as a function of applied heat load for the high fill ratio range (61.18% - 80.37%) of the 1.5 m PHP.

The 1.5 m PHP's high fill ratio performances are plotted simultaneously in Figure 3.6 as functions of applied heat load. Unlike the low and middle fill ratio ranges, the PHP's performance strongly depends on the fill ratio when it is above 60%. The performance drops significantly as the fill ratio increases, regardless of the applied heat load. As described in a later section, this observation is likely caused by a change in the PHP's failure mode from evaporator sensible heating of the fluid (dry-out) to excessive viscous impedance. With increasing fill ratio, there is an increase in the viscous forces resistive to fluid motion that arise from a higher liquid volume fraction. While interesting from a thermodynamic phase perspective, the high fill ratios performed poorly compared to the low and middle fill ratios and likely should be avoided in practice.

The time-averaged performance and temperature trends of the 1.5 m helium PHP with increasing applied heat load reveal rich fluid phase behavior of alternating adiabatic tubes that correlate with thermal performance and flow direction. Five different fully or partial single-phase

PHP operating states have been identified, all reaching stable pseudo-steady states and performing well relative to traditional conductive thermal linkages. However, the classic fully two-phase and two-phase hot tube/sub-cooled cold tube phase regimes performed significantly better than others and were most prevalent in the optimal fill ratio range. Most importantly, phase change in either tube suggests that a mass imbalance exists between adjacent tubes, which in turn suggests that gravity is the dominant fluid driving force.
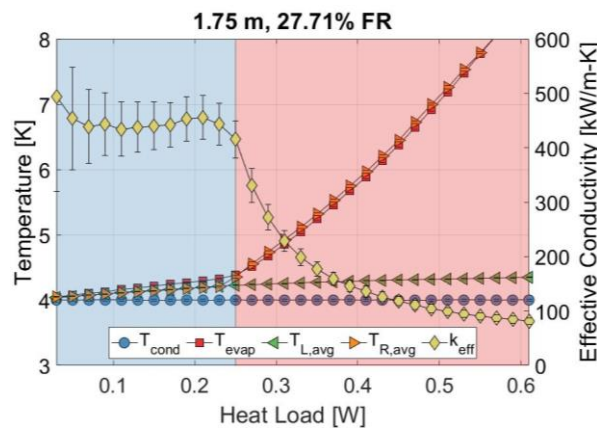
(a)
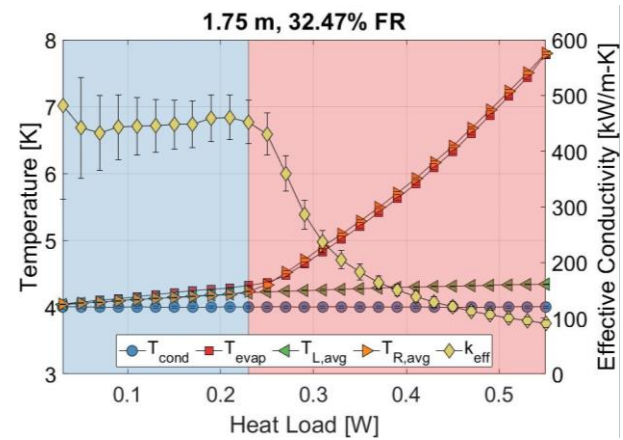
(b)
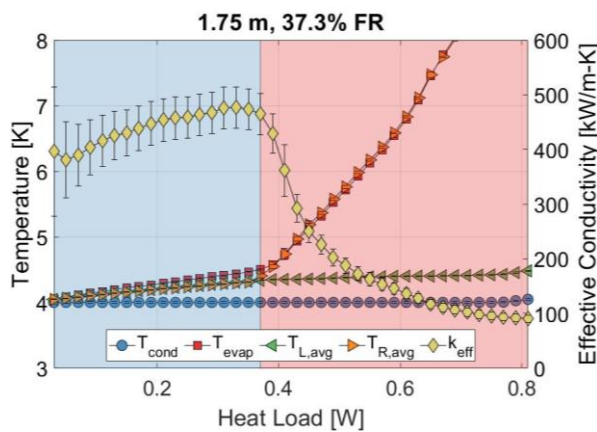
(c)
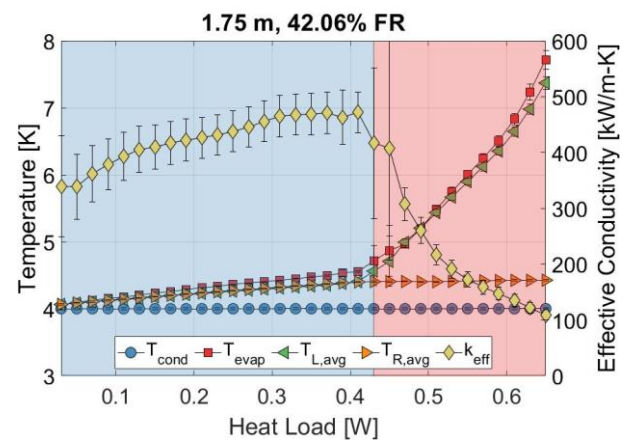
(d)
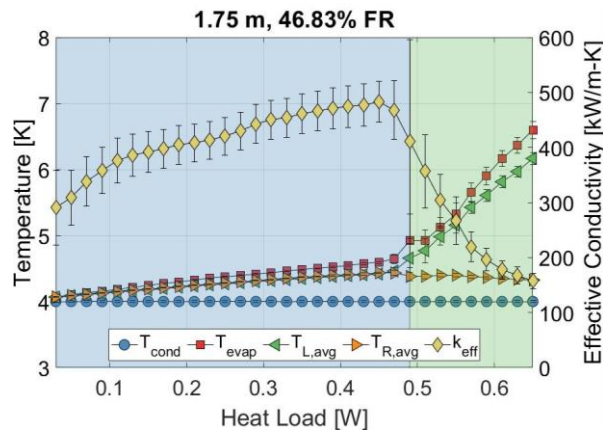
(e)
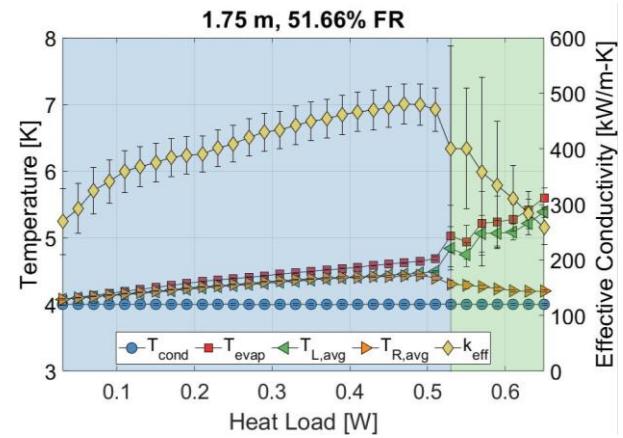
(f)
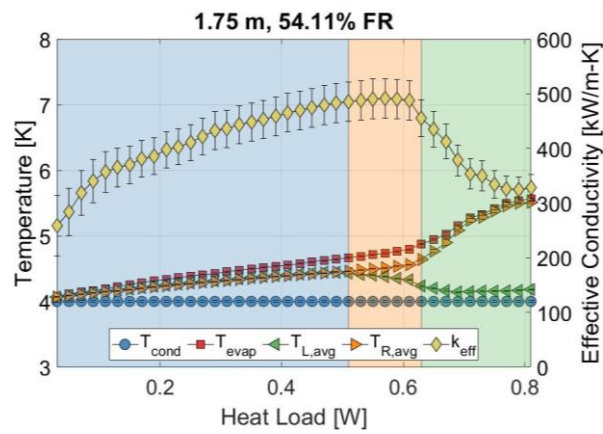
(g)
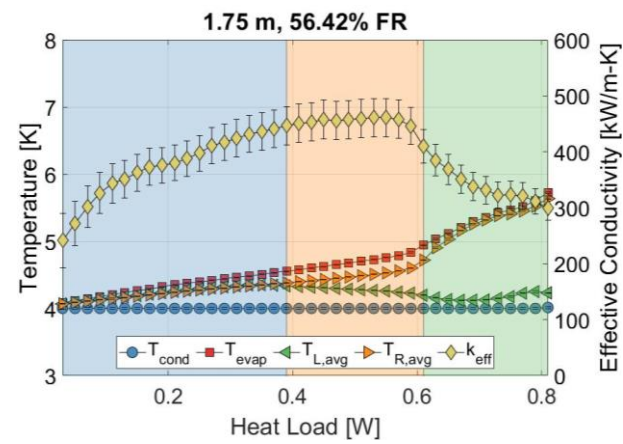
(h)
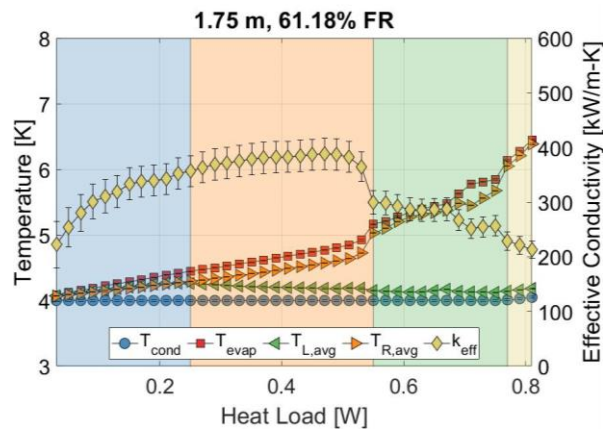
(i)
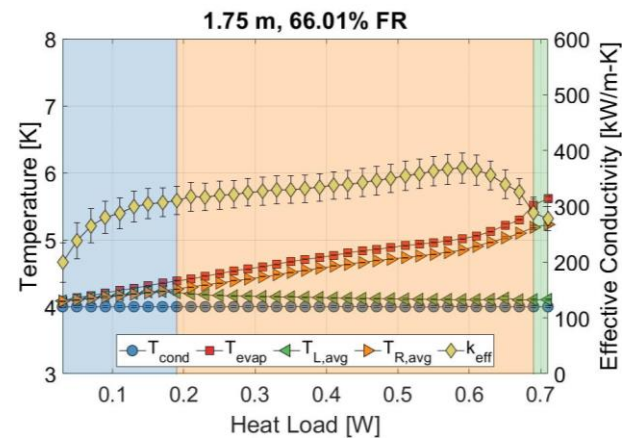
(j)
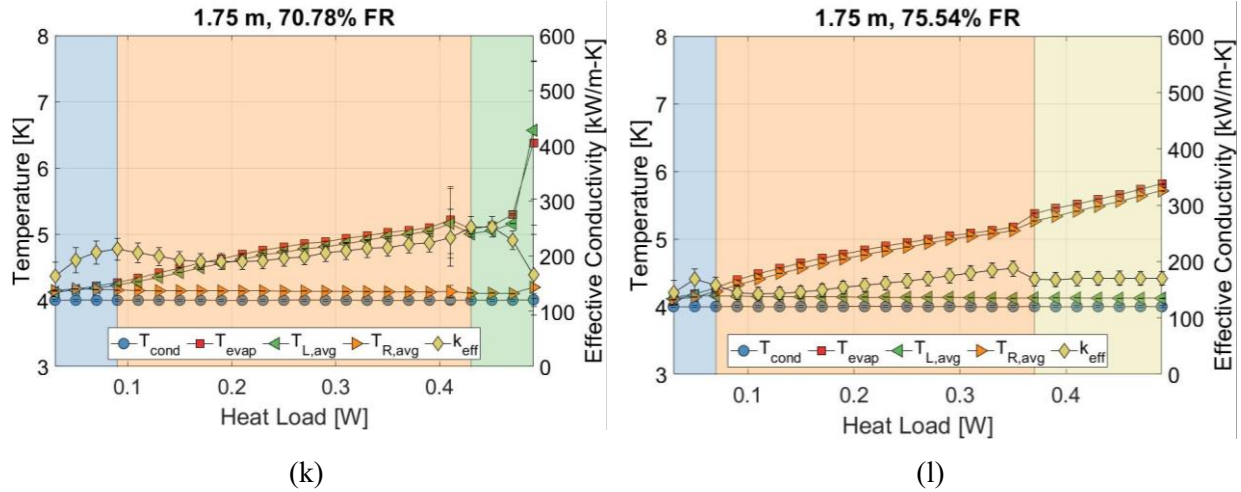
Figure 3.7. Time-averaged effective conductivity and condenser, evaporator, and spatially-averaged adiabatic temperatures as functions of applied heat load of the 1.75 m PHP for all fill ratios tested.

Moreover, the time-averaged performances (right axes) and temperature measurements (left axes) as functions of applied evaporator heat load of the 1.75 m PHP for all fill ratios tested are shown in Figure 3.7. Generally, the trends and observations described in detail in this section for the 1.5 m PHP are the same for the 1.75 m PHP, and as such, are not considerably affected by the slight increase in adiabatic length.

3.2. Temperature-Volume Phase Diagrams

The fluid phase within each of the adjacent adiabatic tubes is of interest to further characterize the phase change behavior with increasing heat load for the spectrum of fill ratios and better understand the vapor and liquid distribution. For each tube, the temperature and pressure measurements are averaged spatially and temporally, resulting in one temperature and pressure value per tube, per heat load/fill ratio combination. This method is valid because, as described in a previous section, the adjacent adiabatic tubes are essentially isothermal across their lengths. Additionally, the pressure difference between the condenser and evaporator sections is thermodynamically insignificant. Although this pressure difference is relevant hydrodynamically,

the saturation temperature difference of the fluid corresponding to the measured pressure difference is not relevant, and is typically on the order of 0.02 K. This observation is likewise the reason that phase change in the adiabatic tubes is easily identified: When the fluid transitions from two-phase to single-phase, the resulting temperature change is large compared to the saturation temperature difference implied by the pressure measurements, especially for transitions to superheated vapor.

Unfortunately, when the fluid is two-phase in a given adiabatic tube, the temperature and pressure measurements are redundant as they both measure the same saturation condition, preventing a complete thermodynamic characterization of the state since the distribution of saturated liquid and vapor is unknown. If only one of the adiabatic tubes is single-phase, the thermodynamic state, and therefore the total mass of the single-phase tubes, can be determined exactly. Since PHPs are constant mass systems, the mass contained in the adjacent two-phase tubes is constrained when the mass contained in the single-phase tubes is known, resulting in a known specific volume of the two-phase tubes, which, when paired with the measured temperature and pressure, result in a fully defined two-phase thermodynamic state. Figures 3.8 – 3.10 show the obtainable thermodynamic states of the adjacent adiabatic tubes (excluding cases where both tubes contain two-phase fluid) on temperature-volume phase diagrams for the low, middle, and high fill ratio ranges.

The phase diagram in Figure 3.8 shows states for the adiabatic tubes in the low fill ratio range. Since, in this range, the hot tube fluid boils before the cold tube changes phase, the states for the cold tube are two-phase while the states for the hot tube are superheated. Since the cases where the hot tube fluid is two-phase always coincide with two-phase cold tube states for this fill ratio range, two-phase states for the hot tube cannot be predicted. For all fill ratios in this range,

the cold tube fluid's phase behavior with increasing heat load is consistent: the fluid's temperature increases and volume decreases within the vapor dome and below the critical specific volume of helium, corresponding to a decreasing vapor mass quality. Thus, the mass imbalance between adjacent tubes grows with increasing applied heat load. Furthermore, the quality of the cold tube's fluid decreases with increasing fill ratio, which is expected with additional mass in the system and implies that the observed mass imbalance between adjacent tubes also grows with increasing fill ratio. For the hot tube, all calculable thermodynamic states are superheated.
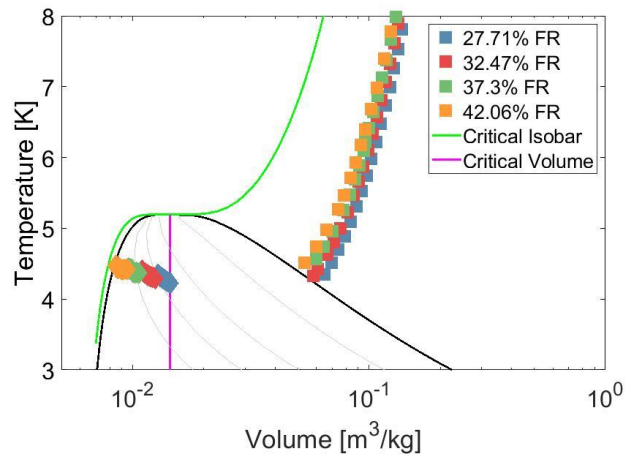
Figure 3.8. T-v phase diagram of the fluid contained in the two adjacent adiabatic tubes for the low fill ratio range (27.71% - 42.06%) of the 1.5 m PHP.

Figure 3.9 shows the phase diagram for the adjacent adiabatic tube fluid states for the middle fill ratio range. Within this range, both adiabatic tubes change phase at similar heat loads, resulting in cold tube two-phase states with essentially zero vapor quality since the applied heat loads at which the cold tube phase becomes calculable are high. Above a fill ratio of 54.11%, the cold tube changes phase before the hot tube, so the two-phase state of the hot tube is calculable instead of the cold tube. Interestingly, the hot tube two-phase states in Figure 3.9 follow a trend opposite to the cold tube two-phase states in Figure 3.9, yet the conclusion is the same: the vapor mass quality of the fluid in the hot tube increases with increasing heat load, indicating that the

mass imbalance between adjacent tubes increases with increasing heat load. Furthermore, similar to the cold tube two-phase states for the low fill ratios, the hot tube's two-phase fluid quality is inversely proportional to the fill ratio. Since the condenser temperature is constant, single-phase cold tube states are not a strong function of the fill ratio. The single-phase hot tube states tend to decrease in specific volume when the fill ratio increases.
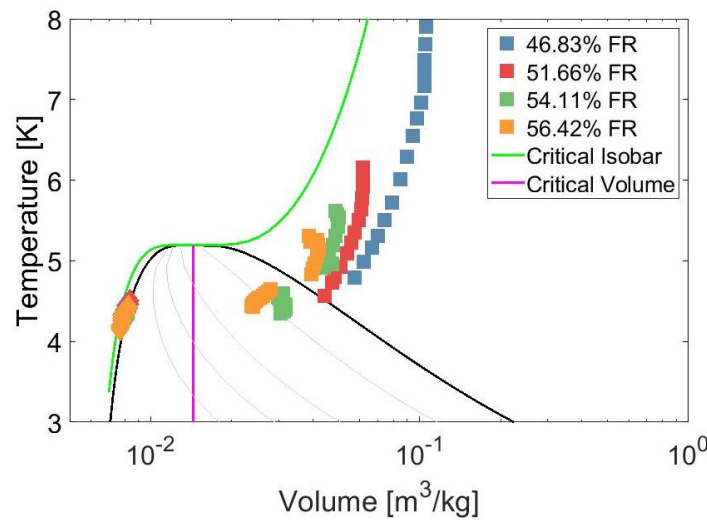
Figure 3.9. T-v phase diagram of the fluid contained in the two adjacent adiabatic tubes for the middle fill ratio range (46.83% - 56.42%) of the 1.5 m PHP.
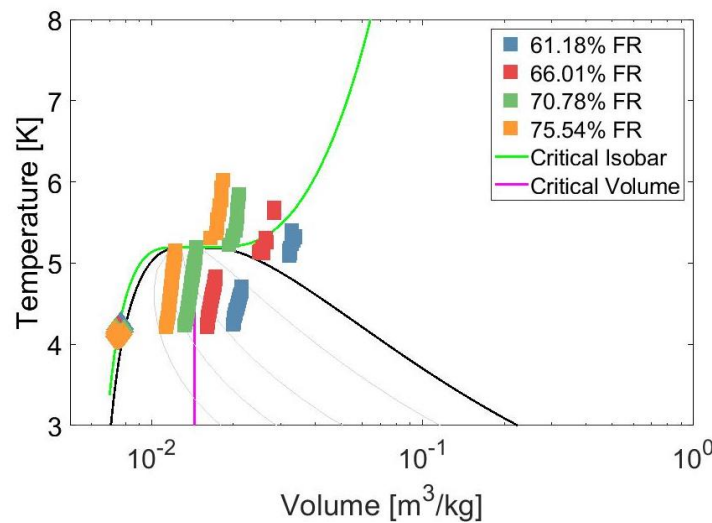
Figure 3.10. T-v phase diagram of the fluid contained in the two adjacent adiabatic tubes for the high fill ratio range (61.18% - 75.54%) of the 1.5 m PHP.

Figure 3.10 shows the phase diagram for the high fill ratio range. Since subcooling of the cold tube fluid tends to occur at lower applied heat loads for high fill ratios, the hot tube has more calculable two-phase states. Nevertheless, the trends observed of the adjacent tubes in the middle fill ratio range extend to the high fill ratio range in Figure 3.10. The most noticeable difference is in the single-phase states of the hot tube, where it is observed that at the highest fill ratios, supercritical operating states become possible

Moreover, thermodynamic phase diagrams for the three fill ratio ranges of the 1.75 m PHP tests are shown in Figure 3.11. Generally, the trends and observations detailed in this section regarding the 1.5 m PHP are the same for the 1.75 m PHP.
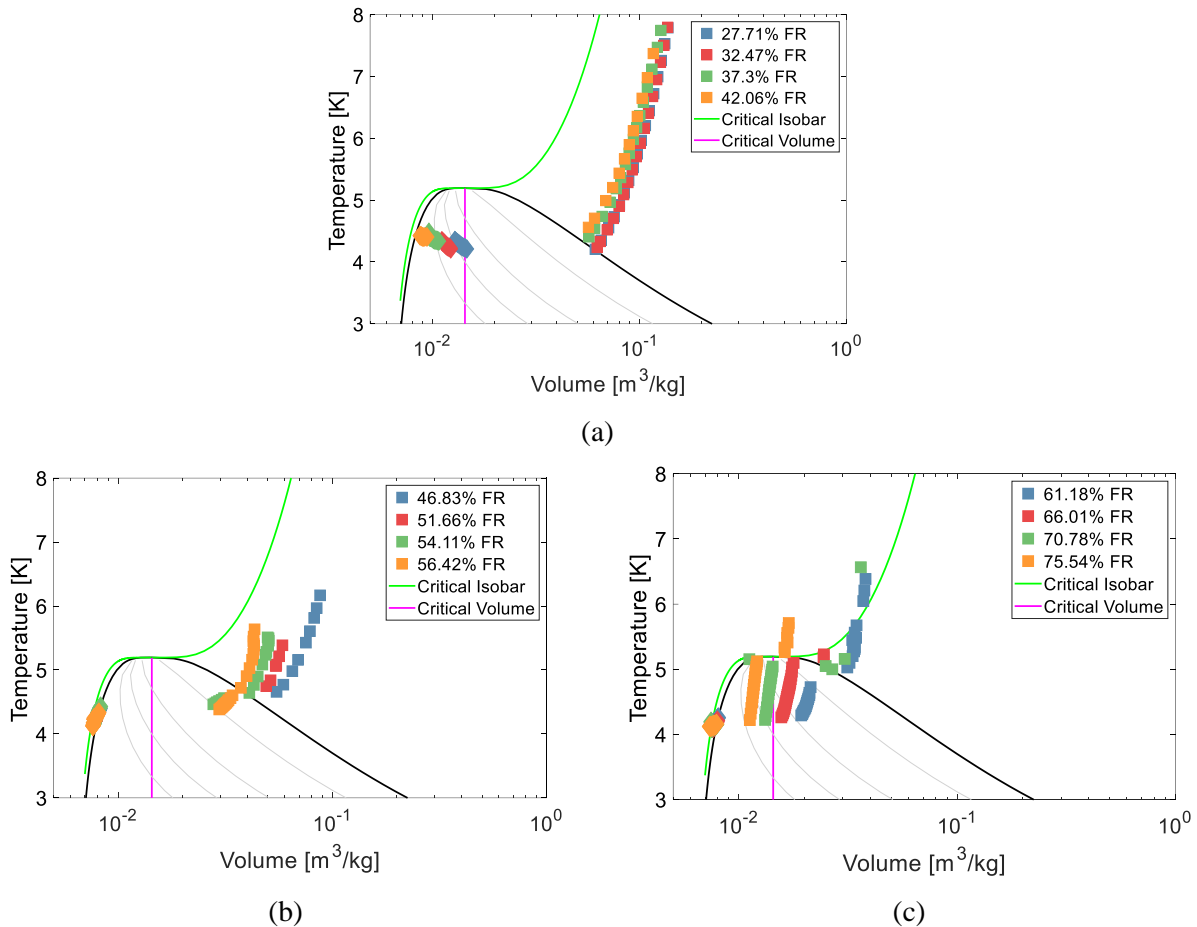
Figure 3.11. T-v phase diagram of the fluid contained in the two adjacent adiabatic tubes for the (a) low, (b) medium, and (c) high fill ratio ranges of the 1.75 m PHP.

3.3. Adiabatic Length Comparison

The insights gained through analyzing the time-averaged adiabatic tube temperature measurements of the 1.5 m PHP are essentially the same for the 1.75 m PHP. The phase change phenomena, resulting performance trends, and the identification of flow directionality for the 1.75 m PHP tests are consistent with the observations from the 1.5 m PHP tests. Moreover, the fill ratio ranges (low: 27.72% - 42.06%; middle: 46.83% - 56.11%; high: 60% +) also remain the same since the phase change and performance trends that define the fill ratio ranges are identical. For the 1.75 m PHP, the peak performance is 491.4 kW/m-K with a fill ratio of 54.11% at an applied heat load of 0.57 W; however, a heat load of 0.61 W is achieved prior to failure at a fill ratio of 54.11%, albeit with a slightly lower effective conductivity. The primary differences between the two different adiabatic lengths arise in the magnitude of the effective conductivity, the heat loads at which phase change occurs, and the magnitude of the viscous losses at high fill ratios.

For the optimal fill ratio range, defined between 46.83% - 56.42%, the effective conductance of both the 1.5 m and 1.75 m PHP are plotted simultaneously as functions of increasing applied heat load in Figure 3.12. Indeed, over an extensive range of applied heat loads, the thermal resistance is essentially independent of adiabatic length prior to dry-out, consistent with the helium PHP experiments from Fonseca [12, 13]. Therefore, this study verifies that the length-independent performance of helium pulsating heat pipes persists for adiabatic lengths up to 1.75 m at the optimal fill ratio.

Additionally, instead of a single optimal fill ratio, the observed length-independent performance is prevalent over a range of fill ratios, implying that within this range, the conductance is also independent of the fill ratio. Although the adiabatic length does not affect PHP performance when operating prior to dry-out, the adiabatic length, along with the fill ratio, both affect the heat

load at which dry-out occurs, an effect seen in both Figures 3.13 (b) and 3.14. Given that the maximum heat load only decreased slightly, from 0.63 W to 0.57 W for a fill ratio of 51.66%, when the adiabatic length was increased from 1.5 m to 1.75 m, it is likely that the observed length-independent conductance of helium PHPs would continue for adiabatic lengths beyond 2 m.
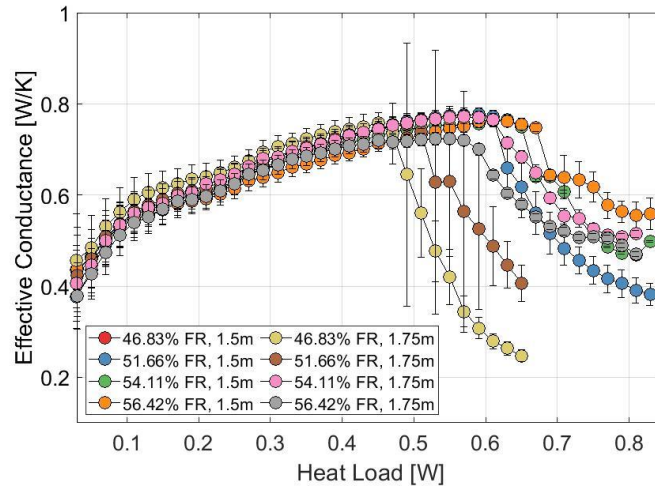
Figure 3.12. Time-averaged effective conductance as a function of applied heat load for the 1.5 m and 1.75 m PHPs in the middle fill ratio range (46.83% - 56.42%), displaying length and fill ratio independence.

Deviations in the behavior of the two PHPs with differing lengths become apparent when considering the effect of the fill ratio on the peak conductance, maximum allowable heat load, and phase-change heat loads. Figure 3.13 shows (a) the maximum conductance prior to failure, and (b) the maximum allowable heat load prior to failure as functions of fill ratio for both PHP lengths. Figure 3.13 (a) shows that the maximum conductance before failure is essentially the same for both adiabatic lengths for fill ratios below 60%. Beyond a 60% fill ratio, both PHPs exhibit severe performance degradation, with the effect being more pronounced for the 1.75 m PHP. This degradation can be attributed to excessive viscous losses, which are linearly proportional to both the adiabatic length and the fill ratio. However, viscous forces alone cannot explain the fill ratio

and adiabatic length independence of the performance observed for fill ratios below 60% in Figures 3.12 and 3.13.

(a)   (b)
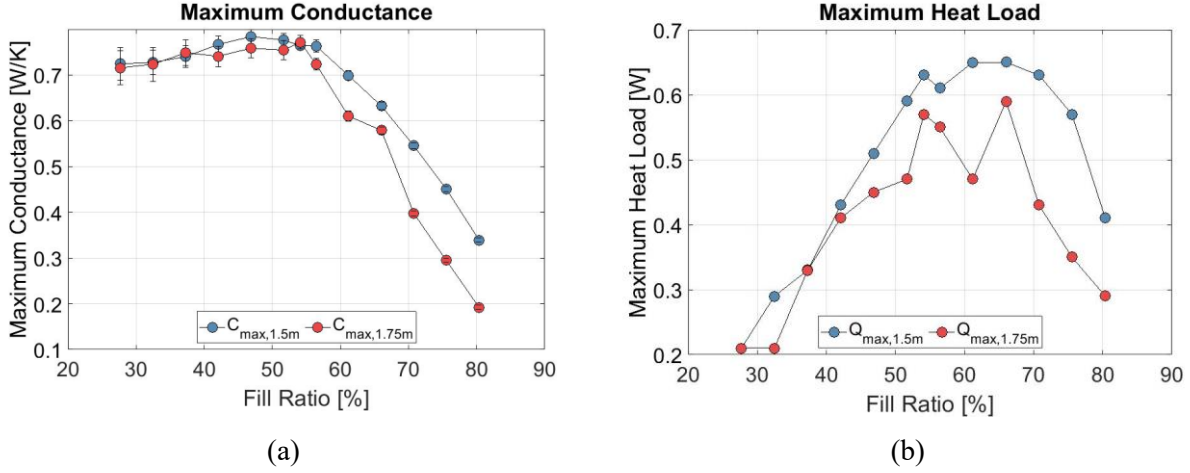
Figure 3.13. Maximum conductance (a) and maximum allowable heat load (b) as functions of fill ratio for the 1.5 m and 1.75 m PHPs.

The viscous resistance, R_v, and the buoyant force, F_b, acting on the two-phase fluid are defined as:

$$R_v = \frac{8\mu L}{\pi r^4} = \frac{8}{\pi r^4} L_{ad}[FR\mu_l + (1 - FR)\mu_v] \qquad (3.1)$$

$$F_b = \Delta \rho g L_{ad} A_c \qquad (3.2)$$

Where:

$$\Delta P_v = R_v \dot{V} \qquad (3.3)$$

Where μ is viscosity, L is the tube length, r is the tube radius, L_{ad} is the adiabatic length, FR is the fill ratio, μ_l and μ_v are the saturated liquid and vapor viscosities, $\Delta\rho$ is the density difference between adjacent adiabatic tubes, g is the gravitational acceleration, A_c is the tube cross-sectional area, ΔP_v is the pressure drop due to viscosity, and $\dot{V}$ is the volumetric flow rate. Both equations illustrate the dependencies of the viscous resistance and buoyant force on the fill ratio and the adiabatic length. Since the fluid velocity profile is generally unknown and complicated

due to random flow oscillations, the viscous flow resistance cannot be converted to a force, prohibiting a quantitative comparison to the buoyant force. Additionally, experimental evidence from section 3.2 suggests the relationship for fill ratios below 60%:

$$\Delta\rho \propto FR, \dot{Q} \tag{3.4}$$

Where $\dot{Q}$ is the applied heat load. The viscous losses and the gravitational force responsible for driving the fluid flow are proportional to the length and fill ratio but act in opposite directions. Thus, the increasing gravitational forces counteract the increasing viscous losses when either the fill ratio or adiabatic length is increased, resulting in an independent thermal performance. However, this effect is prevalent only for low and middle fill ratios. Indeed, the cold adiabatic tubes are limited in the amount of liquid they can store, so when the liquid inventory is high enough, the excess liquid must be stored in the hot tubes instead, reducing the mass imbalance and significantly increasing viscous losses in the hot tube. Therefore, at high fill ratios, the buoyant driving forces are low and the dissipative viscous forces are high, resulting in poor thermal performance of the PHP. Notably, the balance between gravitational and viscous forces is broken when the fill ratio is increased beyond the optimal value, indicating that the optimal fill ratios are such that the amount of liquid is maximized without filling the hot adiabatic tubes. This argument implies that PHPs' optimal fill ratio should be exactly 50%. However, the fill ratio depends on the fluid temperature [12, 15], especially for helium PHPs, which means that the initial fill ratio is different from the fill ratio at dry-out, and the optimal will not be precisely 50%.

Moreover, surface tension forces still play a role in the PHP's thermohydraulic behavior, albeit with seemingly less importance than the buoyancy and viscous forces. These dynamic capillary forces resist fluid motion similarly to the viscous forces when the fluid is in motion. Since the mass imbalance grows with increasing applied heat load, the number of vapor-liquid interfaces

likely decreases as either tube tends towards fully vapor or liquid, reducing the effect of surface tension. Frequency spectra data support this hypothesis in a following section (3.6). Additionally, capillary resistance occurs only at an interface as opposed to the entire length of the tube as with viscous resistance, making the opposing surface tension forces small relative to the viscous forces. However, the nature of the surface tension forces acting on the fluid evades the simple qualitative analyses possible for the viscous and gravitational forces. Specifically, the shape and quantity of the liquid-vapor interfaces are generally unknown, along with their dependencies on the various operational parameters such as fill ratio and applied heat load.

The viscous and buoyant force contributions also depend on the applied heat load. As observed in the phase diagrams in Figures 3.8 – 3.11, the mass imbalance between the two adjacent tubes increases with increasing heat load, which corresponds to an increasing buoyant driving force with increasing heat load. Furthermore, while the PHP's fill ratio has been referred to as constant, it is a function of temperature. The fill ratio values referenced are initial fill ratios, or the fill ratios at zero applied heat load. For initial fill ratios that correspond to a specific volume greater than the critical specific volume of helium, the fill ratio tends to decrease with increasing temperature [15], suggesting that for low and middle fill ratios, the viscous losses decrease with increasing applied heat load by virtue of the fill ratio decreasing. These two effects partially explain why the PHP's performance increases with increasing heat load prior to failure.

The phase change points for the two PHPs as functions of fill ratio are plotted in Figure 3.14. First, Figure 3.14 (a) shows the heat load at which the cold tube fluid changes phase to subcooled liquid, and it can be observed that as the fill ratio increases, subcooling of the cold tube fluid tends to occur at decreasing heat loads. As the fill ratio increases, more liquid is present in the PHP, and when the applied heat load is increased, the mass imbalance between the adjacent

tubes also increases. Therefore, higher fill ratios will experience subcooling at lower heat loads because less heat is required to drive the mass imbalance to the point where the cold tubes fill completely with saturated liquid and begin changing phase. These conclusions are valid for both adiabatic lengths, and there does not seem to be a significant difference between the two adiabatic lengths.

Furthermore, the heat load at which the hot tube fluid changes phase to superheated vapor is displayed in Figure 3.14 (b). Here, the opposite relationship to the subcooling heat load is observed: the heat load at which superheating occurs tends to increase with increasing fill ratio. Because superheating of the hot tube fluid is due to sensible heating of the fluid in the evaporator, the increased liquid replenishment to the evaporator section for higher fill ratios will allow for higher applied heat loads since a two-phase fluid with a higher fraction of saturated liquid can absorb more latent heat. Moreover, while the difference between the 1.5 m PHP and the 1.75 m PHP is subtle, it can be observed that the shorter PHP tends to have a higher superheating heat load than the longer PHP for the same fill ratio. Here, it is likely that the slightly higher viscous losses somewhat impede liquid replenishment to the evaporator for the 1.75 m PHP compared to the 1.5 m PHP. However, with an average difference of 54 mW, this effect is not very significant, likely due to the small adiabatic length difference relative to the PHPs' total adiabatic lengths.

Figure 3.14 (c) shows the supercritical phase change points for the two adiabatic lengths as functions of the fill ratio. For both adiabatic lengths, supercritical phase change only occurs at fill ratios higher than 60%, and the heat load at which this phase change occurs tends to decrease with increasing fill ratio. Regardless of the adiabatic length, the global pressure of PHPs will increase with increasing fill ratio, which results in an inverse relationship between the supercritical

phase transition and the applied heat because less heat is required as the fill ratio increases to drive

the global pressure beyond the critical pressure.
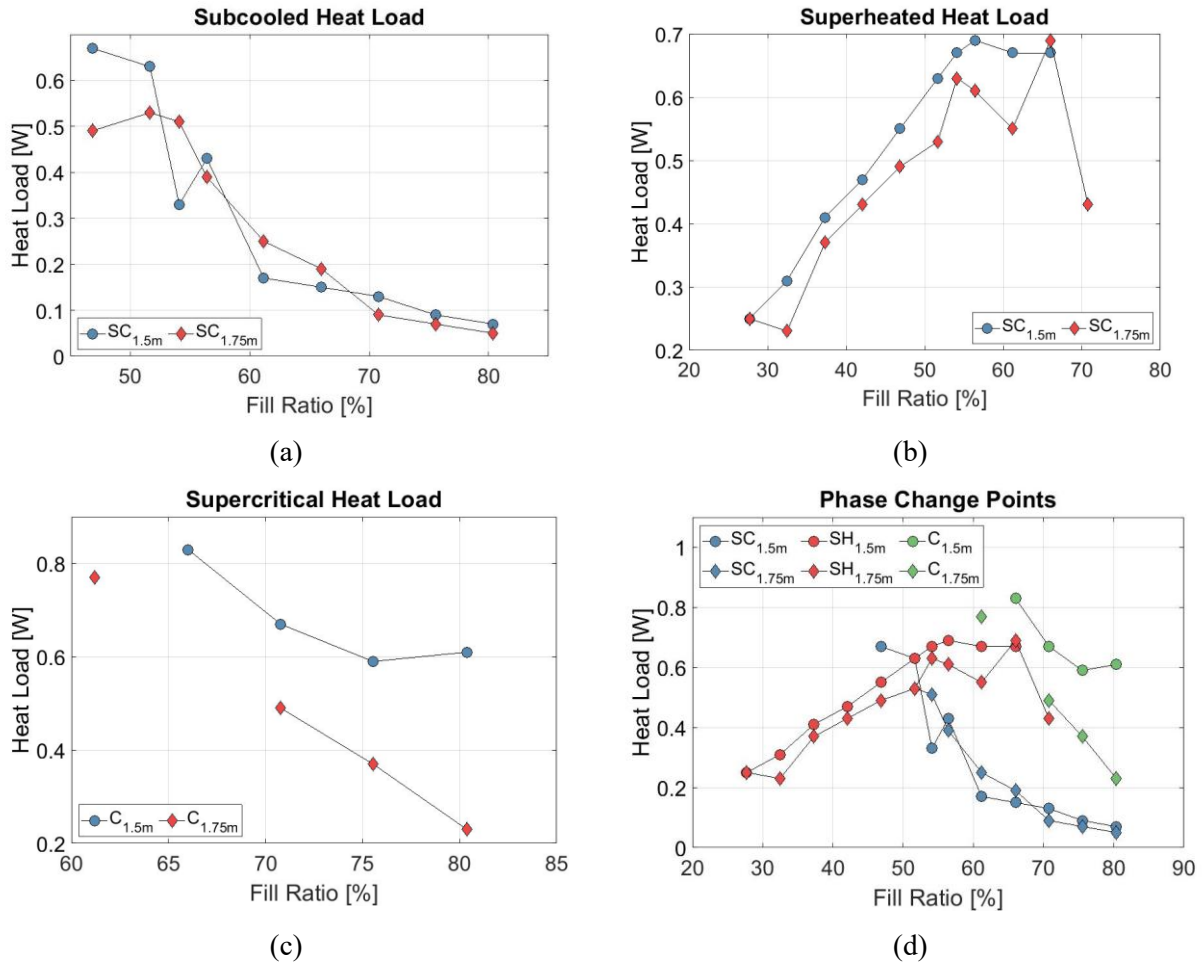
Figure 3.14. Phase change occurrence heat loads as functions of fill ratio for the 1.5 m and 1.75 m PHPs, with (a) showing subcooled heat loads, (b) showing superheated heat loads, (c) showing supercritical heat loads, and (d) showing all phase change heat loads simultaneously.

However, the 1.75 m PHP experiences the supercritical phase change at significantly lower

applied heat loads, implying that global PHP pressures are generally higher for the longer PHP at

high fill ratios. This observation is likely due to the excessive viscous impedances, typical at high

fill ratios and more pronounced for the longer PHP, since the velocity of the fluid, especially in the

hot tubes, is lower due to an increased liquid content. The cold tubes are already filled with

subcooled liquid when the supercritical phase change occurs, so the velocity of the fluid in the cold

tubes is less affected because the viscous losses cannot be further increased. Finally, for a scale comparison, all phase change heat load points are plotted simultaneously in Figure 3.14 (d).

3.4. Transient Adiabatic Section Temperature Behavior

Although the analysis of the time-averaged data resulted in the identification of adjacent tube thermodynamic phases and the onset of uni-directional flow, further insight into the fluid behavior and flow patterns can be gleaned by analyzing the temperature oscillations of the adjacent adiabatic tubes as functions of time. Figure 3.15 shows the time series data of the temperature measurements on each adiabatic tube for the 1.75 m PHP with a 56.42% fill ratio at applied heat loads within the three phase-defined regimes in Figure 3.3. Although these plots show only one minute of the time-series data, the qualitative features of the oscillation patterns are consistent throughout the entire test period for a given applied heat load after the PHP has reached steady-state operation. Furthermore, all observations made for this specific combination of fill ratio and adiabatic length extend for any combination within the parameter space.

Figures 3.15 (a) and (d) show the data with an applied heat load of 230 mW when both tubes contain two-phase fluid (blue background region in Figure 3.3). While these data were indistinguishable when time-averaged since the temperature measurements oscillate around the same average temperature, the oscillation patterns are qualitatively different: The temperature oscillations of the left/cold tube in Figure 3.15 (a) are more stochastic and have multiple oscillation modes while the temperatures of the right/hot tube in Figure 3.15 (d) oscillate uniformly with the same amplitude and only one mode of oscillation. Indeed, even before the fluid in either tube has transitioned from a two-phase fluid, there is a noticeable difference in the temperature oscillations, which are inextricably linked to the vapor quality and the way in which the fluid contained within the tubes moves. Thus, this observation suggests that the fluid is moving unidirectionally and that

there is a mass imbalance between adjacent tubes even before phase change has occurred in either tube.
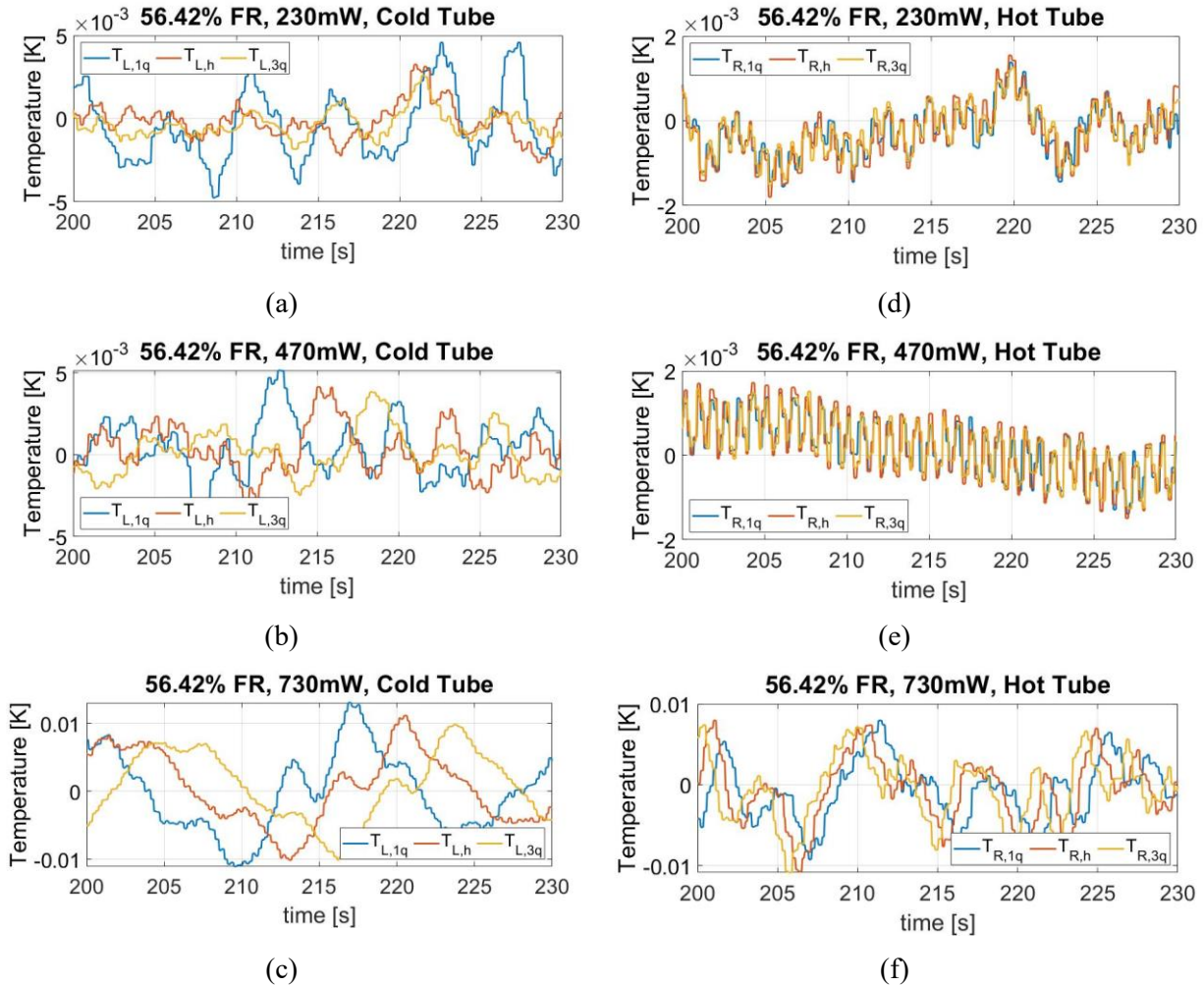
Figure 3.15. Transient time-series adiabatic temperature measurements for the 1.75 m PHP with a 56.42% fill ratio of the cold tube (a), (b), and (c), and the hot tube (d), (e), and (f), for 230 mW applied heat (a) and (d), 470 mW applied heat (b) and (e), and 730 mW applied heat (c) and (f). The heat loads correspond to PHP operating states with different phase behavior.

Moreover, Figures 3.15 (b) and (e) show the temperature oscillations of the left/cold and right/hot tubes, respectively, for an applied heat load of 470 mW, which corresponds to the phase regime with the cold tube containing subcooled liquid and the hot tube containing two-phase fluid (orange background in Figure 3.3). In this phase-defined heat load range, the behavior of the single-phase fluid in the cold tube is markedly different from the two-phase fluid in the adjacent

hot tube. In the cold tube, the stochastic temperature oscillations cease in favor of an unchanging temperature profile that translates through the adiabatic section from the condenser towards the evaporator. This feature is most easily observed in Figure 3.15 (b) between 210 and 220 seconds, where two subsequent temperature peaks are first observed for the sensor closest to the condenser (blue line), followed by the sensor in the middle of the adiabatic section (red line), and finally for the sensor closest to the evaporator (yellow line).

Indeed, the directionality of the flow is confirmed since the temperature profile of the cold tube is first observed at the sensor closest to the condenser, which is consistent with the flow direction required by the first law. Moreover, since the temperature sensors are equally spaced along the length of the adiabatic section, the time it takes for the temperature profile to move from one sensor to the next is constant. Thus, the velocity at which this thermal wave propagates in the direction of the fluid flow is constant for a given applied heat load. Although only a fraction of the test period is shown, these observations are consistent for any time after the PHP has reached a steady state. The adjacent hot tube, still two-phase, retains its previous behavior at lower heat loads where all sensors oscillate with the same amplitude and frequency and a single oscillation mode, as one would expect for a continuous saturated fluid phase responding to the single-frequency pressure oscillations originating from the evaporator and condenser sections.

Time-series temperature data for the phase regime (730 mW applied heat load) in which both tubes contain single-phase fluid, one with subcooled liquid and the other with superheated vapor, are shown in Figures 3.15 (c) and (f), respectively. This situation corresponds to the green background in Figure 3.3. The temporal phase shifting of a temperature profile is now observed for both adiabatic tubes, confirming that this phenomenon is only possible when the fluid is single-phase, although whether liquid or vapor does not matter. Although the flow is primarily uni-

directional, there are random oscillations superimposed on the DC flow that result in uneven heating or cooling of the fluid, which could explain the presence of the uni-directional thermal waves: Since single-phase fluid can be sensibly heated and cooled, fluid parcels that spend more time than others in either the condenser or evaporator section will have a different temperature than adjacent parcels, resulting in an axially non-uniform fluid temperature. Additionally, due to the very low thermal diffusivity of both vaporous and liquid helium, these adjacent fluid parcels do not thermally equilibrate in the axial direction by the time they have traversed the adiabatic section, which explains why the temperature profile is unchanging. This argument, however, is not true for a two-phase fluid, which would instead tend to change phase upon heat transfer instead of changing temperature, which is why this observation is not present when the adiabatic tubes' fluid is two-phase.

Additionally, while both tubes contain single-phase fluid and display uni-directional thermal wave propagation with 730 mW applied heat, there are some qualitative differences between the nature of these thermal waves for the adjacent tubes. First, the propagation direction of the thermal wave in the hot tube is from the evaporator to the condenser, which is opposite to that of the cold tube. This observation further solidifies that fluid flow is primarily uni-directional by first law arguments. Additionally, the temporal phase shifting of the hot tube is much smaller than that of the cold tube, suggesting that the thermal wave velocity is much higher for the hot tube. Since the thermal wave propagation velocity is linked to the characteristic velocity of the fluid, it follows that the low-density vapor contained in the hot tube has a higher velocity than the high-density liquid in the cold tube via mass conservation arguments. This result is another indication of a large mass imbalance between adjacent tubes.

3.4.1. Thermal Wave Velocity Evaluation

Since the distance between the adiabatic section thermometers is known, the temporal phase shifting observed in the time-series temperature data gives enough information to determine a time-of-flight velocity measurement of the propagating thermal waves. Although this is not a direct measurement of the fluid's mean velocity, it is certainly characteristic of the fluid behavior and thus serves as a reasonable estimate of the actual time-averaged fluid velocity in adjacent adiabatic tubes. This inference of fluid velocities is made possible by the instantaneous fluid temperature measurement technique described in section 2.4.

(a)   (b)

(c)   (d)
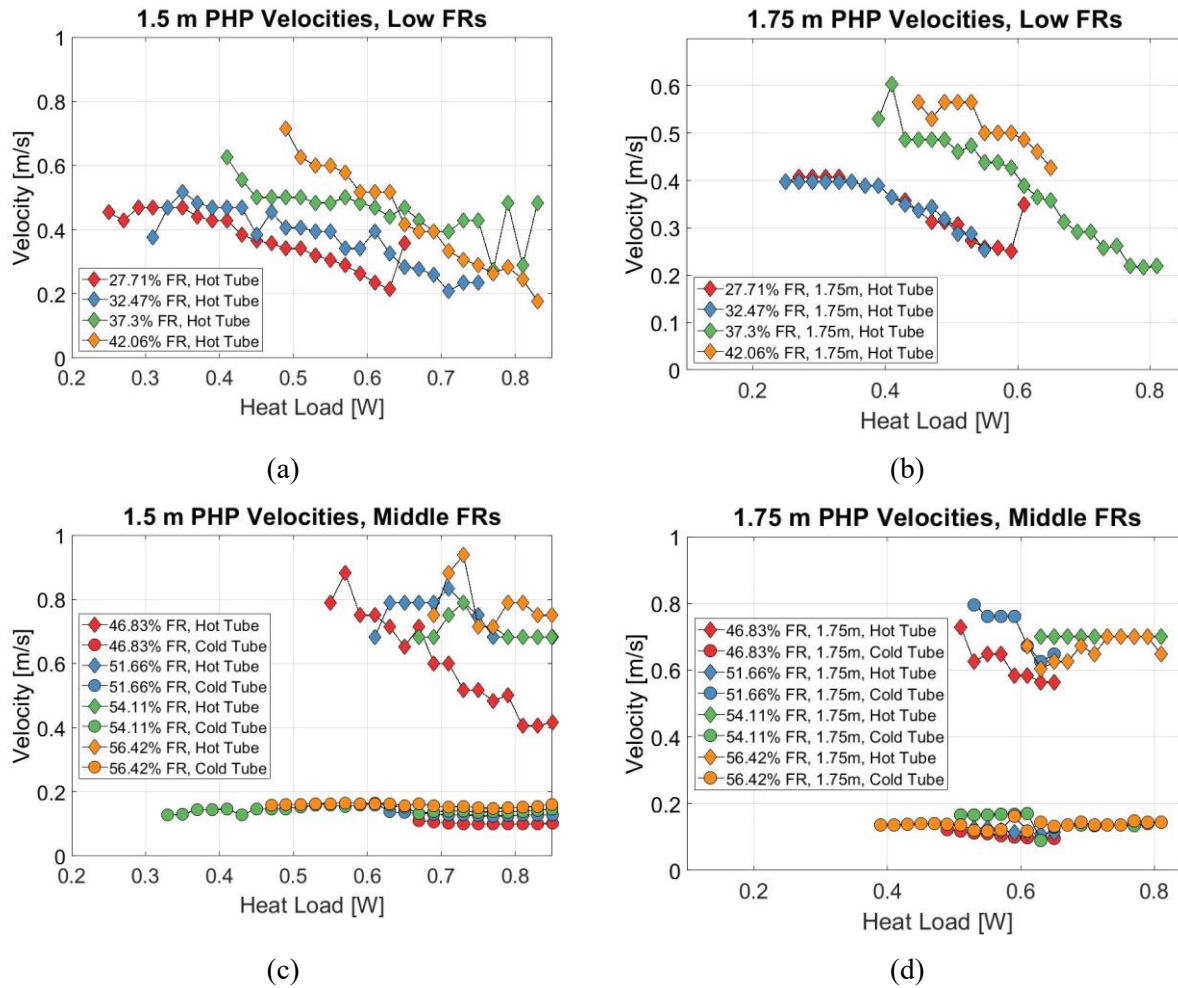
Figure 3.16. Time-of-flight velocities calculated from the temperature profile temporal phase shifting observed when the fluid is single-phase in either adiabatic tube.

Figure 3.16 shows the time-averaged thermal wave velocities as a function of applied heat load for each adiabatic tube, with various fill ratios within the optimal range and for both adiabatic lengths. The average temporal phase shift for a given applied heat load was obtained by averaging the phase shift for every datum over the ten-minute recording period. For the cold tube fluid, Figures 3.16 (c) and (d) show that once the fluid has changed phase to subcooled liquid, the fluid velocity was not a strong function of applied heat load, fill ratio, or adiabatic length, with values ranging from 0.12 m/s – 0.2 m/s. Since these velocity predictions are only possible for single-phase states, the mass imbalance between adjacent tubes has already reached the point at which the cold tube is filled entirely with liquid, which results in a constant fluid velocity with increasing applied heat load since both the viscous impedance of the cold tube fluid and buoyant force contribution from the cold tube fluid are at their respective maximums. At lesser heat loads when the cold tube fluid is two-phase, the mean velocity likely decreases with increasing heat load since the increasing mass imbalance favors higher liquid content in the cold tube.

Moreover, the observation that the cold tube fluid velocity is constant upon subcooling somewhat deviates from the intuitive notion that PHPs' performance increases with applied heat load due to higher fluid velocities, especially since in the optimal fill ratio range, the PHP's best performance occurs when the cold tube is sub-cooled, and the hot tube is two-phase. Instead, the positive correlation between performance and heat load is likely a result of the increase in heat transfer coefficients in the evaporator and condenser sections due to the decrease in the liquid film thickness with increasing heat flux [7, 64], despite a constant inlet velocity.

However, the hot tube fluid velocities display significant dependencies on fill ratio and heat load after the fluid has become single-phase. Also, note that the single-phase hot tube operating states for any combination of parameters for which the velocities are measurable correspond to

poor thermal performances relative to two-phase hot tube states. First, the hot tube velocities tend to increase with increasing fill ratio in the low fill ratio range, as seen in Figures 3.16 (a) and (b). This occurs because, for these low fill ratios, the cold tubes contain two-phase fluid, and the mass imbalance is still growing despite the change in the phase of the hot tube. Thus, the mass imbalance increases with increasing fill ratio, resulting in a greater gravitational potential and, therefore, a greater pressure differential between the evaporator and condenser sections that drives greater fluid velocities. When the fill ratio is increased to the middle range, subcooling of the cold tube fluid occurs, which reduces the fill ratio's effect on the hot tube fluid velocity because the pressure differential resulting from gravity in the cold tube is already maximized.

Moreover, the hot tube gaseous velocities tend to decrease with increasing heat load, which is unintuitive since a mass balance on the evaporator section would seem to imply that an increasing density difference between adjacent tubes would result in an increasing hot tube velocity. However, the sensible heating of the hot tubes' fluid causes the viscosity to increase, which is an unexpected relationship. Indeed, the fluid velocity is proportional to the mass imbalance and inversely proportional to viscosity, and the growing mass balance with applied heat load is not great enough to counteract the effect of the increasing gaseous viscosity with increasing applied heat load, resulting in an inverse relationship between the hot tube velocities and the applied heat load. Like the fill ratio, the hot tube velocities are more dependent on the applied heat load only when in the low fill ratio range, and the relationship is weaker when the fill ratio is increased above 45%. Regardless, the unique fluid properties of liquid and gaseous helium are responsible for the unintuitive velocity trends observed.

3.5. Adiabatic Section Temperature Frequency Spectra

Frequency spectra of the adiabatic temperature measurements for two-phase operating states reveal further disparities between the two adjacent tubes. With the same operating conditions as the data in Figure 3.15 (1.75 m adiabatic length and 56.42% fill ratio), Figures 3.17 and 3.18 show the frequency spectra of the cold and hot tube, respectively, for (a) 30 mW, (b) 70 mW, and (c) 130 mW applied heat loads. The applied heat loads correspond to operating conditions in which the fluid of both adiabatic tubes is two-phase. For the cold tube frequency spectra, shown in Figure 3.17, there is a high number of oscillation modes below the cryocooler frequency (1.2 Hz). As the applied heat load increases, the number of oscillation modes decreases. The hot tube frequency spectra also display many oscillation modes at 30 mW applied heat load; however, the number of oscillation modes decreases significantly more suddenly than the cold tube with increasing applied heat load. At 130 mW, the hot tube temperatures oscillate at only the cryocooler frequency, while the cold tube temperatures retain additional modes.

These observations suggest that the mass imbalance observed for single-phase states extends to low heat loads when the PHP is fully two-phase because the number of oscillation modes corresponds to the number of individual plugs and slugs contained in the adiabatic section assuming that they behave like nonlinear mass-spring-damper systems. At low applied heat, the two adjacent tubes contain a similar number of individual plugs and slugs, and the mass imbalance is small. As the heat load increases, the cold tube loses some oscillation modes as mass transfers from the hot tube, causing a reduction in the number of liquid slugs as they coalesce. Meanwhile, the hot tube loses significantly more oscillation modes as mass transfers to the cold tube due to the density difference between saturated liquid and vapor states. Thus, the mass imbalance has increased, suggesting that even at very low heat loads, the gravitational forces are dominant in

driving the PHP fluid. This observation also implies that the mass imbalance between adjacent tubes positively correlates with applied heat, a condition on which analyses from a previous section (3.4) were contingent.

(a) (b) (c)
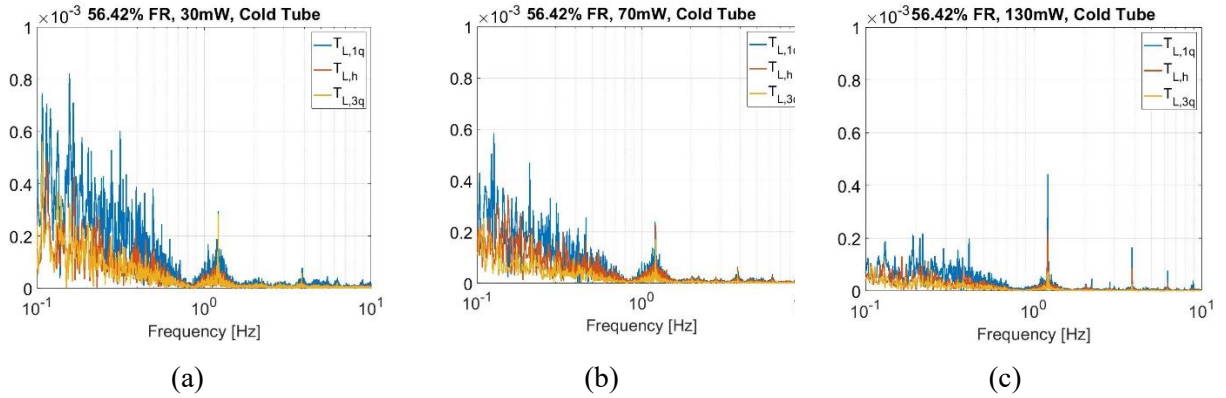
Figure 3.17. Frequency spectra of the cold tube temperature oscillations for the 1.75 m PHP with 56.42% fill ratio for (a) 30 mW, (b) 70 mW, and (c) 130 mW, all heat loads for which the PHP fluid is entirely two-phase.

(a) (b) (c)
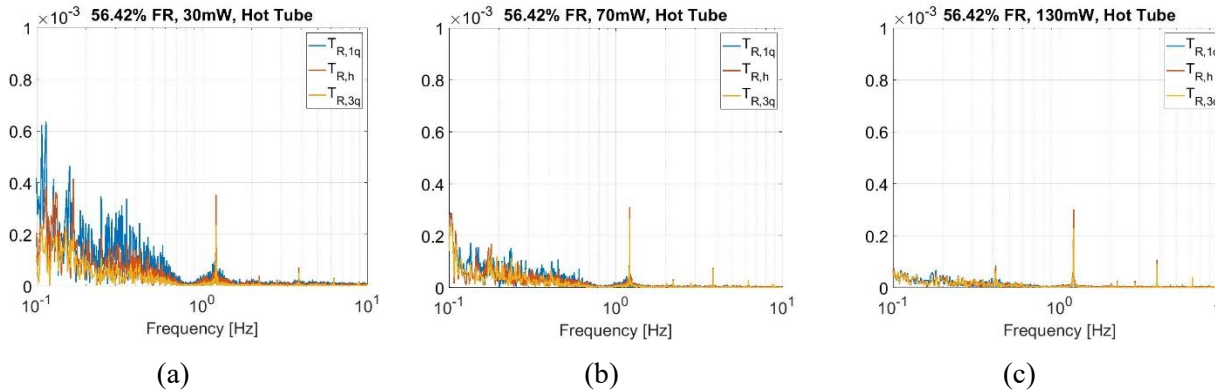
Figure 3.18. Frequency spectra of the hot tube temperature oscillations for the 1.75 m PHP with 56.42% fill ratio for (a) 30 mW, (b) 70 mW, and (c) 130 mW, all heat loads for which the PHP fluid is entirely two-phase.

Moreover, the cold tube will continue to lose oscillation modes gradually as the heat load further increases until the fluid changes phase to a sub-cooled liquid. Since the hot tube temperatures display only one oscillation mode starting at around 100 mW, it is unlikely above this heat load that any liquid slugs are contained in the hot tube. Instead, the hot tube likely contains just one long vapor core surrounded by a thin liquid film, representing the annular two-phase flow

regime, which has also been observed in visualization studies [28, 29, 65]. These observations are consistent for both adiabatic lengths and all fill ratios within the optimal range.

3.6. Thermosiphon-like Behavior

In previous sections, evidence from many analyses and perspectives indicate that the helium PHPs tested in these studies are driven primarily by gravity and, therefore, operate more like a thermosiphon than a traditional pulsating heat pipe; a conclusion that is supported by many previous studies [14, 29, 65 - 67]. This conclusion likely holds for all vertically oriented PHPs with extended adiabatic lengths where purely oscillatory modes are insignificant. First, in section 3.1, identifying single-phase states and circulatory flow suggests that a mass imbalance, or density difference, develops between adjacent adiabatic tubes. This persistent density difference implies that gravity drives the cold, dense fluid toward the evaporator, allowing the warm, light fluid to return to the condenser. The temperature-volume phase diagrams in section 3.2 also support the mass imbalance observation and show that the density difference increases with increasing heat load and fill ratio. Furthermore, the comparison between the two adiabatic lengths described in section 3.3 further argues that gravity is the dominant driving force for vertical PHPs and that it is resisted primarily by viscosity. Although the time-averaged data indicates that a mass imbalance exists for partial or fully single-phase states, the frequency spectra data of the adjacent adiabatic tube temperatures in section 3.5 show that the mass imbalance extends to the low heat load, fully two-phase states.

An alternative test procedure for studying PHP behavior is to incrementally increase the condenser temperature while maintaining a constant applied heat load, as opposed to the reverse scenario. Doing so effectively varies the Bond number of the fluid in the condenser section, which is the lowest Bond number in the system since it is the coldest. Figure 3.19 shows the results of

the variable Bond number tests for the 1.75 m PHP with all fill ratios. Indeed, at Bond numbers less than 2, the PHP is expected to perform well since the plug-slug flow is enforced via the Bond number criterion. When the condenser Bond number is precisely 2, Figure 3.19 displays significant performance spikes and significantly increased variances stemming from very large condenser temperature oscillation amplitudes. Indeed, this observation results from a two-phase flow instability in which the formation of two-phase interfaces perpendicular to the flow direction is an equally preferred energy configuration to stratified flow. Therefore, two-phase interfaces constantly form and collapse, causing large temperature oscillations. These instabilities are more prevalent at the low and middle fill ratios as there are more two-phase interfaces than at high fill ratios.
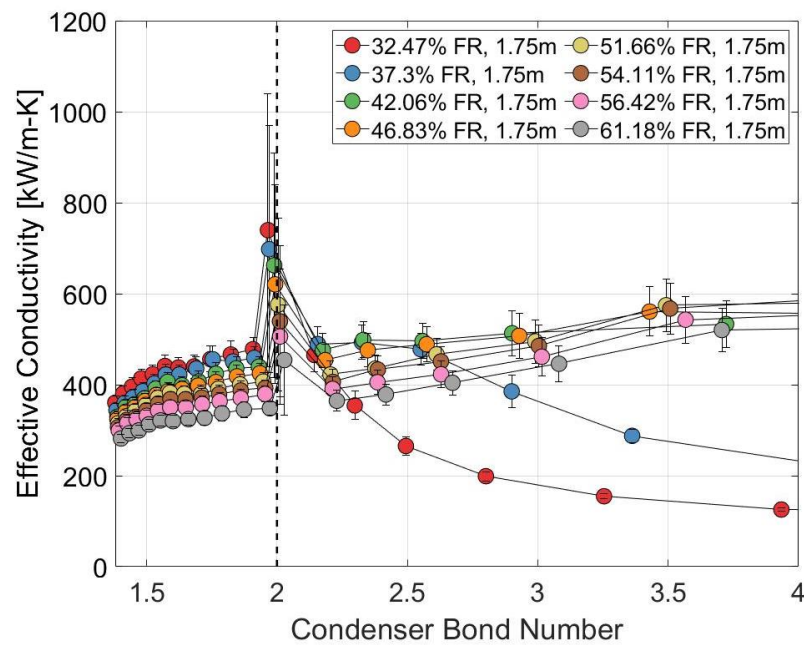
Figure 3.19. Effective conductivity as a function of condenser Bond number for the 1.75 m PHP with all fill ratios.

Increasing the condenser Bond number beyond 2 yields results that confirm vertical helium PHPs' thermosiphon-like behavior. With Bond numbers greater than 2, two-phase interfaces do not form, and the plug-slug mass distribution is absent. If the helium PHPs tested were operating as

proper pulsating heat pipes, then it would be expected that the performance would drop when the Bond number criterion is no longer met. However, after the instability, the performance remains excellent, suggesting that two-phase interfaces are unnecessary, so the flow must be gravitationally driven.

Figure 3.20 shows pairs of operating states for the fluid in the two adjacent tubes for the 66.01% fill ratio test with variable condenser temperature, along with helium's saturation curve. Notably, there is at least one pair of operating states in which both the cold and hot tubes contain supercritical fluid. This case is especially interesting because the fluid does not experience phase change as it circulates. Instead, the evaporator and condenser sections sensibly heat/cool the fluid to lower/higher density supercritical states. Indeed, the fluid is in the same phase everywhere in the PHP, implying that the flow is gravitationally driven because there are no fluid interfaces to prevent the denser fluid from collecting in the evaporator.
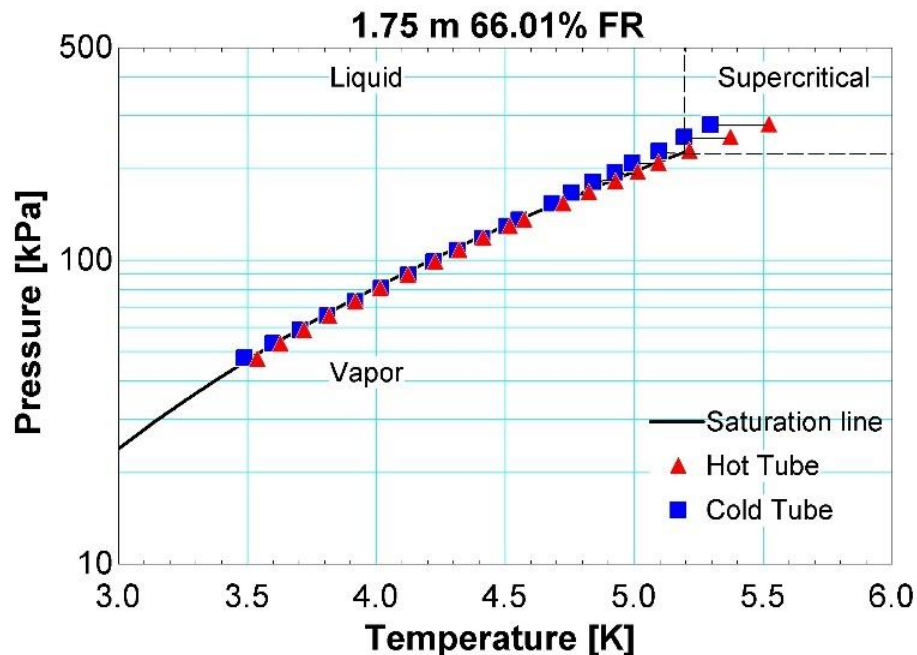
Figure 3.20. Pairs of thermodynamic states of the cold and hot tube for the variable condenser temperature test of the 1.75 m PHP with a 66.01% fill ratio, overlayed with the saturation curve of helium.

Overall, the arguments made (regarding the fluid flow behavior, mass distribution, and thermodynamic phases of the adjacent adiabatic tubes) using the experimental data presented in this chapter are summarized qualitatively with the visualizations shown in Figures 3.21 – 3.23. These visualizations show how the mass contained in adjacent tubes evolves with increasing heat load for different fill ratios, demonstrating uni-directional flow driven primarily by gravity.
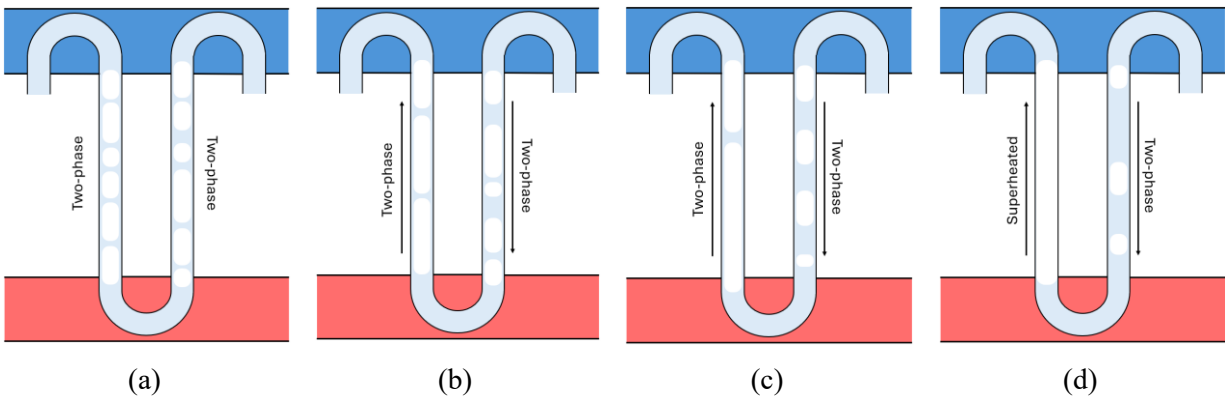
Figure 3.21. Qualitative visualization of the mass distribution, flow direction, and thermodynamic phases of the adjacent adiabatic tubes for low fill ratios with (a) no applied heat, (b) low applied heat, (c) medium applied heat, and (d) high applied heat.
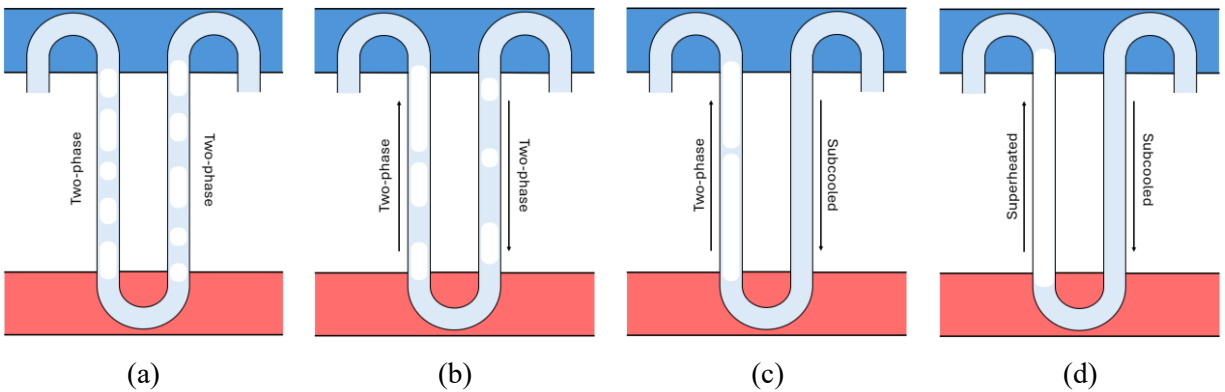
Figure 3.22. Qualitative visualization of the mass distribution, flow direction, and thermodynamic phases of the adjacent adiabatic tubes for medium (optimal) fill ratios with (a) no applied heat, (b) low applied heat, (c) medium applied heat, and (d) high applied heat.
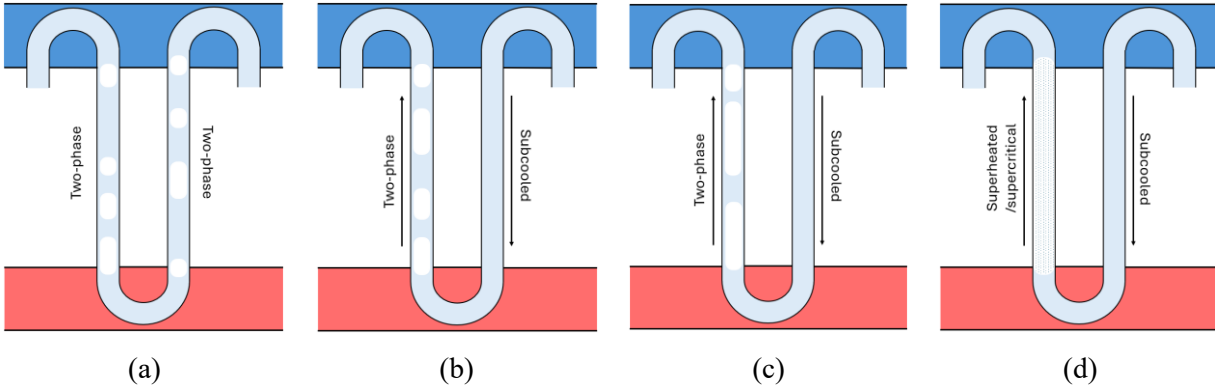
Figure 3.23. Qualitative visualization of the mass distribution, flow direction, and thermodynamic phases of the adjacent adiabatic tubes for high fill ratios with (a) no applied heat, (b) low applied heat, (c) medium applied heat, and (d) high applied heat.

3.7. Heat Transfer Coefficient Evaluation and Thermal Resistance Comparison

The temperature sensor configuration of these experiments, particularly of the adiabatic section, allows for the average heat transfer coefficients in both the evaporator and condenser sections to be determined. Indeed, the PHP performance is computed using measured temperatures on the outside of the PHP plates. Thus, multiple thermal resistances between the measured condenser/evaporator temperatures and the fluid temperatures dictate the performance. Since the plates are identical, the convective thermal resistances of the evaporator and condenser sections primarily determine the PHP's performance, which depends entirely on the flow characteristics in those sections. Furthermore, since the adiabatic section temperatures essentially measure the fluid temperature, as described in section 2.5, and the conduction thermal resistances can be computed from the known materials and geometry, the convection resistances and heat transfer coefficients can also be determined.

Newton's law of cooling defines the heat transfer coefficient in either section:

$$\bar{h} = \frac{q''}{T_w - T_f} \tag{3.5}$$

Where $\bar{h}$ is the heat transfer coefficient, q'' is the heat flux, T_w is the wall temperature, and T_f is the fluid temperature. Additionally, Figure 3.24 gives the thermal resistance diagram of the evaporator or condenser section. R_{cu} is the resistance of the copper plate, $R_{ss,i}$ are the conduction resistances through each individual tube pair, $R_{conv,i}$ are the convection resistances of each tube pair, and $T_{w,i}$ are the wall temperatures of each tube pair. Indeed, all heat will transfer through the copper plate, but each tube turn in the evaporator/condenser section constitutes a parallel heat transfer path for the heat to flow.
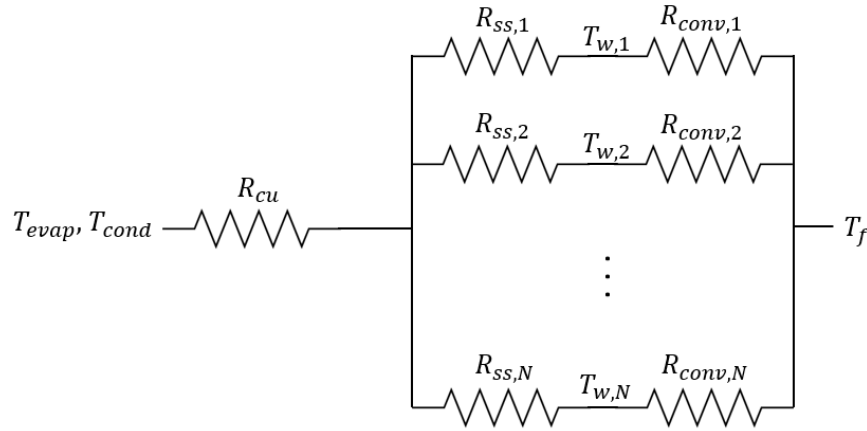
Figure 3.24. Thermal resistance network between the evaporator/condenser temperature sensor location and the fluid.

Due to material and geometric symmetric, all tube thermal resistances, $R_{ss,i}$ are equal. Furthermore, it can be assumed that the fluid temperature, T_f, is uniform for the two sets of alternating tubes, which contain fluid moving in opposite directions. In other words, all tubes supplying fluid from either the condenser or evaporator are assumed to have the same temperature, implying that heat is uniformly distributed to and from every tube pair. Despite adiabatic temperature measurements only being made on 1 of 7 tube pairs, this is a reasonable assumption due to the geometric symmetry of the PHP. If the fluid temperature is uniform across all tube pairs, then the wall temperature, convection resistance, and, therefore, the heat transfer coefficient must

also be uniform across all tubes. The thermal resistance network can be simplified using these assumptions, as shown in Figure 3.25.
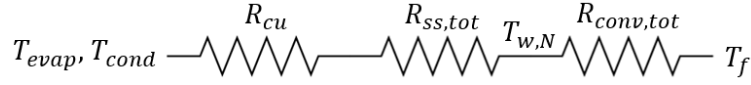
Figure 3.25. A simplified thermal resistance network assuming the thermal resistance between the evaporator/condenser thermometer and each tube is the same.

$R_{ss,tot}$ is the combined conduction thermal resistance of all tube pairs, and $R_{conv,tot}$ is the combined convection thermal resistance of all tube pairs. The copper plate thermal resistance, R_{cu}, can be evaluated as a plane wall thermal resistance:

$$R_{cu} = \frac{th_{cu}}{k_{cu}A_{cu}} \tag{3.6}$$

Where th_{cu} is the thickness of the plate, k_{cu} is the thermal conductivity of copper evaluated at the measured temperature, and A_{cu} is the cross-sectional area of the plate (lateral to the thickness dimension). Furthermore, the conduction resistance of the stainless steel capillary tubes can be expressed as:

$$R_{ss,i} = \frac{\ln\left(D_o/D_i\right)}{2L_e\pi k_{ss}} \tag{3.7}$$

Where D_o is the outer diameter of the capillary tube, D_i is the inner diameter of the capillary tube, L_e is the length dimension of the evaporator parallel with the tubes, and k_{ss} is the thermal conductivity of AISI 304 stainless steel evaluated at the calculated tube temperature that can be calculated from the completed thermal resistance network. Likewise, the convection thermal resistance of a single tube pair is:

$$R_{conv,i} = \frac{1}{\bar{h}A_s} \tag{3.8}$$

Where $\bar{h}$ is the appropriate average heat transfer coefficient in the section being evaluated, and A_s is the surface area of convective heat transfer. The total thermal resistance of the combined parallel heat flow paths to each tube pair is:

$$R_{ss,tot} = \left[\sum_i \frac{1}{R_{ss,i}}\right]^{-1} \cong \frac{R_{ss,i}}{N_p} \tag{3.9}$$

Where N_p is the number of tube pairs, 7. Similarly, the combined convection resistance can be evaluated:

$$R_{conv,tot} = \left[\sum_i \frac{1}{R_{conv,i}}\right]^{-1} \cong \frac{R_{conv,i}}{N_p} \tag{3.10}$$

Due to the thermal, geometric, and material symmetries of the evaporator and condenser sections, the temperature differences between the inner wall and the measurement location are essentially the same for both sections, with insignificant differences due to the temperature-dependent thermal conductivities of the metals. Thus, the wall temperatures can then be determined:

$$T_{w,e} = T_{evap} - \dot{Q}(R_{cu} + R_{ss,tot}) \tag{3.11}$$

$$T_{w,c} = \dot{Q}(R_{cu} + R_{ss,tot}) - T_{cond} \tag{3.12}$$

Where $T_{w,e}$ and $T_{w,c}$ are the evaporator and condenser tube inner wall temperatures, respectively, and $\dot{Q}$ is the total heat applied to the evaporator section, which is the same as the heat transferred to the cryocooler in the condenser section. Finally, the heat transfer coefficients in both sections can be computed:

$$\bar{h}_e = \frac{\dot{Q}}{2\pi D_i L_e (T_{w,e} - T_f)} \tag{3.13}$$

$$\bar{h}_c = \frac{\dot{Q}}{2\pi D_i L_e (T_f - T_{w,c})} \tag{3.14}$$

Where $\bar{h}_e$ and $\bar{h}_c$ are the average heat transfer coefficients of the flow in the evaporator and condenser sections, respectively. This analysis is only possible in the phase regime where both tubes contain two-phase fluid since the fluid temperature remains constant. If sensible heating occurs in either the evaporator or condenser, the fluid temperature in Equations 3.13 and 3.14 will depend on the position in each section, which cannot presently be determined. Therefore, the heat transfer coefficients presented constitute those of pure boiling and condensation and do not include single-phase heat transfer.

Figures 3.26 – 3.28 show the spatially averaged heat transfer coefficients of the evaporator and condenser sections as functions of heat load for the two PHPs within each fill ratio range. There is considerable error when calculating the evaporator heat transfer coefficient at very low heat loads. This observation is likely due to the parasitic heat leak to the adiabatic thermometers from thermal radiation, which is significant only at very low heat loads because the mass flow rate is not large enough to prevent a thermal gradient between the thermometer and the fluid from existing. Thus, the measured temperature is greater than the actual fluid temperature, causing arbitrarily high, and sometimes negative, calculated heat transfer coefficients. The condenser heat transfer coefficients are affected less since a small rise in fluid temperature in Equation 3.15 does not cause the solution to asymptote as a decrease in fluid temperature would. Fortunately, this effect is insignificant at higher heat loads when the mass flow through the adiabatic section is greater.
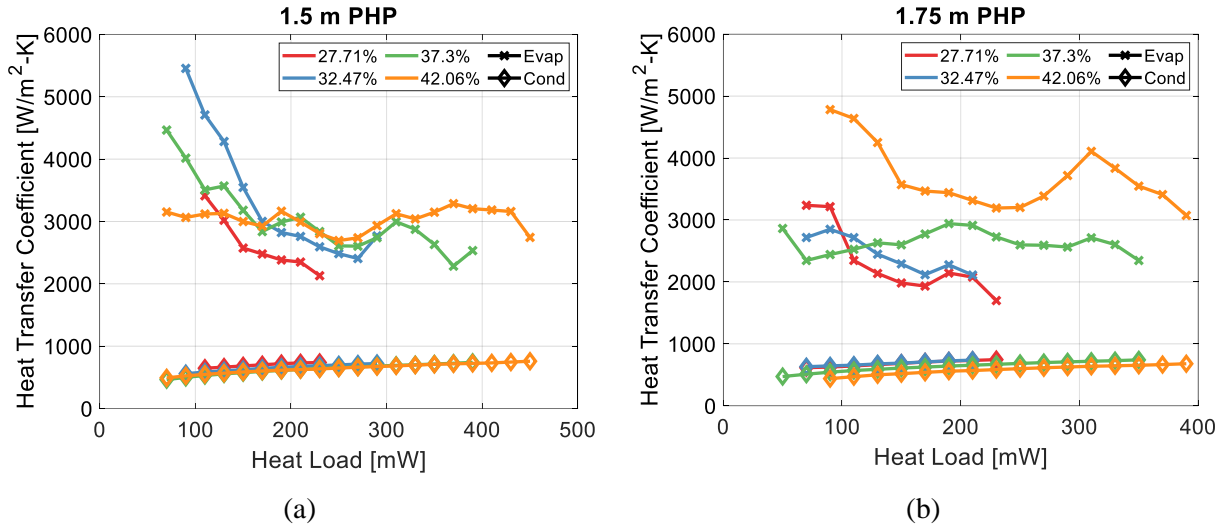
Figure 3.26. Boiling and condensation heat transfer coefficients as functions of applied heat load for the low fill ratio range (27.71% - 42.06%) for the (a) 1.5 m PHP and (b) 1.75 m PHP.
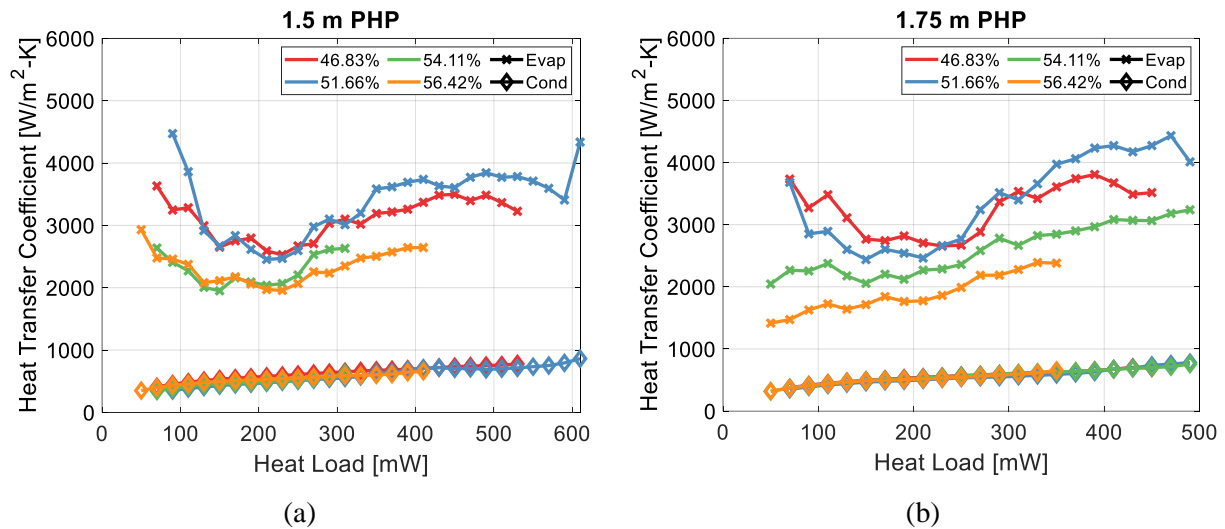
Figure 3.27. Boiling and condensation heat transfer coefficients as functions of applied heat load for the medium fill ratio range (46.83% - 56.42%) for the (a) 1.5 m PHP and (b) 1.75 m PHP.

Miraculously, the condensation heat transfer coefficient is consistent for a given applied heat for nearly all combinations of fill ratio and adiabatic length. Generally, the condensation heat transfer coefficient increases with increasing heat load, starting around 200 W/m²-K and ending around 800 W/m²-K. There is considerably more variation in the boiling heat transfer coefficient concerning the fill ratio; however, the adiabatic length does not have a significant effect until the

fill ratio exceeds 60%. For low fill ratios, as shown in Figure 3.26, the boiling heat transfer coefficient generally decreases with increasing applied heat and increases with increasing fill ratio. Values between 2000 W/m^2-K and 4500 W/m^2-K are common within this fill ratio range. Furthermore, the trends change when the fill ratio is increased. Figure 3.27 shows that the boiling heat transfer coefficient generally increases with increasing applied heat and decreases with increasing fill ratio, the opposite of the low fill ratio range. However, the heat transfer coefficient values remain approximately between 2000 W/m^2-K and 4500 W/m^2-K. In the high fill ratio range, shown in Figure 3.28, the boiling heat transfer coefficients are reduced significantly and generally decrease with increasing fill ratio. Typical values are between 1000 W/m^2-K and 2500 W/m^2-K.
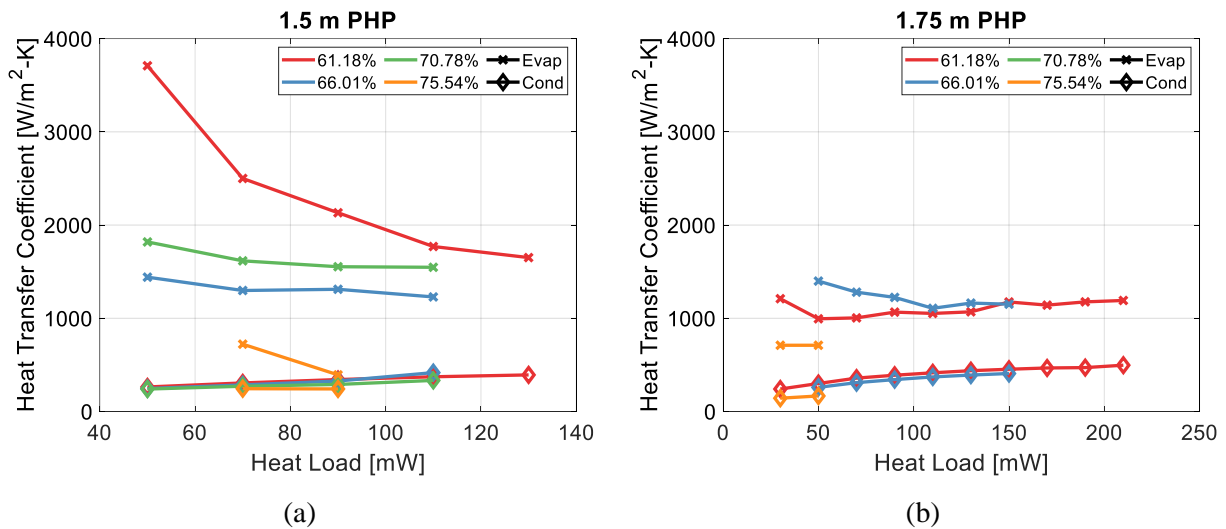
Figure 3.28. Boiling and condensation heat transfer coefficients as functions of applied heat load for the high fill ratio range (61.18% - 75.54%) for the (a) 1.5 m PHP and (b) 1.75 m PHP.

Relative to general convective flows, the heat transfer coefficients at both ends of the PHP are high, contributing to the excellent observed thermal conductance. These results could be helpful for future PHP modeling efforts since two-phase helium heat transfer coefficients are difficult to predict for PHPs' unique flow conditions.

Several past research efforts have studied the heat transfer coefficients of flow boiling and condensation of helium. First, Sato and Ogata investigated helium's flow condensation heat transfer coefficients, finding heat transfer coefficient values between 500 W/m2-K and 700 W/m2-K [68], which agrees with the values derived in this study. The same researchers also investigated helium's flow boiling heat transfer coefficients, finding values between 400 W/m^2-K and 4000 W/m^2-K [69], which again generally agrees with the results of these PHP experiments. In flow boiling and condensation studies, the heat transfer coefficient values depend on the applied heat flux, vapor mass quality, and mass flow rate. Unfortunately, when both PHP tubes contain two-phase fluid, the vapor mass quality and mass flow rate cannot be determined, so a more in-depth comparison to past experimental results is not presently possible. The flow geometry may also be important, as the PHP microchannels are much smaller than the channels used in past heat transfer studies. Regardless, the general agreement observed between the helium PHP flows and the general two-phase helium heat transfer studies is encouraging.

Despite the PHPs in this study behaving as thermosiphons, their flow characteristics are unique and have not been studied sufficiently. While it has been shown in previous sections of this chapter that the fluid circulates the PHP unidirectionally, oscillating flow modes are still superimposed over the steady flow. The heat transfer characteristics of oscillating boundary layers, such as those of Stokes' second problem, have been shown experimentally to reduce the critical Reynolds number for the turbulent flow transition [70]. Since the typical Reynolds numbers for this experiment are within the transition regime for both liquid and vapor (using the velocities predicted in section 3.5.1), the flow oscillations may induce turbulence, increasing local heat transfer coefficients. Furthermore, flow oscillations could encourage phase mixing and rewetting of dry areas since the fluid is two-phase, resulting in improved heat transfer [71].

Additionally, the contribution of capillary action to the fluid dynamics likely causes further deviations from the typical pipe flow thermohydraulic behavior. Indeed, flow boiling/condensation in microchannels is a rigorous field of study with considerable contemporary research efforts [72], and is largely beyond this project's scope. However, it is generally known that two-phase oscillations and persistent liquid film coverage tend to result in enhanced heat transfer for microchannels [71 - 73].

Per Figure 3.25, the total thermal resistance between the evaporator/condenser thermometer and the fluid consists of two conduction and one convection resistance in series. It is important to understand the relative magnitude of each thermal resistance in order to inform future PHP designs. Assuming the adiabatic section is truly adiabatic and that viscous heating can be neglected, the total thermal resistance of the PHP can be evaluated:

$$R_{tot} = 2R_{ss,tot} + 2R_{cu,tot} + R_{evap} + R_{cond} \tag{3.14}$$

Where R_{tot} is the total PHP thermal resistance, and R_{evap} and R_{cond} are the convection thermal resistances of the evaporator and condenser sections, respectively. With the total thermal resistance known, the resistance fractions can be determined:

$$RF_{ss} = \frac{2R_{ss,tot}}{R_{tot}} \tag{3.15}$$

$$RF_{cu} = \frac{2R_{cu,tot}}{R_{tot}} \tag{3.16}$$

$$RF_{cond} = \frac{R_{cond}}{R_{tot}} \tag{3.17}$$

$$RF_{evap} = \frac{R_{evap}}{R_{tot}} \tag{3.18}$$

These four resistance fractions, which signify the relevance of each component's contribution to the total thermal resistance of the PHP, are plotted simultaneously for the 1.75 m PHP with a 51.66% fill ratio in Figure 3.29. The general trends and observations for all fill ratios and both adiabatic lengths are the same. First, it is clear that in all cases, the thermal resistance of the copper plates is an insignificant fraction of the overall thermal resistance, primarily due to the relatively high conductivity of copper, along with the geometry of the plates. Interestingly, the conduction resistance through the stainless steel contributes significantly to the overall thermal resistance of the PHP, limiting its thermal performance. Indeed, the stainless steel conduction resistance typically constitutes around 15% to 20% of the overall thermal resistance. However, the PHPs' heat transfer is ultimately dominated by condensation, which accounts for 60% to 80% of the overall thermal resistance.
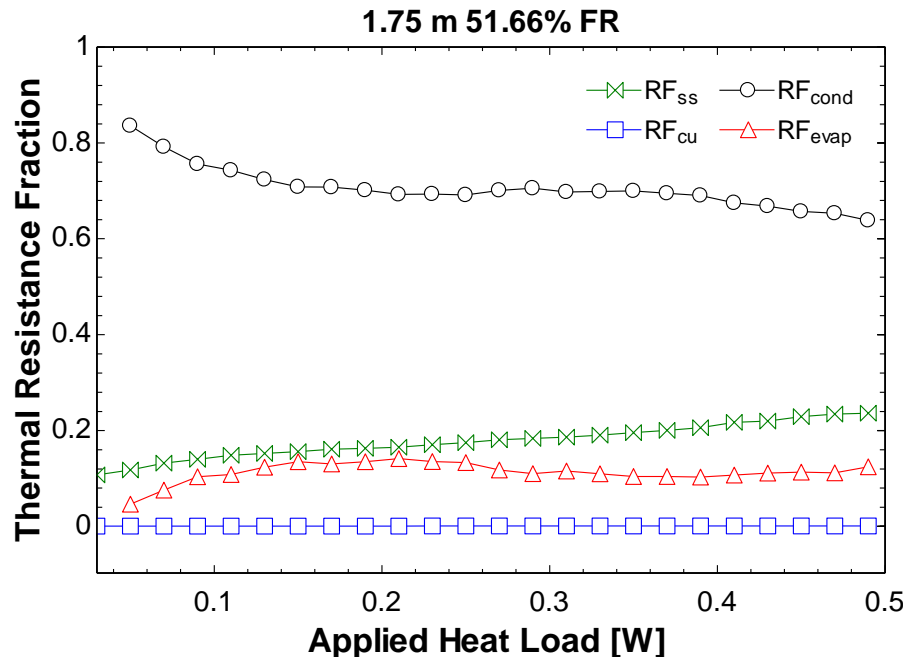
Figure 3.29. Calculated thermal resistance fractions for the 1.75 m PHP for fill ratios of (a) 37.3%, (b) 56.42%, and (c) 75.54%, showing the relative importance of each thermal resistance.

Therefore, future PHP designs should consider techniques to reduce condensation and tube conduction thermal resistances to optimize PHP performance. For example, a more conductive

metal could be used for the tubes in the evaporator and condenser sections, or the tube wall thickness could be minimized. Potentially, a more advanced treatment of the tube's inner structure in the condenser sections that reduces convection resistances could be considered, although such a task would require significant additional fabrication complexity.

3.8. 1.25 m Results and Effect of Build Quality

The results of the 1.25 m PHP tests were not included in previous sections due to incomparable results. Indeed, the 1.25 m PHP was constructed and tested first and was an entirely different PHP than the 1.5 m and 1.75 m PHPs, which were identical except for an extended adiabatic section. Interestingly, the fact that the 1.25 m PHP was constructed differently impacted thermal performance more than any other experimental parameter. As mentioned in section 2.7, the fabrication processes and techniques can immensely impact the performance and maximum allowable heat load of helium PHPs. Primarily, the bend quality, tube cleanliness, partially clogged braze joints, and gas purity can significantly reduce a helium PHP's heat transfer ability. It is nearly certain that the 1.5 m and 1.75 m PHPs were constructed with greater adherence to the guidelines listed in section 2.7, resulting in a significantly better thermal performance.

Figure 3.30 compares the effective conductance of the original (labeled "Old") helium PHP with the following sets of parameters: (1) 1.25 m adiabatic length with 56.42% fill ratio, and (2) 1.5 m adiabatic length with 55.13% fill ratio, along with the effective conductance of an improved (labeled "New") helium PHP with (3) a 1.5 m adiabatic length and 56.42% fill ratio. For the same fill ratio, the "Old" PHP shows a reduction in ultimate heat load and thermal conductivity when the adiabatic length was increased from 1.25 m to 1.5 m. This result is somewhat consistent with the time-averaged results of the "New" PHP (sections 3.1 – 3.3). However, the negative impact of increasing length, especially at around 55% fill ratio which is within the optimal range, was much

more significant for the "Old" PHP. This observation is likely due to a greater viscous flow resistance stemming from flow path inconsistencies created by poor construction.

Moreover, the effect of build quality is clearly observed in Figure 3.30 when the "Old" and "New" PHPs are compared for the same length and fill ratio. Indeed, the "New" PHP outperformed both "Old" PHP lengths. Although the conductance is nearly constant for all cases up to around 400 mW, the "New" PHP with a 1.5-meter adiabatic length was able to continue with regular operation up to 650 mW – higher even than the maximum heat load of the "Old" PHP with a 1.25-meter adiabatic length (590 mW). Therefore, the quality of construction is an equally, if not more, important factor than the adiabatic length when evaluating the performance of helium PHPs.
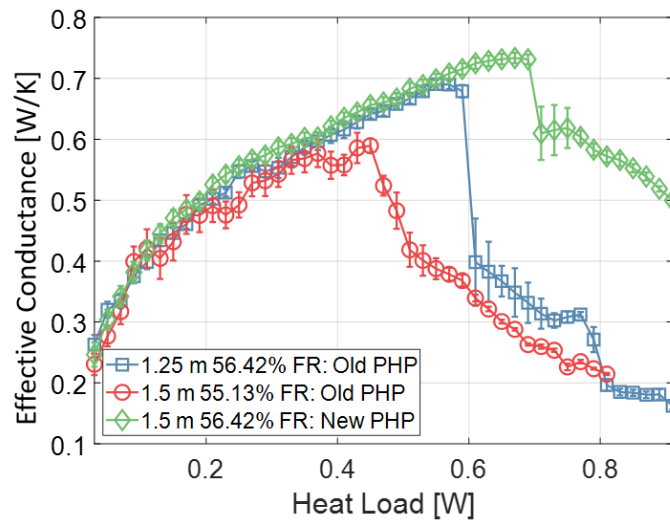
Figure 3.30. Comparison of the "Old" and "New" PHPs at different lengths, demonstrating the significant effect of build quality.

One indicator of a poorly fabricated helium PHP is an invariant flow direction. If there is a significant partial blockage or flow constriction, one flow direction will be favored due to an uneven viscous resistance. For the 1.25 m PHP, when uni-directional flow was observed, the flow was always in the same direction. In other words, the cold and hot adiabatic tubes never switched for any combination of experimental parameters. However, for the 1.5 m and 1.75 m ("New") PHP

tests, it was essentially 50/50 for whether a given adiabatic tube would be the cold or hot tube, for any combination of experimental parameters. Because the flow path was uniform for the" New" PHP, the viscous resistance for each flow direction was the same, and therefore, there was no preferred flow direction. Thus, if the observed flow direction of a helium PHP is always the same, its thermal performance could likely be improved by more careful manufacturing.

Figure 3.31 displays the time-averaged performances (right axes) and temperature measurements (left axes) as functions of applied evaporator heat load for all fill ratios of the 1.25 m PHP. As in section 3.1, the background color indicates the thermodynamic phases of the adjacent adiabatic tubes, as shown in Table 3.1. Although these results are not directly comparable to the 1.5 m and 1.75 m PHP tests, the general observations regarding performance and thermodynamic phases are the same for the 1.25 m PHP tests. Moreover, like in section 3.2, thermodynamic temperature-volume phase diagrams for the three fill ratio ranges of the 1.25 m PHP tests are shown in Figure 3.32. Generally, the trends and observations detailed in section 3.2 regarding the 1.5 m and 1.75 m PHPs are the same for the 1.25 m PHP.

(a)   (b)
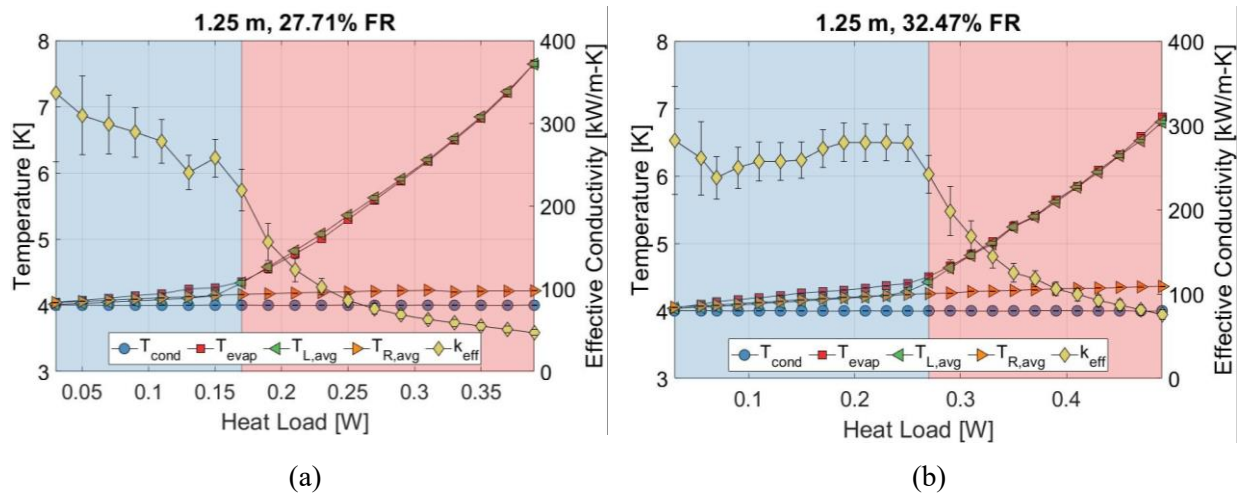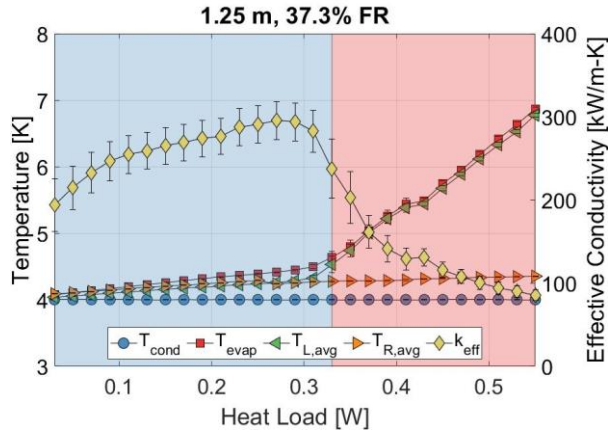
(c)
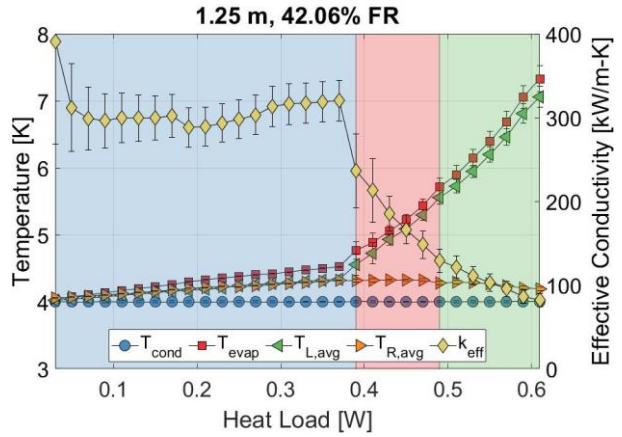
(d)
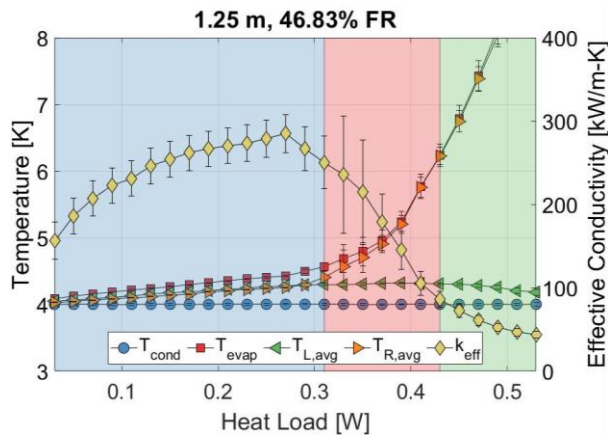
(e)
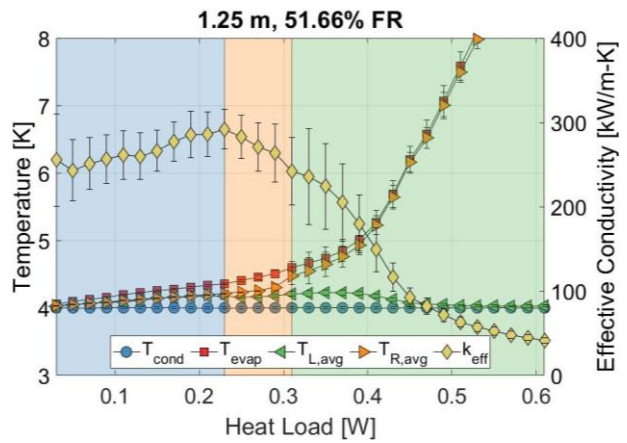
(f)
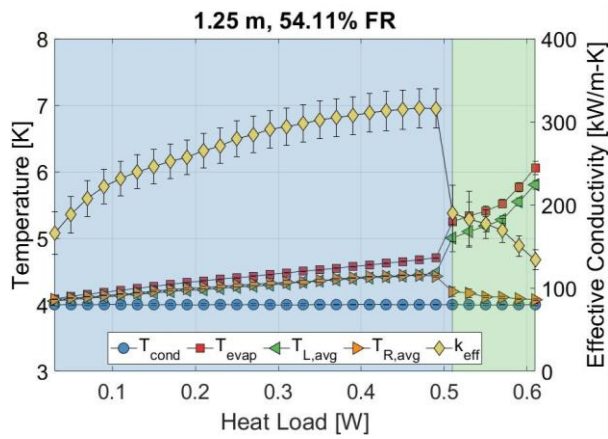
(g)
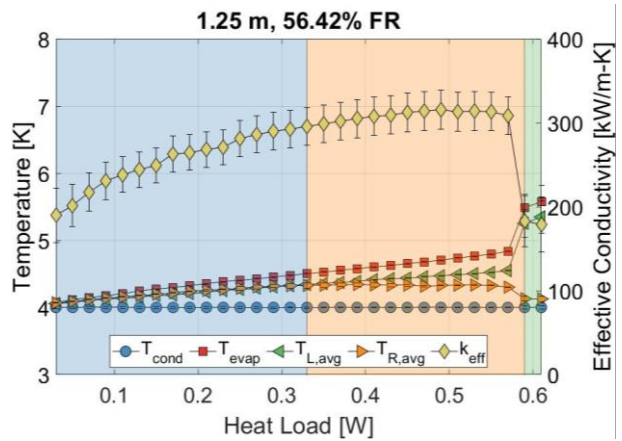
(h)
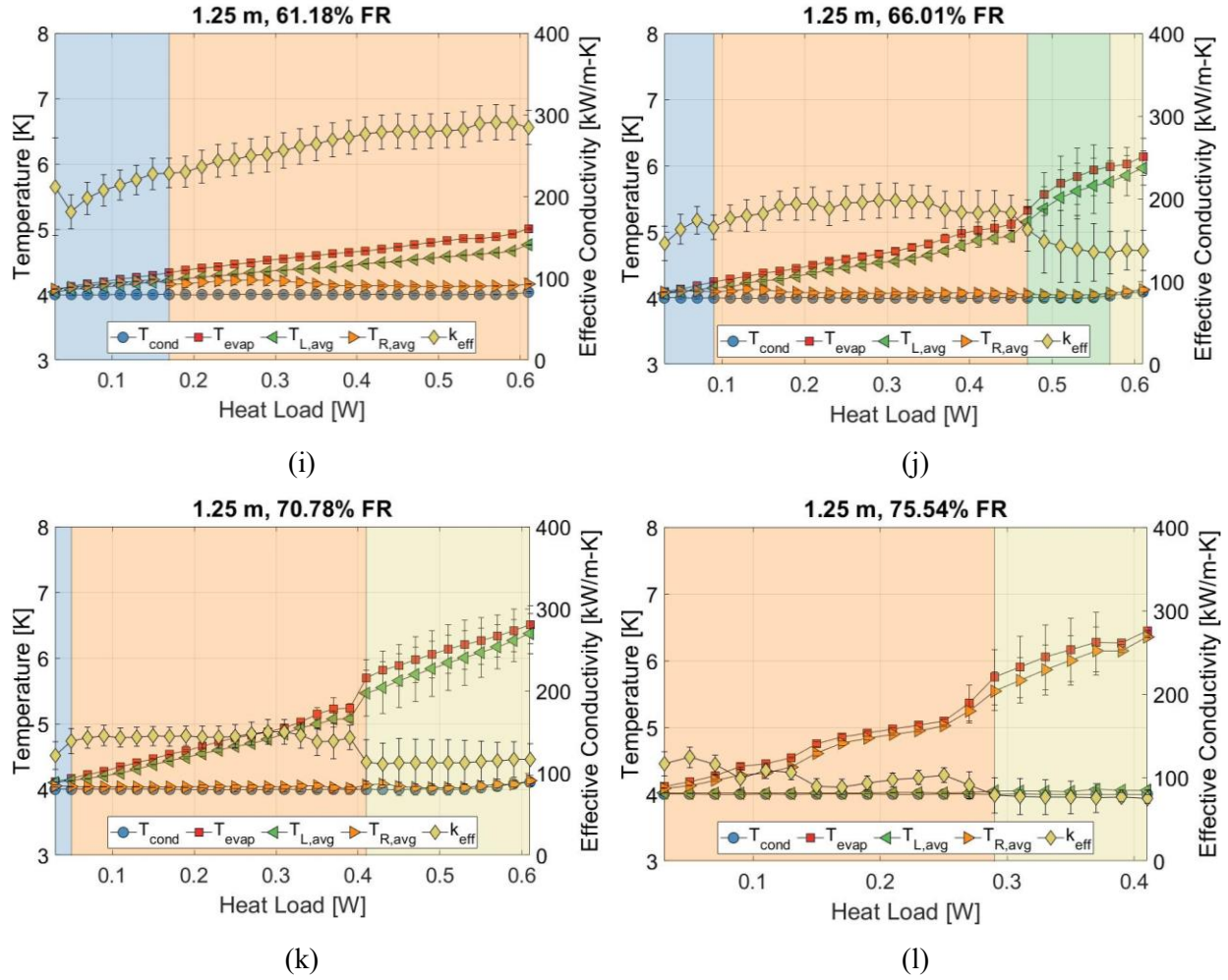
Figure 3.31. Time-averaged effective conductivity and condenser, evaporator, and spatially-averaged adiabatic temperatures as functions of applied heat load of the 1.25 m PHP for all fill ratios tested.
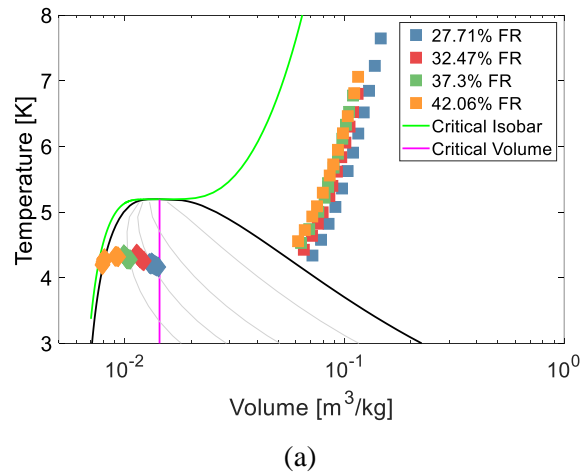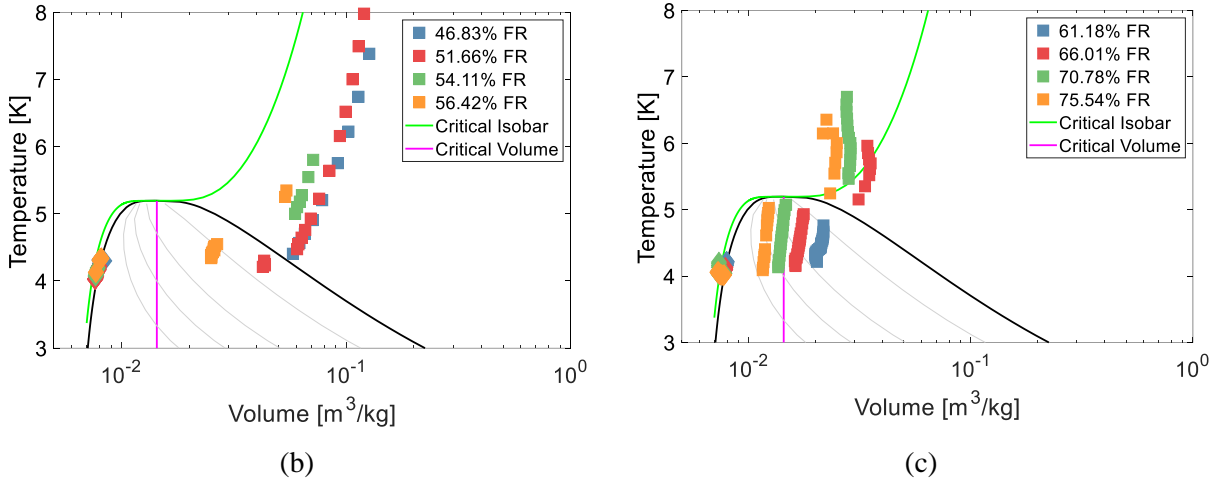
Figure 3.32. T-v phase diagram of the fluid contained in the two adjacent adiabatic tubes for the (a) low, (b) medium, and (c) high fill ratio ranges of the 1.25 m PHP.

3.9. Thermal Stability Tests

In addition to the progressively increasing heat load tests to which this chapter's previous sections are dedicated, additional tests concerning the thermal stability of helium PHPs were also conducted. These tests consist of a randomized evaporator heat load test and an extended-period test. The complex dynamics of the alternating train of liquid slugs and vapor plugs in the capillary tubes, driven by inherently stochastic phase change phenomena, result in the fluid's chaotic motion. However, despite their stochastic nature, pulsating heat pipes typically achieve pseudo-thermal equilibrium on a large scale such that evaporator and condenser temperatures become steady with few oscillation modes. As expected, the previously described progressive heat load tests were thermally stable. Incrementing the heat load resulted in very short transient periods, around one minute long, where the PHP would subsequently reach a pseudo-steady state. Hence, the underlying chaotic nature of pulsating heat pipes brings into question the resulting thermal steadiness observed. Indeed, many experimental studies have observed or theorized metastable states [74, 75], thermal runaway [30, 31, 76], and start-up difficulties [30, 77]. Future implementation of cryogenic pulsating heat pipes, especially in aerospace applications, will rely

on the robustness and predictability of their thermal performance; therefore, investigation of potential performance instabilities is essential.

(a) (b)

(c) (d)

(e) (f)
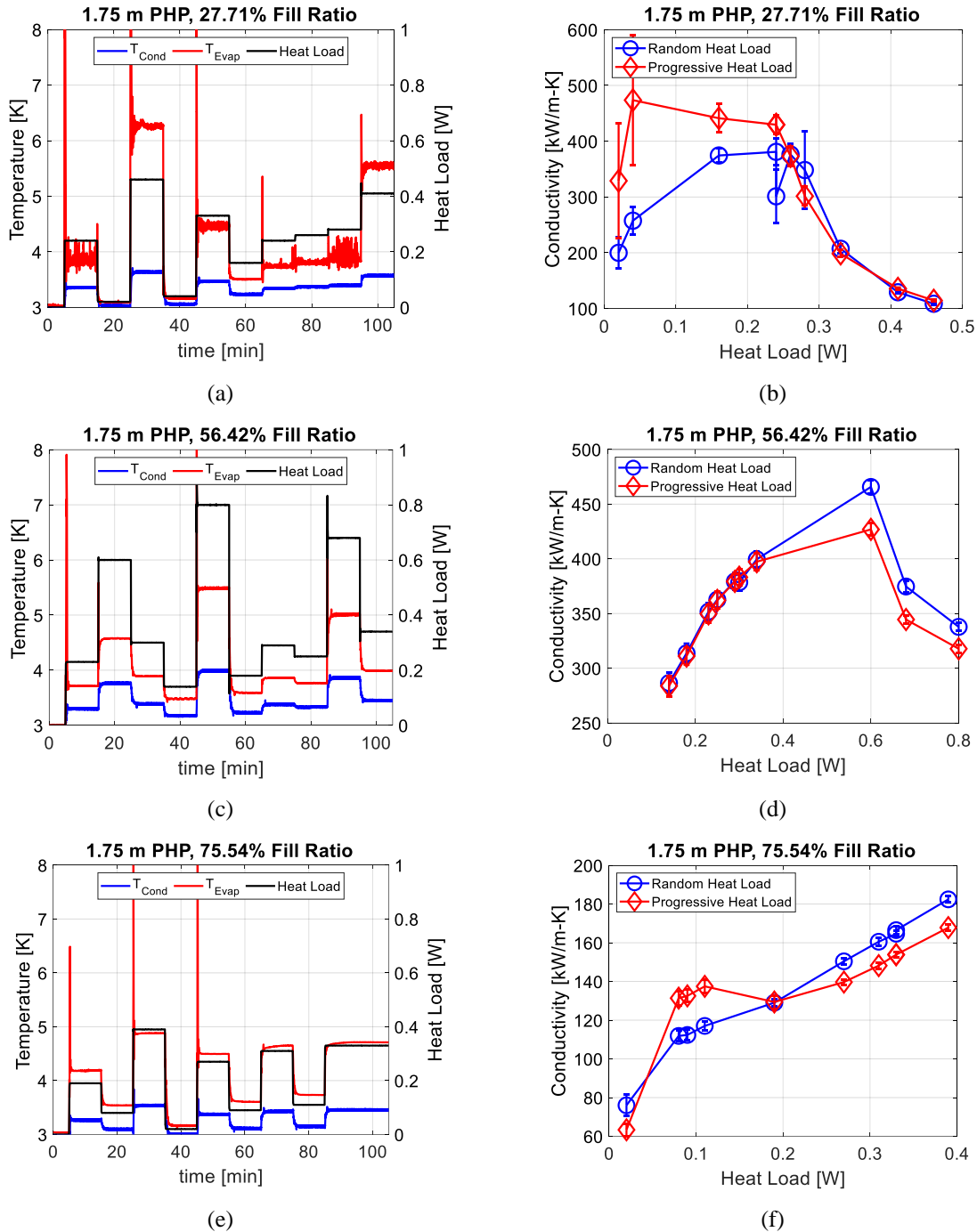
Figure 3.33. Randomized heat load results, with (a), (c), and (e) showing time series data of the heat load, evaporator, and condenser temperatures, and with (b), (d), and (f) showing the time-averaged performance compared to the progressively increasing heat load tests for 27.71%, 56.42%, and 75.54% fill ratios, respectively.

Although randomized heat load tests were done for all combinations of fill ratio and adiabatic length, only a few parameter combinations are presented that show the most important thermal behavior, for brevity. Figure 3.33 shows the results of the randomized heat load tests for the 1.75 m PHP with fill ratios 27.71%, 56.42%, and 75.54% - one for each of the three fill ratio ranges described in section 3.1. The results and general observations were consistent for fill ratios within the same range and between the two adiabatic lengths. Moreover, Figures 3.33 (a), (c), and (e) display the time progression of the evaporator and condenser temperatures, as well as the applied heat load, and Figures 3.33 (b), (d), and (f) compare the resulting performance to the progressive heat load tests from section 3.1.

For the 27.71% fill ratio case, the performance at low applied heat loads – typically the best for low fill ratios – was considerably lower for the randomized case versus the progressive case, as shown in Figure 3.33 (b). Indeed, the initial condition seems to affect subsequent conditions significantly, implying that helium PHPs' operation can be history-dependent. Figure 3.33 (a) shows that the lowest heat loads are preceded by very high heat loads in which the evaporator and corresponding hot tubes contain superheated vapor. When comparing global PHP pressures of the randomized and progressive heat load experiments for the 1.75 m PHP at a 27.71% fill ratio at the lowest heat loads, it was observed that system pressures were greater for the randomized test versus the progressively increasing test, typically by about 1 kPa. Thus, for the randomized test, the PHP must be operating at a different metastable state with a greater fraction of saturated vapor since it is transitioning from a high heat load, dried-out state, implying that multiple metastable operating states are possible. However, system pressures seem to match between the two evaporator heating patterns at greater heat loads when the performances match, which implies that metastable states might not always be possible for all parameter combinations.

Interestingly, for this fill ratio, the metastable states were observed when both adiabatic tubes contained two-phase fluid but not when the hot tube contained superheated vapor. Despite the discrepancies, the PHP recovered from 300 – 400 mW heat load spikes with no thermal runaway.

The 56.42% fill ratio case performed excellently under randomized heat load conditions. Despite multiple large heat load spikes from a fully two-phase operation to a dry-out condition, the PHP did not thermally run away and quickly recovered, as observed in Figure 3.33 (c). Furthermore, Figure 3.33 (d) shows that at this optimal fill ratio, the PHP's performance in a fully two-phase operating state was independent of the starting condition over a range of applied heat loads. However, at high heat loads beyond dry-out (above 630 mW), there is a slight deviation in the resulting performance between the two testing procedures, with the randomized test outperforming the progressive test. Interestingly, these observations are opposite to those of the 27.71% fill ratio. Additionally, system pressures no longer indicate a deviation between the two test procedures, as several matching-performance heat loads have significantly different system pressures, and some nonmatching-performance heat loads have the same system pressures. Thus, metastable states could be present with different saturated vapor fractions, but the flow characteristics may be of greater importance here than at lower fill ratios. Indeed, the global PHP pressure determines the saturation temperature and the flow characteristics dictate the heat transfer coefficients, both of which influence the overall thermal performance and likely each other. Regardless, it has been demonstrated that the PHP swiftly recovered its previous performance after a sudden 600 mW heat load increase. These results also suggest optimizing the fill ratio maximizes performance and increases thermal stability under non-ideal conditions.

Figures 3.33 (e) and (f) show the results of the randomized heat load tests for the 75.54% fill ratio case. For this test, none of the heat load values chosen exceeded the supercritical heat load

(470 mW) determined via the progressive heat load test due to potentially excessive system pressures caused by large heat load spikes at high fill ratios. Therefore, the test was essentially a randomization of heat loads within the anticipated normal operating range. Nevertheless, Figure 3.33 (f) shows some deviation in performance between the two procedures – significantly more than the 56.42% case in the normal operating heat load range. Despite the history-dependent performance, the evaporator temperature was steady throughout the test, similar to the 56.42% fill ratio test. Like in the 27.71% fill ratio randomized test, higher system pressures (greater saturated vapor fraction) for the same applied heat load for the 75.54% fill ratio randomized test correspond to a poorer thermal performance when compared to the progressive test. Moreover, while these randomized heat load tests probe some of the interesting metastable phenomena of helium PHPs, a more intentional approach could be adopted that more carefully considers heat load jumps between specific thermodynamic phase and flow behavior regimes to induce metastable states purposefully.
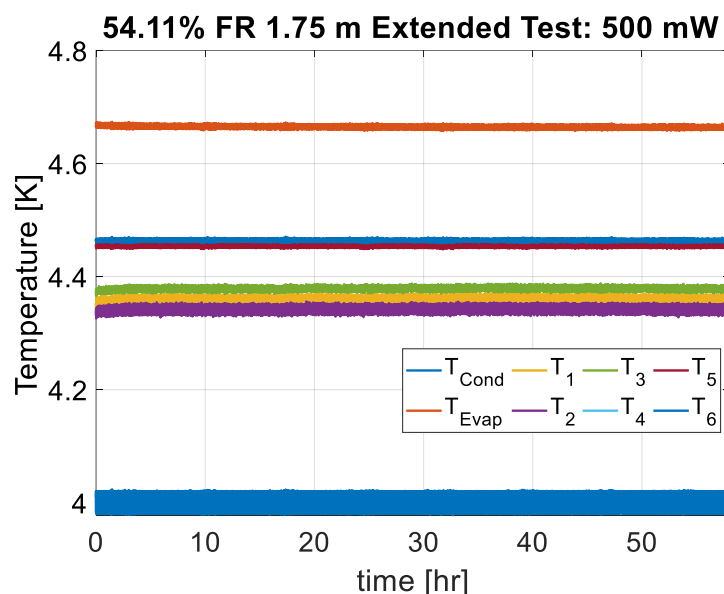
Figure 3.34. Time-series evolution of the evaporator, condenser, and adiabatic temperature measurements for the extended period test.

Time series data of the extended period test, which lasted for about 58 hours, are displayed in Figure 3.34. The 1.75 m PHP with a fill ratio within the optimal range, 54.11%, was used for this test. A heat load of 500 mW was chosen for this test due to the excellent performance observed for this fill ratio and applied heat load combination during the corresponding progressive heat load tests. Thus, the extended period test was conducted under the most ideal operating conditions.

As seen in Figure 3.34, all temperature measurements, regardless of location, remained stable for the duration of the test, demonstrating that helium PHPs' excellent thermal performance is perpetual rather than a transient artifact. The largest oscillations were observed in the condenser temperature measurement, which is strongly affected by the cryocooler's cycle, where a standard deviation (0.0125 K) of 0.31% of the mean value (4 K) was observed. The evaporator temperature measurements, however, only had a standard deviation (0.0021 K) of 0.045% of the mean value (4.66 K). As such, this test also demonstrates the helium PHP's thermal damping ability, which is typically difficult to achieve at saturated helium temperatures due to most solids' extremely low heat capacity. Additionally, the performance during this extended period test was 478.86 W/m-K. Extended tests of non-optimal fill ratios were not conducted but may serve as an interesting comparison due to the more noticeable metastable behavior described previously in this section. Furthermore, extended tests for parameter combinations corresponding to different thermodynamic phase regimes (Table 3.1) could show which of the many possible PHP operating states are thermally stable for long periods of time.

4. Long-Distance Horizontal PHP Experiments

4.1 Introduction

The substantial evidence of the gravity dependence of long-distance helium pulsating heat pipes detailed in the previous chapter warrants a similar investigation of helium PHPs operating in the horizontal orientation. Indeed, the horizontal orientation almost certainly eliminates the positive effect of gravity on PHP thermal performance, although gravity is not negated entirely as it still acts perpendicular to the flow direction. Therefore, although horizontal PHPs still experience gravity in some capacity, their operation is not assisted by gravity and, as such, more closely resembles PHPs' operation in microgravity environments. This chapter outlines the considerable experimental efforts to test a long-distance helium pulsating heat pipe with a 1.5 m adiabatic length in multiple horizontal orientations.

4.2. Horizontal Helium PHP Experimental Configuration

Much of the experimental facility described in Chapter 2 did not require substantial modifications. Indeed, the vacuum chamber, external plumbing, data collection system, instrumentation, and cryocooler remained the same for the horizontal PHP tests. Most of the modifications of the experimental facility were related to the radiation shield and adiabatic PHP supports.
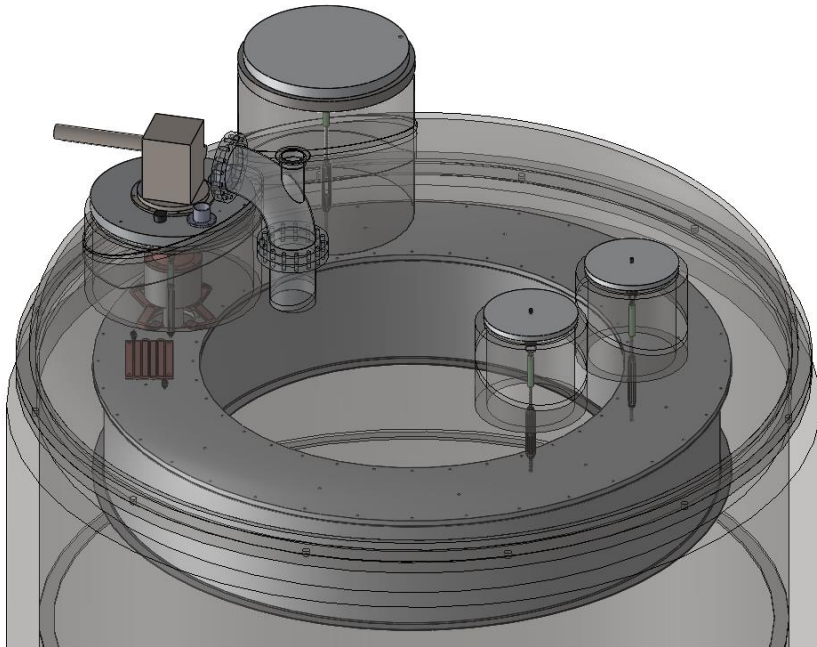
(a)
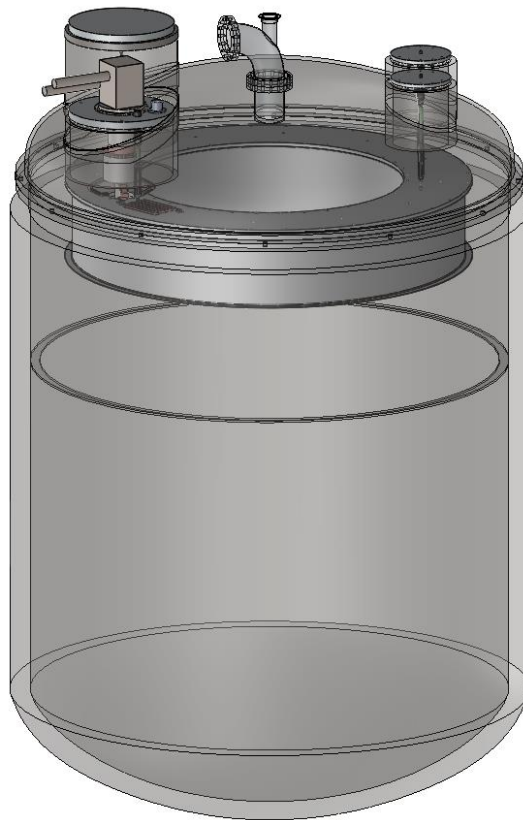
(b)

Figure 4.1. CAD model of the modified facility used for testing helium PHPs in the sideways and horizontal orientations.

Instead of the vertical experiments' radially symmetric cylindrical radiation shield, the horizontal experimental configuration features a toroidal shield that mounts to the cryocooler significantly askew from the toroid center, as seen in Figure 4.1, which shows a CAD model of the horizontal PHP test rig. This mounting configuration, although necessary, warrants concern for the undesirable stresses the shield may cause the cryocooler due to its cantilever-like positioning. Excessive shear stress on the cryocooler cold head could cause distortions in the very tight-tolerance displacer cylinder, preventing the cryocooler from working properly (lock up) or even causing permanent damage. Therefore, significant design efforts were made to ensure that the cryocooler is mechanically isolated from the shield while maintaining an excellent thermal connection.

First, special support rods were manufactured to support the radiation shield from the vacuum chamber cover at four locations. Figure 4.2. shows a picture of one radiation shield support rod for the horizontal experimental configuration. These support rods were designed to conform to multiple constraints: Thermal, structural, and the abilities to be flexible and adjustable.

The rods must be somewhat thermally insulated to minimize the parasitic heat leak from the ambient-temperature vacuum chamber cover. Material selection is the primary method for minimizing conduction heat leaks, as the supports are made primarily from stainless steel and G10, which are not thermally conductive between room temperature and the first-stage temperature. Moreover, the support rods consist of large springs and turnbuckles connected in series. The purpose of the springs is to reduce the rigidity of the assembly, and the purpose of the turnbuckles is to allow for height adjustments. Reducing rigidity is essential because the vacuum chamber cover with the shield attached must be moved frequently for experimental adjustments, which likely induces transient forces and moments on the support rods. These unwanted forces and

moments could cause damage to the rods, so the springs are included to absorb the impulse energy and dissipate it slowly. Additionally, allowing for height adjustments is necessary to ensure that the shield is level with the chamber cover. Moreover, the vacuum chamber end of the support rod assembly is simply-supported, allowing for rotation and eliminating some bending moments on the support rod. Four support rods hold the shield from the vacuum chamber cover, eliminating stresses on the cryocooler's cold head.
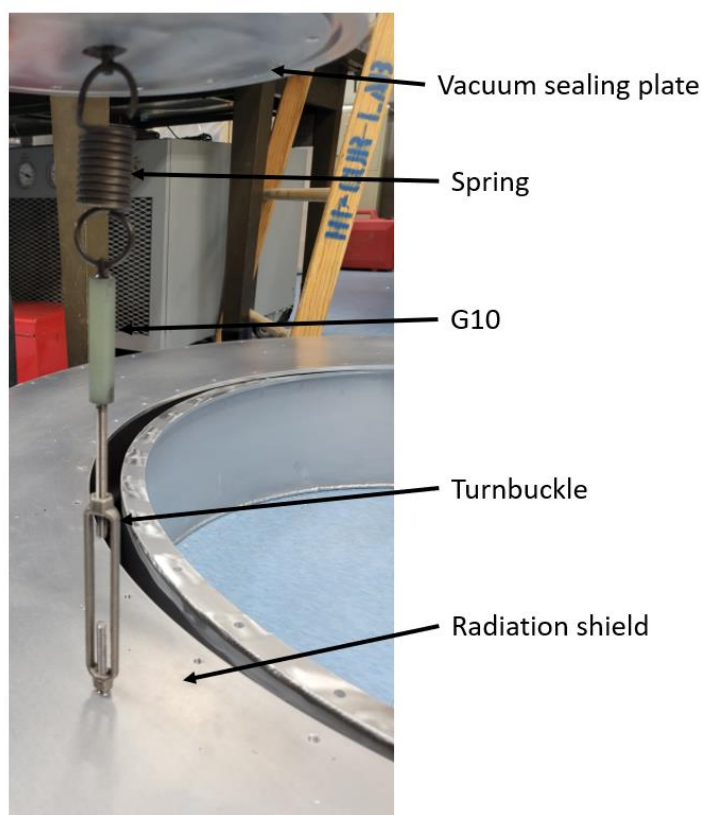
Figure 4.2. The shield support rods consisting of a spring, a G10 rod, and a turnbuckle, providing thermal isolation, flexibility, and adjustability.

While the support rods mechanically isolate the shield from the cryocooler, the two must remain in good thermal contact. To achieve mechanical isolation and thermal connection simultaneously, flexible thermal straps made from copper were installed between the cryocooler's first stage and the shield, as shown in Figure 4.3. Copper is an excellent material for thermal straps

in this temperature range since copper's thermal conductivity peaks between 10 K and 60 K due to the metal's electrons' primary scattering agent transitioning from phonons to lattice defects. Thus, a minimal temperature gradient is generated between the shield and the cryocooler despite their mechanical isolation. The entire horizontal test rig mounted to the cover of the vacuum chamber is displayed in Figure 4.4.
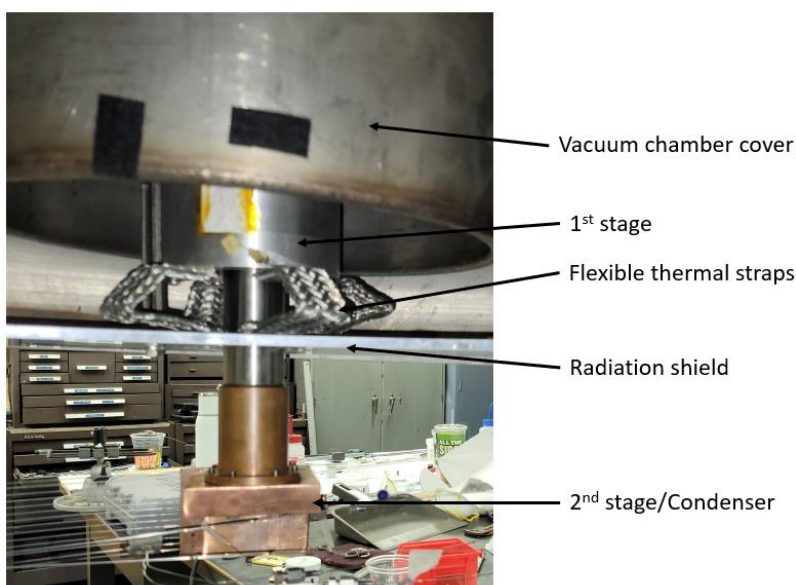
Figure 4.3. The flexible thermal straps connecting the cryocooler's first stage to the radiation shield.
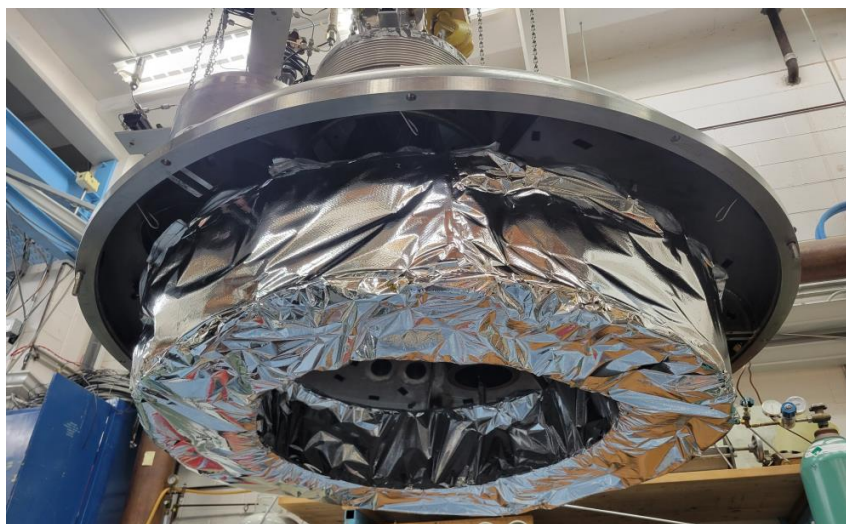
Figure 4.4. The experimental facility for testing sideways and horizontal helium PHPs, closed and covered with a 20-layer MLI blanket.

4.2.1. Sideways Orientation

The first non-vertical PHP orientation tested was the "sideways" orientation in which each tube lays within a slightly higher horizontal plane than the previous. Figure 4.5 shows the PHP in the sideways orientation along with the adiabatic supports. Unlike the vertical PHPs, which hang from the cryocooler's second stage, sideways and horizontal PHPs must be supported to maintain their orientation. For the sideways orientation, the adiabatic section is supported by grooved G10 blocks that hang from the top of the radiation shield by small G10 rods. Unfortunately, this is not a good design choice because, while the G10 rods minimize the heat leak to the adiabatic section, the blocks have significant heat capacity at low temperatures, significantly increasing the cool-down time. Furthermore, the heat leak originating from incidental contact between the adiabatic section tubes at second-stage temperatures and the G10 blocks at the first-stage temperature may be detrimental to the heat pipe's operation.

While the gravity vector is not parallel to the PHP flow path, as in the vertical PHPs, the mass distribution of the working fluid in the sideways orientation is still influenced by gravity. Since each adiabatic tube lays within a different horizontal plane, the bottom-most tubes are likely to fill with saturated liquid and the upper-most with saturated vapor, stratifying the two-phase fluid among the entire PHP. Thus, the sideways orientation is not fully representative of a gravity-independent PHP.

As described in section 2.3.3, parasitic heat leaks to the evaporator section must be eliminated almost entirely so that the evaporator can cool below the critical temperature of helium. Of course, a thermal strap connecting the evaporator to the cryocooler's second stage is necessary. Figure 4.6 shows the stainless-steel wire supports of the evaporator section, which are preferred

over the G10 supports to reduce both the conduction heat leak and the thermal mass of the

evaporator and its supports.

Radiation shield   2nd stage/ Condenser   Adiabatic supports   Evaporator   Vacuum chamber cover
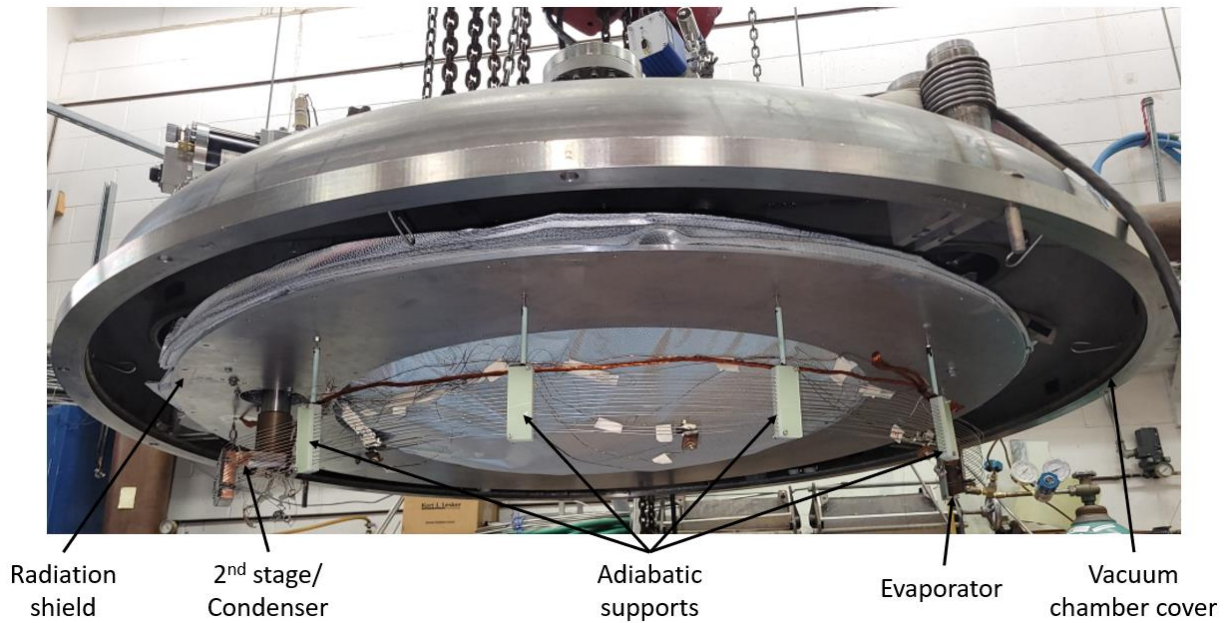
Figure 4.5. The 1.5 m PHP held in the sideways orientation by multiple G10 adiabatic support structures.
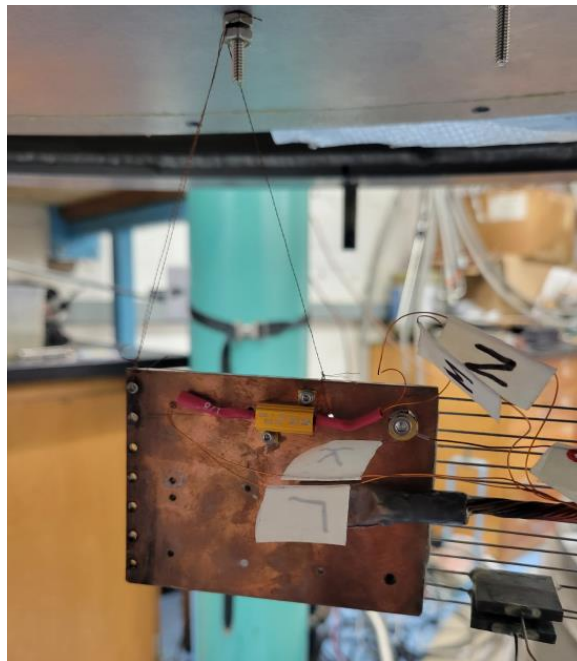
Figure 4.6. The wire support technique of the evaporator section for the sideways orientation experiments.

4.2.2. Horizontal Orientation

The horizontal orientation is simply a 90-degree rotation of the sideways orientation about the axis of the PHP's length. Here, each adiabatic tube lies within the same horizontal plane, so the effect of gravity is minimized in this orientation. Thus, this is the preferred orientation for isolating the effects of gravity and the true PHP oscillatory flows.

Due to the perceived design issues associated with the G10 supports, an improved adiabatic and evaporator section support technique is employed. Figure 4.7 shows the adiabatic and evaporator supports for the horizontal PHP experiments. First, an aluminum frame connected to the top of the radiation shield encapsulates the PHP at a point along the adiabatic section. Aluminum is chosen to reduce the cool-down time and because the heat leak to the PHP does not travel through the highly conductive aluminum. The aluminum frame has good thermal contact with the shield, so it remains at the shield temperature. Next, a grooved aluminum block holds the PHP adiabatic tubes separate from each other. Each tube lies within a groove in the block, which is coated with Kapton (polyimide) tape to thermally isolate the tubes from one another. The grooved block is thermally connected to the cryocooler's second stage via a thermal strap; therefore, it is at second-stage temperatures instead of first-stage temperatures. Finally, the grooved block is suspended from the frame by multiple stainless-steel wires, which provide mechanical support but thermal isolation. Five of these supports are used to suspend the PHP horizontally while maintaining excellent thermal isolation from the radiation shield. Figure 4.7 shows the details of these adiabatic supports, and Figure 4.8 shows the 1.5 m PHP held in the horizontal orientation by multiple supports. Moreover, the height of each support was carefully measured and adjusted to ensure the PHP was level.
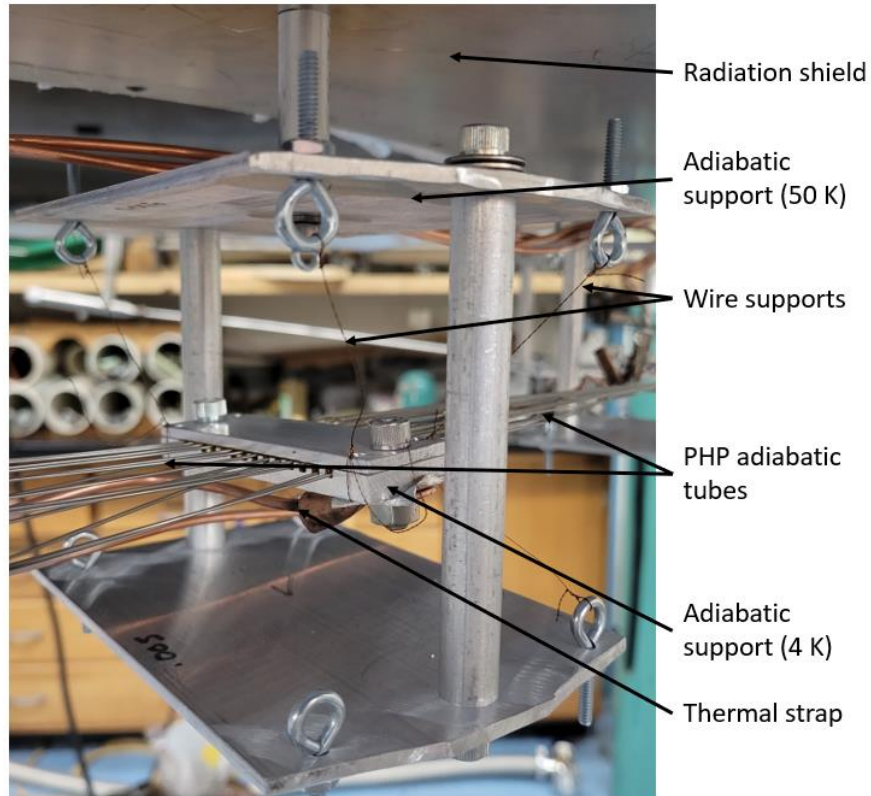
Figure 4.7. The improved adiabatic support method for the horizontal orientation experiments which provides greater thermal isolation from the radiation shield.
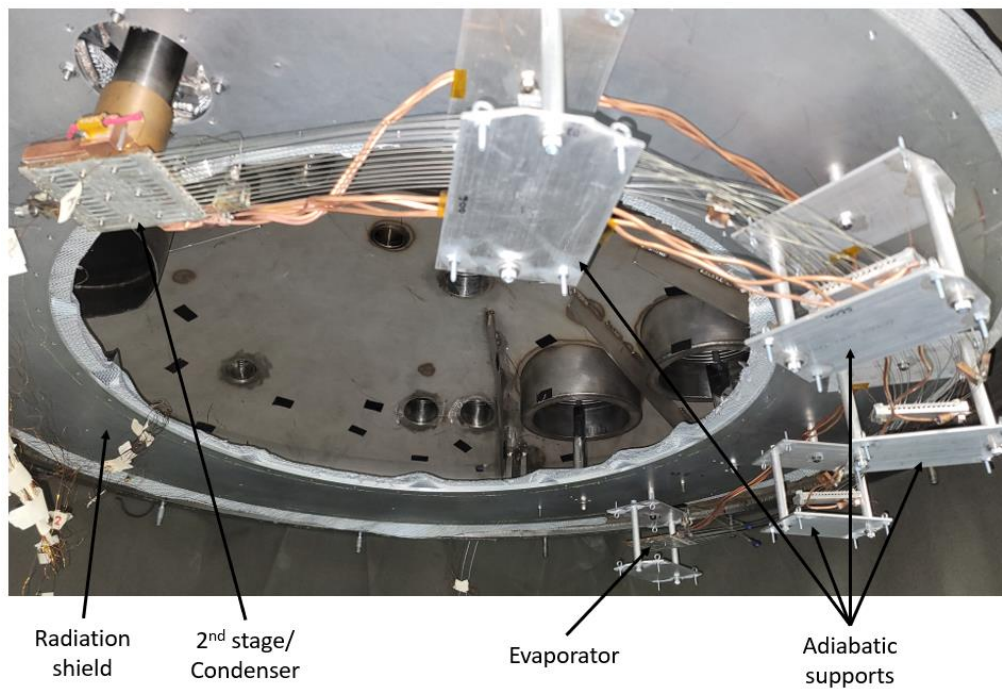
Figure 4.8. The 1.5 m PHP held in the horizontal orientation by multiple aluminum adiabatic supports.

4.3. Radiation Shield Modeling and Design

The toroidal shape of the radiation shield is too complex to thermally model analytically, like the cylindrical shield in section 2.3.2. Thus, ANSYS was used to solve for the temperature profile of the toroidal shield for a prescribed shield thickness and number of MLI layers. The problem is specified in Figure 4.9, where a radiation heat flux, estimated from Equation 2.11, is incident on all external surfaces, and the cryocooler feedthrough is held at a fixed temperature.
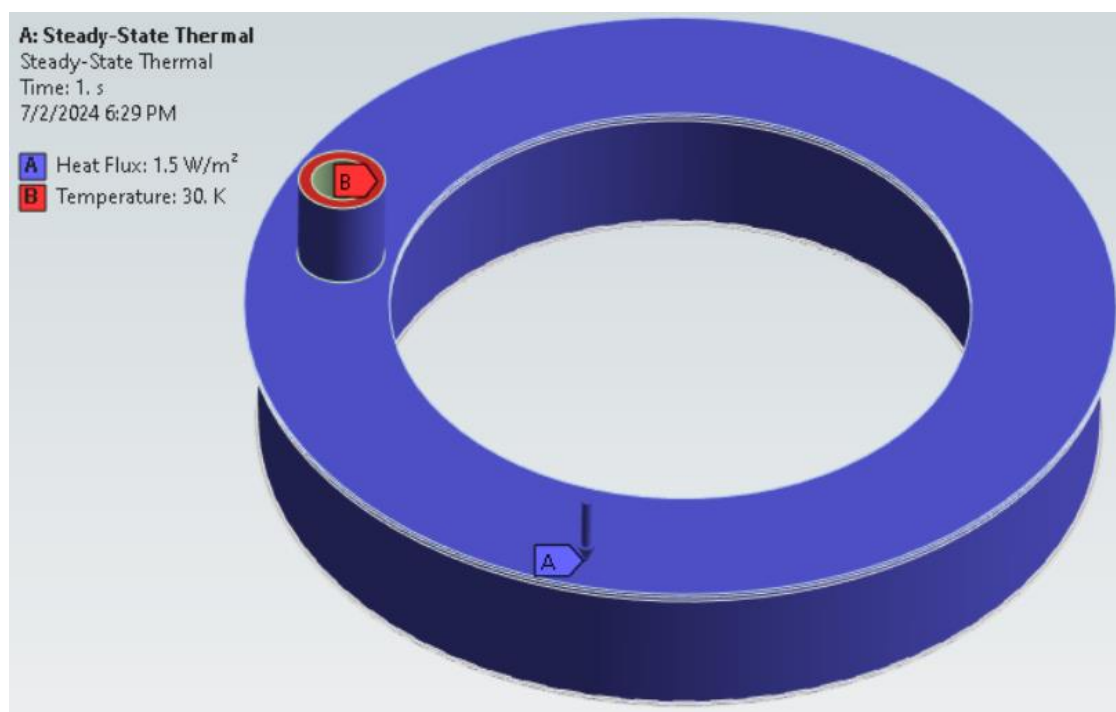
Figure 4.9. The definition of the radiation shield thermal problem to be solved in ANSYS.

For manufacturing and design purposes, the thickness of the top of the shield was chosen to be 12.7 mm (0.5"), and the sides and bottom 1.59 mm (1/16"). The material was chosen to be Aluminum 6061. These parameters were decided intuitively, resulting in acceptably small thermal gradients for reasonable MLI blanket sizes. Furthermore, three ANSYS simulations were performed with the abovementioned parameters for 10, 20, and 30 layers of MLI. The results of these simulations are summarized in Table 4.1, and an example of the shield temperature profile

generated from these simulations is shown in Figure 4.10. An MLI blanket comprised of 20 layers was ultimately chosen for the experiment since the temperature gradient for a 10-layer blanket is too large, and the minimal benefit gained with a 30-layer blanket is not worth the increased fabrication efforts.

Table 4.1. ANSYS shield modeling results.

Number of Layers [-]	Heat Flux [W/m^2]	Maximum Gradient [K]
10	2.59	17.63
20	1.32	9.75
30	0.88	6.71
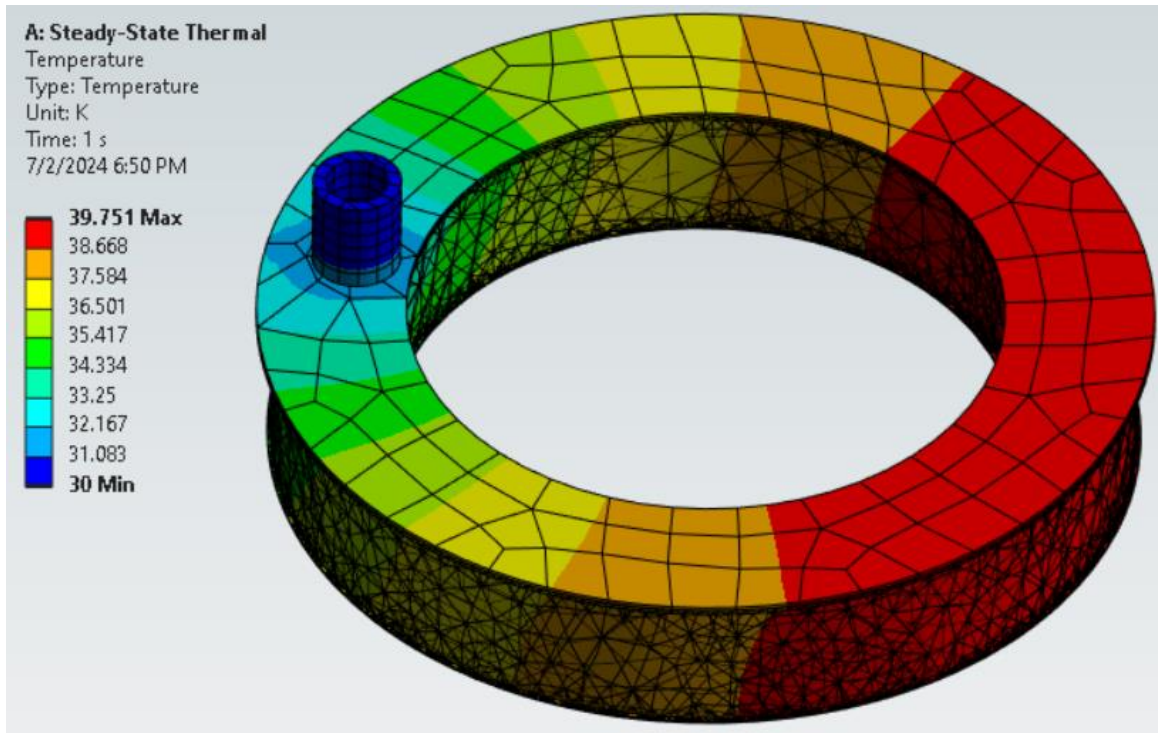
Figure 4.10. The temperature profile of the toroidal radiation shield solved in ANSYS.

The simulation was repeated to investigate the effect of the parasitic heat leaks through the support rods. Indeed, the support rods do not significantly affect the shield's temperature gradient. Moreover, while the predicted temperature gradient agrees with the experimentally observed

shield temperatures, the magnitude of the shield temperatures was much higher than expected (50 K instead of 30 K). Since the gradient is still small, the radiation flux is likely not the cause of this issue; rather, it is an unidentified heat leak directly occurring near the cryocooler's first stage.

4.4. Heat Leak Management

The heat leak accounting extensively described in section 2.3.3 was repeated, accounting for conduction heat leaks through the heater and thermometer wiring, and the shield supports, residual gas heat transfer, and radiation. The results of the heat leak calculations are summarized in Table 4.2.

Table 4.2. Summary of heat leaks.

	First stage	Second stage
Radiation	3.25 W	16.97 mW
Instrumentation wiring	800 mW	70.74 mW
Miscellaneous conduction	4.42 W	15.06 mW
Residual gas conduction	172.26 mW	1.01 mW
Total	**8.64 W**	**103.78 mW**

Of particular concern is the increased radiative heat load incident on the cryocooler's second stage due to the radiation shield's elevated temperatures. Indeed, the radiative heat flux to the second stage is nearly eight times greater for a 50 K shield than for a 30 K shield. To partially alleviate this issue, the PHP is covered with aluminum foil. Since the peak wavelength of the thermal radiation emanating from the shield at 30 K – 50 K is greater than the thickness of a typical aluminized mylar sheet, MLI blankets are effectively transparent and are poor insulators for second-stage components. Thus, a single thicker layer of aluminum foil can reflect around 80% of the incident radiation on second-stage components, reducing the heat load. However, due to the strong temperature dependence of radiation heat flux, evident via the Stefan-Boltzmann law, the

incident radiation is still up to twice as much for the 50 K shield with the aluminum foil installed than for the 30 K shield.

4.5. Sideways Orientation Results and Analysis

Time series temperature data for the 1.5 m PHP in the sideways orientation with a 50% fill ratio is displayed in Figure 4.11. Other fill ratios between 30% and 70% were also attempted but were not functional. The condenser temperature was uncontrolled for the semi-functional 50% fill ratio test and remained slightly above 3 K for all heat loads tested. The applied heat load was increased from 0 mW in increments of 10 mW until failure. Interestingly, even with no heat applied, the evaporator and adiabatic section temperatures were hotter than the condenser temperature by more than 1 K. Moreover, the evaporator temperature was nearly always colder than one entire adiabatic tube, which is impossible if the adiabatic section is genuinely adiabatic. Indeed, the increased radiation from the warmer shield temperature, coupled with the stagnant or slow-moving fluid in the PHP, likely causes fluid temperature measurement errors. Additionally, it should be noted that for the sideways orientation tests, the adiabatic thermometers were located on the second and third lowest adiabatic tubes, where the colder adiabatic tube was below the hotter adiabatic tube.

All temperatures remain stable for all applied heat loads between 10 and 40 mW, after which significant evaporator temperature oscillations begin. Increasing the heat load further to 50 mW causes all temperatures to rise rapidly and PHP failure. Unlike the vertical PHP experiments, the sideways PHP experiences a thermal runaway failure in which the evaporator temperature rises continuously without reaching a steady state.
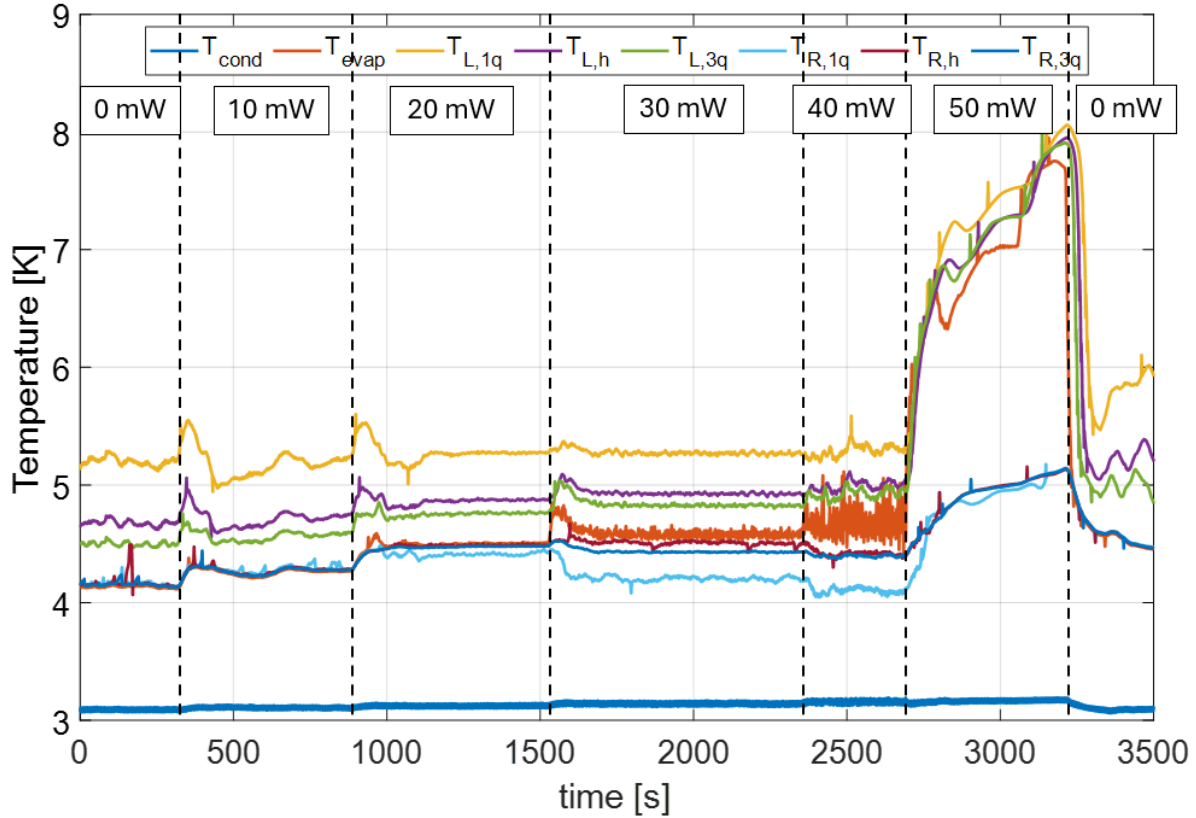
Figure 4.11. Time series temperature data for the 1.5 m PHP in the sideways orientation with a 50% fill ratio for applied heat loads between 0 and 50 mW.

Furthermore, Figure 4.12 shows the time series thermal conductance data for the sideways orientation test. The thermal strap conductance is plotted simultaneously and acts in parallel with the PHP. Evidently, for all applied heat loads, the PHP does not perform significantly better than the solid strap. Overall, the thermal performance of the 1.5 m PHP in the sideways orientation is significantly reduced relative to the vertical orientation. The maximum allowable heat load is reduced from 650 mW to 40 mW, and the maximum conductance is reduced from 784 mW/K to 27 mW/K. Unfortunately, it is believed that the somewhat stable operation observed for the sideways orientation PHP test is also driven by gravity.
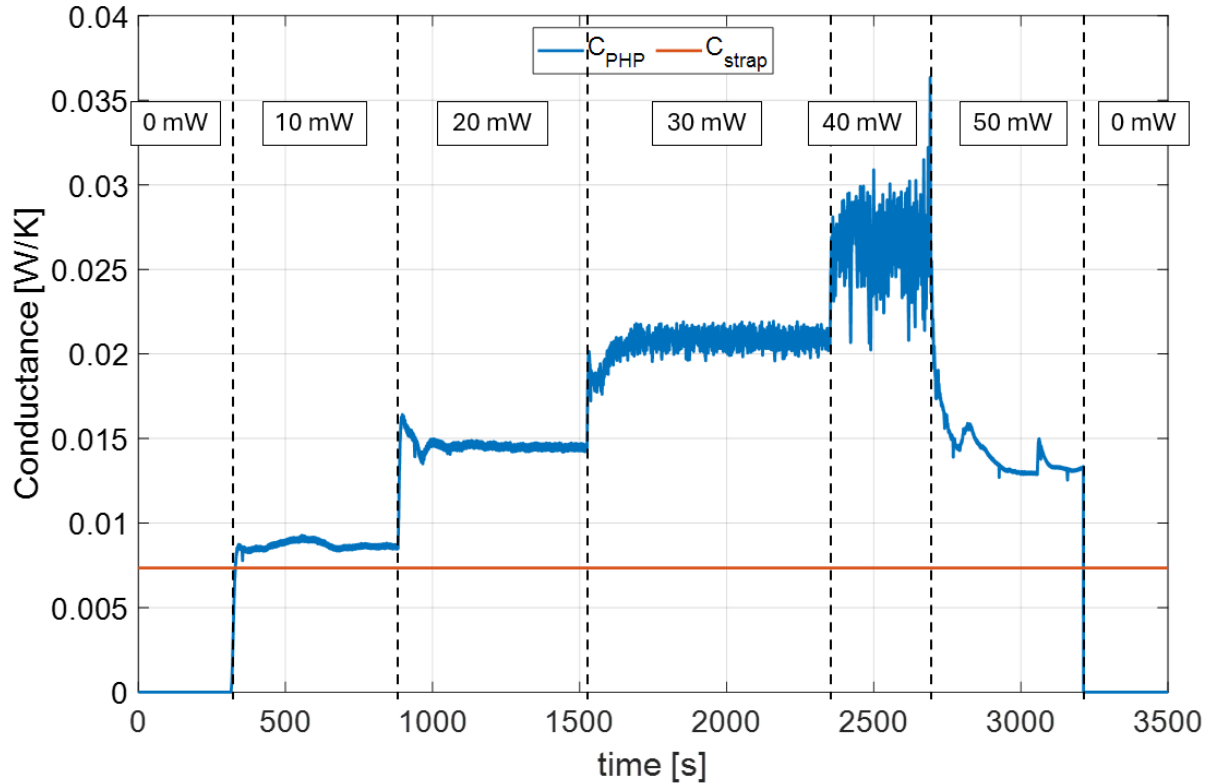
Figure 4.12. Time series thermal conductance data for the 1.5 m PHP in the sideways orientation with a 50% fill ratio for applied heat loads between 0 and 50 mW.

4.6. Horizontal Orientation Results and Analysis

Despite significant experimental efforts, the 1.5 m PHP in the horizontal orientation was entirely nonfunctional. Efforts to initiate fluid motion through various heating patterns of the condenser and evaporator sections were unsuccessful, as the fluid remained stagnant within the heat pipe. Indeed, this result, paired with the extensive experimental observations and analyses of the vertical PHPs from Chapter 3, proves that long-distance helium pulsating heat pipes rely on gravity for their operation. This result is especially unfortunate given the initial impetus for this research: mirror array cooling of large space telescopes. Indeed, helium PHPs, in their current state, are not appropriate for microgravity applications, and alternative helium heat pipe options should be investigated instead.

5. Capillary-Driven and Orientation-Independent Helium Heat Pipes

5.1. Introduction

Chapters 3 and 4 show experimentally that long-distance helium pulsating heat pipes require gravity for operation and that their observed length independence is also an artifact of their gravity-driven nature. This chapter establishes an analytical framework from a one-dimensional momentum balance that separates a PHP's AC and DC flow components and demonstrates that PHPs' gravity dependence is proportional to their adiabatic length. Indeed, the unfortunate discovery of helium PHPs' gravity dependence warrants further research to develop helium heat pipes that can operate regardless of orientation. This chapter presents the experimental results of a fully operational prototype of a new Hybrid Conventional-Pulsating Heat Pipe (HCPHP) capable of transferring substantial heat at two-phase helium temperatures over extended distances, regardless of orientation. This was achieved with an improved bundled microtube wicking structure in alternating adiabatic PHP tubes inspired by the dual-diameter design.

Indeed, several researchers have identified the benefit of non-uniform PHP channel geometries in inducing unidirectional flow via capillary forces [66, 78 - 81]. The most common method to achieve this is to reduce the diameter of half of the PHP's adiabatic tubes such that alternating tubes have different internal diameters. These dual-diameter PHPs outperform uniform-diameter PHPs in all orientations. First, Chien et al. [66] studied relatively long uniform and dual-diameter PHPs (122 mm overall length) in multiple orientations. Not only was the thermal performance improved with the dual-diameter PHP in the vertical orientation, but the dual-diameter design also allowed for horizontal operation while the uniform design could not function in the horizontal orientation. Another study by Kwon and Kim [79] presents an optimized internal diameter difference for their ethanol dual-diameter PHP, which enhanced thermal performance by

45%. Also noteworthy is the work of Jung and Kim [82], in which topology-optimized passive check valves were developed and installed near the condenser section on every tube of uniform and dual-diameter PHPs. These valves acted as fluid diodes, forcing the oscillatory flow to become steady and unidirectional. Significant reductions of the thermal resistances in both the horizontal and vertical orientations were achieved.

Only one previous study available in the current literature considered horizontal helium PHPs. This study was conducted by Li, Li, and Xu [14], and found that a purely horizontal helium PHP could only operate with a 31.8% fill ratio at 0.1 W (0.16 W/K). Moreover, their helium PHP had a short adiabatic section (100 mm) and a very high number of turns (24), both of which are typically beneficial design parameters for PHP thermal performance. Given the geometry of this PHP, the resulting effective conductance and maximum allowable heat load were poor, especially in contrast to their vertical orientation results, which showed a 7.5 times greater conductance and a 5.5 times greater maximum allowable heat load. Furthermore, the transient behavior of these horizontal helium PHP tests, including thermal stability, is not mentioned, so whether the performance reported persisted for an appreciable time or was a transient artifact is unknown.

Furthermore, helium heat pipes generally have not been studied extensively. Other than helium PHP experimental studies [12-14, 22, 26, 30, 33 - 44], only two other studies available in the literature have investigated helium heat pipes. Ku and Robinson studied the thermal performance of a helium LHP at NASA Goddard [83], which could transfer a maximum of 140 mW over a meager 40 mm, with significant design complexity. Another helium heat pipe study utilizes a design that utilizes superfluid helium film flow [84, 85]. However, this heat pipe cannot operate above the lambda point (2.17 K), and therefore it addresses a different operating temperature range and applications than helium conventional and pulsating heat pipes. Indeed, due

to their many potential applications and the lack of related experimental and theoretical research, there is an unmet need for two-phase helium heat pipes that can operate regardless of orientation.

5.2. PHP Equations of Motion

The gravity-dependence of pulsating heat pipes can be demonstrated analytically by considering the one-dimensional force/momentum balance, depicted in Figure 5.1, on a single saturated liquid slug contained in a capillary tube:

$$F_i = F_g - F_v + F_{\Delta P} \tag{5.1}$$

Where F_i is the inertial force due to momentum, F_g is the gravitational body force, F_v is the viscous force, and $F_{\Delta P}$ is the force due to the pressure differential of the two vapor plugs surrounding the liquid slug. It is the saturation pressure differential force, $F_{\Delta P}$, which is the source of PHPs' unique oscillatory flow behavior. This force is dictated by the complex dynamics of the alternating train of saturated liquid and vapor sections, along with phase change in the evaporator and condenser. However, the gravitational and viscous forces are simply steady DC flow contributions that alter the oscillatory flow modes. Indeed, the extensive theoretical and experimental work by Yoon and Kim [7, 19, 20] has described the complexity of this pressure differential force and the physical mechanisms by which purely oscillatory flow modes in pulsating heat pipes transfer heat uni-directionally.

Since Yoon and Kim's PHP was very short, the gravitational and viscous forces were negligible, and they were able to model the pressure differential force as a nonlinear spring and further model an entire PHP as a series of multiple masses (liquid slugs) connected by nonlinear springs (vapor plugs). This model, validated through visualization experiments, showed that while the liquid slugs oscillated in place (without streaming), adjacent liquid slugs oscillated out of phase

due to the non-linearity of the vapor plug springs, resulting in unidirectional mass and heat transfer. Furthermore, it was observed from these studies that the number of liquid slugs was equal to the number of PHP turns and that the slug length was on the same order as the adiabatic length, so as the liquid slugs oscillated in place, one end would reach into the evaporator during the oscillation peak, and the other end would reach into the condenser during the oscillation trough.
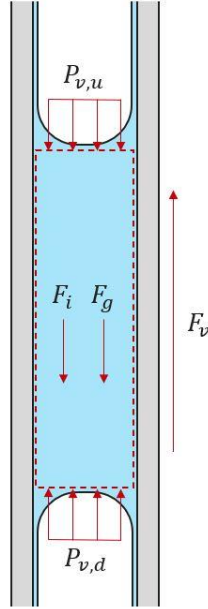
Figure 5.1. A schematic of the one-dimension force/momentum balance for a single liquid plug surrounded by two vapor plugs, accounting for the inertial, gravitational, viscous, and pressure differential forces.

However, the liquid slug equation of motion changes significantly when the PHP length is extended. Each of the forces in Equation 5.1 can be expanded with appropriate expressions to show the equation of motion's dependence on length and orientation angle:

$$\rho A_c L \ddot{x} = 2\rho A_c g\cos(\theta)L^* - 8\pi\mu L\dot{x} + A_c\left(P_{v,u} - P_{v,d}\right) \tag{5.2}$$

Where ρ, μ, L, $\dot{x}$, and $\ddot{x}$ are the density, viscosity, length, velocity, and acceleration of the liquid slug, g is the gravitational constant, A_c is the cross-sectional area of the tube, θ is the PHP's orientation angle, $P_{v,u}$ and $P_{v,d}$ are the saturation pressures of the vapor plugs adjacent to the liquid

slug, and L^* is an effective slug length, which depends on the overall slug length, L, along with the slug's location (the effective length may be shorter than the actual length if the slug is located within a PHP turn). Indeed, the assertion that the gravitational and viscous forces are negligible is not valid if the PHP length is appreciable, and therefore, these DC flow components may contribute significantly to the oscillatory flow modes or render them insignificant entirely. Furthermore, the gravitational body force depends on the PHP's orientation angle: The contribution of this force becomes negligible when the PHP is horizontal. Table 5.1 details the PHP equations of motion in the limiting cases.

Table 5.1. PHP equations of motion in length and orientation extrema.

		Orientation			
		Vertical		Horizontal	
Length	Long	$F_i = F_g - F_v$	(5.3)	$F_i = -F_v$	(5.4)
	Short	$F_i = F_{\Delta P}$	(5.5)	$F_i = F_{\Delta P}$	(5.5)

Indeed, for very short PHPs, the purely oscillatory modes stemming from the saturation pressure differential forces are dominant, and the equation of motion shown in Equation 5.5 matches that of Yoon and Kim [7]. Furthermore, the equation of motion for short PHPs does not significantly depend on the orientation angle since the gravitational force is small relative to the pressure differential force. For very long PHPs in the vertical orientation, the oscillatory flow modes are negligible, and the DC gravitational and viscous contributions dominate the motion of liquid slugs. Chapter 3 describes in detail the gravity-dependence of long-distance helium PHPs in the vertical orientation and how the thermal performance as a function of applied heat load, fill ratio, and adiabatic length can be explained by considering only the gravitational and viscous forces. When considering a long PHP in the horizontal orientation, an issue arises in the PHP

equation of motion. The relevant equation of motion for this situation (Equation 5.4) can be expanded:

$$\rho A_c L \ddot{x} = -8\pi \mu L \dot{x} \tag{5.6}$$

Equation 5.6 represents the equation of motion of an undriven damped mass, an ODE with no nontrivial solutions. Indeed, upon solving the ODE described in Equation 5.6, one finds that the liquid slug velocity tends to zero for times on the order of the viscous relaxation time. Hence, long-distance PHPs without the assistance of a body force cannot operate with either the DC or oscillatory flow modes since the fluid remains stagnant, resulting in an inoperable heat pipe. Indeed, the 1.5 m helium PHP tested in the horizontal orientation was entirely nonfunctional, with no observed evidence of fluid movement (Chapter 4). In summary, the orientation and length of a PHP determine the relative contributions of the DC and oscillatory flow modes and show that PHPs can only be independent of orientation if their adiabatic length is sufficiently small and that long PHPs depend on a DC body force, such as gravity, to operate. Mixed modes where the DC and oscillatory forces are of similar magnitude are possible between these limiting cases. It is also important to note that the maximum length at which the oscillatory modes can effectively transfer heat strongly depends on the working fluid's properties. As such, some PHPs may be able to operate in the horizontal orientation for appreciable lengths, depending on the working fluid.

The helium pulsating heat pipes experimentally investigated in previous chapters were between 1 m and 2 m long and fell firmly within the extrema in which the oscillatory flow modes are irrelevant. Furthermore, since the ratio of saturated liquid density to saturated vapor density is very small for helium (7.4 at atmospheric pressure) compared to typical PHP working fluids like nitrogen, ethanol, or water (145, 447, and 1604, respectively), the oscillatory driving force is significantly weaker for helium since the fluid expansion and contraction due to phase change in

the evaporator and condenser sections is minimal. This argument further suggests that oscillatory flow modes are essentially a non-factor, especially for helium PHPs.

Due to their dependence on gravity, long-distance helium pulsating heat pipes (in their current state) are not viable options for the aerospace applications mentioned above, which exist in microgravity environments. Therefore, an adjustment to the typical pulsating heat pipe design is required to address the issue of gravity dependence. One way is to supplant the gravitational driving force with a different DC driving force, the most intuitive option of which is surface tension. Thus, a heat pipe design that operates like a conventional heat pipe is better suited for microgravity environments than pulsating heat pipes, especially for extended heat transfer distances.

The PHP equation of motion in the horizontal orientation, including a capillary force contribution, is:

$$F_i = F_s - F_v \qquad (5.7)$$

Where F_s is the steady surface tension force. Equation 5.7 shares the same ODE form as Equation 5.3, which is a viable equation of motion. By substituting with appropriate expressions for each force, Equation 5.7 becomes:

$$\rho A_c L \ddot{x} = \frac{2\sigma}{r_m} A_c - 8\pi \mu L \dot{x} \qquad (5.8)$$

Where σ is the two-phase surface tension and r_m is the meniscus radius of curvature for the two-phase interface. The driving term in Equation 5.8 is independent of the orientation angle, unlike in Equation 5.3, which makes this equation of motion valid regardless of PHP orientation, and in microgravity. Therefore, it is necessary to develop a passive heat pipe design that relies on surface tension instead of gravity, like a conventional heat pipe, while retaining the desirable

aspects of pulsating heat pipes, like physical flexibility and routability, vibration damping, low mass, and uncomplicated fabrication.

5.3. Potential Heat Pipe Geometries

Helium is, without a doubt, the most difficult working fluid with which to design a capillary-driven heat pipe. Due to the helium atom's electronic structure, lack of permanent polarity, and small kinetic mass, the intermolecular forces between atoms are extremely weak at all temperatures. As a result, the two-phase surface tension and saturated viscosities are significantly lower for helium than for any other fluid. Indeed, even compared to other nonpolar and light molecules such as H_2 and Ne, the relevant fluid properties for heat pipe design are much smaller, as detailed in Table 5.2.

Table 5.2. Properties of common PHP fluids relevant to heat pipe design, evaluated at atmospheric pressure [60].

	Surface tension [N/m]	Saturated liquid viscosity [Pa-s]	Saturated vapor viscosity [Pa-s]
Helium	0.00008846	0.000003169	0.000001246
Hydrogen (H_2)	0.001913	0.00001375	9.963E-07
Neon	0.004517	0.0001272	0.000005096
Water	0.05891	0.0002818	0.00001227
Ethanol	0.01764	0.0004475	0.00001043
Ammonia	0.03412	0.0002551	0.000008054

One may think that the effects of helium's very low viscosity and surface tension fluid properties may counteract each other; however, although the capillary and viscous resistive forces oppose one another in a heat pipe, these forces scale with channel size in significantly different ways. For a two-phase fluid in a circular pipe (a circular arterial wick), the capillary pumping pressure can be estimated as [18]:

$$\Delta P_{cap} = \frac{2\sigma}{r} \tag{5.9}$$

Where ΔP_{cap} is the capillary pumping pressure across a two-phase interface, σ is the two-phase surface tension of the fluid, and r is the radius of the circular pipe. Additionally, the resistive viscous pressure drop for laminar flow in a circular pipe can be expressed as:

$$\Delta P_{visc} = \frac{8\mu L}{\pi r^4} \dot{V} \tag{5.10}$$

Where ΔP_{visc} is the viscous pressure drop, μ is the effective viscosity of the two-phase fluid, L is the pipe length, and $\dot{V}$ is the volumetric flow rate of the fluid. It is evident through a comparison of Equations 5.9 and 5.10 that reducing the channel radius increases the capillary pumping force linearly but simultaneously increases the viscous resistive force quartically. Thus, there is no way to increase the capillary pumping pressure for a single circular artery without significantly increasing the viscous resistive forces. If the working fluid's two-phase surface tension is small, as with helium, then alternative wicking structures should be investigated.

Indeed, the wicks of nearly all traditional heat pipe designs provide multiple parallel flow channels that reduce the bulk liquid velocity while maintaining a high mass flow rate, which reduces the viscous forces without perturbing the capillary forces. Contrast this with the geometries of uniform or dual-diameter pulsating heat pipes, which consist of single uniform circular channels. Due to the small size of PHP channels in contrast with conventional heat pipe flow paths, incorporating traditional wicking structures, such as wrapped screens or sintered metal, into PHPs is impractical and would eliminate many of PHPs' advantages. Instead, a simple liquid wicking structure design is proposed in this work that interfaces well with the typical PHP geometry and manufacturing methods and allows the heat pipe to be capillary-driven (and able to operate without assistance from gravity) for substantial applied heat loads.

5.3.1. The Dual-Diameter PHP

The most straightforward capillary-driven PHP-like heat pipe design features capillary tubes of two different diameters alternating across the adiabatic section. The smaller of the two tubes acts as an arterial wick, while the larger tube acts as a vapor return passage. Moreover, as mentioned previously, dual-diameter PHPs have been tested in a few room-temperature studies [66, 79, 81]. Two helium dual-diameter PHPs were tested with capillary tube combinations 0.4/0.5 mm and 0.25/0.8 mm and with a 250 mm adiabatic length. Figure 5.2 shows pictures of these heat pipes. Unfortunately, neither of the dual-diameter PHPs was operable. Indeed, the fluid properties of helium, as mentioned above, are not conducive to capillary-driven heat pipe design; therefore, alternative wick structure options are required.

(a)

(b)

Figure 5.2. Dual-diameter helium PHPs with capillary sizes of (a) 0.4/0.5 mm and (b) 0.25/0.8 mm.

5.3.2. The Hybrid Conventional-Pulsating Heat Pipe

Evidently, the dual-diameter design is inadequate for helium heat pipes, as it does not provide sufficient capillary pumping pressure to circulate the fluid against the viscous resistive forces. Thus, developing an improved wick structure is necessary for a capillary-driven PHP-like

helium heat pipe. Figure 5.3 displays the relevant geometric features of an improved heat pipe featuring a microtube bundle encapsulated by a larger shell tube as the wick structure. Additionally, Table 5.3 lists the values and variable definitions for this heat pipe's geometric features. Since this heat pipe resembles a pulsating heat pipe but operates like a conventional heat pipe, it is referred to as a "Hybrid Conventional-Pulsating Heat Pipe" (HCPHP).
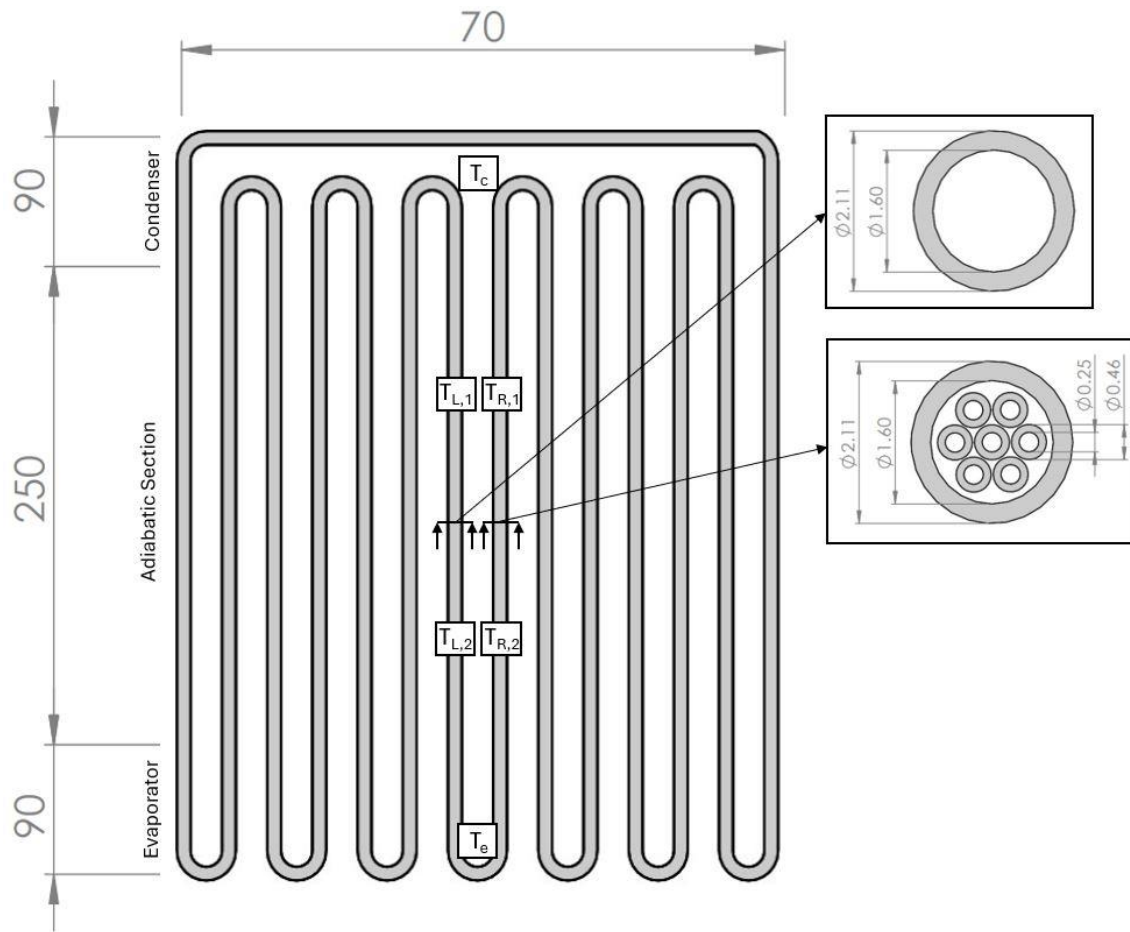
Figure 5.3. A schematic of the HCPHP geometry, showing the important geometric features and dimensions, along with the temperature measurement locations.

Like dual-diameter PHPs, the flow path cross-section of adjacent tubes is significantly different to encourage unidirectional flow. The two tube designs are featured in the adiabatic section of the HCPHP in an alternating fashion. Indeed, the bundle of microtubes constitutes a wick structure and should contain primarily saturated liquid, which is transported through these

passages from the condenser to the evaporator. The adjacent tubes, which lack internal features, should act as vapor return tubes that transport primarily saturated vapor from the evaporator to the condenser, resulting in capillary-driven unidirectional flow. Moreover, per section 5.4, the design of the liquid side should minimize viscous losses while maximizing the capillary pumping force, which requires thoughtful wick design. The vapor side design is also nuanced, and the optimal tube size is presently unknown, as described in section 5.3.3.

This novel geometry retains the aforementioned advantages of PHPs yet allows the heat pipe to operate without the assistance of gravity, like a conventional heat pipe in the horizontal orientation. In essence, the HCPHP is multiple conventional heat pipes connected in series, which resembles a PHP. Moreover, the microtube bundle acting as the liquid wick is one of many countless potential wicking structures for the HCPHP. There are likely several other simple and easy-to-fabricate wick structures that may provide further performance improvements, such as the cable-in-conduit geometry, which has been studied hydrodynamically in the past [86].

Table 5.3. HCPHP design specifications.

Adiabatic Length (L_a)	250 mm
Evaporator Length (L_e)	90 mm
Condenser Length (L_c)	90 mm
PHP width	70 mm
Number of turns (N_t)	7
Number of wick microtubes (N_w)	7
Microtube inner diameter ($r_{w,i}$)	0.25 mm
Microtube outer diameter ($r_{w,o}$)	0.46 mm
Vapor return tube inner diameter (r_v)	1.60 mm
Vapor return tube outer diameter	2.11 mm

A picture of the HCPHP is shown in Figure 5.4. The 304 stainless steel tubes that constitute the heat pipe are connected with braze joints and are soft soldered to the condenser and evaporator

sections, which are thin copper plates. The fluid pressure of the heat pipe is measured with an additional pressure transducer at the heat pipe's fill point. Since the capillary pumping pressure is very small (around 10 Pa), this pressure measurement is not made directly in the heat pipe's flow path, as with the vertical PHPs, to circumvent minor flow losses. Moreover, Figure 5.5 shows a simplified schematic of the HCPHP test facility, as described in Chapters 2 and 4.

Figure 5.4. A picture of the HCPHP prototype specifying the locations of the fill line, pressure tap, and the three standard heat pipe sections.
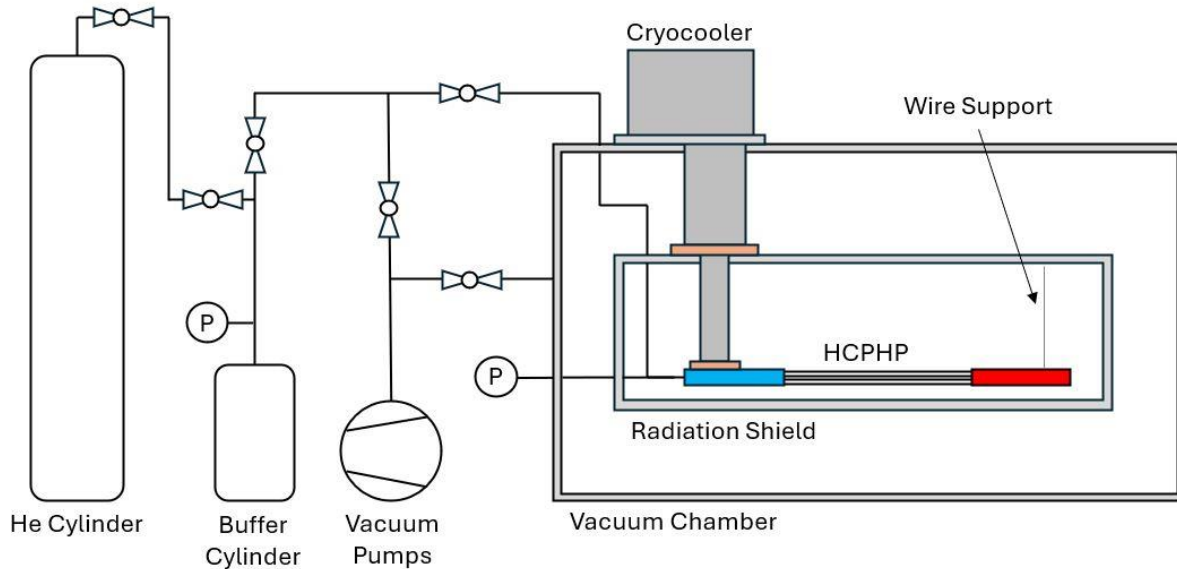
Figure 5.5. A diagram of the experimental test facility displaying internal and external helium plumbing components.

5.3.3. Vapor Return Passage Design

An interesting discussion arises from the question of what happens when a saturated vapor bubble trapped inside a vertical capillary by surface tension forces is rotated horizontally so that gravity acts perpendicular to the tube rather than parallel? Of course, when vertical, the Bond number dictates the formation of static two-phase interfaces perpendicular to the tube. Furthermore, Equation 1.5 gives an alternative orientation-dependent bond number which attempts to describe the formation of static interfaces for non-vertical orientations. However, Equation 1.5 tends to infinity as the orientation angle approaches horizontal, suggesting that two-phase interfaces should never form in a horizontal capillary. This result is certainly false implying that the

Fortunately, Rascon, Perry, and Aarts [87] provide an excellent mathematical description of the horizontal capillary problem. The mathematical treatment of the problem is rigorous and beyond the scope of this work, however it involves determining whether solutions to the Young-Laplace equation exist for a given cross-sectional area, capillary length, and contact angle via variational calculus. The capillary length is defined as:

$$a = \sqrt{\frac{\sigma}{\Delta \rho g}} \qquad (5.11)$$

Where a is the capillary length and $\Delta \rho$ is the density difference between the saturated phases. Figure 5.6 shows the results for a circular capillary. For two-phase helium, the surface tension contact angle is essentially zero, leading to the interface criterion that the tube radius should equal the capillary length. This is miraculously the same condition required for vertical capillaries, that is, the Bond number must be equal to or less than 2 in order for perpendicular two-phase interfaces to form. For nearly every other fluid, the contact angle is greater than zero, and

surprisingly, according to Figure 5.6, the horizontal interface criterion is more permissible of larger diameters than the vertical interface criterion. For example, the formation of interfaces for a fluid with a 90-degree contact angle will be permitted in horizontal tubes with up to $\sqrt{3}$ times greater diameter than in vertical tubes. This result is unintuitive and may necessitate revisiting the Bond number criterion established by White and Beardmore [9] or further experimental studies.
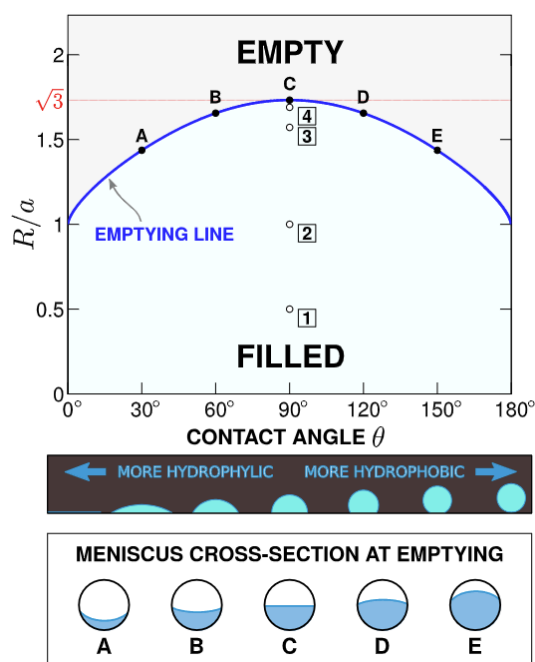
Figure 5.6. Conditions for capillary emptying as a function of tube size, capillary length, and contact angle for circular cross-sections [87].

Regardless, the work of Rascon, Perry and Aarts provides a tool for rapidly determining if interfaces will form for a given tube geometry. This discussion is particularly relevant in the design of the vapor return passages for HCPHP-like heat pipes. Whether it is favorable to allow interfaces to form or not is unknown. If the vapor return passage is large, interfaces will not form, and the vapor may flow freely from the evaporator to the condenser with low viscosity. As discussed in a later section, this condition results in a stagnant stratified liquid phase and limits the mass flow in the vapor return passage to be entirely saturated vapor.

Decreasing the vapor passage size will increase the viscous forces and permit the formation of two-phase interfaces. Dynamic resistive surface tension forces may also be relevant. Thus, instead of gravitationally stratified phases, plugs and slugs will form in the capillary, like in a PHP. Therefore, the mass flow is not limited to just saturated vapor and the fluid leaving the evaporator must push the train of alternating plugs and slugs through the tube. It is unknown whether this condition results in clogged vapor tubes that block the capillary-driven flow entirely, or if the formation of plugs and slugs enhances the mass transport through the vapor return tubes. The HCPHP features large vapor passages that do not permit the formation of two-phase interfaces, which were chosen conservatively to increase the likelihood that the heat pipe would operate Moreover, in microgravity, the capillary number approaches infinity, corresponding to a condition in which the tube forms interfaces regardless of its size. Thus, despite greater viscous resistance, vapor return tubes that permit the formation of two-phase interfaces will likely be more characteristic of a heat pipe operating in microgravity.

5.4. Theoretical Capillary Limits

The following analysis closely follows that of Faghri [18]. Assuming the flow in both the liquid and vapor paths are steady (inertial effects are negligible), the equation of motion for one heat pipe loop results in the following requirement:

$$\Delta P_{cap} \geq \Delta P_{visc,l} + \Delta P_{visc,v} \tag{5.12}$$

Where $\Delta P_{visc,l}$ and $\Delta P_{visc,v}$ are the viscous pressure drops of the liquid and vapor flow channels, respectively. That is, the pumping pressure generated by the two-phase interface menisci must be large enough to overcome the total viscous resistance of the flow. This balance is the well-known capillary limit of conventional heat pipes. By equating both sides of Equation 5.12, the

maximum allowable heat load of the heat pipe can be evaluated. Assuming the flow is laminar, the viscous pressure drop of the circular vapor return tubes can be expressed as:

$$\Delta P_{visc,v} = \frac{8\mu_v}{\pi\rho_v r_v^4} \frac{\dot{Q}}{h_{fg}} (L_e + L_a + L_c) \tag{5.13}$$

Where μ_v is the saturated vapor viscosity, ρ_v is the saturated vapor density, r_v is the radius of the vapor return tubes, $\dot{Q}$ is the heat load incident on the evaporator section, h_{fg} is the enthalpy of vaporization, and L_e, L_a, and L_c are the lengths of the evaporator, adiabatic, and condenser sections, respectively. Treatment of the viscous pressure drop in the liquid tubes requires slightly more care due to the strong dependence of the wicking structure geometry on pressure drop for laminar flows. The liquid side viscous pressure drop can be expressed as:

$$\Delta P_{visc,l} = \frac{\mu_l}{\rho_l A_w K} \frac{\dot{Q}}{h_{fg}} (L_e + L_a + L_c) \tag{5.14}$$

Where μ_l is the saturated liquid viscosity, ρ_l is the saturated liquid density, A_w is the wick cross-sectional area, and K is the wick permeability. By equating Equation 5.12 and substituting Equations 5.9, 5.13, and 5.14, The capillary heat load limit can be expressed explicitly as:

$$\dot{Q} = N_t \frac{2\sigma}{r_m} \frac{h_{fg}}{(L_e + L_a + L_c)} \left[\frac{8\mu_v}{\pi\rho_v r_v^4} + \frac{\mu_l}{\rho_l A_w K} \right]^{-1} \tag{5.15}$$

Where N_t is the number of turns. For an arbitrary geometry, the wick permeability can be written as:

$$K = \frac{2r_{l,h}^2 \varphi}{f Re_{l,h}} \tag{5.16}$$

Where $r_{l,h}$ is the hydraulic radius of the liquid side flow path, φ is the wick porosity, f is the Fanning friction factor, and $Re_{l,h}$ is the hydraulic Reynold's number of the liquid flow. Indeed, for a circular duct ($\varphi = 1$ and $fRe_{l,h} = 16$), the permeability is:

$$K = \frac{r_l^2}{8} \tag{5.17}$$

Which is the appropriate wick permeability for calculating the capillary limit of dual-diameter PHPs, where r_l is the radius of the smaller channels that contain primarily saturated liquid. When substituting Equation 5.17 into Equation 5.14, the expressions for $\Delta P_{visc,l}$ and $\Delta P_{visc,v}$ differ only in the channel radius size and fluid properties. However, for more complex wick geometries, such as that of this study's HCPHP, evaluating K is slightly more complicated. First, the laminar flow correlation, $fRe_{l,h} = 16$, may not be accurate for the HCPHP's wick geometry. For a more accurate correlation, the wick cross-section was simulated using ANSYS Fluent's laminar flow solver, which resulted in $fRe_{l,h} = 13.99$. Additionally, the wick cross-section's hydraulic radius is required, defined as the ratio between the flow cross-sectional area and the wetted perimeter. The hydraulic radius of the HCPHP wick, which is a microtube bundle encapsulated by a larger tube, can be evaluated as:

$$r_{l,h} = \frac{1}{2} \frac{r_v^2 - N_w(r_{w,o}^2 - r_{w,i}^2)}{r_v + N_w(r_{w,o} + r_{w,i})} \tag{5.18}$$

Where N_w is the number of microtubes in the bundle, $r_{w,o}$ is the outer diameter of the microtubes, and $r_{w,i}$ is the inner diameter of the microtubes. The wick porosity, φ, is defined as the ratio between the cross-sectional area of the liquid flow and the total cross-sectional area of the wick. For the HCPHP's bundled microtube wick, the porosity is:

$$\varphi = 1 - \frac{N_w \left(r_{w,o}^2 - r_{w,i}^2 \right)}{r_v^2} \tag{5.19}$$

For most conventional heat pipes, the interface meniscus radius of curvature, r_m, is simply the pore size of the wick, which can easily be measured. Similarly, for dual-diameter PHPs with circular arterial wicks, r_m is simply the radius of the smaller PHP tubes. However, the appropriate r_m for the HCPHP is somewhat vague since saturated vapor-liquid interfaces almost certainly exist between the outer diameters of adjacent microtubes in the bundle. Thus, an adequate estimate of r_m for the HCPHP is the radius of the largest circle that fits within the gap created by three adjacent tubes in the bundle, which is approximately 0.043 mm. In the results section, it is shown that this is a reasonable estimate for the fill ratio assumed by the capillary limit calculation (37.15%), although r_m seems to be a function of the fill ratio for this heat pipe.

Table 5.4 lists the capillary limit estimates evaluated via Equation 5.15 for the two dual-diameter PHPs, along with the HCPHP for an adiabatic length of 250 mm. This capillary limit analysis suggests that the wicking structure of the HCPHP significantly increases the heat transfer capability versus the dual-diameter PHP design.

Table 5.4. Predicted capillary limits for two dual-diameter helium PHPs and the HCPHP.

	3.5 K	4 K	4.5 K
Dual Diameter (0.4/0.5 mm)	4.29 mW	3.41 mW	1.92 mW
Dual Diameter (0.25/0.8 mm)	1.93 mW	1.27 mW	0.61 mW
HCPHP	81.99 mW	50.19 mW	21.98 mW

Furthermore, as shown in Figure 5.7, the maximum allowable heat load of the HCPHP estimated via the capillary limit is a strong function of both temperature and adiabatic length.

Unlike in the vertical orientation, the primary driving force of the HCPHP, surface tension, is not a function of length and, therefore, does not counteract the viscous resistive force which grows linearly with increasing adiabatic length. Additionally, the two-phase surface tension fluid property strongly depends on temperature since intermolecular forces weaken with increasing temperature. Thus, to increase the maximum allowable heat load for greater heat pipe lengths, improvements primarily to the HCPHP's wicking structure are required. While the capillary limit calculation gives a prediction for the maximum allowable heat load of the heat pipe, predicting the HCPHP's thermal resistance is a more complex task since it depends on the boiling and condensation heat transfer coefficients in the evaporator and condenser, respectively, which further depend on the characteristics of the fluid flow. A more detailed numerical model of the HCPHP that predicts thermal resistance as a function of applied heat load could aid in optimizing the wick structure design.
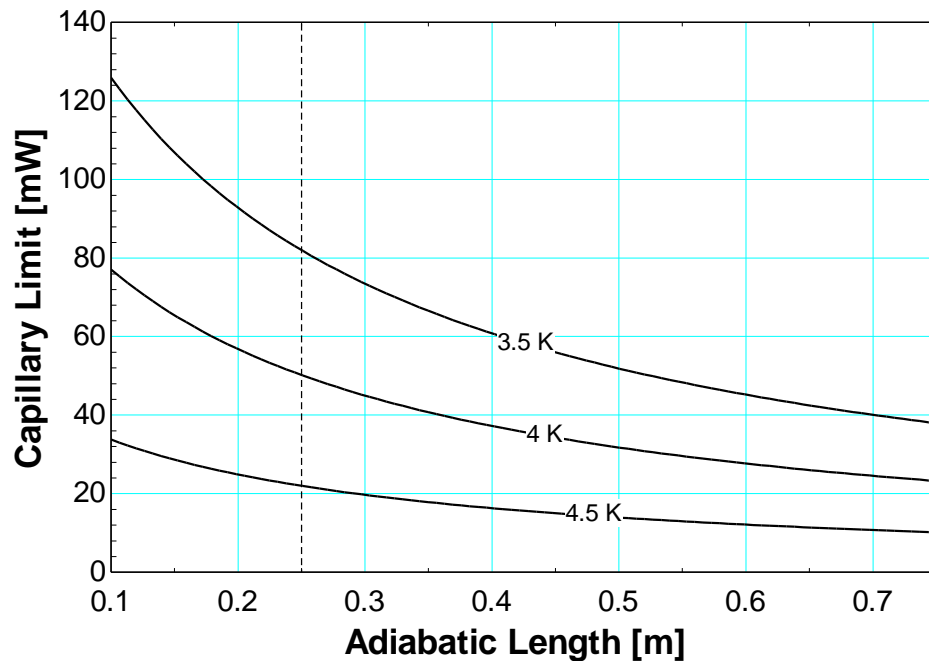
Figure 5.7. The HCPHP capillary limit as a function of adiabatic length for multiple relevant operating temperatures.

5.5. HCPHP Performance Characterization

The behavior of the HCPHP was evaluated with progressively increasing heat load tests, which is the standard PHP testing procedure. Starting from zero, the heat load applied to the evaporator was incremented upwards by 5 mW, and after a transient period of around 1-2 minutes, steady-state data was recorded for 10 minutes for each heat load. Each test was concluded when the evaporator temperature exceeded 8 K. Moreover, the data presented is time-averaged over the 10-minute steady-state recording period. Uncertainties were calculated as described by Moffat [63], with the standard deviation of the temperature oscillations over the recording period being included as an uncertainty. Seven fill ratios between 30.89% and 69.96% were tested for three condenser temperatures: 3.5 K, 4 K, and 4.5 K, for a total of 21 progressively increasing heat load tests.

5.5.1. Effect of Operating Temperature

The effect of the controlled condenser temperature on the effective conductance of the HCPHP with a constant fill ratio is shown in Figure 5.8 for all fill ratios. For all fill ratios, the condenser temperature significantly affects the HCPHP's conductance and maximum allowable heat load. As expected, increasing the condenser temperature negatively impacts the heat pipe's thermal conductance and maximum allowable heat load due to helium's two-phase surface tension fluid property decreasing strongly with increasing temperature. With a fill ratio of 30.89%, the HCPHP performs somewhat well only for a condenser temperature of 3.5 K, where effective conductances greater than 100 mW/K are observed for heat loads up to 50 mW. At higher condenser temperatures, the HCPHP with a 30.89% fill ratio does not perform well, even at low applied heat loads. Moreover, the maximum allowable heat loads of the HCPHP with a 40.12% fill ratio, which most closely matches the fill ratio assumed by the capillary limit calculation,

matches somewhat well with the calculation. In fact, the HCPHP with a 40.12% fill ratio can outperform the capillary limit prediction. Furthermore, increasing the fill ratio to 40.12% significantly increases the HCPHP's maximum conductance: 302 mW/K at 50 mW, 304 mW/K at 35 mW, and 261 mW/K at 15 mW for constant condenser temperatures of 3.5 K, 4 K, and 4.5 K, respectively. The maximum allowable heat loads with a 40.12% fill ratio are 115 mW, 100 mW, and 80 mW (3.5 K, 4 K, and 4.5 K condenser temperatures).
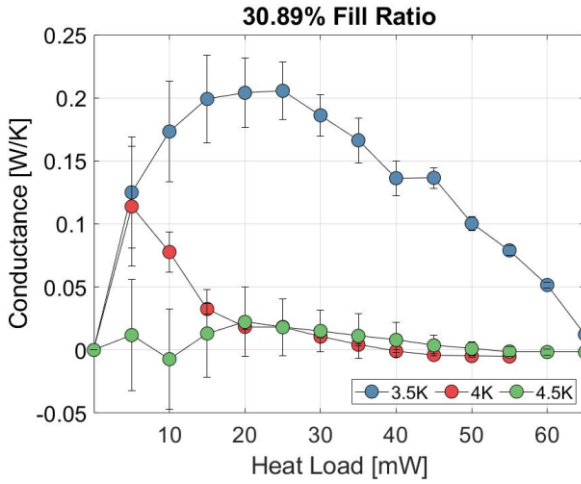
(a)
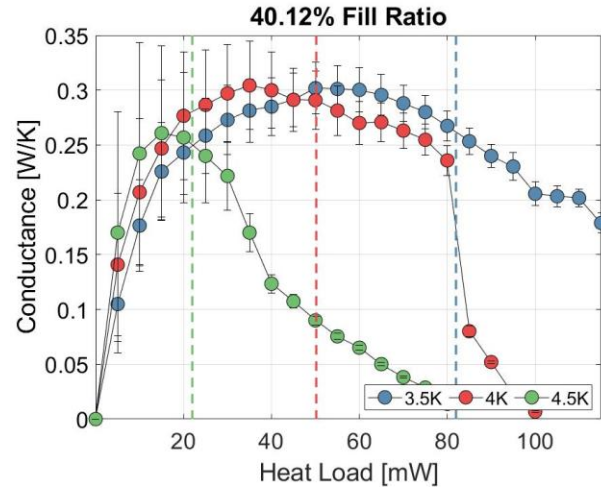
(b)
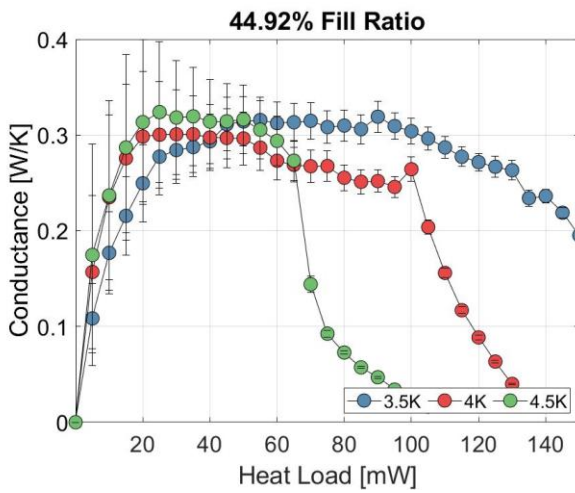
(c)
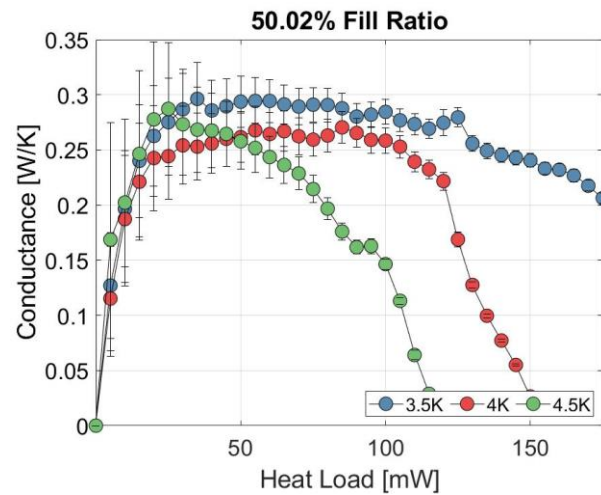
(d)
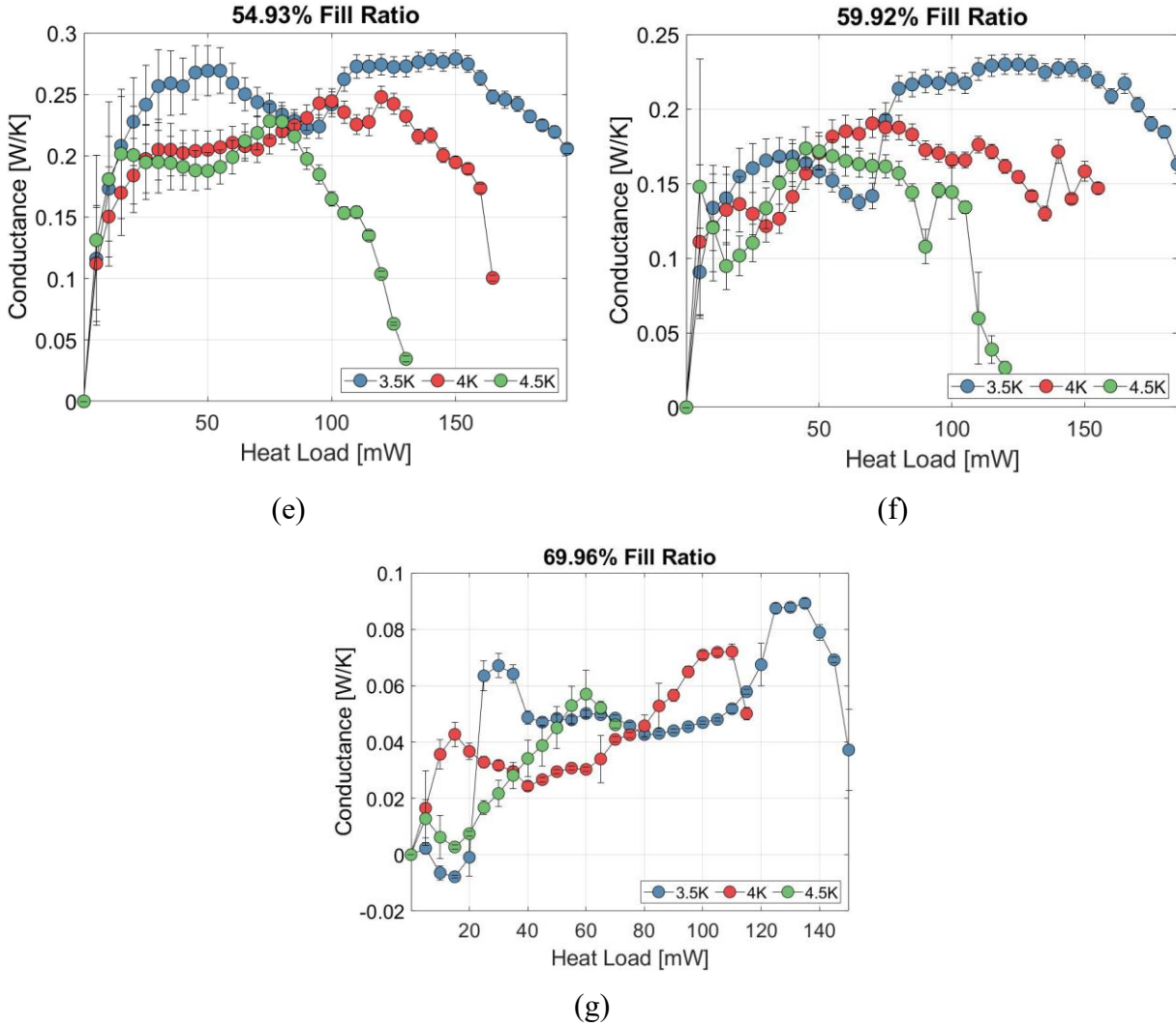
Figure 5.8. The HCPHP's effective conductance as a function of applied heat load for fixed fill ratios and variable condenser temperatures. The dashed lines in (b) represent calculated capillary limits per section 2.2.

As evident in Figure 5.8, the maximum conductance achieved does not occur at the maximum allowable heat load for any given combination of fill ratio and condenser temperature. Indeed, the HCPHP can operate at applied heat loads far greater than the heat load at which the best performance is observed, albeit with reduced thermal performance. This effect is observed for all fill ratios but is especially prevalent for fill ratios below 54.93% and is not dependent on the condenser temperature. Furthermore, the condenser temperature seems to influence the HCPHP's failure mode. A thermal runaway effect is observed with a 3.5 K condenser temperature, while for

a 4 K or 4.5 K condenser temperature, a low-performing steady-state is established after a precipitous performance drop.

The HCPHP's best performance is observed for the 44.92% fill ratio, slightly above the fill ratio assumed by the capillary limit. The maximum conductances for the 44.92% fill ratio are: 319 mW/K at 90 mW, 301 mW/K at 35 mW, and 324 mW/K at 25 mW for constant condenser temperatures of 3.5 K, 4 K, and 4.5 K, respectively. Moreover, the maximum allowable heat load is improved even further by increasing the fill ratio to 44.92%, which suggests that the capillary limit calculation may not account for all aspects of the HCPHP's flow. The maximum allowable heat loads with a 44.92% fill ratio are: 150 mW, 135 mW, and 105 mW for constant condenser temperatures of 3.5 K, 4 K, and 4.5 K, respectively. Although the performance is slightly reduced with a fill ratio of 50.02%, the maximum allowable heat load is further increased to an impressive 175 mW for a 3.5 K condenser temperature while conducting heat above 200 mW/K. With a 50.02% fill ratio, the maximum conductances are 296 mW/K at 35 mW, 270 mW/K at 85 mW, and 287 mW/K at 25 mW, and the maximum allowable heat loads are 175 mW, 150 mW, and 120 mW, for constant condenser temperatures of 3.5 K, 4 K, and 4.5 K, respectively.

When filled above 50.02%, the HCPHP's thermal performance declines significantly, as detailed in the following section. However, the effect of the condenser temperature is essentially the same as observed for the fill ratios below 50.02%. The maximum values for conductance and applied heat are listed in Table 5.5 for all combinations of condenser temperature and fill ratio. Additionally, these performance maxima are plotted in Figure 5.9. Together, Table 5.5 and Figure 5.9 summarize the results of the HCPHP experiments. Figure 5.9 demonstrates that, for a given fill ratio, the condenser temperature has a much greater effect on the maximum allowable heat load than on the maximum conductance. Indeed, within the optimal range (40.12% - 54.93%), the effect

of the condenser temperature on the maximum conductance is ambiguous. However, Table 5.5 shows that the maximum conductance generally occurs at a higher heat load for colder condenser temperatures, with a fixed fill ratio.

Table 5.5. Performance summary of HCPHP tests.

3.5 K condenser temperature

Fill Ratio	Maximum allowable heat load [mW]	Maximum Conductance [mW/K]	Heat load at maximum conductance [mW]
30.89%	65	206	25
40.12%	115	302	50
44.92%	150	319	90
50.02%	175	296	35
54.93%	195	279	150
59.92%	185	230	120
69.96%	150	89	135

4 K condenser temperature

Fill Ratio	Maximum allowable heat load [mW]	Maximum Conductance [mW/K]	Heat load at maximum conductance [mW]
30.89%	5	114	5
40.12%	100	304	35
44.92%	135	301	35
50.02%	150	270	85
54.93%	165	248	120
59.92%	155	190	70
69.96%	115	72	110

4.5 K condenser temperature

Fill Ratio	Maximum allowable heat load [mW]	Maximum Conductance [mW/K]	Heat load at maximum conductance [mW]
30.89%	N/A	N/A	N/A
40.12%	80	261	15
44.92%	105	324	25
50.02%	120	287	25
54.93%	130	228	75
59.92%	120	175	45
69.96%	70	57	60

(a)   (b)
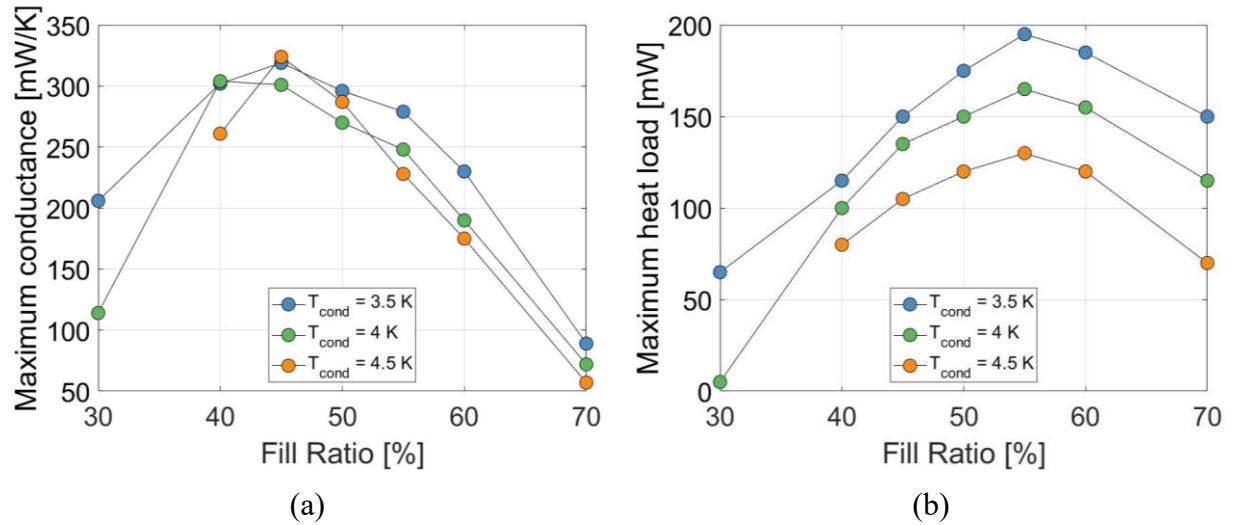
Figure 5.9. Maximum (a) conductance and (b) heat load as functions of fill ratio for multiple fixed condenser temperatures.

5.5.2. Effect of Fill Ratio

The influence of the fill ratio on the HCPHP's performance can be illuminated by replotting the data with constant condenser temperature. Figures 5.10, 5.11, and 5.12 show the HCPHP's thermal conductance as a function of heat load for low and high fill ratio ranges, with 3.5 K, 4 K, and 4.5 K condenser temperatures, respectively. The low fill ratio range is chosen to be 50.02% and below, and the high range is 54.93% and above due to consistent features within each range.

Figure 5.10 (a) shows that the performances with a 3.5 K condenser temperature follow a similar trend with increasing heat load. The fill ratio, within this low range, essentially dictates the heat load at which deviations from the global trendline occur; however, the global performance trendline is seemingly independent of the fill ratio. Interestingly, a global trendline is not observed for the low fill ratio range when the condenser temperature is increased to 4 K or 4.5 K, as shown in Figures 5.11 (a) and 5.12 (a). Within the high fill ratio range, the HCPHP's thermal conductance generally decreases with increasing fill ratio for all condenser temperatures. Beyond 54.93%, the thermal performance is significantly reduced from the peak at 44.92%.

(a)   (b)
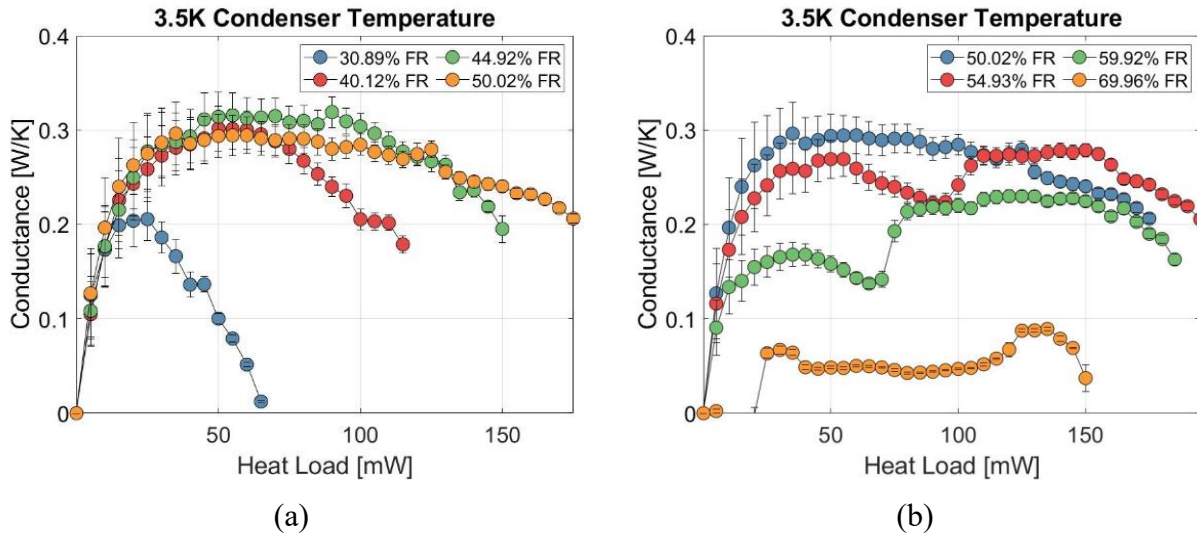
Figure 5.10. The HCPHP's effective conductance as a function of applied heat load for a 3.5 K condenser temperature with (a) low and (b) high fill ratios.

Furthermore, the maximum allowable heat load increases with increasing fill ratio within the low fill ratio range for all condenser temperatures. In the high fill ratio range, however, the maximum allowable heat load continues to increase until a fill ratio of 54.93% is reached, beyond which it begins to decrease with increasing applied heat. The peak maximum allowable heat load is achieved at a 54.93% fill ratio for all condenser temperatures tested. Additionally, despite the significantly reduced thermal conductance values observed with high fill ratios, the HCPHP can

transfer more heat at higher fill ratios. However, for all condenser temperatures tested, as the fill ratio is increased beyond 50.02%, the HCPHP's effective conductance swiftly deteriorates, evident in Figures 5.10 (b), 5.11 (b), and 5.12 (b).

(a)   (b)
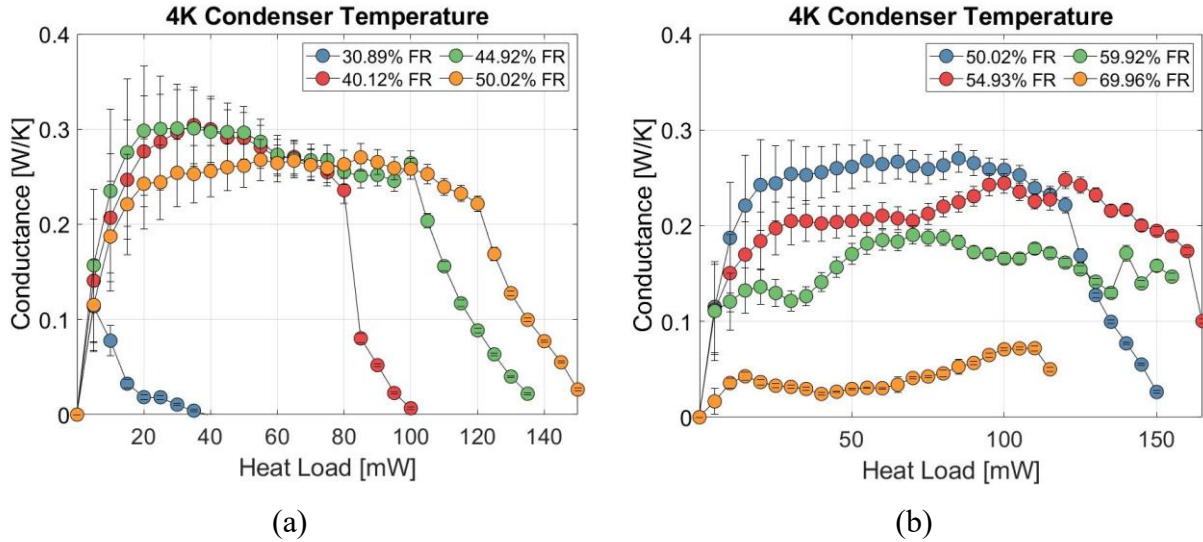
Figure 5.11. The HCPHP's effective conductance as a function of applied heat load for a 4 K condenser temperature with (a) low and (b) high fill ratios.

(a)   (b)
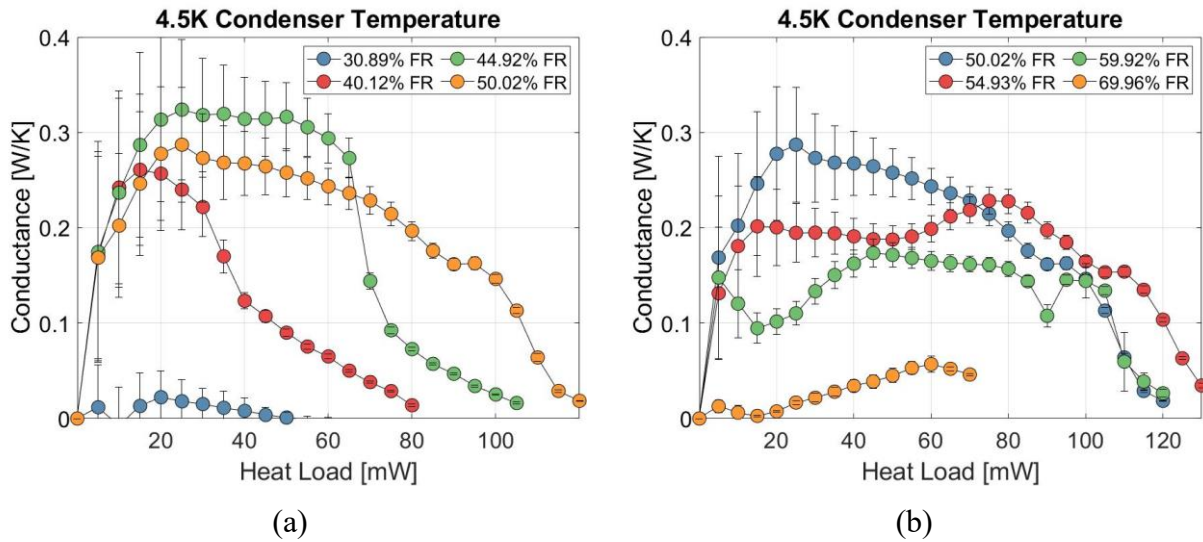
Figure 5.12. The HCPHP's effective conductance as a function of applied heat load for a 4.5 K condenser temperature with (a) low and (b) high fill ratios.

Moreover, when filled above 50.02%, the HCPHP's performance trend with increasing applied heat changes significantly. Notably, with a 3.5 K condenser temperature, a typical performance trend is initially observed for low heat loads until an unexpected sharp performance increase occurs. This observation is also somewhat evident for high condenser temperatures, but the performance increases more gradually.

5.6. HCPHP Thermohydraulic Analysis

Notably, the HCPHP can conduct more heat than the helium LHP developed by Ku and Robinson (175 mW versus 140 mW), with significantly less physical complexity and over a significantly greater distance (250 mm versus approximately 40 mm) [83]. Additionally, the HCPHP has greater thermal conductance (45.7 mW/K/turn versus 6.7 mW/K/turn) and can transfer more heat (27.9 mW/turn versus 4.2 mW/turn) than the horizontal helium PHP tested by Li, Li, and Xu [14], again over a greater distance (250 mm versus 100 mm). Thus, the HCPHP design constitutes a significant improvement over contemporary helium heat pipes in terms of both thermal performance and physical characteristics (flexibility, vibration damping, cost/ease of manufacturing). However, while the HCPHP's thermal performance is impressive compared to other helium heat pipes unassisted by gravity, helium PHPs in the vertical orientation display significantly greater thermal conductance (324 mW/K versus 784 mW/K) and can transfer more heat (195 mW versus 590 mW) over significantly longer distances (250 mm versus 1750 mm).

A heat pipe's performance is generally dictated by the fluid's effectiveness in transferring heat to the evaporator and to the condenser sections. Indeed, only the convective resistances in the overall thermal resistance network can vary depending on the heat pipe's various operational parameters. Therefore, the heat transfer coefficients of the evaporator and condenser sections serve as the link between the thermodynamic and hydrodynamic characteristics of the heat pipe, so the

HCPHP conductance is worse than a gravity-assisted PHP because the heat transfer coefficients in the evaporator and/or condenser section are reduced. First, the hydrostatic pressure differential that pumps the fluid in a gravity-assisted PHP (around 1000 Pa) is much greater than the capillary pumping pressure that drives the fluid flow in the HCPHP (around 10 Pa). Greater driving forces permit greater viscous resistive forces, resulting in a faster-moving fluid that can more effectively transfer heat to a solid boundary. Second, gravity-assisted helium PHPs are comprised uniformly of capillary tubes (0.5 mm ID) smaller than the shell tubes of the HCPHP (1.6 mm ID), which likely affects the coverage of saturated liquid in the evaporator section. Indeed, boiling heat transfer is enhanced in microtubes due to the saturated liquid wicking and coating the internal surfaces of the tubes [71 - 73], resulting in enduring thin liquid film boiling. The larger HCPHP tubes likely benefit less, or not at all, from this capillary enhancement, while the PHP tubes are likely small enough to achieve greater heat transfer coefficients. Similar capillary enhancements may also occur in the condenser section.

Additionally, the HCPHP's failure modes differ from those of PHPs and depend on the condenser temperature. For a low condenser temperature (3.5 K), the failure mode is a thermal runaway in which complete thermal isolation is achieved between the condenser and evaporator. However, for warmer condenser temperatures (4 K and 4.5 K), thermal runaway was not observed prior to the arbitrarily imposed high-temperature limit (8 K), and instead, the HCPHP operated at a steady state with poor heat transfer performance due to an elevated evaporator temperature. These observations are likely a result of the different temperature dependencies of the relevant two-phase fluid properties. First, the surface tension of helium is reduced by approximately 32% and 63% when the temperature is increased from 3.5 K to 4 K and from 3.5 K to 4.5 K, respectively. However, the saturated liquid viscosity of helium decreases only by approximately 6% and 14%

for the same temperatures increases. Thus, increasing the condenser temperature affects the capillary pumping force significantly more than the viscous resistive forces.

For low fluid temperatures (3.5 K), the capillary pumping force is strong enough to ensure adequate circulation against the resistive viscous forces. Failure at high heat loads occurs due to the boiling limit in the wick being reached, in which the wick-containing portion of the evaporator section does not contain enough saturated liquid to form substantial interfaces. Thus, the capillary pumping force vanishes and circulation of the flow ceases, causing a thermal runaway effect. The capillary limit is reached before the boiling limit for high condenser temperatures (4 K and 4.5 K). Since the capillary pumping force is reduced significantly (but not eliminated entirely) at high operating temperatures, the viscous resistive forces can become large relative to the capillary pumping force, resulting in abated fluid velocities in both tubes. Thus, the fluid is not stagnant and does not thermally run away, but its movement is slow enough to result in very poor heat transfer in the evaporator and condenser sections. In either case, superheating of the fluid in the evaporator section and vapor return tubes does not occur, suggesting that the "dry-out" condition typical for PHP failure does not occur in the HCPHP. Therefore, the rise in temperature of the evaporator section results from very poor heat transfer to the fluid rather than sensible heating of the fluid. If the heat load were to continue to be increased, the boiling limit would likely be reached for the high-temperature cases, and thermal runaway would be observed. Moreover, the complete thermal disconnection between the evaporator and condenser sections due to the boiling limit indicates that the HCPHP could be a valid option for a passive thermal switch [33, 39, 55].

For fill ratios 50.02% and below, the performance trend as a function of heat load generally initially increases rapidly until a peak is reached, then subsequently decreases gradually with increasing heat load. The strong initial influence of the heat load starting from zero applied heat

may be explained by the evolving meniscus shapes in the evaporator and condenser sections with increasing heat load. With no heat load applied, the menisci of the evaporator and condenser sections have the same radius of curvature, resulting in a zero net capillary pumping force. With heat applied to the evaporator (and extracted by the condenser), the opposing phase changes at each end affect the meniscus shapes differently. Vaporization in the evaporator causes the saturated liquid to recede into the wick, decreasing the meniscus radius, while condensation at the opposite end causes the wick to flood with saturated liquid, increasing the meniscus radius. With increasing heat load, the evaporator meniscus will tend to a small radius of curvature limited by the wick geometry, while the condenser meniscus radius of curvature will tend to infinity. Developing the maximum capillary pumping force may require an appreciable heat load to drive the mass transfer across the two-phase interfaces such that the meniscus radius of curvature is minimized in the evaporator and maximized in the condenser. Thus, the capillary pumping force increases significantly with increasing heat load due to the evolving shapes of the two-phase interfaces at each end, which further explains the strong heat load dependence of the heat pipe's conductance at low heat loads.

After the peak value, the heat pipe's conductance gradually decreases as the applied heat load increases. Since the capillary pumping force is maximized, the loss of thermal performance must be due to growing viscous forces. Unlike conventional heat pipes, the constrained flow path of the HCPHP may result in a nontrivial saturated liquid and vapor distribution. First, the incoming vapor flow to the condenser may exit to the wick-containing tubes without fully condensing, and the gaps between microtubes in the wick-containing adiabatic tubes are small enough such that alternating liquid plugs and vapor slugs can form, much like in a PHP. Moreover, the physical

separation of the intended liquid and vapor flow paths does not allow the vapor trapped in the wick to escape to the vapor side.

Unlike in the wick-containing tubes, the hollow vapor return tubes are too large for two-phase interfaces perpendicular to the flow direction to form [87]. Therefore, distinct plugs and slugs are not formed, and the excess liquid is instead stagnant and stratified, held to the bottom of the tube by gravity. These arguments suggest that although the vapor return tubes can contain liquid, the mass flow in these tubes is essentially entirely saturated vapor, while the mass flow in the wick-containing tubes may be a combination of saturated liquid and vapor. Notably, the characteristics of the stagnant liquid contained in the vapor return tubes may depend on the heat load, temperature, and fill ratio and may significantly affect the flow characteristics of the hollow tubes and the heat transfer in the evaporator and condenser sections. Regardless, the mass distribution envisioned within by the constrained HCPHP flow path is variable depending on the fill ratio, applied heat, and temperature, which differs from conventional heat pipes, which feature a static mass distribution where the wick contains only saturated liquid and the return flow path contains only saturated vapor.

For a fixed fill ratio and temperature, as the heat load increases, the mass distribution, which is inherently variable due to the HCPHP's constrained flow path, likely favors additional liquid in the wick-containing tubes. Initially unutilized liquid inventory contained in the hollow vapor return tubes becomes active in the flow circuit as the applied heat increases. Therefore, because the wick-containing tubes are more tortuous than the hollow tubes, the increasing saturated liquid fraction of the wick-containing tubes with increasing heat load results in greater viscous resistance, which reduces the flow velocities and the heat transfer coefficients in the evaporator and/or condenser.

Another somewhat unintuitive implication of the HCPHP's constrained flow path is that the mass flow rate may not be linearly proportional to the applied heat, as in conventional heat pipes. For a conventional heat pipe, since the opposing mass flows are strictly saturated liquid or saturated vapor, the mass flow rate equals the applied heat divided by the enthalpy of vaporization. Since the mean thermodynamic phase of the fluid flowing through the wick-containing tubes can vary depending on the various operational parameters, the enthalpy difference between adjacent tubes is also variable and is a function of the applied heat. Therefore, mass flow rates and flow velocities can remain constant or even decrease with increasing applied heat if the enthalpy difference between the hollow and wick-containing tubes increases with increasing applied heat.

For all fill ratios, increasing the condenser temperature results in a significant reduction in the amount of heat that the heat pipe can transfer; A result consistent with the capillary limit evaluation. Indeed, increasing the operating temperature reduces the capillary pumping force since the two-phase surface tension fluid property decreases significantly with increasing temperature. However, the calculated capillary limit is fortuitously exceeded by significant margins for fill ratios above 40.12%. This phenomenon is likely a result of an incorrect assumed saturated liquid/vapor distribution and an overestimation of the meniscus radius of curvature in the evaporator. First, the capillary limit calculation assumes that the wick-containing tubes contain only saturated liquid and that the adjacent hollow tubes contain only saturated vapor. While this may be true for a conventional heat pipe, the aforementioned constrained flow path of the HCPHP does not guarantee this saturated fluid distribution. Stagnant liquid can exist in the hollow tubes, and vapor plugs can flow through the wick-containing tubes, corresponding to lower-than-expected viscous resistance forces since the wick-containing tubes are more tortuous.

Second, the meniscus radius of curvature, which determines the magnitude of the capillary pumping force, is somewhat ambiguous due to the HCPHP's wick geometry. Indeed, there is no convenient "pore radius" value to use in the calculation. The two-phase interfaces responsible for generating the largest pumping pressures likely exist between the outer surfaces of adjacent microtubes in the wick, as opposed to the inside of the microtubes, and as such, can be arbitrarily small. In this regard, the microtube bundle is a somewhat effective wick structure despite its simplicity. Furthermore, it is believed that the heat pipe outperformance of the capillary limit is due to the aforementioned calculation errors, as opposed to a heat transfer enhancement via oscillatory flow modes. First, perpendicular two-phase interfaces are unlikely to form in the vapor return tubes, making oscillatory PHP-like flows impossible. Second, due to helium's meager saturated density ratio (7.4 at atmospheric pressure), the oscillatory flow modes typical for PHPs are likely ineffective at distances comparable to the HCPHP's adiabatic length.

6. Conclusions and Future Work

This experimental study has characterized many aspects of the performance of helium PHPs as a function of fill ratio, adiabatic length, and applied heat load and explained them in terms of the forces acting on the fluid. First, performance was determined via temperature measurements of the evaporator and condenser sections. However, characterizing the measured performance required a novel configuration of temperature and pressure sensors in the adiabatic section, providing substantial fluid phase and flow behavior information. Notably, this experimental study has determined the thermosiphon-like nature of vertically oriented helium PHPs, the different failure modes dependent on fill ratio, an improved definition of the optimal fill ratio, the importance of the balance between viscous and buoyancy forces acting on the fluid, characteristic fluid velocity measurements, and transitions between different two-phase flow regimes.

The most important conclusions drawn from this work are summarized in the following points:

- Helium pulsating heat pipes are primarily gravity-driven in the vertical orientation, behaving like a thermosiphon. This result is evidenced by the observed mass imbalance between adjacent tubes and uni-directional flow in both the time-averaged and time-series data analyses. This mass imbalance, or density difference, between adjacent tubes increases with increasing heat load and fill ratio.

- Many variations of partial or fully single-phase operating modes are stable and common, an observation that deviates significantly from the typical PHP two-phase plug-slug flow regime.

- The dominant forces for vertically oriented pulsating heat pipes are the gravitational forces driving the fluid flow and the viscous forces opposing the fluid flow.

- The optimal fill ratio corresponds to the scenario in which the amount of liquid is maximized without occupying the hot adiabatic tubes. Any additional liquid inventory will increase viscous losses and reduce the gravitational driving forces, resulting in performance degradation.

- Failure occurs below the optimal fill ratio when the liquid replenishment to the evaporator cannot overcome the applied heat load, resulting in sensible heating or dry-out. Above the optimal fill ratio, failure occurs due to excessive viscous losses.

- The effective conductivity, prior to dry-out, increases with applied heat load due to the increasing heat transfer coefficients of boiling and condensation, which may be affected more by the characteristics of the thin liquid film than the inlet/outlet fluid velocities.

- Length-independent performance can be explained by proportional increases in both the gravitational driving forces and the viscous resistive forces with increasing adiabatic length, which effectively negates each other.

- Global plug-slug flow in helium pulsating heat pipes is only observed at very low applied heat loads before half the tubes transition to annular flow.

An equation of motion can be derived by analyzing a simple one-dimensional momentum balance for a liquid plug contained in a PHP that describes the general fluid motion. In extremes of length and orientation, the equation of motion is simplified, and the AC and DC flow modes are separated. In summary, very short PHPs are not significantly affected by gravity or viscosity, and their motion depends primarily on the stochastic AC flow modes generated through phase change in the evaporator and condenser. However, the relevant forces are the opposite for very long PHPs, where gravity and viscosity dominate, and only the DC flow modes generated by gravity remain. Thus, a PHP becomes more gravity-dependent as its length increases, so horizontal PHPs are

unlikely to work if their adiabatic sections are long. Notably, thermal modeling of long-distance and vertically oriented PHPs may not be challenging since the AC flow modes, which are notoriously difficult to characterize, can be neglected.

Furthermore, the vastly improved heat transport ability of the Hybrid-Conventional Pulsating Heat Pipe over the current state-of-the-art helium heat pipes is demonstrated in this work. The HCPHP is capable of carrying up to 195 mW of heat with thermal conductances up to 324 mW/K over a 250 mm heat transfer distance. While the operating principles of the HCPHP align closely with those of a conventional heat pipe, a few key design differences result in distinctive thermal behaviors. Inspired by dual-diameter PHPs, the HCPHP is the first heat pipe of its kind to intentionally incorporate a wicking structure within alternating adiabatic section tubes of a multi-turn pulsating heat pipe to drive fluid circulation via capillary forces. Heat pipes utilizing helium, a poor working fluid choice (yet necessary for the desired temperature range), require a more effective wicking structure than single capillary tubes, so a rudimentary bundled microtube wick is adopted instead of the dual-diameter design. Developing improved HCPHP-compatible wick structures that allow for appreciable and effective heat transport over farther distances is particularly important.

Presently, many characteristics of the HCPHP's thermohydraulic behavior implied by the performance measurements cannot be explained by surface tension and viscosity alone. For example, the effect of the HCPHP's fill ratio is not straightforward. The storage of excess liquid due to high fill ratios reduces thermal conductance but does not significantly affect the maximum allowable heat load. Additionally, while gravity does not drive the HCPHP's flow, it likely affects the distribution of saturated liquid/vapor and, thus, the heat transfer characteristics. Further investigations of the exact HCPHP mass distribution as a function of heat load, fill ratio, and

temperature are required for a more complete thermohydraulic characterization considering all operational parameters. Steady-state and transient data from adiabatic section temperature measurements may aid such analyses. Additionally, repeatability, hysteresis, and thermal stability tests may be necessary to further probe the robustness of the HCPHP's observed performance. In summary, the high demand for orientation-independent heat pipes operating at saturated helium temperatures has warranted the design of a novel helium heat pipe geometry, the Hybrid-Conventional Pulsating Heat Pipe, which has experimentally demonstrated significant thermal performance improvements over contemporary options.

This work has demonstrated the inefficacy of helium PHPs in gravitationally unfavorable conditions for long-distance applications. This result is unfortunate but provides researchers with the correct direction for future studies. General knowledge of pulsating heat pipe operations is not gained through vertically oriented and long-distance PHP experimental studies, as these heat pipes operate as thermosiphons. Researchers should instead only investigate uniform-diameter PHPs in the horizontal orientation so that the oscillatory flow modes can be separated and studied. Moreover, the lack of heat pipe options for the saturated helium temperature range, coupled with the fact that helium PHPs are strongly dependent on gravity, strongly indicates that future research should focus on alternative helium heat pipe solutions. The hybrid conventional-pulsating heat pipe (HCPHP) developed in this work is the first step towards a long-distance helium heat pipe that can operate without gravity assistance.

References

[1] H. Akachi, "Structure of a Heat Pipe," US Patent 4921041, May. 1, 1990.

[2] X. Han, X. Wang, H. Zheng, X. Xu, and G. Chen, "Review of the development of pulsating heat pipe for heat dissipation," *Renewable and Sustainable Energy Reviews*, vol. 59, pp. 692–709, Jun. 2016. doi:10.1016/j.rser.2015.12.350.

[3] M. Alhuyi Nazari *et al.*, "A review on pulsating heat pipes: From solar to cryogenic applications," *Applied Energy*, vol. 222, pp. 475–484, Jul. 2018. doi:10.1016/j.apenergy.2018.04.020.

[4] S. Khandekar, N. Dollinger, and M. Groll, "Understanding operational regimes of closed loop pulsating heat pipes: An experimental study," *Applied Thermal Engineering*, vol. 23, no. 6, pp. 707–719, Apr. 2003. doi:10.1016/s1359-4311(02)00237-5.

[5] P. Charoensawan, S. Khandekar, M. Groll, and P. Terdtoon, "Closed loop pulsating heat pipes part A: parametric experimental investigations," *Applied Thermal Engineering*, vol. 23, no. 16, pp. 2009–2020, Nov. 2003. doi:10.1016/s1359-4311(03)00168-6.

[6] S. Khandekar, P. Charoensawan, M. Groll, and P. Terdtoon, "Closed loop pulsating heat pipes part B: Visualization and semi-empirical modeling," *Applied Thermal Engineering*, vol. 23, no. 16, pp. 2021–2033, Nov. 2003. doi:10.1016/S1359-4311(03)00159-5.

[7] A. Yoon and S. J. Kim, "Understanding of the thermo-hydrodynamic coupling in a micro pulsating heat pipe," *International Journal of Heat and Mass Transfer*, vol. 127, pp. 1004–1013, Dec. 2018. doi:10.1016/j.ijheatmasstransfer.2018.06.092.

[8] E. Silk, *Introduction to Spacecraft Thermal Design*. Cambridge, United Kingdom: Cambridge University Press, pp. 165 – 226, 2020.

[9] E. T. White and R. H. Beardmore, "The velocity of rise of single cylindrical air bubbles through liquids contained in vertical tubes," *Chemical Engineering Science*, vol. 17, no. 5, pp. 351–361, 1962. doi:10.1016/0009-2509(62)80036-0.

[10] B. L. Drolen and C. D. Smoot, "Performance limits of oscillating heat pipes: Theory and validation," *Journal of Thermophysics and Heat Transfer*, vol. 31, no. 4, pp. 920–936, Oct. 2017. doi:10.2514/1.t5105.

[11] J. Eninger and D. Edwards, "Excess liquid in heat-pipe vapor spaces," *12th Thermophysics Conference*, Jun. 1977. doi:10.2514/6.1977-748.

[12] L. D. Fonseca, "Experimental characterization of cryogenic helium pulsating heat pipes," Ph.D. dissertation, University of Wisconsin – Madison, 2016.

[13] L. D. Fonseca, J. Pfotenhauer, and F. Miller, "Short communication: Thermal performance of a cryogenic helium pulsating heat pipe with three evaporator sections," *International Journal of Heat and Mass Transfer*, vol. 123, pp. 655–656, Aug. 2018. doi:10.1016/j.ijheatmasstransfer.2018.03.013.

[14] M. Li, L. Li, and D. Xu, "Effect of filling ratio and orientation on the performance of a multiple turns helium pulsating heat pipe," *Cryogenics*, vol. 100, pp. 62–68, Jun. 2019. doi:10.1016/j.cryogenics.2019.04.006.

[15] X. Sun et al., "Investigation on the temperature dependence of filling ratio in cryogenic pulsating heat pipes," *International Journal of Heat and Mass Transfer*, vol. 126, pp. 237–244, Nov. 2018. doi:10.1016/j.ijheatmasstransfer.2018.05.147.

[16] A. Faghri, "Review and advances in Heat pipe science and technology," *Journal of Heat Transfer*, vol. 134, no. 12, Oct. 2012. doi:10.1115/1.4007407.

[17] P. Nemec, "Gravity in heat pipe technology," *Gravity - Geoscience Applications, Industrial Technology and Quantum Aspect*, Feb. 2018. doi:10.5772/intechopen.71543.

[18] A. Faghri, *Heat Pipe Science and Technology*. Global Digital Press, 1995.

[19] A. Yoon and S. J. Kim, "Understanding of the thermo-hydrodynamic coupling in a micro pulsating heat pipe," *International Journal of Heat and Mass Transfer*, vol. 127, pp. 1004–1013, Dec. 2018. doi:10.1016/j.ijheatmasstransfer.2018.06.092.

[20] A. Yoon and S. J. Kim, "Experimental and theoretical studies on oscillation frequencies of liquid slugs in micro pulsating heat pipes," *Energy Conversion and Management*, vol. 181, pp. 48–58, Feb. 2019. doi:10.1016/j.enconman.2018.11.060.

[21] M. Barba, R. Bruce, A. Bonelli, and B. Baudouy, "Experimental study of large-scale cryogenic pulsating heat pipe," *IOP Conference Series: Materials Science and Engineering*, vol. 278, p. 012156, Dec. 2017. doi:10.1088/1757-899x/278/1/012156.

[22] J. M. Pfotenhauer, L. D. Fonseca, C. Xu, and F. K. Miller, "Characterizing helium pulsating heat pipes," *IOP Conference Series: Materials Science and Engineering*, vol. 502, p. 012058, Apr. 2019. doi:10.1088/1757-899x/502/1/012058.

[23] J. Gu, M. Kawaji, and R. Futamata, "Microgravity performance of micro pulsating heat pipes," *Microgravity - Science and Technology*, vol. 16, no. 1–4, pp. 181–185, Mar. 2005. doi:10.1007/bf02945972.

[24] M. Mameli *et al.*, "Thermal response of a closed loop pulsating heat pipe under a varying gravity force," *International Journal of Thermal Sciences*, vol. 80, pp. 11–22, Jun. 2014. doi:10.1016/j.ijthermalsci.2014.01.023.

[25] M. Slobodeniuk *et al.*, "Experimental study of the flat plate pulsating heat pipe operation during dry-out and flow re-activation periods under microgravity conditions," *International Journal of Multiphase Flow*, vol. 147, p. 103888, Feb. 2022. doi:10.1016/j.ijmultiphaseflow.2021.103888.

[26] M. Li, L. Li, and D. Xu, "Effect of number of turns and configurations on the heat transfer performance of helium cryogenic pulsating heat pipe," *Cryogenics*, vol. 96, pp. 159–165, Dec. 2018. doi:10.1016/j.cryogenics.2018.09.005.

[27] J. L. Xu, Y. X. Li, and T. N. Wong, "High speed flow visualization of a closed loop pulsating heat pipe," *International Journal of Heat and Mass Transfer*, vol. 48, no. 16, pp. 3338–3351, Jul. 2005. doi:10.1016/j.ijheatmasstransfer.2005.02.034.

[28] S. Li *et al.*, "Visualization study on the flow characteristics of a nitrogen pulsating heat pipe," *International Communications in Heat and Mass Transfer*, vol. 143, p. 106722, Apr. 2023. doi:10.1016/j.icheatmasstransfer.2023.106722.

[29] Z. H. Xue and W. Qu, "Experimental and theoretical research on a ammonia pulsating heat pipe: New full visualization of flow pattern and operating mechanism study," *International Journal of Heat and Mass Transfer*, vol. 106, pp. 149–166, Mar. 2017. doi:10.1016/j.ijheatmasstransfer.2016.09.042.

[30] D. Xu, L. Li, and H. Liu, "Experimental investigation on the thermal performance of helium based cryogenic pulsating heat pipe," *Experimental Thermal and Fluid Science*, vol. 70, pp. 61–68, Jan. 2016. doi:10.1016/j.expthermflusci.2015.08.024.

[31] R. Bruce, M. Barba, A. Bonelli, and B. Baudouy, "Thermal performance of a meter-scale horizontal nitrogen pulsating heat pipe," *Cryogenics*, vol. 93, pp. 66–74, Jul. 2018. doi:10.1016/j.cryogenics.2018.05.007.

[32] U. Mmeje, "Experimental investigation and analysis of pure fluid and mixture pulsating heat pipes with varying condenser temperatures, heat loads, and fill ratios", Ph.D. dissertation, University of Wisconsin – Madison, 2021.

[33] B. Mueller, "The performance of pulsating heat pipes as thermal switches in redundant cryocooler systems," Ph.D. dissertation, University of Wisconsin – Madison, 2021.

[34] C. Xu, "Performance characterization of a helium PHP via Fluent," Ph.D. dissertation, University of Wisconsin – Madison, 2022.

[35] L. D. Fonseca, J. Pfotenhauer, and F. Miller, "Results of a three evaporator cryogenic helium pulsating heat pipe," *International Journal of Heat and Mass Transfer*, vol. 120, pp. 1275–1286, May 2018. doi:10.1016/j.ijheatmasstransfer.2017.12.108.

[36] J. M. Pfotenhauer, X. Sun, A. Berryhill, and C. B. Shoemaker, "The influence of aspect ratio on the thermal performance of a cryogenic pulsating heat pipe," *Applied Thermal Engineering*, vol. 196, p. 117322, Sep. 2021. doi:10.1016/j.applthermaleng.2021.117322.

[37] L. D. Fonseca, F. Miller, and J. Pfotenhauer, "A helium based pulsating heat pipe for superconducting magnets," *AIP Conference Proceedings*, 2014. doi:10.1063/1.4860679.

[38] L. D. Fonseca, M. Mok, J. Pfotenhauer, and F. Miller, "Progress of cryogenic pulsating heat pipes at UW-Madison," *IOP Conference Series: Materials Science and Engineering*, vol. 278, p. 012052, Dec. 2017. doi:10.1088/1757-899x/278/1/012052.

[39] L. Kossel, J. Pfotenhauer, A. Kashani, and F. Miller, "A novel thermal bus architecture for large cryogenic space telescopes utilizing helium pulsating heat pipes," *Cryogenics*, vol. 139, p. 103807, Apr. 2024. doi:10.1016/j.cryogenics.2024.103807.

[40] L. Kossel, J. Pfotenhauer, and F. Miller, 16-2: "Investigations of the Gravity Dependence of Large-Scale Helium Pulsating Heat Pipes," *Cryocoolers 23: Proceedings of the 23rd International Cryocooler Conference*," ICC Press, Vol. 23, 2024.

[41] L. Kossel, J. Pfotenhauer, and F. Miller, "Experimental investigations of the thermodynamic phases, flow behaviors, and thermal performance for meter-scale helium pulsating heat pipes," University of Wisconsin – Madison, Department of Mechanical Engineering, 2024 (Manuscript submitted for publication).

[42] L. Kossel, J. Pfotenhauer, and F. Miller, O12-C01-4190: "The Effect of Fill Ratio on the Performance and Flow Regime for Long-Distance Helium Pulsating Heat Pipes," *Proceedings of the 28th International Cryogenic Engineering Conference and International Materials Conference 2022*." Springer Nature and Zhejiang University Press, Vol. 70, 2023.

[43] L. Kossel, J. Pfotenhauer, and F. Miller, 14-3: "Performance Comparison of Long-Distance Helium Pulsating Heat Pipes with Varying Adiabatic Lengths," *Cryocoolers 22: Proceedings of the 22nd International Cryocooler Conference*," ICC Press, Vol. 22, 2022.

[44] L. Kossel, J. Pfotenhauer, and F. Miller, 54: "Experimental Investigation of Phase and Flow Behavior Trends of Long-Distance Helium Pulsating Heat Pipes," *Proceedings of the Joint 21st International Heat Pipe Conference and 15th International Heat Pipe Symposium*, 2023, (Accepted for Publication).

[45] NASA Technology Roadmaps, TA 14.1.1: Thermal Management Systems, Cryogenic Systems, Passive Thermal Control, 2015.

[46] M. Schaffer and C. Wenner, "A study of cryogenic propulsive stages for human exploration beyond low earth orbit," *Proc. Global Space Exploration Conference*, 2012.

[47] D. W. Plachta, W. L. Johnson, and J. R. Feller, "Zero boil-off system testing," *Cryogenics*, vol. 74, pp. 88–94, Mar. 2016. doi:10.1016/j.cryogenics.2015.10.009 [48] NASA, Origin Space Telescope Mission Concept 2 Flyer, Dec. 2018.

[49]"Origins Concept-2 Baseline Design," Origins space telescope, https://origins.ipac.caltech.edu/page/technology (accessed Jun. 27, 2023).

[50] D. Leisawitz *et al.*, "Origins space telescope: Trades and decisions leading to the Baseline Mission Concept," *Journal of Astronomical Telescopes, Instruments, and Systems*, vol. 7, no. 01, Jan. 2021. doi:10.1117/1.jatis.7.1.011014.

[51] M. DiPirro, L. Fantano, T. D'Asto, B. Gavares, and The Origins Study Team, "Origins space telescope cryo-thermal system," *Journal of Astronomical Telescopes, Instruments, and Systems*, vol. 7, no. 01, Feb. 2021. doi:10.1117/1.jatis.7.1.011009.

[52] M. Meixner *et al.,* "Origins space telescope mission concept study report," NASA Origins Space Telescope Study Team, Aug. 2019.

[53] M. J. DiPirro *et al.*, "Cryocooling Technologies for the Origins Space Telescope," *Journal of Astronomical Telescopes, Instruments, and Systems*, vol. 7, no. 01, Jan. 2021. doi:10.1117/1.jatis.7.1.011008.

[54] C. Bradford *et al.,* "The PRIMA Far-Infrared Probe: Observatory and Instrumentation," *American Astronomical Society Meeting Abstracts*, vol. 54, no. 6, 2022.

[55] B. Mueller, J. Pfotenhauer, and F. Miller, "Performance of nitrogen pulsating heat pipes as passive thermal switches in a redundant cryocooler application," *Applied Thermal Engineering*, vol. 196, p. 117213, Sep. 2021. doi:10.1016/j.applthermaleng.2021.117213.

[56] M. Mahesh and P. B. Barker, "The MRI helium crisis: Past and future," *Journal of the American College of Radiology*, vol. 13, no. 12, pp. 1536–1537, Dec. 2016. doi:10.1016/j.jacr.2016.07.038.

[57] T. Mito *et al.*, "Development of highly effective cooling technology for a superconducting magnet using cryogenic OHP," *IEEE Transactions on Applied Superconductivity*, vol. 20, no. 3, pp. 2023–2026, Jun. 2010. doi:10.1109/tasc.2010.2043724.

[58] F. Bonnet, P. Gully, and V. Nikolayev, "Development and test of a cryogenic pulsating heat pipe and a precooling system," *AIP Conference Proceedings*, vol. 1434, pp. 607–614, Jun. 2012. doi:10.1063/1.4706970.

[59] D. Ortiz-Vega, "A new wide range equation of state for helium-4," Ph.D. dissertation, Texas A&M University, 2013

[60] S. Klein, EES-Engineering Equation Solver, 2020

[61] Sumitomo Cryogenics Group, SRDK-415D2 Cold Head Capacity Map, 2019. https://www.shicryogenics.com/product/rdk-415d2-4k-cryocooler-series/

[62] J. E. Fesmire and W. L. Johnson, "Cylindrical cryogenic calorimeter testing of six types of multilayer insulation systems," *Cryogenics*, vol. 89, pp. 58–75, Jan. 2018. doi:10.1016/j.cryogenics.2017.11.004

[63] R. J. Moffat, "Describing the uncertainties in experimental results," *Experimental Thermal and Fluid Science*, vol. 1, no. 1, pp. 3–17, Jan. 1988. doi:10.1016/0894-1777(88)90043-x

[64] H. Ma, "Thin Film Evaporation," in *Oscillating Heat Pipes*, Springer, 2015, pp. 47–75

[65] V. K. Karthikeyan, S. Khandekar, B. C. Pillai, and P. K. Sharma, "Infrared thermography of a pulsating heat pipe: Flow regimes and multiple steady states," *Applied Thermal Engineering*, vol. 62, no. 2, pp. 470–480, Jan. 2014. doi:10.1016/j.applthermaleng.2013.09.041

[66] K.-H. Chien, Y.-T. Lin, Y.-R. Chen, K.-S. Yang, and C.-C. Wang, "A novel design of pulsating heat pipe with fewer turns applicable to all orientations," *International Journal of Heat and Mass Transfer*, vol. 55, no. 21–22, pp. 5722–5728, Oct. 2012. doi:10.1016/j.ijheatmasstransfer.2012.05.068

[67] D. Mangini *et al.*, "Hybrid pulsating heat pipe for space applications with non-uniform heating patterns: Ground and microgravity experiments," *Applied Thermal Engineering*, vol. 126, pp. 1029–1043, Nov. 2017. doi:10.1016/j.applthermaleng.2017.01.035

[68] S. Sato and H. Ogata, "Film condensation heat transfer of helium in a vertical tube," *Cryogenics*, vol. 16, no. 4, pp. 221–224, Apr. 1976. doi:10.1016/0011-2275(76)90264-2

[69] H. Ogata and S. Sato, "Forced convection heat transfer to boiling helium in a tube," *Cryogenics*, vol. 14, no. 7, pp. 375–380, Jul. 1974. doi:10.1016/0011-2275(74)90077-0

[70] J. A. Miller, "Heat transfer in the Oscillating Turbulent Boundary Layer," *ASME 1969 Gas Turbine Conference and Products Show*, Mar. 1969. doi:10.1115/69-gt-34

[71] F. Yang *et al.*, "Enhanced flow boiling in microchannels by self-sustained high frequency two-phase oscillations," *International Journal of Heat and Mass Transfer*, vol. 58, no. 1–2, pp. 402–412, Mar. 2013. doi:10.1016/j.ijheatmasstransfer.2012.11.057

[72] S. G. Kandlikar, "History, advances, and challenges in liquid flow and flow boiling heat transfer in microchannels: A critical review," *2010 14th International Heat Transfer Conference, Volume 8*, Jan. 2010. doi:10.1115/ihtc14-23353

[73] D. E. Kim, D. I. Yu, D. W. Jerng, M. H. Kim, and H. S. Ahn, "Review of boiling heat transfer enhancement on micro/nanostructured surfaces," *Experimental Thermal and Fluid Science*, vol. 66, pp. 173–196, Sep. 2015. doi:10.1016/j.expthermflusci.2015.03.023

[74] S. Khandekar, A. P. Gautam, and P. K. Sharma, "Multiple quasi-steady states in a closed loop pulsating heat pipe," *International Journal of Thermal Sciences*, vol. 48, no. 3, pp. 535–546, Mar. 2009. doi:10.1016/j.ijthermalsci.2008.04.004

[75] M. Rao, F. Lefèvre, S. Khandekar, and J. Bonjour, "Understanding transport mechanism of a self-sustained thermally driven oscillating two-phase system in a capillary tube," *International Journal of Heat and Mass Transfer*, vol. 65, pp. 451–459, Oct. 2013. doi:10.1016/j.ijheatmasstransfer.2013.05.067

[76] Y. Li, Q. Wang, S. Chen, B. Zhao, and Y. Dai, "Experimental investigation of the characteristics of Cryogenic Oscillating Heat Pipe," *International Journal of Heat and Mass Transfer*, vol. 79, pp. 713–719, Dec. 2014. doi:10.1016/j.ijheatmasstransfer.2014.08.061

[77] D. Zhang, Z. He, E. Jiang, C. Shen, and J. Zhou, "A review on start-up characteristics of the pulsating heat pipe," *Heat and Mass Transfer*, vol. 57, no. 5, pp. 723–735, Nov. 2020. doi:10.1007/s00231-020-02998-4

[78] X. Han, X. Wang, H. Zheng, X. Xu, and G. Chen, "Review of the development of pulsating heat pipe for heat dissipation," *Renewable and Sustainable Energy Reviews*, vol. 59, pp. 692–709, Jun. 2016. doi:10.1016/j.rser.2015.12.350

[79] G. H. Kwon and S. J. Kim, "Operational characteristics of pulsating heat pipes with a dual-diameter tube," *International Journal of Heat and Mass Transfer*, vol. 75, pp. 184–195, Aug. 2014. doi:10.1016/j.ijheatmasstransfer.2014.03.032

[80] B. Holley and A. Faghri, "Analysis of pulsating heat pipe with capillary wick and varying channel diameter," *International Journal of Heat and Mass Transfer*, vol. 48, no. 13, pp. 2635–2651, Jun. 2005. doi:10.1016/j.ijheatmasstransfer.2005.01.013

[81] K.-S. Yang, Y.-C. Cheng, M.-S. Jeng, K.-H. Chien, and J.-C. Shyu, "An experimental investigation of micro pulsating heat pipes," *Micromachines*, vol. 5, no. 2, pp. 385–395, Jun. 2014. doi:10.3390/mi5020385

[82] C. Jung and S. J. Kim, "Investigation into the effects of passive check valves on the thermal performance of pulsating heat pipes," *International Journal of Heat and Mass Transfer*, vol. 204, p. 123850, May 2023. doi:10.1016/j.ijheatmasstransfer.2023.123850

[83] J. Ku and F. Robinson, "Thermal Vacuum Testing of a Helium Loop Heat Pipe for Large Area Cryocooling," *Proc. 46th International Conference on Environmental Systems*, vol. ICES-2016-25, pp. 1–14, Jul. 2016.

[84] P. Gully, "Superfluid helium heat pipe," *Physics Procedia*, vol. 67, pp. 625–630, 2015. doi:10.1016/j.phpro.2015.06.106

[85] P. Gully, "Long and high conductance helium heat pipe," *Cryogenics*, vol. 64, pp. 255–259, Nov. 2014. doi:10.1016/j.cryogenics.2014.04.002

[86] K. Takahata *et al.*, "Hydraulic characteristics of cable-in-conduit conductors for large helical device," *Advances in Cryogenic Engineering*, vol. 45, pp. 1111–1118, 2000. doi:10.1007/978-1-4615-4215-5_20

[87] C. Rascón, A. O. Parry, and D. G. Aarts, "Geometry-induced capillary emptying," *Proceedings of the National Academy of Sciences*, vol. 113, no. 45, pp. 12633–12636, Oct. 2016. doi:10.1073/pnas.1606217113